

Conical Diffraction: Complexifying Hamilton's Diabolical Legacy

Mike R. Jeffrey

A thesis submitted to the University of Bristol in
accordance with the requirements of the degree of
Ph.D. in the Faculty of Science

H. H. Wills Physics Laboratory
September 2007

word count 32,795

Abstract

The propagation of light along singular directions in anisotropic media teems with rich asymptotic phenomena that are poorly understood. We study the refraction and diffraction of light beams through crystals exhibiting biaxial birefringence, optical activity, and dichroism. The optical properties and length of the crystal are related to the beam's width, wavenumber, and alignment, by just three parameters defined by the effect of the crystal on a paraxial plane wave.

Singular axes are crystal directions in which the refractive indices are degenerate. In transparent biaxial crystals they are a pair of optic axes corresponding to conical intersections of the propagating wave surface. This gives rise to the well understood phenomenon of conical diffraction. Our interest here is in dichroic and optically active crystals. Dichroism splits each optic axis into pairs or rings of singular axes, branch points of the complex wave surface. Optical activity destroys the optic axis degeneracy but creates a ring of wave surface inflection points. We study the unknown effect of these degeneracy structures on the diffracted light field, predicting striking focusing and interference phenomena. Focusing is understood by the coalescence of real geometric rays, while geometric interference is included by endowing rays with phase to constitute complex rays. Optical activity creates a rotationally symmetric cusped caustic surface threaded by an axial focal line, which should be easy to observe experimentally. Dichroism washes out focusing effects and the field is dominated by exponential gradients crossing anti-Stokes surfaces.

A duality is predicted between dichroism and beam alignment for gaussian beams: both are described by a single parameter controlling transition between conical and double refraction. For transparent crystals we predict simple optical angular momentum effects accompanied by a torque on the crystal. We also report new observations with a biaxial crystal that test the established theory of conical diffraction.

For Fiona.

Acknowledgments

A debt of gratitude to my supervisor, Michael Berry, for presenting me with such a wonderfully old problem, the opportunity to delve into dusty volumes penned by the giants of 19th century physics, conjure phenomena with echoes through two centuries of researches on light, and dabble in the mathematical heart of physics old and new.

My perspective on physics owes so much to the insightful teaching of John Hannay and Michael Berry, and I thank them for a glimpse of that curious geometric world with which physics is rendered comprehensible. For their guidance, encouragement, and nudging in new directions, I am thankful to: John Hannay, John Nye, John Alcock, Jonathan Robbins, and Jon Keating. In my work I have occasionally relied on the help of people not called Jo(h)n, among them: Matthias Schmidt, who I thank for his daring and patience in confronting a century old german tome; James Lunney and Masud Mansuripur who I thank for their collaborative contribution; Miss Turner and Mr Everitt (and his pet brick), who helped mould a young enquiring mind; and Mark Dennis, whose advice was invaluable in the transition of this unlearned undergrad into a naive but infinitesimally more learned postgrad.

I would like to thank Michael and his family for their hospitality throughout my PhD research. Also, even the solitary musings of a theorist turn stale without the distractions of one's fellow theory group inmates (listed in order of decoherence on an average Friday): Tony, Cath, Bramms, Luis, another John, Morgan, Nadav, Gary, Andy \times 2. Thanks also to Steve for helping me master $\La\{\tau\}ek\$\%$.

My dearest thanks to those who have made it easy for me to indulge, and even encouraged me to continue, in endless distractions mathematical and physical, above all: my wife and her family, Fluffy, and the distinguished UH alumni.

We are all students, but some of us will never learn.

Authors Declaration

I declare that the work in this thesis was carried out in accordance with the regulations of the University of Bristol. The work is original except where indicated by special reference in the text, and no part of the thesis has been submitted for any other academic award. Any views expressed in the thesis are those of the author.

SIGNED

DATE

*“They, that will, may suppose it an aggregate of various peripatetic qualities.
Others may suppose it multitudes of unimaginable small and swift corpuscles ..
springing from shining bodies at great distances one after another;
but yet without any sensible interval of time, and continually urged forward ..
But they, that not like this, may suppose light any other corporeal emanation,
or any impulse or motion of any other medium,
or aethereal spirit diffused through the main body of aether,
or what else they can imagine proper for this purpose ..
To avoid dispute, and make this hypothesis general,
let every man here take his fancy;
only whatever light be, I suppose it consists of rays
differing from one another in contingent circumstances,
as bigness, form or vigour.”*

Isaac Newton on the nature of light, Royal Society, 1675
(Whittaker 1951)

This thesis includes the following content published by the author:

Chapter 4.1

Berry M V, & Jeffrey M R, (2007) Progress in Optics *in press*
Hamilton's diabolical point at the heart of crystal optics

Chapter 4.2

Berry M V, & Jeffrey M R, (2006) J.Opt.A **8** 363-372
Chiral conical diffraction

Chapters 3 and 4.2

Jeffrey M R, (2006) Photon06 online conference proceedings
<http://photon06.org/Diffractive%20optics%20Thurs%2014.15.pdf>
Conical diffraction in optically active crystals

Chapter 4.3

Berry M V, & Jeffrey M R, (2006) J.Opt.A **8** 1043-1051
Conical diffraction complexified: dichroism and the transition to double refraction

Chapter 4.4

Jeffrey M R, (2007) J.Opt.A **9** 634-641
The spun cusp complexified: complex ray focusing in chiral conical diffraction

Chapter 4.5

Berry M V, Jeffrey M R & Mansuripur M J, (2005) J.Opt.A **7** 685-690
Angular momentum in conical diffraction

Chapter 4.6

Berry M V, Jeffrey M R & Lunney J G, (2006) Proc.R.Soc.A **462** 1629-1642
Conical diffraction: observations and theory

Contents

1	Introduction	1
1.1	Historical Context	4
1.2	History of the Phenomenon	7
2	Paraxial Optics and Asymptotics	17
2.1	Optics of Anisotropic Crystals	18
2.2	Principles of Paraxial Light Propagation	23
2.3	Hamiltonian Formulation	26
2.4	Complex Ray Directions: So Where Should We Point The Beam?	32
2.5	Eigenwave Representation	35
2.6	Asymptotics of the Geometrical Optics Limit	37
2.7	. . . and Hamilton’s Principle	41
2.8	Inside the Crystal	44
3	The Wave Surfaces	47
3.1	Fresnel’s Wave Surface and Hamilton’s Cones	48
3.2	The Paraxial Phase Surfaces	54
4	The Phenomena of “So-Called” Conical Diffraction	59
4.1	Biaxial Crystals	61
4.1.1	So-called conical refraction	64
4.1.2	Diffraction in the rings	66
4.1.3	Uniformisation and rings in the focal image plane	71
4.1.4	The bright axial spike	74
4.2	Biaxial Crystals with Optical Activity	77
4.2.1	The “trumpet horn” caustic of chiral conical refraction	80

4.2.2	Voigt's "Trompeten Trichters": rays inside the chiral crystal	81
4.2.3	Diffraction and the caustic horn	84
4.2.4	Uniformisation over the caustic	86
4.2.5	The Stokes set	88
4.2.6	The spun cusp and axial spot	90
4.2.7	Fringes near the focal plane	94
4.3	Dichroic Biaxial Crystals	97
4.3.1	Conical refraction complexified	99
4.3.2	Complex geometric interference	101
4.3.3	Gaussian beams and the transition to double refraction	104
4.3.4	A note on circular dichroism	111
4.3.5	Imaginary conical refraction	112
4.4	Dichroic Biaxial Crystals with Optical Activity	114
4.4.1	Chiral conical refraction complexified	116
4.4.2	The complex whisker	118
4.4.3	Diffraction	120
4.4.4	The complexified spun cusp	122
4.5	Angular Momentum in Conical Diffraction	124
4.5.1	Paraxial optical angular momentum	124
4.5.2	Nonchiral	125
4.5.3	Chirality dominated	126
4.5.4	Strongly biaxial or chiral crystals	127
4.5.5	Torque on the crystal	127
4.6	Observations of Biaxial Conical Diffraction	129
5	Concluding Remarks	137
A	Solutions to the chiral quartic	145
B	Spherical conical refraction	147
C	Glossary of key symbols	151
	Bibliography	153

List of Figures

1.1	Lloyd's discovery of conical refraction	8
1.2	Conical diffraction of a pencil of rays	9
1.3	The conical refraction lunes	10
1.4	Photographs of chiral conical diffraction	11
1.5	The diabolical point	13
2.1	Fresnel's wave surface and rotated coordinates	22
2.2	The parameters of paraxial conical refraction	26
2.3	The Poincaré Sphere	31
2.4	Real and complex rays in stationary phase analysis	43
3.1	The optic axes	49
3.2	Duality of the wave and ray surfaces	52
3.3	Geometry of internal and external conical refraction	53
3.4	The paraxial wave surfaces	57
4.1	Evolution of the conical diffraction rings	62
4.2	Simulation of the conical diffraction ring evolution	63
4.3	The rays of internal conical refraction	65
4.4	The rays of external conical refraction	65
4.5	Asymptotics of the secondary rings	69
4.6	The regimes of conical diffraction	70
4.7	Rings in the focal image plane	73
4.8	Aperture-induced oscillations in the focal plane	74
4.9	Intensity of the axial spike	75
4.10	Intensity sections of the bright caustic horn	78

4.11	The rings of chiral conical diffraction	79
4.12	Rays of chiral conical refraction	81
4.13	Ray intensity through the crystal	83
4.14	Projected ray intensity through the crystal	83
4.15	Ray trajectories through the crystal	83
4.16	Saddlepoints of the wave function	84
4.17	Geometrical optics with phase	86
4.18	Asymptotics of the chiral Airy fringes	88
4.19	Stokes' phenomenon	88
4.20	Geometry of chiral conical diffraction	90
4.21	The spun cusp catastrophe	91
4.22	Cusp and spot competition	92
4.23	Stokes' phenomenon on the axis	93
4.24	Focal image plane intensity profile	94
4.25	The chiral conical diffraction coffee swirl	96
4.26	Loci of critical points of dichroic conical refraction	100
4.27	Dominant asymptotics of dichroic conical diffraction	101
4.28	Transition from transparent to dichroic conical diffraction for a pinhole incident beam	102
4.29	Complex ray interference for a pinhole incident beam	103
4.30	Transition from conical diffraction to double refraction for a gaussian inci- dent beam	105
4.31	Complex ray interference for a gaussian incident beam	106
4.32	Dichroic spots and Bessel shoulders	107
4.33	Dichroic endpoint interference for a gaussian beam	108
4.34	Higher order interference fringes	109
4.35	The transition from double refraction to conical diffraction	110
4.36	Circular dichroism in conical diffraction	112
4.37	Imaginary conical refraction	113
4.38	Chiral transition	115
4.39	Dichroic chiral wave intensity profiles	116
4.40	Dichroic intensity in 3D	117
4.41	Ray intensity and Stokes lines	118

4.42	Geometry of the complex whisker	120
4.43	Geometrical interference	121
4.44	Exponential swamping of the chiral conical diffraction rings	121
4.45	The complexified spun cusp	122
4.46	Angular momentum of conical diffraction	126
4.47	Asymptotic angular momentum oscillations	127
4.48	Observing conical diffraction	130
4.49	Photographs of the transition from conical diffraction to double refraction .	130
4.50	Photographs of conical diffraction	132
4.51	Conical diffraction profiles	133
4.52	Experimental rings	134
4.53	Experimental secondary fringes	134
4.54	Experimental axial spike	135
A.1	Elements of the solutions to the quartic chiral ray equation	146
B.1	Spherical conical refraction	147

List of Tables

1.1	Historical summary of conical diffraction experiment parameters	7
2.1	Symmetries of non-centrosymmetric crystals	20

Chapter 1

Introduction

*“This phenomenon was exceedingly striking.
It looked like a small ring of gold viewed upon a dark background;
and the sudden and almost magical change of the appearance,
from two luminous points to a perfect luminous ring,
contributed not a little to enhance the interest.”*

Lloyd’s description of internal conical refraction (Lloyd 1837)

In 1832 William Rowan Hamilton predicted an observable singularity within Fresnel’s theory of double refraction. In one stroke, the field of singular optics was born and a sensation began that would take 173 years to run its course. Despite its prompt confirmation by experiment and the beautiful mathematical simplicity of Hamilton’s theory, the phenomenon was long hindered by controversy and misconception. Victorian mathematics contained only the initial sparks of the asymptotic techniques which would be needed to achieve a full understanding.

When light is incident along the optic axis of a biaxial crystal, the surface of a refracted wave as described by Fresnel develops a *conoidal cusp* or *diabolical point*, and a single ray refracts into an infinity of rays forming a hollow cone. This is the mathematical phenomenon of conical refraction. Over the years further questions have been raised as to how other natural properties of crystals, such as optical activity and absorption, would alter the phenomenon, and attempts to understand these have also met with little success.

For such a simple and fundamental phenomenon, conical refraction has retained re-

markably strong ties to advances both in mathematical and experimental physics. The theory has proven to be a playground in which to explore, test, and pose new questions of the evolving field of asymptotics. Numerical simulations continue to test the power of computational simulation. Experimentally, new technologies in lasers and synthetic crystals have made it possible to begin viewing, with unprecedented accuracy, the refraction and diffraction phenomena predicted by theory. Throughout, the defining principle of conical refraction appears to be that it exists in the middleground between physical limits: the short wavelength limit of geometrical optics embraced by Hamilton, and the long wavelength limit of diffraction optics embraced by Huygens. It is this straddling of theories that places neither in a position to fully explain the phenomenon, and it is this obstacle that has characterised the struggle to tame Hamilton's diabolical legacy.

Conical refraction is of profound historical significance to mathematical physics as well as singular optics. It appears to have been the earliest example in history of a mathematical construction making a prediction that preceded experimental observation, particularly one so counterintuitive. (The nearest precedent came in 1816 when Augustin Fresnel presented his diffraction theory to the French Academy of Sciences, prompting Poisson's objection that it would predict a bright spot at the centre of the shadow of a circular screen, upon which Dominique Arago verified its existence experimentally. However, Giacomo Maraldi and Joseph-Nicolas Delisle had pre-empted this discovery by a century). Humphrey Lloyd's 1833 experimental confirmation of conical refraction was the first hard evidence favouring Fresnel's wave theory of light over the corpuscular point of view, and the origin of singular optics.

Hamilton's original theory represents the first substantial use of phase space in physics, and marks the first discovery of a conical (or diabolical) intersection. Such conical intersections have arisen abundantly since, as fundamental degeneracies central to processes as diverse as quantum mechanics, chemical dynamics, geophysics, and photo-biochemistry. Commonly they manifest as degeneracies in potential energy surfaces, for example in the Jahn-Teller effect (Herzberg & Longuet-Higgins 1963, Applegate et al. 2003), in the Born-Oppenheimer adiabatic theory applied to nuclear motion (Mead & Truhlar 1979, Juanes-Marcos et al. 2005, Clary 2005, Halász et al. 2007) where they provide a pathway for radiationless decay between electronic states of atoms, in seismic shear waves propagating through the Earth modelled as a slow varying anisotropic medium (Rümpker & Thompson 1994, Rümpker & Kendall 2002), in determining DNA stability with respect

to UV radiation (Schultz 2004), and in the photo-biochemical processes of vision (Hahn & Stock 2001, Andruniow et al. 2004, Kukura & etc 2007), to barely scratch the surface.

Gradual advances in the theory of conical refraction have awaited the coming of age of integral phase methods (Heading 1962), primarily their interpretation through physical asymptotics (Keller 1961, Berry & Mount 1972). Recently the theory has led to the discovery of new and seemingly paradoxical mathematics, whereby asymptotic phenomena are dominated by subdominant exponential contributions within diffraction integrals (Berry 2004*a*). This effect is characteristic of the defiance of conical refraction towards limiting behaviour in physics, and we will meet it in detail later.

The evolution of conical diffraction, that is conical refraction and the wave effects central to it, is well suited to presentation in a historical setting. However, the techniques brought in to tackle the problem over the years have varied greatly. Instead I will reformulate the theory. For example, our starting point will be to find Fresnel's wave surface from Maxwell's equations, though these were unknown in Fresnel's lifetime and barely within Hamilton's. Instead their insights were derived by pure geometrical reasoning. We will show that such geometric induction still has a role to play throughout the optical theory.

The interplay of rays and waves underlying even the basic phenomenon will make its own importance known. We will see the necessity of geometrical optics in discovering focal effects and absorption gradients. Then we shall see how (to use a phrase coined by Kinber in Kravtsov (1968)), 'sewing the wave flesh on the classical bones' leads eventually to a full understanding of the physics behind conical diffraction. Thus we marry two disparate limits: the basic ray theory of geometrical optics derived from Hamilton's principle, and the exact diffraction theory derived, appropriately, by a Hamiltonian formulation. The simplification of paraxiality will be paramount. This reduces the number of parameters that specify the incident beam and refracting crystal from twenty-three to just four. The theory will include polarisation effects and we discuss these where important, though our main concern will be the intensity structure revealed by unpolarised incident light beams.

A rigorous derivation of crystal optics based on Maxwell's equations will be made in chapter 2. This is rendered soluble by the powerful approximation of paraxiality, leading to a Hamiltonian description of plane wave propagation in a crystal possessing biaxial birefringence, optical activity, and anisotropic absorption. The physical asymptotics required to understand the paraxial theory are outlined and interpreted through geometrical optics. In chapter 3 we consider a vital intuitive object, Fresnel's wave surface, and its

counterpart in our Hamiltonian theory. The main original contribution of these chapters is the extension of their content to absorbing crystals, and the relating of the diffraction theory to geometrical optics. Chapter 4 reveals the rich phenomena of conical diffraction by applying the preceding theory, beginning with a reformulation of the theory of conical diffraction in biaxial crystals including a few minor new results. Subsequently we discover new phenomena that arise from optical activity and dichroism, uncover the optical angular momentum and torque associated with conical diffraction, and report an experimental verification of the biaxial theory. In an appendix we extend the theory to crystals of arbitrary geometry.

First let me present the foundations of conical diffraction, beginning with the scientific setting in which the phenomenon was conceived. Then, although historically theory has remained ahead of experiment, I shall review the latter first. The aim is to present the basic phenomenon in a nontechnical way and to motivate the theory which is the main subject of this thesis. This background serves as a literature review and will not be a prerequisite for the foregoing chapters, since we shall reformulate the theory in a unified and coherent manner.

1.1 Historical Context

Conical refraction enters at the peak of historical interest in the nature of light, amidst a climax in the contest between undulatory and corpuscular theories, entwined in the earliest roots of wave asymptotics and singular optics.

The modern theory of light has its origins in Christian Huygens' 1677 wave theory, with which he explained the observation of double refraction (bifurcation of rays) in crystals such as Iceland spar (calcite) and quartz. But this failed to explain David Brewster's 1813 discovery of biaxiality in the mineral topaz, whereby double refraction disappears along two *optic axis* directions in the crystal. This profound observation was the first step towards Hamilton's discovery of conical diffraction. Huygens' theory also did not explain diffraction and did not account for polarisation, seeming to need two different luminous media to produce double refraction. This failure favoured the corpuscular theories backed by the intellectual might of Pierre-Simon Laplace and Isaac Newton. Newton posited an explanation for polarisation in which rays have 'sides' (though his exact predisposal towards the corpuscular view is summed up by his quotation in the matter fronting this

thesis). Sensing defeat of the wave theory, double refraction was chosen as the subject of a prize competition by the French Academy of Sciences in 1808. Etienne-Louis Malus was the victor following his discovery of polarisation by reflection, and his winning theory was questionably interpreted as unpholding the corpuscular philosophy.

Augustin Fresnel reversed this triumph in 1816 by presenting his transverse wave theory, developing on principles established by Thomas Young (transverse waves) and Huygens (wavefront propagation). In a few short years he discovered the wave theories of refraction and diffraction, and gained the Academy prize for Diffraction in 1818. Details of this fascinating period in history are in Whittaker (1951).

Hamilton's formulation of geometrical optics married the wave theory of Fresnel with the ray method of Newton. Describing light rays as the normals to level surfaces of some characteristic function, the theory was first published in 1828 (Hamilton 1828). In it he also discussed light caustics, which will arise later in our predictions for chiral conical diffraction. In his first supplement Hamilton extended his method to diffraction, but the most refined and general form is given in the extensive 3rd supplement (Hamilton 1837), where lies the theoretical prediction of conical refraction. This phenomenon, considered "in the highest degree novel and remarkable" (Lloyd 1837), was a consequence of four degeneracies in Fresnel's wave surface.

In a biaxial medium Fresnel's wave surface has two sheets associated with two (ordinary and extraordinary) rays of double refraction. A pair of distorted ellipsoids, the surfaces intersect at four points that lie along Brewster's optic axes. This was known to Fresnel and Airy, and had been studied extensively by James MacCullagh who unsuccessfully tried to claim that the physical effect was implicit in his work "when optically interpreted" (Graves 1882). But the connection between the precise geometry and the physical phenomena resulting were conceived of only by Hamilton (Graves 1882, O'Hara 1982). Along the optic axes, the wave surfaces are conical in shape, their apexes touching to form a diaboloid. Rays normal to the surface would then be infinite in number, and form a narrow cone.

The experimental verification of this theoretical triumph is not historically viewed as the final condemnation of the corpuscular theory in favour of the transverse wave theory. That honour goes to more extensive experiments devised by François Arago (colours of thin plates 1831) and George Airy (speed of light in air and water, carried out by Foucault and Fizeau 1850), testing the constructions of Huygens and Fresnel to a high degree of precision. The discovery did much to increase scientific confidence in the theory, but is

typically regarded as verifying only a single feature of the wave surface. Stokes (1863), not fully appreciating the subtlety of Hamilton's work, stated that "the phenomenon is not competent to decide between several theories leading to Fresnel's construction as a near approximation" because, to some approximation, the geometry exploited by Hamilton "must be a property of the wave surface resulting from any reasonable theory". But according to Potter (1841), "many waverers were confirmed in their belief by so singular a coincidence of theory and experiment", and indeed Lloyd, who worked closely with Hamilton and furnished those important first experimental discoveries, "had a harvest of reputation from them, such as is seldom reaped in the field of science."

Later in life Hamilton, in correspondence with Guthrie Tait, reformulated his theory of conical refraction in terms of his quaternions (Wilkins 2005). Gibbs would not develop the vector algebra descending from quaternions for another twenty years.

The asymptotic methods now used to understand conical diffraction can be traced back to the study of Bessel's equation by Carlini in 1817 mentioned by Watson (1944). Profound contributions to the burgeoning field of integral asymptotics were made by Stokes, who in his study of Bessel functions confessed in correspondence to his future wife that "I tried till I almost made myself ill" until, at 3 o'clock in the morning, "I at last mastered it" (Stokes 1907). Although the Victorian importance of asymptotics in rendering integrals calculable is less significant in the computer age, it has become clear that only through asymptotics can the wave and ray phenomena of conical diffraction be understood. A detailed history of phase integral asymptotics can be found in Heading (1962).

Experiments in conical diffraction have been revolutionised by the advent of the laser, and in return conical diffraction has provoked interest in focusing and transforming laser beam modes. With technological advances in the manufacture of novel synthetic crystals, conical diffraction may prove to be of further interest. Recent years have also seen an explosion of experimentation in the optics of microspheres, minimal energy surfaces formed in the phase transitions that produce aerosols, colloids, and photonic crystals (Fève et al. 1994, Kofler & Arnold 2006). In light of this we include in Appendix B the extension of the theory to spherical crystals and arbitrarily curved interfaces. Discoveries reported here of simple angular momentum effects within conical diffraction, and a resulting torque on the crystal, have sparked interest in the phenomenon applied to optical trapping and manipulation (optical "tweezers"), currently undergoing preliminary study by a group at Trinity College, Dublin (Ireland).

1.2 History of the Phenomenon

There are two varieties of conical refraction predicted by Hamilton: *internal conical refraction* occurs when a ray strikes a crystal along its optic axis direction, refracts into a hollow cone inside the crystal, and refracts at the exit face into a hollow cylinder; *external conical refraction* occurs when a ray of light passes through a crystal internally along its optic axis, then refracts into a hollow cone at the exit face. The distinction is in the direction of incident rays, and that the cone appears inside the crystal in the former, outside it in the latter. We will review first the 173 years of experimental investigations into Hamilton’s prediction, summarised in table 1.1.

reference	crystal	n_1, n_2, n_3	A°	l/mm	$w/\mu\text{m}$	ρ_0
Lloyd ⁽¹⁸³⁷⁾	aragonite	1.533,1.686,1.691	0.96	12	≤ 200	≥ 1.0
Potter ⁽¹⁸⁴¹⁾	aragonite	1.533,1.686,1.691	0.96	12.7	12.7	16.7
Raman <i>et al</i> ⁽¹⁹⁴¹⁾	naphthalene	1.525,1.722,1.945	6.9	2	0.5	500
Schell <i>et al</i> ^(1978a)	aragonite	1.530,1.680,1.695	1.0	9.5	21.8	7.8
Mikhail. <i>et al</i> ⁽¹⁹⁷⁹⁾	sulfur	not provided	3.5	30	17	56
Fève <i>et al</i> ⁽¹⁹⁹⁴⁾	aragonite	1.764,1.773,1.864	0.92	2.56	53.0	1210
section 4.6 ⁽²⁰⁰⁶⁾	MDT	2.02, 2.06, 2.11	1.0	25	7.1	60

Table 1.1: Historical summary of conical diffraction experiment parameters, including principal refractive indices n_1, n_2, n_3 , cone angle A , crystal length l , beam width w , and the image-to-object ratio ρ_0 encompassing all six.

Lloyd had verified Hamilton’s prediction of conical refraction by December 1832, overcoming poor quality specimens of macled (polycrystalline) aragonite with a “fine specimen” obtained from Dollond, London. Lloyd possessed a profound understanding of the phenomenon, mentioning to Hamilton in a letter of December 18, 1832 (Graves 1882) that one should expect his prediction to be affected by some perturbation due to diffraction. He did not subsequently take this up, perhaps because he was unable to resolve such effects in his experiments, the most detailed description of which is given in Lloyd (1837). Figure 1.1(a) taken from this paper shows why: the thickness of the bright ring is such that it appears almost as a filled disc, because Hamilton’s cone, of which the ring is a section, has barely reached a great enough radius to exceed the incident beam width. Nevertheless

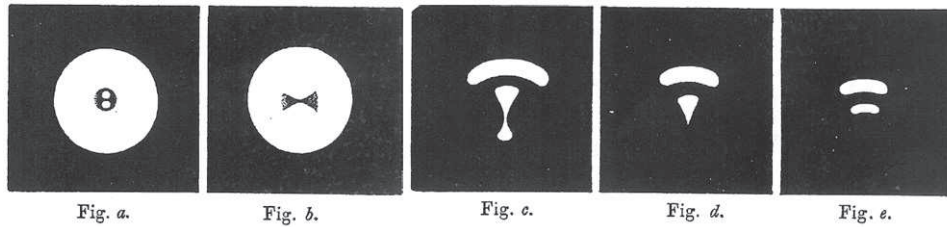


Figure 1.1: Lloyd's discovery of conical refraction: the transition from conical (a) to double (e) refraction, viewed through aragonite with a pinhole on the entrance face, illuminated by a distant lamp, reproduced from Lloyd (1837).

the transition, from conical refraction when the Lloyd's beam is aligned with his crystal's optic axis, to double refraction as the crystal is tilted off axis, can be clearly seen. The bright arches would eventually become the circular spots of double refraction under further misalignment. Lloyd describes this process in reverse in the quotation introducing this chapter.

Lloyd discovered that the polarisation in the external cone is linear and rotates only half a turn in a circuit of the axis (he then proved this theoretically, in analogy to the same effect for the internal cone already predicted by Hamilton). Lloyd's measured cone angle (see table 1.1) differed from Hamilton's prediction by only five minutes of arc. The conical refraction pattern of a nonchiral transparent crystal can be characterised by just one dimensionless parameter, the ratio ρ_0 of the cone radius at the exit face to the incident beam width. Lloyd's experiment utilised various pinholes that he did not specify, but the largest, used by ingenious method to determine the cone angle, was 0.016 inch (to 1-500th inch) in diameter, giving a measured ratio $\rho_0 = 0.98$ compared to Hamilton's theoretical $\rho_0 = 1.02$. This small ratio explains the poor resolution of figure 1.1(a), barely sufficient to verify the existence of the singularity predicted by Hamilton, but little improvable using the technology – oil lamps, sunlight, and handmade pinholes – of the time.

A wonderfully detailed account of an internal conical refraction experiment carried out on aragonite was given by Potter (1841), achieving a much better cone radius to beam width ratio of $\rho_0 = 16.7$ and vastly extending Lloyd's basic observations. A century before the effects would be rediscovered and explained, Potter noticed the importance of the focal image plane at a distance $1/n_2$ from the crystal exit face, where the most focused ring

image of the light source appears. In moving away from this plane he observed that there were two rings, not one. The outer spreads and fades with increasing distance from the focal plane as if it were a diverging cone, the inner converges onto a spot as if it were a converging cone with the bright spot in the farfield as its apex. Such a transformation is depicted in figure 1.2. Potter also emphasised, long before it was appreciated, the importance of imaging lenses enabling the virtual image inside the crystal to be realised. His invitation to controversy that his “results are certainly not in accordance with the theoretical investigations of Sir William Hamilton” appear to have been overlooked throughout the history of conical refraction, as have his observations, except for a reference in Melmore (1942). Unfortunately his theoretical understanding, and his polemic condemnation of the work of Hamilton and Lloyd due to it, was flawed. In 175 years of literature on conical refraction this work stands out for its probing depth of inquiry, both in far exceeding any other experiments to be conducted for another century, and in scrutinising the problems in the theory, of prime importance at a time when doubts over Fresnel’s wave theory were to linger for many years after.

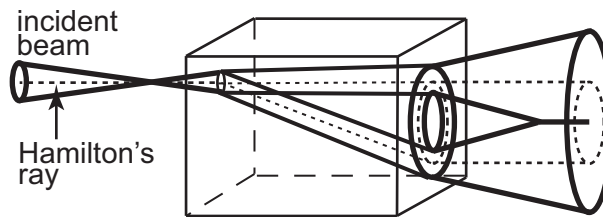


Figure 1.2: Conical diffraction of a pencil of rays along the optic axis of a biaxial crystal: the range of ray directions give rise to a pair of ray cones (bold) which encompass the dark cone (dashed) of Hamilton’s mathematical conical refraction, and their refraction at the exit face.

With Potter’s experiments overlooked, the first major revision of the phenomenon is attributed to Poggendorff (1839), and a single statement in a one page article that “diese beiden Bilder sich zu einem hellen Ringe vereinigen, der ein kohlschwarzes Scheibchen einschließt” (“the two [double refraction] images merge into a bright ring that encompasses a coal-black sliver”). This stimulated further experiments by Haidinger (1855), confirming that the bright ring of conical refraction was in fact a pair of concentric bright rings with a dark ring between. A simulation of this is shown in figure 1.3, including the polarisation pattern observed by Lloyd.

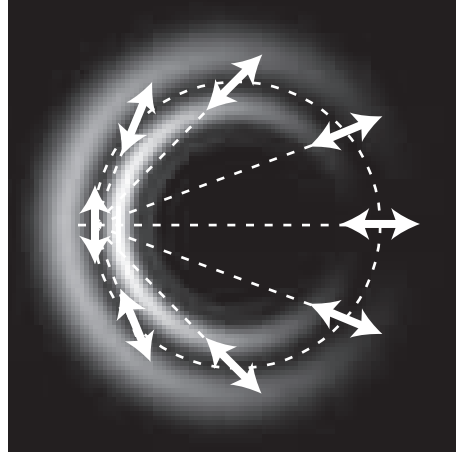


Figure 1.3: The conical refraction lunes: a pair of bright rings encompassing Poggendorff’s “coal black sliver”. The polarisation pattern in the rings is shown, overlaying a typical theoretical intensity image obtained either: with a vertically polarised incident beam, or with an unpolarised incident beam viewing the refracted rings through a vertical polariser.

According to Poggendorff the experiments seem to have obtained the reputation of being hard to carry out, at least ‘on the continent’. Indeed little detailed experimentation was reported as having been done, despite a few references to cursory examinations by Voigt in theoretical papers around 1905 (1905*a*, 1906, 1905*b*, 1905*c*) and an article by Raman (1921); Raman described an “arrangement for demonstrating conical refraction usually found in laboratories”, and noted that the observed field beyond the crystal was not yet well described, let alone understood.

This was corrected by Raman et al. (1941, 1942) using purpose-grown crystals of naphthalene. With a cone angle more than ten times greater than aragonite, naphthalene is much more suited to observing conical refraction. Although naphthalene sublimates at room temperature, images were obtained which remained unsurpassed throughout the century. These showed the conical refraction pattern evolving from focused rings to a farfield axial focal spot. They concluded incorrectly from their observations that there is only a single ring in the focal plane because they could not resolve the dark ring, a consequence of their extremely large ring-radius to beam-width ratio shown in table 1.1.

A detailed comparative study of theory and experiment was carried out by Schell &

Bloembergen (1978*a*), who were hampered by reverting to aragonite, but aided by lasers with a 30 micrometer beam width (see table 1.1). They obtained very good agreement with theory, but limited their investigation to the exit face. They also provided the first, and to our knowledge only, detailed images of the phenomenon in the presence of optical activity (Schell & Bloembergen 1978*b*). They again did not go beyond the exit face but photographed a polarisation pattern resembling a coffee swirl. This pattern occurs with a linearly polarised incident beam and was first described by Voigt (1905*b*), but has evaded any detailed understanding. Photographic images obtained from Schell & Bloembergen (1978*b*) are shown in figure 1.4 for later comparison to our theory.

Limited nonchiral images were obtained more recently by Perkal'skis & Mikhailichenko (1979) with sulfur. Far more striking is an experiment described by Fève et al. (1994) with a spherical crystal of KTP, where curvature modifies the evolution of the pattern but does not fundamentally alter the phenomenon. This approach offers a useful method for studying conical diffraction and is deserving of the further discussion in appendix B. Recent advances in the technologies of lasers and synthetic crystals also make possible a more detailed study of the original phenomenon, given here in section 4.6.

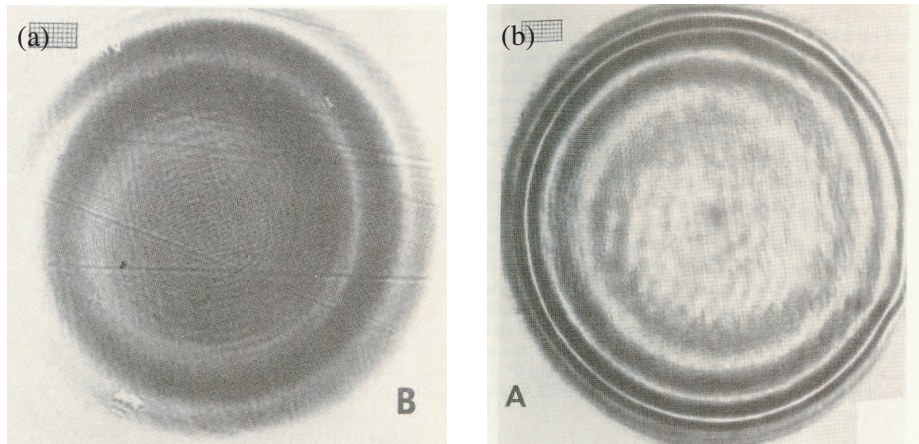


Figure 1.4: Photographs of chiral conical diffraction in α -iodic acid crystals with a gaussian incident beam: (a) crystal length 1.4mm, beam width $60\mu\text{m}$, and beam vertically polarised; (b) crystal length 2.5mm, beam width $30\mu\text{m}$, and beam horizontally polarised. Reproduced from (Schell & Bloembergen (1978*b*) fig.5B and fig.6A) with permission of the publisher.

We now turn to the theoretical development of conical diffraction. Hamilton's most extensive, refined, and characteristically loquacious account of his approach to geometrical optics was published in his *3rd Supplement to an Essay on the Theory of Systems of Rays* (Hamilton 1837). In this he introduced his method of characteristics, showing that light rays are paths of minimal optical path length. This is now known as Hamilton's principle, on which we base the geometric theory in section 2.7. When applying his method to double refraction, Hamilton rederived Fresnel's equations for the two-sheeted surface formed by a wave front propagating from a point within a biaxial medium. By a detailed study of the surface he discovered four singular points, lying along two crystal directions called the optic axes, at which the two sheets of the wave surface intersect at a point. Importantly he showed that, close to the intersection, each of the sheets is conical in shape, so that the degeneracy is often referred to as a conical or diabolical intersection, or "conoidal cusp" by Hamilton and his contemporaries. Rays of light are given, in accordance with Hamilton's principle and the constructions of Huygens and Fresnel, by the normals to the wave surface, and so in general there are two such normals in any given direction. At the conical point, however, there are an infinite number of normals forming the surface of a cone. This is the phenomenon of internal conical refraction: a light ray incident upon a biaxial crystal in the direction of an optic axis will be refracted into a cone of rays. This cone is refracted into a hollow cylinder at the exit face, and should be observed as a bright ring of light beyond the crystal.

Hamilton also found a circle of contact surrounding each conical point, where the surface could be laid "as a plum can be laid down on a table so as to touch and rest on the table in a whole circle of contact" (Graves 1882). This gives rise to external conical refraction, whereby a ray in the crystal aligned with the optic axis refracts out of the crystal into a diverging cone. We will be concerned mainly with internal conical refraction. The two are subtly connected by geometry familiar to Hamilton, though he seemed to overlook the physical relation. This would not be understood by Raman for another 110 years.

The history of conical refraction contains many such curious oversights: Fresnel was aware of the optic axes but missed the conical point; MacCullagh studied the conical intersection but missed its physical significance; Hamilton studied the conoidal cusps and tangent circles and the physical phenomena they produced but missed their interrelation; Hamilton and Lloyd neglected the differences between a physical light beam and an ideal ray, though Hamilton gave it thought, expressing in a letter dated January 1st 1833

(Graves 1882) that he had “predicted the *facts* of conical refraction, but I suspect that the *exact* laws of it depend on things as yet unknown”.

Conical refraction is a rich haven of singularities. Not until 1905 did Waldemar Voigt (1905*a*) realise an interesting paradox: the infinity of rays refracted in the cone is nulled by the zero intensity of Hamilton’s ideal axial ray, so Hamilton’s cone should be dark, not bright. This prompted him to call the phenomenon “sogenannte konische refraction”, signifying that Hamilton’s ideal conical refraction does not exist. Instead, double refraction in the neighbourhood of the conical point gives rise to pair of concentric cones, separated by a dark cone where Hamilton’s bright one should be. This is in keeping with Potter’s overlooked observations depicted in figure 1.2, and the corresponding wave surface construction shown in figure 1.5. Voigt’s description is qualitative, though following Hamilton he gave equations for ray directions, a practice that would be followed by many future authors. Voigt noted that the intensity of light, propagated through a crystal in a given direction, is proportional to the area element of the wave surface from which light rays originate. Since the area of the conical point is zero, the intensity of light coming from it is zero. But any beam of light contains a range of wavevector directions, a statement of practicality in Voigt’s time that would later become embodied in the Uncertainty Principle.

Voigt was also the first to extensively discuss conical refraction in optically active crystals, noting firstly that optical activity removed the conical point degeneracy (Voigt 1905*c*) and therefore conical refraction was destroyed. Elaborating on this later, Voigt (1905*b*) noted that the exact geometry of the surface still led to a brightening in the optical axis direction. In a detailed investigation of the wave surface he showed that the

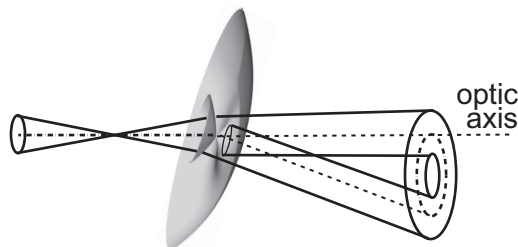


Figure 1.5: The diabolical point: the mathematical picture corresponding to figure 1.2, showing the diabolical intersection of the biaxial wave surface, Hamilton’s cone of normals (dashed), and the cones of rays refracted from around the conical point described by Voigt (bold).

normals formed a caustic, though neither he nor future authors seem to have concluded the striking physical phenomenon that would result. He also discussed the effect of pleochroism (Voigt 1902, Voigt 1907), identifying two further directions in the neighbourhood of each optic axis, the singular axes, where light would be completely circularly polarised. Later Pancharatnam (1955*a*) considered absorption in the vicinity of the optic axis, superposing the effects of birefringence and dichroism, though not in the conical regime.

The connection between internal and external conical refraction was first correctly appreciated by Raman et al. (1941, 1942). They described the importance of focusing and the changing light pattern away from the crystal. The most focused image of the conical refraction pattern appears in the focal image plane inside the crystal. They correctly described that by moving away from the focal plane one explores directions on the wave surface (figure 1.5) away from the conical point. As the two sheets of the wave surface separate, the rings – one from each sheet – separate and diffuse. The extraordinary sheet has a turnover where a tangent plane touches the sheet in Hamilton’s contact circle, and where ray normals are focused along the axis. As this direction is approached, the inner ring focuses into an axial spot and dominates the intensity. This level of geometric description is very powerful in describing the phenomenon of conical diffraction.

A quantitative understanding requires many levels of geometrical optics and diffraction theory, the development of which has proved troublesome over the last 60 years. Attempts to quantify the theory continued with calculations of the Poynting vectors of wave bundles in the crystal (Portigal & Burstein 1969, Portigal & Burstein 1972), an approach which had been successful in the study of acoustic conical refraction (McSkimin & Bond 1966). These, and other attempts expressing the electric field as an angular spectrum of plane waves (Lalor 1972), with improvement and a stationary phase approximation by Schell & Bloembergen (1978*a*), Uhlmann (1982), and for nonlinear crystals Shih & Bloembergen (1969), contained analytical formulae too complicated to yield a much greater understanding of the phenomenon than had already been achieved. But these marked a resurgence in interest that was rewarded by the triumphant diffraction theory of Belskii & Khapalyuk (1978), where simple circularly symmetric diffraction integrals were first written down. Though the underlying theory has evolved and improved, the resulting integrals for biaxial crystals remain the same. Their success showed that a paraxial diffraction theory could capture the long familiar polarisation structure. They gave the first simple expressions for conical diffraction of light from an illuminated pinhole for thin slabs in terms of Legendre

functions. At the time a lack of experimental data prevented verification of their theory.

Little progress was subsequently made though interest remained, largely in using conical refraction for transforming the growing array of beam modes made available by laser technology (Belafhal 2000, Stepanov 2002), as well as for laser beam focusing (Warnick & Arnold 1997), and exploiting the dispersive stability of conically diffracted beams (Brodskii et al. 1969, Brodskii et al. 1972, McGloin & Dholakia 2005). Recent interest has also centered around inhomogeneous media, where diabolicity is a localised phenomenon (Naida 1979). Conical refraction was also used by De Smet (1993) to demonstrate the efficacy of the 4×4 matrix approach to optics.

The next major breakthrough came in the form of numerical computations by Warnick & Arnold (1997). Seemingly unaware of the Belskii-Khapalyuk theory, they represented the electric field by a dynamical Green's function (Moskvin et al. 1993), and were able to uncover structure beyond that seen by Schell & Bloembergen (1978*a*). They simulated the spread of the bright rings away from the crystal to discover secondary oscillations on the inner ring. They also drew attention to the fact that oscillations had been seen in the chiral images of Schell & Bloembergen (1978*b*), the theory for which was unknown, remarking on whether the two interference phenomena were related (we will see they bear no relation). Belsky & Stepanov (1999) extended the theory to gaussian beams, and presented numerical calculations in the thin slab regime similar to Lloyd's experiments where the rings are barely resolvable. They did not consider thick enough slabs to correspond to experiments with good resolution, a distinction embodied in the cardinal ring-to-beam ratio ρ_0 . Therefore they were unable to see the well developed conical diffraction rings or Warnick and Arnold's secondary oscillations.

The importance of diffraction in the phenomenon was emphasised by Dreger (1999), though with a theory too complicated to see the effects. Belsky & Stepanov (2002) extended the Belskii-Khapalyuk diffraction theory to optically active crystals. They verified the polarisation pattern observed by Schell & Bloembergen (1978*b*) and described as long ago as Voigt (1905*b*), though without a good qualitative understanding of the origin of the structure.

Berry & Dennis (2003) studied the polarisation singularities associated with conical and singular points in direction space within the crystal. They described three key types of degeneracy: (i) in a nonchiral transparent crystal there are the optic axes, marking conical points of the wave surface, which in the presence of dichroism split into a pair of

singular axes, branch points of the complexified wave surface which approach as chirality is added, eventually annihilating when optical activity dominates; (ii) there are C points in direction space where plane wave eigenstates are circularly polarised, on the optic or singular axes in absence of optical activity, which obey a ‘haunting theorem’ as optical activity is introduced, remaining fixed in the location of the departed singular axes; and (iii) there are L lines where polarisation is linear, separating space into regions of right and left handed circular polarisation.

The stage for this thesis was set by Berry (2004*b*), with a Hamiltonian reformulation of the Belskii-Kapalyuk theory. Through an asymptotic study of the diffraction integrals for general incident beams, the first detailed explanation of the conical diffraction phenomenon was achieved, both qualitative and quantitative. The current state of affairs was thus raised to a sophisticated level of understanding, and all aspects of the biaxial phenomenon thus far observed were explained. It was in this paper that Berry introduced the ratio ρ_0 that characterises the phenomenon. This thesis complements and extends that work.

We will take an approach contrary to historical development, giving first the exact Hamiltonian wave formalism, followed by its interpretation in the geometrical optics limit as a simplest approximation. Then we ‘sew the wave flesh on the classical bones’. This is the methodology of asymptotics since Keller (1961): interpreting the exact solution by building up from its dominant asymptotic behaviour and then adding on diffraction piece by piece, thus extracting the full physical phenomenon from an intractable wave theory. In this manner we extend the theory to study conical diffraction in optically active and anisotropically absorbing media. As it stood prior to the present thesis, little was known about how chirality would effect the phenomenon of conical diffraction, and nothing was known regarding dichroism.

Chapter 2

Paraxial Optics and Asymptotics

*“The design of physical science is ..
to learn the language and interpret the oracles of the Universe.”*

William Rowan Hamilton, Lecture on Astronomy, 1831

In this chapter we review the theory of the optical properties of nonmagnetic crystals (Born & Wolf 1959, Landau et al. 1984). Derived from Maxwell’s equations for anisotropic media in section 2.1, we consider the effects of the refraction, absorption, and optical (phase and polarisation) rotation of light. For collimated beams of light, the simplifying principle of paraxiality in section 2.2 is essential to understanding optical phenomena. In section 2.3 we will develop a plane wave Hamiltonian theory for light beams propagating close to the optic axis of a crystal (Berry 2004*b*). The central result is a diffraction integral for the image light field known to Belskii & Khapalyuk (1978) for biaxial crystals and extended by Belsky & Stepanov (2002) to chiral crystals, here generalised to include dichroism, analysis of which requires complex transformations derived in section 2.4. In sections 2.5 and 2.6 we discuss the general asymptotic theory used to understand the physics behind the integral, not included in previous publication of the theory, and in section 2.7 we relate the wave theory in the asymptotic limit to Hamilton’s geometrical optics. Finally in section 2.8 we will remark on the physical, but unobservable, light field inside the crystal, filling the final chasm between conical diffraction theories pre- and post- Belskii & Khapalyuk.

2.1 Optics of Anisotropic Crystals

The optical properties of a nonmagnetic crystal are specified by constitutive relations between the complex-valued electric (\mathbf{E}) and electric displacement (\mathbf{D}) vector fields, and between the complex-valued magnetic (\mathbf{H}) and magnetic induction (\mathbf{B}) vector fields, in terms of a dielectric tensor (\mathcal{N}) which specifies the crystal:

$$\mathbf{E} = \frac{1}{\epsilon_0} \mathcal{N} \cdot \mathbf{D}, \quad \mathbf{B} = \mu_0 \mathbf{H}. \quad (2.1.1)$$

We will be concerned with the three simplest optical properties a crystal may possess: birefringence, chirality, and dichroism; these are defined by decomposing the dielectric tensor into real and imaginary $\mathcal{N} = \text{Re}\mathcal{N} + i\text{Im}\mathcal{N}$, and symmetric and antisymmetric $\mathcal{N} = \mathcal{N}^{\text{sym}} + \mathcal{N}^{\text{ant}}$, parts.

The real symmetric part of \mathcal{N} describes birefringence of the crystal,

$$\text{Re}\mathcal{N}_{ij} = \text{Re}\mathcal{N}_{ji} = \frac{1}{n_{ij}^2}, \quad (2.1.2)$$

where indices run from one to three. The three eigenvalues, which we label $1/n_j^2$, define three *principal refractive indices*

$$n_1 < n_2 < n_3, \quad (2.1.3)$$

and the matrix is diagonalised by choosing coordinate directions along the *principal axes*, which we label the $\{1, 2, 3\}$ axes. The parameters

$$\alpha \equiv \frac{1}{n_1^2} - \frac{1}{n_2^2}, \quad \beta \equiv \frac{1}{n_2^2} - \frac{1}{n_3^2}, \quad (2.1.4)$$

are small for weak anisotropy, and nonzero for crystals of orthorhombic or lower symmetry, where $\text{Re}\mathcal{N}^{\text{sym}}$ has three distinct eigenvalues. We will not be interested in *uniaxial* crystals, for which α or β vanishes, or isotropic crystals, for which both vanish.

The hermitian antisymmetric part of \mathcal{N} gives rise to *optical activity* in the crystal, characterised by an optical activity vector, $\mathbf{g} = \{g^1, g^2, g^3\}$, as

$$\mathcal{N} \cdot \mathbf{D} = \mathcal{N}^{\text{sym}} \cdot \mathbf{D} + i\mathbf{g} \times \mathbf{D} \quad (2.1.5)$$

$$= (\mathcal{N}^{\text{sym}} + \mathcal{N}^{\text{ant}}) \cdot \mathbf{D}, \quad (2.1.6)$$

where

$$\mathcal{N}_{ij} = -\mathcal{N}_{ji} = -i\epsilon_{ijk}g^k, \quad (2.1.7)$$

summing over the index k . The Levi-Civita symbol ϵ_{ijk} is zero for repeated indices, $+1$ if the indices are a cyclic permutation of $\{123\}$, and -1 otherwise. The components of \mathbf{g} can be written in terms of a rank 2 *optical activity tensor* \mathcal{G} as

$$\mathbf{g} = \mathcal{G} \cdot \mathbf{v}, \quad (2.1.8)$$

where \mathbf{v} may be either an external magnetic field, causing optical rotation by the Faraday effect (Landau et al. 1984), or the wavevector itself, implying chirality of the crystal structure. A crystal is *chiral* or *enantiomorphous* when it may exist in either of two mirror symmetric forms, this chirality of the lattice or molecular structure then causing optical rotation. This form of natural optical activity may actually arise in crystals which are nonchiral but are non-centrosymmetrical. For a detailed study of these crystal classes see Nye (1985). In either case the optical effect is equivalent, and we shall refer to it simply as *chirality*. It is common (Landau et al. 1984) to relate \mathbf{E} to \mathbf{D} in terms of the inverse tensor to \mathcal{N} , considering the dual relation to (2.1.5) for \mathbf{E} , in which case it is typical to refer to *gyrotropy* instead of optical activity.

A nonhermitian part of \mathcal{N} implies absorption. This is in general anisotropic, described by *absorption indices* m_{ij} satisfying

$$\text{Im}\mathcal{N}_{ij} = \text{Im}\mathcal{N}_{ji} = \frac{1}{m_{ij}^2}. \quad (2.1.9)$$

These are responsible for *linear dichroism*, for which it will be useful to define anisotropy parameters

$$\tilde{\alpha} \equiv \frac{1}{m_{11}^2} - \frac{1}{m_{22}^2}, \quad \tilde{\beta} \equiv \frac{1}{m_{22}^2} - \frac{1}{m_{33}^2}. \quad (2.1.10)$$

We will consider weak anisotropic absorption, for which these anisotropy parameters and the off-diagonal dielectric matrix elements $1/m_{ij}^2$ are small. For biaxial crystals of orthorhombic symmetry, the principal axes of the birefringent $\text{Re}\mathcal{N}^{\text{sym}}$ and dichroic $\text{Im}\mathcal{N}^{\text{sym}}$ parts coincide, but we will not limit ourselves to this class. We require only that the eigenvalues of $\text{Re}\mathcal{N}^{\text{sym}}$ and $\text{Im}\mathcal{N}^{\text{sym}}$ are distinct, which is true in general. We will assume that \mathcal{N} has no real antisymmetric part, which would constitute circular dichroism, and introduces no fundamental degeneracy not already contained within the more general effects of linear dichroism and chirality; I shall comment on this where relevant. The crystal classes are summarised in table 2.1.

symmetry class	axiality	indicatrix	
cubic	isotropic	sphere	principal axes of birefringence and absorption tensors coincide
trigonal/tetragonal/hexagonal	uniaxial	spheroid	
orthorhombic	biaxial	ellipsoid	principal axes of $\text{Re}\mathcal{N}^{\text{sym}}$ and $\text{Im}\mathcal{N}^{\text{sym}}$ distinct
monoclinic			
triclinic			

Table 2.1: Symmetries of non-centrosymmetric crystals, summarising some key optical properties. The indicatrix is also known as the index ellipsoid.

For plane waves with frequency σ and wavevector $\mathbf{k} = k\hat{\mathbf{k}}$ (i.e. a wave of the form $e^{i(\mathbf{k}\cdot\mathbf{r}-\sigma t)}$), Maxwell's source-free curl equations take the form

$$\sigma\mathbf{B} = \mathbf{k} \times \mathbf{E}, \quad \sigma\mathbf{D} = \mathbf{H} \times \mathbf{k}, \quad (2.1.11)$$

which, using the constitutive relations (2.1.1) in a crystal direction with refractive index $n = \sigma/ck$, can be written as

$$\frac{1}{n^2}\mathbf{D} = -\hat{\mathbf{k}} \times \hat{\mathbf{k}} \times (\mathcal{N}\cdot\mathbf{D}). \quad (2.1.12)$$

This expresses \mathbf{D} as the part of \mathbf{E} transverse to the wavevector, and therefore simplifies in rotated coordinates where the wavevector lies along some $3'$ -axis. Then $D_{3'} = 0$ so henceforth \mathbf{D} is a 2-vector, and (2.1.12) becomes the eigenequation

$$\frac{1}{n^2}\mathbf{D} = \mathcal{M}\cdot\mathbf{D}, \quad (2.1.13)$$

The 2×2 operator matrix \mathcal{M} can be expressed generally in terms of complex numbers $f_j = F_j + iG_j$ as

$$\begin{aligned} \mathcal{M} &= \begin{pmatrix} f_0 + f_1 & f_2 - if_3 \\ f_2 + if_3 & f_0 - f_1 \end{pmatrix} \\ &= (F_0\mathcal{I} + \mathbf{F} \cdot \boldsymbol{\Sigma}) + i(G_0\mathcal{I} + \mathbf{G} \cdot \boldsymbol{\Sigma}), \end{aligned} \quad (2.1.14)$$

where \mathcal{I} is the 2×2 identity matrix, and the matrix 3-vector $\boldsymbol{\Sigma}$ consists of the Pauli matrices

$$\boldsymbol{\Sigma} = \{\sigma_3, \sigma_1, \sigma_2\} = \left\{ \begin{pmatrix} 1 & 0 \\ 0 & -1 \end{pmatrix}, \begin{pmatrix} 0 & 1 \\ 1 & 0 \end{pmatrix}, \begin{pmatrix} 0 & -i \\ i & 0 \end{pmatrix} \right\}. \quad (2.1.15)$$

This naturally separates out the different degeneracy structures of \mathcal{M} , contained in the 3-vectors

$$\mathbf{F} = \{F_1, F_2, F_3\} \quad \text{and} \quad \mathbf{G} = \{G_1, G_2, G_3\}, \quad (2.1.16)$$

which respectively describe the hermitian and nonhermitian parts of \mathcal{M} . The exact expression for the coefficients is obtained by lengthy but straightforward algebra, and though we will not need to make use of the full result we give it here for completeness. We will express it in terms of the wavevector $\mathbf{k} = k \{\hat{k}_1, \hat{k}_2, \hat{k}_3\}$ in the principal axis frame, but it can also be written simply in polar coordinates, or in an elegant stereographic representation given by Berry & Dennis (2003). More important is the generic degeneracy structure of \mathcal{M} (places where its two eigenvalues are equal), which is well understood (Berry 2004c) for general \mathbf{F} and \mathbf{G} .

A plane wave incident upon the crystal refracts into a pair of waves with refractive indices n_{\pm} , which form the eigenvalues of \mathcal{M} in (2.1.14),

$$\begin{aligned} \frac{1}{n_{\pm}^2} &= f_0 \pm \langle \mathbf{f} \rangle \\ &= F_0 + iG_0 \pm \sqrt{\mathbf{F} \cdot \mathbf{F} - \mathbf{G} \cdot \mathbf{G} + 2i\mathbf{F} \cdot \mathbf{G}} \end{aligned} \quad (2.1.17)$$

where, here and hereafter, we define the *length* of any vector by

$$f \equiv \langle \mathbf{f} \rangle \equiv \sqrt{\mathbf{f} \cdot \mathbf{f}}. \quad (2.1.18)$$

(Note that we distinguish the *length* $f = \langle \mathbf{f} \rangle$ which may be complex, from the *magnitude* $|\mathbf{f}| = \sqrt{\mathbf{f}^* \cdot \mathbf{f}}$ which is real, * denoting the complex conjugate.)

The real scalar F_0 and 2-vector $\{F_1, F_2\}$ specify birefringence,

$$\begin{aligned} F_0 &= -\frac{1}{2}\beta \left(1 - \hat{k}_3^2\right) + \frac{1}{2}\alpha \frac{\hat{k}_3^2 \hat{k}_1^2 + \hat{k}_2^2}{1 - \hat{k}_3^2} + \frac{1}{n_2^2} \\ F_1 &= -\frac{1}{2}\beta \left(1 - \hat{k}_3^2\right) + \frac{1}{2}\alpha \frac{\hat{k}_3^2 \hat{k}_1^2 - \hat{k}_2^2}{1 - \hat{k}_3^2} \\ F_2 &= -\alpha \frac{\hat{k}_1 \hat{k}_2 \hat{k}_3}{1 - \hat{k}_3^2}, \end{aligned} \quad (2.1.19)$$

in terms of the anisotropy parameters defined in (2.1.4). This real symmetric part of \mathcal{M} has a degeneracy of codimension two, a point at the origin of the parameter space $\{F_1, F_2\}$, which has only two real wavevector solutions,

$$k_2 = 0, \quad |k_1/k_3| = \sqrt{\alpha/\beta} \equiv \tan \theta_{\text{OA}}. \quad (2.1.20)$$

These are the *optic axes*, lying in the plane of the principal 1-3 axes making an angle θ_{OA} with the 3-axis. We will refer to these directions as the optic axes even in the general case ($F_1 \neq 0 \neq F_2$) when they no longer constitute a degeneracy.

The optic axis degeneracy corresponds to a conical point of the eigenvalue surface where its two sheets, n_{\pm} , are connected by a conical intersection. The eigenvalue surface is directly related to the wave surface of Fresnel to be described in chapter 3 and shown in Figure 2.1, generated by a wavevector in a transparent nonchiral crystal whose length $k_0 n$ is given by the eigenvalues (2.1.17) of \mathcal{M} .

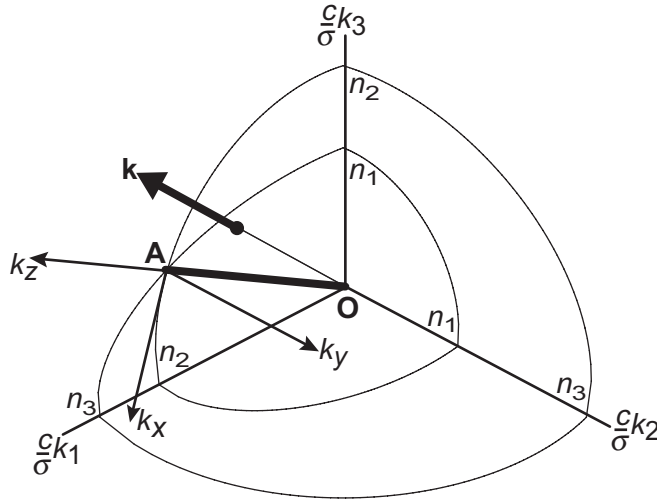


Figure 2.1: Fresnel's (biaxial) wave surface, and coordinates rotated about the 2-direction so that z lies along the optic axis OA . Wavevectors \mathbf{k} are considered paraxially, that is with small displacement $\{k_x, k_y\}$ from the optic axis. The full surface is obtained by reflection.

In the presence of chirality \mathcal{M} is hermitian but complex, containing

$$F_3 = g_1 \hat{k}_1 + g_2 \hat{k}_2 + g_3 \hat{k}_3, \quad (2.1.21)$$

in terms of the optical activity vector of (2.1.5). The degeneracy is then of codimension three, a point at the origin of the parameter space $\{F_1, F_2, F_3\}$, which will not be visited by the eigenvalue/wave surface for $F_3 \neq 0$.

In the presence of absorption \mathcal{M} is nonhermitian, and \mathbf{G} can be considered as a vector in the parameter space of \mathbf{F} . The degeneracies are of codimension two, forming a circular ring of radius G in the plane perpendicular to $\hat{\mathbf{G}}$, corresponding to a ring of branch points

in the eigenvalue surface. The scalar G_0 specifies a uniform absorption coefficient which will not be of interest to us, and linear dichroism involves only the 2-vector $\{G_1, G_2\}$. These are given in terms of the coefficients (2.1.9) & (2.1.10) by

$$\begin{aligned}
 G_0 &= -\frac{1}{2}\tilde{\beta}\left(1 - \hat{k}_3^2\right) + \frac{1}{2}\tilde{\alpha}\frac{\hat{k}_3^2\hat{k}_1^2 + \hat{k}_2^2}{1 - \hat{k}_3^2} - \left(\frac{\hat{k}_2\hat{k}_3}{m_{23}^2} + \frac{\hat{k}_1\hat{k}_3}{m_{13}^2} + \frac{\hat{k}_1\hat{k}_2}{m_{12}^2}\right) - \frac{1}{m_{22}^2} \\
 G_1 &= -\frac{1}{2}\tilde{\beta}\left(1 - \hat{k}_3^2\right) + \frac{1}{2}\tilde{\alpha}\frac{\hat{k}_3^2\hat{k}_1^2 - \hat{k}_2^2}{1 - \hat{k}_3^2} - \left(\frac{\hat{k}_2\hat{k}_3}{m_{23}^2} + \frac{\hat{k}_1\hat{k}_3}{m_{13}^2} - \frac{\hat{k}_1\hat{k}_2}{m_{12}^2}\frac{1 + \hat{k}_3^2}{1 - \hat{k}_3^2}\right) \\
 G_2 &= -\tilde{\alpha}\frac{\hat{k}_1\hat{k}_2\hat{k}_3}{1 - \hat{k}_3^2} + \left(\frac{\hat{k}_3}{m_{12}^2}\frac{\hat{k}_1^2 - \hat{k}_2^2}{1 - \hat{k}_3^2} + \frac{\hat{k}_2}{m_{13}^2} - \frac{\hat{k}_1}{m_{23}^2}\right). \tag{2.1.22}
 \end{aligned}$$

The degeneracy ring intersects the nonchiral ($F_3 = 0$) parameter plane $\{F_1, F_2\}$ at a pair of branch points. Each optic axis is thus split into a pair of directions called *singular axes* (Voigt 1902). Chirality is added by increasing F_3 , whereby the two branch points (singular axes) approach with a separation $\sqrt{G^2 - F_3^2}$, and annihilate at $F_3 = G$, so there is no degeneracy in the chirality dominated regime $F_3 > G$.

The only remaining part of \mathcal{M} is a real antisymmetric (and therefore nonhermitian) term which specifies circular dichroism. If $\{G_1, G_2\} = 0$ then the degeneracy ring lies in the $\{F_1, F_2\}$ parameter plane, and the optic axis spreads into a *ring of singular axis directions*, corresponding to a ring of branch points in the wave surface where its Riemann surfaces meet. This case leads to no fundamental aspects of the theory not already included in linear dichroism and optical activity, and can be incorporated into the theory by making the chirality parameter F_3 complex.

The behaviour of these degeneracies will be more readily apparent when studied on the paraxial wave surface in chapter 3.

2.2 Principles of Paraxial Light Propagation

Suppose we rotate the principal axes about the 2-direction to axes $\{x, y, z\}$, so that z lies along an optic axis (see figure 2.1). Let the wavevector in the new coordinates be

$$\mathbf{k} = \{k_x, k_y, k_z\} \equiv \{k\mathbf{k}_\perp, k_z\}. \tag{2.2.1}$$

Supposing that this lies close to an optic axis we expand on the \mathbf{k}_\perp unit circle in terms of the small ($k_\perp \ll 1$) transverse part $\mathbf{k}_\perp = \{\hat{k}_x, \hat{k}_y\}$, whereby

$$k_1 \approx k \left(\sin \theta_{\text{OA}} + \hat{k}_x \cos \theta_{\text{OA}} \right), \quad k_2 \approx k \hat{k}_y, \quad k_3 \approx k \left(\cos \theta_{\text{OA}} - \hat{k}_x \sin \theta_{\text{OA}} \right). \tag{2.2.2}$$

The crystal wavenumber k combines the vacuum wavenumber k_0 and refractive index n ,

$$k = nk_0. \quad (2.2.3)$$

Expanding (2.1.14) to leading order in the transverse wavevector \mathbf{k}_\perp , including the lowest order perturbations introduced by the crystal parameters, gives the paraxial refraction matrix

$$\frac{1}{2}\mathcal{M} \approx \frac{1}{n_2^2} \left[\left(\frac{1}{2} - A\hat{k}_x \right) \mathcal{I} - \{A(\mathbf{k}_\perp - i\mathbf{\Delta}), \Gamma\} \cdot \mathbf{\Sigma} \right], \quad (2.2.4)$$

and, from its eigenvalues $1/n^2$, the refractive indices

$$n_\pm \approx n_2 \left[1 + A\hat{k}_x \pm \sqrt{A^2(\mathbf{k}_\perp - i\mathbf{\Delta})^2 + \Gamma^2} \right]. \quad (2.2.5)$$

This is the *parabolic* approximation. Formally, the multi-variable expansion is in terms of small k_x/k and k_y/k , and in terms of small (weak) crystal parameters α , β , $\tilde{\alpha}$, $\tilde{\beta}$, m_{ij}^{-1} , \mathcal{G}_{ij} , by means of convex hull construction in index space (a method due to Newton, where each term in a Taylor expansion inhabits a point whose coordinates are its powers in each expansion parameter, forming a polyhedron or “convex hull”, and all coefficients not at a vertex of the polyhedron can be discarded to leading order), whereby $n_2^2 F_0 \approx 1 - 2A\hat{k}_x$, $n_2^2 F_1 \approx 2A(i\Delta_x - \hat{k}_x)$, $n_2^2 F_2 \approx 2A(i\Delta_y - \hat{k}_y)$, introducing parameters A , Γ , $\mathbf{\Delta}$, which naturally split the refraction matrix \mathcal{M} into real symmetric (biaxial), hermitian antisymmetric (chiral), and nonhermitian (dichroic) parts.

Paraxiality thus reduces threefold the twelve parameters ($3[\text{Re}\mathcal{N}^{\text{sym}}] + 3[\text{Im}\mathcal{N}^{\text{ant}}] + 6[\text{Im}\mathcal{N}^{\text{sym}}]$) specifying the crystal as follows. Biaxiality is specified by the geometric mean of the refractive indices differences

$$A \equiv \frac{n_2^2}{2} \sqrt{\alpha\beta}, \quad (2.2.6)$$

which we will see is the half-angle of Hamilton’s conical refraction cone, obtained along the optic axis direction $\mathbf{k}_\perp = 0$ where (2.2.5) is degenerate, $n_+ = n_-$. Dichroism is specified by the 2-vector

$$\mathbf{\Delta} = \frac{n_2^2}{2A} \left\{ \frac{\sqrt{\beta}/m_{12}^2 - \sqrt{\alpha}/m_{23}^2}{\sqrt{\alpha + \beta}}, \frac{\bar{\alpha}\beta - \alpha\bar{\beta} - 2\sqrt{\alpha\beta}/m_{31}^2}{2(\alpha + \beta)} \right\}, \quad (2.2.7)$$

splitting the degeneracies of n_\pm into the singular axes $\mathbf{k}_\perp = \mathbf{\Delta}$, obtained from the optic axes by a deflection $\pm\mathbf{\Delta}$, in pairs with angular splitting $2\mathbf{\Delta}$. (This includes off-diagonal

absorption indices from the dielectric matrix omitted by Berry & Jeffrey (2006*b*), generalising for the angular deflection of the singular axes which occurs for crystals of lower than orthorhombic symmetry.) Optical activity is specified by an optical rotary power

$$\Gamma = \frac{n_2^2}{2} \frac{\mathcal{G}_{11}\alpha + \mathcal{G}_{33}\beta + 2\mathcal{G}_{31}\sqrt{\alpha\beta}}{\alpha + \beta} \quad (2.2.8)$$

$$= \frac{n_2^2}{2} [(\mathcal{G}_{33} + \mathcal{G}_{11}) + (\mathcal{G}_{33} - \mathcal{G}_{11}) \cos 2\theta_{OA} + \mathcal{G}_{13} \sin 2\theta_{OA}] \quad (2.2.9)$$

for a chiral crystal, and

$$\Gamma = \frac{n_2^2}{2} \frac{(\mathcal{G}_{11}\alpha + \mathcal{G}_{13}\beta) H_1 + (\mathcal{G}_{12}\alpha + \mathcal{G}_{23}\beta) H_2 + (\mathcal{G}_{13}\alpha + \mathcal{G}_{33}\beta) H_3}{\alpha + \beta} \quad (2.2.10)$$

for the Faraday effect with an external magnetic field $\mathbf{H} = \{H_1, H_2, H_3\}$. The singular axis degeneracies of n_{\pm} then lie at $\mathbf{k}_{\perp} = \pm \mathbf{e}_3 \times \Delta \sqrt{1 - (\Gamma/A\Delta)^2}$, existing only in the dichroism dominated regime $|A\Delta| \geq |\Gamma|$, with \mathbf{e}_3 lying along the propagation direction.

Each of these parameters is small. Typical values of the angle A are 0.93° for aragonite, 1.25° for the mono-double-tungstate $\text{KYb}(\text{WO}_4)_2$, and, exhibiting very strong conical refraction, 7.0° for naphthalene. Typical values of the optical rotary power Γ in radians per centimetre are 3.39π for quartz (Kaye & Laby 1973), 12.9π for α -iodic acid (Schell & Bloembergen 1978*b*), both of which are naturally optically active, and 1.38π for terbium gallium garnate in a 1Tesla magnetic field (Kaye & Laby 1973). There seem to be no tabulated values of anisotropic absorption indices. However, to neglect \mathbf{k}_{\perp} dependent (1st order correction) absorption terms as being smaller than Δ , we require $\Delta \ll A$.

Finally, we can now write the two wave eigenstates that propagate in the crystal as

$$\begin{aligned} \mathbf{D} \propto e^{i\mathbf{k}\cdot\mathbf{r}} &= e^{ik(\mathbf{k}_{\perp}\cdot\mathbf{r}_{\perp} + \hat{k}_z z)} \\ &\approx e^{i(k\mathbf{k}_{\perp}\cdot\mathbf{r}_{\perp} + zk_0 [n_{\pm}(\mathbf{k}_{\perp}) - \frac{1}{2}n_2 k_{\perp}^2])}. \end{aligned} \quad (2.2.11)$$

A geometric interpretation of the crystal parameters is thus evident from the phase in (2.2.11) with (2.2.5). Consider first the square root in (2.2.5) with $\Delta = \Gamma = 0$. The refractive index takes the same value everywhere on a circle swept out by a unit wavevector transverse to the optic axis, $\mathbf{k} = \{\mathbf{k}_{\perp}, 0\}$, the locus of which sweeps out a cone with half-angle A as z increases through the crystal. The shift $+A\hat{k}_x$ in (2.2.5) is a skew of this cone so that the optic axis lies in its surface as a generator. This is the phenomenon of conical refraction as it applies to plane waves. The optic axis direction $k_{\perp} = 0$ is degenerate in the sense that the two refractive indices and eigenpolarisations (eigenvectors of \mathcal{M}) are equal there.

The angle A is also the phase difference introduced by birefringence between two eigenwaves after propagating a distance z through the crystal. Γ is the rate at which chirality changes the phase of an eigenwave propagating along the optic axis, and Δ is the rate of absorption of an eigenwave propagating along the optic axis. We will describe these effects in a more general and powerful way to motivate each section in chapter 4, but the derivation above is required to relate rigorously the phenomena of conical diffraction to the dielectric tensor.

2.3 Hamiltonian Formulation

The refraction matrix (2.2.4) and indices (2.2.5) determine the paraxial propagation of a plane wave (2.2.11) as a function of the transverse part of the wavevector. The paraxial theory takes its simplest form expressed in dimensionless variables, scaling out the width w and vacuum wavenumber k_0 of a monochromatic incident beam, and the length l of the crystal.

Let us define a transverse position vector measured in units of the beam width,

$$\boldsymbol{\rho} \equiv \{x + Az, y\} / w. \quad (2.3.1)$$

The shift of origin $Az\mathbf{e}_x$ takes account of the skew of the refracted cone introduced by the $A\hat{k}_x$ term in (2.2.4). Figure 2.2 illustrates the relation between the beam, the crystal,

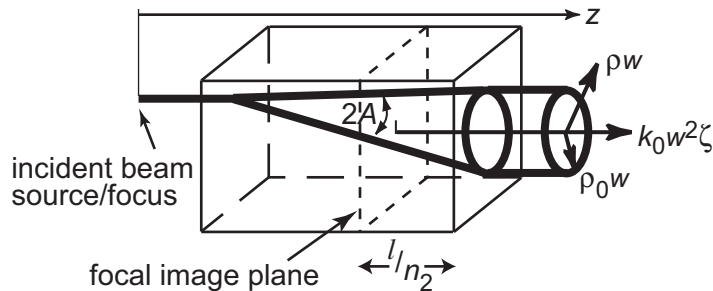


Figure 2.2: The parameters of paraxial conical refraction, showing the dimensionless coordinates: ζ , propagation distance measured in units of the diffraction length $k_0 w^2$ from the focal image plane; and ρ , radial position measured in units of the beam width w from the centre of the conical refraction cylinder, whose radius in these units is ρ_0 . The skew of the refracted cone is shown: the optic axis is a generator of the cone.

and the dimensionless coordinates. The corresponding transverse wavevector, measured in units of $1/w$, is defined by

$$\boldsymbol{\kappa} \equiv w k \mathbf{k}_\perp. \quad (2.3.2)$$

We now wish to consider a time-independent light beam directed onto a crystal along its optic axis, describing the beam by its electric displacement field $\mathbf{D} = D\mathbf{d}$; we will shortly express the spatial dependence of this on dimensionless cylindrical coordinates. This vector comprises the square root of the light intensity $D = |\mathbf{D}|$, and a polarisation vector \mathbf{d} which specifies the orientation of the complex field. Distance from the beam source is measured by the coordinate z , and the incident beam will be specified in the plane $z = 0$ by a vector $\mathbf{D}_0(\boldsymbol{\rho}) = D_0(\boldsymbol{\rho})\mathbf{d}_0$.

A time-independent incident beam with polarisation \mathbf{d}_0 can then be written as a superposition of plane waves with transverse fourier profile $a(\boldsymbol{\kappa})$,

$$\mathbf{D}_0(\boldsymbol{\rho}) = \frac{1}{2\pi} \int \int d\boldsymbol{\kappa} e^{i\boldsymbol{\kappa} \cdot \boldsymbol{\rho}} a(\boldsymbol{\kappa}) \mathbf{d}_0. \quad (2.3.3)$$

We will develop the theory for a general beam as far as possible, but in special cases will consider gaussian beams

$$D_0(\rho) = e^{-\rho^2/2}, \quad a(\kappa) = e^{-\kappa^2/2} \quad (2.3.4)$$

common in lasers, and the beam of light diffracted from a coherently illuminated pinhole

$$D_0(\rho) = \mathbb{T}[1 - \rho], \quad a(\kappa) = J_1(\kappa)/\kappa, \quad (2.3.5)$$

where J_1 is a Bessel function, and henceforth $\mathbb{T}[\cdot]$ is the unit-step function

$$\mathbb{T}[x] \equiv \begin{cases} 0, & x < 0 \\ 1, & x \geq 0 \end{cases}. \quad (2.3.6)$$

For a circularly symmetric beam directed along the optic axis the integral simplifies to

$$\mathbf{D}_0(\boldsymbol{\rho}) = D_0(\rho) \mathbf{d}_0 = \int_0^\infty d\kappa \kappa J_0(\rho\kappa) a(\kappa) \mathbf{d}_0 \quad (2.3.7)$$

in terms of the Bessel function J_0 . In some cases we may make use of the fourier transform

$$a(\boldsymbol{\kappa}) = \int_0^\infty d\rho \rho D_0(\rho) J_0(\kappa\rho). \quad (2.3.8)$$

We will also consider beams with a small misalignment angle κ_0/k_0w off the optic axis in a direction $\hat{\boldsymbol{\kappa}}_0$, for which the transverse profile is simply $a(\boldsymbol{\kappa} - \boldsymbol{\kappa}_0)$.

We specify the crystal in terms of scaled optical parameters:

$$\rho_0 \equiv \frac{Al}{w}, \quad \boldsymbol{\delta} \equiv kw\boldsymbol{\Delta}, \quad \gamma \equiv kw\frac{\Gamma}{A}, \quad (2.3.9)$$

where ρ_0 is the radius of the conical refraction cone at the exit face of the crystal (figure 2.2), $2\boldsymbol{\delta}$ is the separation of the singular axes in transverse direction space, and $\rho_0\gamma$ is the total optical rotation. We group these into a 3-vector specifying a transparent crystal,

$$\mathbf{V}(\boldsymbol{\kappa}) \equiv \rho_0 \{ \boldsymbol{\kappa}, \gamma \}, \quad (2.3.10)$$

and incorporate dichroism by means of the complexifying transformation

$$\mathbf{V}(\boldsymbol{\kappa}) \rightarrow \mathbf{V}(\boldsymbol{\kappa} - i\boldsymbol{\delta}). \quad (2.3.11)$$

The plane waves (2.2.11) are evolving eigenstates of the Hamiltonian

$$\mathcal{H}(\boldsymbol{\kappa}) = \left\{ \begin{array}{ll} \frac{1}{2}n_2\kappa^2\mathcal{I}, & \text{outside crystal} \\ \frac{1}{2}\kappa^2\mathcal{I} + kwA \{ \boldsymbol{\kappa} - i\boldsymbol{\delta}, \gamma \} \cdot \boldsymbol{\Sigma}, & \text{inside crystal} \end{array} \right\}. \quad (2.3.12)$$

That is, the electric displacement vector \mathbf{D} describing plane waves satisfies the equation $ikw^2\partial\mathbf{D}/\partial z = \mathcal{H}\mathbf{D}$. Evolution ‘time’ z is the propagation distance measured from the beam source (this may be the beam focus and need not lie outside the crystal). The total evolution through the crystal can be described by a 2×2 matrix \mathcal{F} , found by integrating the Hamiltonian along the optical path, and defined as

$$\mathcal{F}(\boldsymbol{\kappa}, \boldsymbol{\rho}, \zeta) = -\boldsymbol{\kappa} \cdot \boldsymbol{\rho} \mathcal{I} + \frac{1}{kw^2} \int_0^\zeta dz \mathcal{H}(\boldsymbol{\kappa}) \quad (2.3.13)$$

$$= \left(-\boldsymbol{\kappa} \cdot \boldsymbol{\rho} + \frac{1}{2}\zeta\kappa^2 \right) \mathcal{I} + \mathbf{V}(\boldsymbol{\kappa} - i\boldsymbol{\delta}) \cdot \boldsymbol{\Sigma}. \quad (2.3.14)$$

The dimensionless propagation distance,

$$\zeta \equiv \frac{z - l \left(1 - \frac{1}{n_2} \right)}{k_0w^2}, \quad (2.3.15)$$

is measured from the most focused image of the source, in the *focal image plane* at a distance of $l(1 - 1/n_2)$ from the exit face, in units of the diffraction length k_0w^2 (called the Rayleigh length for a gaussian beam). The refracted beam is then the superposition of

plane waves $a(\boldsymbol{\kappa}) \mathbf{d}_0$, whose diffraction through the crystal is described by the evolution operator $e^{-i\mathcal{F}}$, embodied in a propagator integral

$$\mathbf{D}(\boldsymbol{\rho}, \zeta) = \frac{1}{2\pi} \int \int d\boldsymbol{\kappa} e^{-i\mathcal{F}(\boldsymbol{\kappa}, \boldsymbol{\rho}, \zeta)} a(\boldsymbol{\kappa}) \mathbf{d}_0. \quad (2.3.16)$$

Evaluating the matrix exponential gives

$$e^{-i\mathcal{F}(\boldsymbol{\kappa}, \boldsymbol{\rho}, \zeta)} = e^{i(\boldsymbol{\kappa} \cdot \boldsymbol{\rho} - \frac{1}{2}\zeta\kappa^2)} \left[\mathcal{I} \cos V(\boldsymbol{\kappa} - i\boldsymbol{\delta}) - i \frac{\mathbf{V}(\boldsymbol{\kappa} - i\boldsymbol{\delta}) \cdot \boldsymbol{\Sigma}}{V(\boldsymbol{\kappa} - i\boldsymbol{\delta})} \sin V(\boldsymbol{\kappa} - i\boldsymbol{\delta}) \right], \quad (2.3.17)$$

or more concisely,

$$e^{-i\mathcal{F}(\boldsymbol{\kappa}, \boldsymbol{\rho}, \zeta)} = e^{-i\Phi_+(\boldsymbol{\kappa}, \boldsymbol{\rho}, \zeta)} \mathcal{K}_+(\boldsymbol{\kappa}) + e^{-i\Phi_-(\boldsymbol{\kappa}, \boldsymbol{\rho}, \zeta)} \mathcal{K}_-(\boldsymbol{\kappa}), \quad (2.3.18)$$

where the exponents

$$\Phi_{\pm}(\boldsymbol{\kappa}, \boldsymbol{\rho}, \zeta) = -\boldsymbol{\kappa} \cdot \boldsymbol{\rho} + \frac{1}{2}\zeta\kappa^2 \pm V(\boldsymbol{\kappa} - i\boldsymbol{\delta}) \quad (2.3.19)$$

are both the eigenvalues of \mathcal{F} and the optical path lengths of the refracted waves. In terms of 2×2 matrices

$$\mathcal{K}_{\pm}(\boldsymbol{\kappa}) \equiv \frac{1}{2} \left[\mathcal{I} \pm \frac{\mathbf{V}(\boldsymbol{\kappa} - i\boldsymbol{\delta}) \cdot \boldsymbol{\Sigma}}{V(\boldsymbol{\kappa} - i\boldsymbol{\delta})} \right], \quad (2.3.20)$$

we can simply write

$$\mathcal{F} = \Phi_+ \mathcal{K}_+ + \Phi_- \mathcal{K}_-. \quad (2.3.21)$$

In the absence of dichroism the traceless evolution matrix \mathcal{F} is hermitian and the evolution operator $e^{-i\mathcal{F}}$ is unitary. Both are symmetric in the absence of chirality. We have neglected here the greatest effect of dichroism, a constant absorption which appears in \mathcal{F} as a trace, which is required to make the crystal absorbing overall but is of no consequence in our theory. We have also neglected a phase constant $e^{in_2 k_0 z}$ implied by (2.2.11) which has no effect on the light intensity. The intensity of the refracted wave field beyond the crystal and, by continuation, of the image field inside the crystal, is then given by the square magnitude of the wave field,

$$I(\boldsymbol{\rho}, \zeta) = \mathbf{D}(\boldsymbol{\rho}, \zeta)^* \cdot \mathbf{D}(\boldsymbol{\rho}, \zeta). \quad (2.3.22)$$

The eigenvectors of \mathcal{F} and $e^{-i\mathcal{F}}$ are the plane wave eigenpolarisations

$$\mathbf{d}_{\pm}(\boldsymbol{\kappa}) = \lambda_{\pm}(\boldsymbol{\kappa}) \mathbf{d}_{\uparrow}(\boldsymbol{\kappa}) \pm i\lambda_{\mp}(\boldsymbol{\kappa}) \mathbf{d}_{\downarrow}(\boldsymbol{\kappa}), \quad (2.3.23)$$

in terms of an ellipticity function

$$\lambda_{\pm}(\kappa) \equiv \sqrt{\frac{1 \pm \frac{\kappa}{\sqrt{\kappa^2 + \gamma^2}}}{2}}, \quad (2.3.24)$$

and orthonormal linear polarisations

$$\mathbf{d}_{\uparrow}(\kappa) = \begin{pmatrix} \cos \frac{1}{2}\phi_{\kappa} \\ \sin \frac{1}{2}\phi_{\kappa} \end{pmatrix}, \quad \mathbf{d}_{\downarrow}(\kappa) = \begin{pmatrix} -\sin \frac{1}{2}\phi_{\kappa} \\ \cos \frac{1}{2}\phi_{\kappa} \end{pmatrix}, \quad (2.3.25)$$

in polar coordinates $\kappa = \kappa \{\cos \phi_{\kappa}, \sin \phi_{\kappa}\}$. For a transparent nonchiral crystal, \mathbf{d}_{\pm} reduce to the linear polarisations $\mathbf{d}_{\uparrow\downarrow}$, whose orientation rotates half a turn as κ makes a complete circuit of the optic axis. This geometric phase is associated with the presence of a $\frac{1}{2}$ -index polarisation singularity along the degeneracy direction (Berry & Dennis 2003). Chirality makes the eigenpolarisations elliptical in general, and circular along the (nondegenerate) optic axis. As eigenvectors of a hermitian matrix they are orthonormal, remaining orthogonal as κ approaches the optic axis. Dichroism is introduced by substituting $\kappa \rightarrow \kappa - i\delta$ as in (2.3.11), in which case the eigenpolarisations are generally elliptical, nonorthogonal ($\mathbf{d}_{+}^* \cdot \mathbf{d}_{-} \neq 0$ although $\mathbf{d}_{+} \cdot \mathbf{d}_{-} = 0$), and are normalised only in length (2.1.18) not magnitude ($\mathbf{d}_{\pm}^* \cdot \mathbf{d}_{\pm} \neq 1$).

The polarisation of a wave $\mathbf{d} = \{d_x, d_y\}$ can be characterised by a complex number

$$\omega = \frac{d_x - id_y}{d_x + id_y}, \quad (2.3.26)$$

containing the state's eccentricity $|\omega|$ and orientation $\frac{1}{2} \arg \omega$, or by stereographic projection of ω onto the unit sphere to a point $\Omega(\phi, \theta)$, where $\omega = e^{i\phi} \tan \frac{1}{2}\theta$. Figure 2.3 shows this Poincaré sphere representation.

Linear polarisations, which we will define as vectors

$$\mathbf{d}_{\chi}^{\text{lin}} \equiv \begin{pmatrix} \cos \chi \\ \sin \chi \end{pmatrix}, \quad (2.3.27)$$

lie on the equator of the Poincaré sphere $|\omega| = 1$, and circular polarisations, which we will define as

$$\mathbf{d}_{\pm}^{\text{circ}} \equiv \frac{1}{\sqrt{2}} \begin{pmatrix} 1 \\ \pm i \end{pmatrix}, \quad (2.3.28)$$

lie at the poles $\omega_{\pm} = 0, \infty$. Orthogonal polarisations are antipodal on the sphere, that is

$$\omega_{+}\omega_{-}^* = -1. \quad (2.3.29)$$

The polarisations of refracted plane waves propagating in the crystal are then simply

$$\omega_{\pm}(\boldsymbol{\kappa}) = \frac{\gamma \pm \sqrt{\kappa^2 + \gamma^2}}{\kappa} e^{-i\phi\boldsymbol{\kappa}} = \frac{\lambda_{\pm} \pm \lambda_{\mp}}{\lambda_{\pm} \mp \lambda_{\mp}} e^{-i\phi\boldsymbol{\kappa}}. \quad (2.3.30)$$

For a transparent nonchiral crystal these are orthogonal linear polarisations with orientation angles $\phi_{\boldsymbol{\kappa}}/2$ and $\phi_{\boldsymbol{\kappa}}/2 + \pi/2$. Dichroism is introduced via $\boldsymbol{\kappa} \rightarrow \boldsymbol{\kappa} - i\boldsymbol{\delta}$, resulting in elliptically polarised nonorthogonal eigenstates $\omega_{\pm} = \pm e^{-i\phi\boldsymbol{\kappa}}$ where $\phi_{\boldsymbol{\kappa}}$ is complex. The chiral eigenpolarisations are also generally elliptical. In all cases, singularity ($\omega_{\pm} = 0, \infty$) along the degeneracy axes (optic or singular axes) implies circular eigenpolarisation (C point). (The case of circular dichroism is exceptional, obtained by letting γ be imaginary whence $\omega = ie^{-i\phi\boldsymbol{\kappa}}$, in which case the ring of degeneracy axes is an L (linear polarisation) line separating right and left handed elliptically polarised regions.)

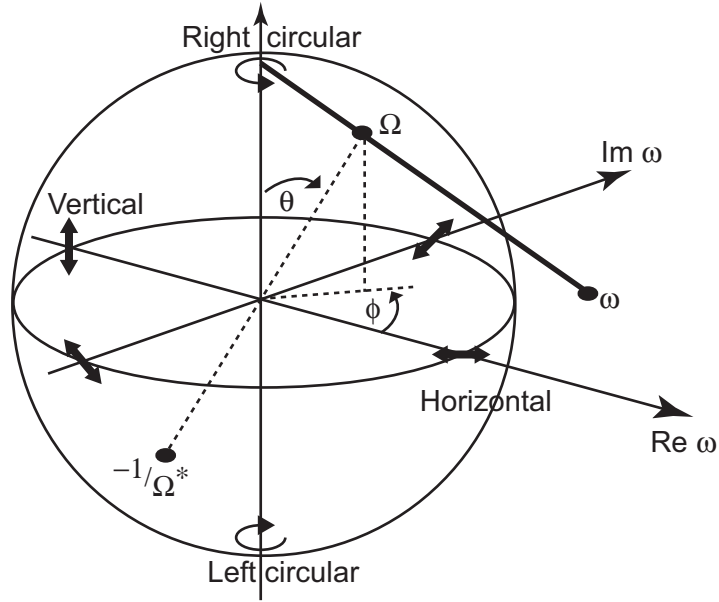


Figure 2.3: The Poincaré Sphere and stereographic projection from the complex plane: polarisation states are characterised by their eccentricity $\frac{1}{2}\theta$ and orientation $\frac{1}{2}\phi$, represented by a point ω in the complex plane or its stereographic projection onto a point $\Omega(\phi, \theta)$ on the unit sphere, such that $\omega = e^{i\phi} \tan \frac{1}{2}\theta$.

2.4 Complex Ray Directions: So Where Should We Point The Beam?

Note that the transparent crystal vector $\mathbf{V}(\boldsymbol{\kappa})$ appears in (2.3.17) either as the function of a scalar $V(\boldsymbol{\kappa})$, or as the rotation matrix $\mathbf{V}(\boldsymbol{\kappa}) \cdot \boldsymbol{\Sigma}$, both of which are symmetric under rotation of $\boldsymbol{\kappa}$. The key obstruction to evaluating the propagator integral (2.3.16) in the presence of dichroism $\boldsymbol{\delta}$ is the breaking of this rotational symmetry introduced by complexification (2.3.11). This suggests that the symmetry can be restored by defining a complex wavevector with an imaginary shift of origin,

$$\tilde{\boldsymbol{\kappa}} \equiv \boldsymbol{\kappa} - i\boldsymbol{\delta}. \quad (2.4.1)$$

By defining a corresponding position vector

$$\tilde{\boldsymbol{\rho}} \equiv \boldsymbol{\rho}' - i\boldsymbol{\mu} \quad (2.4.2)$$

in terms of an ‘accumulated dichroism’ vector $\boldsymbol{\mu}$, and a shift $\boldsymbol{\rho}'$ which is trivial here, but we will soon generalise,

$$\boldsymbol{\rho}' = \boldsymbol{\rho}, \quad \boldsymbol{\mu} = \zeta\boldsymbol{\delta}, \quad (2.4.3)$$

we can write the evolution matrix as

$$\begin{aligned} \mathcal{F}(\boldsymbol{\kappa}, \boldsymbol{\rho}, \zeta) &= \left\{ (-\tilde{\boldsymbol{\kappa}} \cdot \tilde{\boldsymbol{\rho}} + \frac{1}{2}\zeta\tilde{\boldsymbol{\kappa}}^2) \mathcal{I} + \mathbf{V}(\tilde{\boldsymbol{\kappa}}) \cdot \boldsymbol{\Sigma} \right\} - (i\boldsymbol{\delta} \cdot \boldsymbol{\rho} + \frac{1}{2}\zeta\delta^2) \mathcal{I}, \\ &= \mathcal{F}(\tilde{\boldsymbol{\kappa}}, \tilde{\boldsymbol{\rho}}, \zeta) + \mathcal{F}_0(\boldsymbol{\rho}, \zeta), \\ \mathcal{F}_0(\boldsymbol{\rho}, \zeta) &= \mathcal{F}(i\boldsymbol{\delta}, \boldsymbol{\rho}, \zeta). \end{aligned} \quad (2.4.4)$$

This separates out the $\tilde{\boldsymbol{\kappa}}$ dependent evolutionary terms into a matrix $\mathcal{F}(\tilde{\boldsymbol{\kappa}}, \tilde{\boldsymbol{\rho}}, \zeta)$ which is rotationally symmetric in $\tilde{\boldsymbol{\kappa}}$, so we can work entirely in terms of the function (2.3.14). From \mathcal{F}_0 we have an uninteresting ζ -dependent phase shift, and a uni-directional exponential damping $e^{-\boldsymbol{\delta} \cdot \boldsymbol{\rho}}$, which is a ramp modulating the wave amplitude. We can then express the propagator integral in a form where all circular asymmetry is contained in the incident beam profile,

$$\mathbf{D}(\tilde{\boldsymbol{\rho}}, \zeta) = \frac{e^{-i\mathcal{F}_0(\boldsymbol{\rho}, \zeta)}}{2\pi} \int \int d\tilde{\boldsymbol{\kappa}} e^{-i\mathcal{F}(\tilde{\boldsymbol{\kappa}}, \tilde{\boldsymbol{\rho}}, \zeta)} a(\tilde{\boldsymbol{\kappa}} + i\boldsymbol{\delta}) \mathbf{d}_0. \quad (2.4.5)$$

Gaussian beams present a surprising further simplification. Consider the integrand of the propagator integral for a gaussian beam (2.3.4), whose profile is a quadratic exponen-

tial, allowing us to incorporate it into the optical path length:

$$\begin{aligned} e^{-i\mathcal{F}(\boldsymbol{\kappa}, \boldsymbol{\rho}, \zeta)} a(\boldsymbol{\kappa}) &= e^{i\left[\boldsymbol{\kappa} \cdot \boldsymbol{\rho} - \frac{1}{2}\zeta\kappa^2 - \mathbf{V}(\boldsymbol{\kappa}) \cdot \boldsymbol{\Sigma}\right]} e^{-\frac{1}{2}\kappa^2} \\ &= e^{i\left[\boldsymbol{\kappa} \cdot \boldsymbol{\rho} - \frac{1}{2}\tilde{\zeta}\kappa^2 - \mathbf{V}(\boldsymbol{\kappa}) \cdot \boldsymbol{\Sigma}\right]}, \end{aligned} \quad (2.4.6)$$

by complexifying the propagation distance and setting the beam profile to unity,

$$\zeta \rightarrow \tilde{\zeta} \equiv \zeta - i, \quad a(\boldsymbol{\kappa}) \rightarrow 1. \quad (2.4.7)$$

This corresponds to an imaginary shift of origin along the ζ direction originally due to Deschamps (1971), which physically replaces the beam by a bundle of complex rays issuing from a point source at an imaginary coordinate $\zeta = -i$. The surprise comes when we now consider that, for absorbing or chiral crystals, no single well-defined degeneracy direction exists, and we ask the question: “so where should we point the beam?”

The $\boldsymbol{\kappa} = 0$ direction corresponds to a wavevector direction which we can dub the ‘departed optic axis’ defined by (2.1.20). To be general we should consider aligning the beam at an angle κ_0/k_0w away from this axis, along some particular direction, defining a transverse deflection vector $\boldsymbol{\kappa}_0$, and introducing the misaligned beam profile $a(\boldsymbol{\kappa} - \boldsymbol{\kappa}_0)$. When we do so, we must redefine (2.4.3) as

$$\boldsymbol{\rho}' = \boldsymbol{\rho} - \boldsymbol{\delta}, \quad \boldsymbol{\mu} = \zeta\boldsymbol{\delta} + \boldsymbol{\kappa}_0, \quad (2.4.8)$$

whereby the propagator integrand simplifies to

$$\begin{aligned} e^{-i\mathcal{F}(\boldsymbol{\kappa}, \boldsymbol{\rho}, \zeta)} a(\boldsymbol{\kappa} - \boldsymbol{\kappa}_0) &= e^{i\left[\boldsymbol{\kappa} \cdot \boldsymbol{\rho} - \frac{1}{2}\zeta\kappa^2 - \mathbf{V}(\boldsymbol{\kappa} - i\boldsymbol{\delta}) \cdot \boldsymbol{\Sigma}\right]} e^{-\frac{1}{2}(\boldsymbol{\kappa} - \boldsymbol{\kappa}_0)^2} \\ &= e^{i\left[\tilde{\boldsymbol{\kappa}} \cdot \tilde{\boldsymbol{\rho}} - \frac{1}{2}\tilde{\zeta}\tilde{\kappa}^2 - \mathbf{V}(\tilde{\boldsymbol{\kappa}}) \cdot \boldsymbol{\Sigma}\right] - \boldsymbol{\delta} \cdot \boldsymbol{\rho} - \frac{1}{2}\kappa_0^2 + \frac{1}{2}i\zeta\delta^2 + i\boldsymbol{\delta} \cdot \boldsymbol{\kappa}_0} \\ &\equiv e^{-i[\mathcal{F}(\tilde{\boldsymbol{\kappa}}, \tilde{\boldsymbol{\rho}}, \tilde{\zeta}) + \mathcal{F}_0(\boldsymbol{\rho}, \tilde{\zeta})]}. \end{aligned} \quad (2.4.9)$$

Thus to obtain the dichroic propagator integral from the simpler transparent integral, we need only make the transformation

$$\begin{aligned} \mathcal{F}(\boldsymbol{\kappa}, \boldsymbol{\rho}, \zeta) &\rightarrow \mathcal{F}(\tilde{\boldsymbol{\kappa}}, \tilde{\boldsymbol{\rho}}, \tilde{\zeta}) + \mathcal{F}_0(\boldsymbol{\rho}, \tilde{\zeta}) \\ \mathcal{F}_0(\boldsymbol{\rho}, \tilde{\zeta}) &= \mathcal{F}(i\boldsymbol{\delta}, \boldsymbol{\rho} - i\boldsymbol{\kappa}_0, \tilde{\zeta}) - \frac{1}{2}i\kappa_0^2\mathcal{I}. \end{aligned} \quad (2.4.10)$$

The evolution terms have again been separated out into the rotationally symmetric function $\mathcal{F}(\tilde{\boldsymbol{\kappa}}, \tilde{\boldsymbol{\rho}}, \tilde{\zeta})$, wherein the dichroism of the crystal and the misalignment of the beam are combined into a single vector $\boldsymbol{\mu}$.

This is a surprising result: the nonhermiticity δ of the dielectric matrix (2.1.9) and the symmetry breaking of the beam shift κ_0 are equivalent in effect. This means that for any dichroic crystal we can choose a beam direction, for any given propagation distance, to counteract (or conversely to simulate) the effects of dichroism.

Of course there remains a constant damping from \mathcal{F}_0 which distinguishes the two effects. Either cause a uniform exponential damping quadratic in the dichroism or misalignment parameter, as well as the exponential ramp particular to dichroism, but these are overall constants which are not of interest to us. For gaussian beams we thus obtain a propagator integral separable into radial and azimuthal parts,

$$\mathbf{D}(\tilde{\rho}, \tilde{\zeta}) = \frac{e^{-i\mathcal{F}_0(\tilde{\rho}, \tilde{\zeta})}}{2\pi} \int \int d\tilde{\mathbf{k}} e^{-i\mathcal{F}(\tilde{\mathbf{k}}, \tilde{\rho}, \tilde{\zeta})} d\mathbf{d}. \quad (2.4.11)$$

The optical path length complexifies in a manner analogous to the evolution matrix. Considering a plane wave $a(\boldsymbol{\kappa}) e^{-i\Phi(\boldsymbol{\kappa}, \boldsymbol{\rho}, \zeta)}$ we derive the transformation

$$\begin{aligned} \Phi(\boldsymbol{\kappa}, \boldsymbol{\rho}, \zeta) &= -\tilde{\mathbf{k}} \cdot \tilde{\boldsymbol{\rho}} + \frac{1}{2}\zeta\tilde{\kappa}^2 \pm V(\tilde{\mathbf{k}}) - i\boldsymbol{\delta} \cdot \boldsymbol{\rho} - \frac{1}{2}\zeta\delta^2 \\ &= \Phi(\tilde{\mathbf{k}}, \tilde{\boldsymbol{\rho}}, \zeta) + \Phi_0(\boldsymbol{\rho}, \zeta) \\ \Phi_0(\boldsymbol{\rho}, \zeta) &= \Phi(i\boldsymbol{\delta}, \boldsymbol{\rho}, \zeta). \end{aligned} \quad (2.4.12)$$

For a gaussian beam misaligned with the optic axis, considering the integrand of the propagator integral gives similarly

$$\begin{aligned} e^{-i\Phi(\boldsymbol{\kappa}, \boldsymbol{\rho}, \zeta)} a(\boldsymbol{\kappa} - \boldsymbol{\kappa}_0) &= e^{i[\boldsymbol{\kappa} \cdot \boldsymbol{\rho} - \frac{1}{2}\zeta\kappa^2 \mp V(\boldsymbol{\kappa} - i\boldsymbol{\delta})]} e^{-\frac{1}{2}(\boldsymbol{\kappa} - \boldsymbol{\kappa}_0)^2} \\ &= e^{i[\tilde{\mathbf{k}} \cdot \tilde{\boldsymbol{\rho}} - \frac{1}{2}\zeta\tilde{\kappa}^2 \mp V(\tilde{\mathbf{k}})]} e^{-\boldsymbol{\delta} \cdot \boldsymbol{\rho} - \frac{1}{2}\kappa_0^2 + \frac{1}{2}i\zeta\delta^2 + i\boldsymbol{\delta} \cdot \boldsymbol{\kappa}_0} \\ &\equiv e^{-i[\Phi(\tilde{\mathbf{k}}, \tilde{\boldsymbol{\rho}}, \zeta) + \Phi_0(\boldsymbol{\rho}, \zeta)]}, \end{aligned} \quad (2.4.13)$$

so the phase in the presence of dichroism or misalignment is obtained from the transparent phase by the transformation

$$\begin{aligned} \Phi_{\pm}(\boldsymbol{\kappa}, \boldsymbol{\rho}, \zeta) &\rightarrow \Phi_{\pm}(\tilde{\mathbf{k}}, \tilde{\boldsymbol{\rho}}, \zeta) + \Phi_0(\boldsymbol{\rho}, \zeta) \\ \Phi_0(\boldsymbol{\rho}, \zeta) &= \Phi(i\boldsymbol{\delta}, \boldsymbol{\rho} - i\boldsymbol{\kappa}_0, \zeta) - \frac{1}{2}i\kappa_0^2. \end{aligned} \quad (2.4.14)$$

Henceforth we need only emphasize the wavevector dependence of the evolution matrix \mathcal{F} and optical path length Φ , with dependence on the complexified wavevector implying fully complexified variables, that is

$$\mathcal{F}(\tilde{\mathbf{k}}) \equiv \mathcal{F}(\tilde{\mathbf{k}}, \tilde{\boldsymbol{\rho}}, \zeta), \quad \Phi(\tilde{\mathbf{k}}) \equiv \Phi(\tilde{\mathbf{k}}, \tilde{\boldsymbol{\rho}}, \zeta). \quad (2.4.15)$$

2.5 Eigenwave Representation

How are we to extract any physics from these complexified (or rather, simplified!) integrals? By complexifying (2.3.18), the propagator integral can be expressed generally as

$$\mathbf{D}(\tilde{\boldsymbol{\rho}}, \zeta) = \frac{e^{-i\Phi_0}}{2\pi} \sum_{\pm} \int \int d\tilde{\boldsymbol{\kappa}} e^{-i\Phi_{\pm}(\tilde{\boldsymbol{\kappa}})} \mathcal{K}_{\pm}(\boldsymbol{\kappa}) a(\boldsymbol{\kappa}) \mathbf{d}_0. \quad (2.5.1)$$

This describes a superposition of plane waves which have refracted through the crystal. It contains scalar information in their amplitude $a e^{\text{Im}\Phi_{\pm}}$ and phase $e^{-i\text{Re}\Phi_{\pm}}$, and vector information in their polarisation $\mathcal{K}_{\pm}\mathbf{d}_0$. The scalar can be understood asymptotically and linked back to geometrical optics, which we consider in the next two sections. First we will make the polarisation structure of the field explicit.

We can exploit the rotational symmetry of \mathcal{K}_{\pm} by considering the product $\mathbf{V}(\tilde{\boldsymbol{\kappa}}) \cdot \boldsymbol{\Sigma} = \rho_0 \{\tilde{\boldsymbol{\kappa}}, \gamma\} \cdot \boldsymbol{\Sigma}$. Ignoring the third component, we can write

$$\tilde{\boldsymbol{\kappa}} \cdot \boldsymbol{\Sigma} = \frac{(\tilde{\boldsymbol{\kappa}} \cdot \tilde{\boldsymbol{\rho}}) \tilde{\boldsymbol{\rho}} \cdot \boldsymbol{\Sigma} + (\tilde{\boldsymbol{\kappa}} \times \tilde{\boldsymbol{\rho}}) \times \tilde{\boldsymbol{\rho}} \cdot \boldsymbol{\Sigma}}{\tilde{\rho}^2}. \quad (2.5.2)$$

The cross term is an odd function of angle in $\tilde{\boldsymbol{\kappa}}$ and therefore vanishes in the azimuthal part of the integral. This vanishing is exact for transparent crystals with a circularly symmetric incident beam. It is also exact for gaussian beams in absorbing crystals since we set $a \rightarrow 1$. For general beams in absorbing crystals the circular symmetry is broken by $a(\boldsymbol{\kappa}) = a(\tilde{\boldsymbol{\kappa}} + i\boldsymbol{\delta})$, but for slow varying beams this constitutes only a small perturbation, so we continue to neglect the cross term.

Thus substituting $\tilde{\boldsymbol{\kappa}} \cdot \boldsymbol{\Sigma} \rightarrow (\tilde{\boldsymbol{\kappa}} \cdot \tilde{\boldsymbol{\rho}}) \tilde{\boldsymbol{\rho}} \cdot \boldsymbol{\Sigma} / \tilde{\rho}^2$ into the propagator integral, we get

$$\mathbf{D}(\tilde{\boldsymbol{\rho}}, \zeta) = \frac{e^{-i\Phi_0}}{2} \left(\mathcal{I} + \left\{ \frac{\tilde{\boldsymbol{\rho}}}{\tilde{\rho}\rho_0\gamma} \frac{\partial^2}{\partial\tilde{\rho}\partial\gamma}, \frac{i\partial}{\rho_0\partial\gamma} \right\} \cdot \boldsymbol{\Sigma} \right) \sum_{\pm} b_{\pm}(\tilde{\boldsymbol{\rho}}, \zeta) \mathbf{d}_0, \quad (2.5.3)$$

extracting two scalar diffraction integrals

$$b_{\pm}(\tilde{\boldsymbol{\rho}}, \zeta) = \frac{1}{2\pi} \int \int d\tilde{\boldsymbol{\kappa}} e^{-i\Phi_{\pm}(\tilde{\boldsymbol{\kappa}})} a(\boldsymbol{\kappa}), \quad (2.5.4)$$

associated with the ‘ \pm ’ eigenpolarisations of the diffracted field.

To derive the field’s eigenpolarisations we can make another decomposition (obvious from (2.5.3)) of \mathbf{D} into three scalar diffraction integrals:

$$\mathbf{D}(\tilde{\boldsymbol{\rho}}, \zeta) = e^{-i\mathcal{F}_0} \left[B_0(\tilde{\boldsymbol{\rho}}, \zeta) \mathcal{I} + \left\{ \frac{\tilde{\boldsymbol{\rho}}}{\tilde{\rho}} B_1(\tilde{\boldsymbol{\rho}}, \zeta), B_2(\tilde{\boldsymbol{\rho}}, \zeta) \right\} \cdot \boldsymbol{\Sigma} \right] \cdot \mathbf{d}_0, \quad (2.5.5)$$

where

$$\begin{aligned}
B_0(\tilde{\boldsymbol{\rho}}, \zeta) &\equiv \frac{1}{2\pi} \int \int d\tilde{\boldsymbol{\kappa}} a(\boldsymbol{\kappa}) e^{i\left(-\frac{1}{2}\zeta\tilde{\boldsymbol{\kappa}}^2 + \tilde{\boldsymbol{\kappa}} \cdot \tilde{\boldsymbol{\rho}}\right)} \cos V(\tilde{\boldsymbol{\kappa}}) \\
B_1(\tilde{\boldsymbol{\rho}}, \zeta) &\equiv \frac{1}{\rho_0 \gamma} \frac{\partial^2}{\partial \tilde{\rho} \partial \gamma} B_0(\tilde{\boldsymbol{\rho}}, \zeta) \\
B_2(\tilde{\boldsymbol{\rho}}, \zeta) &\equiv \frac{i}{\rho_0} \frac{\partial}{\partial \gamma} B_0(\tilde{\boldsymbol{\rho}}, \zeta).
\end{aligned} \tag{2.5.6}$$

In the forthcoming asymptotics we need only study B_0 , which contains the sum over the two polarisations

$$B_0 = \frac{b_+ + b_-}{2}, \tag{2.5.7}$$

and then derive the asymptotics of $B_{1,2}$ by differentiation.

The eigenvectors of the matrix [..] in (2.5.5) are the eigenpolarisations of the diffracted light field:

$$\mathbf{d}_{\pm}(\tilde{\boldsymbol{\rho}}, \zeta) = \Lambda_{\pm}(\tilde{\boldsymbol{\rho}}, \zeta) \mathbf{d}_{\uparrow}(\tilde{\boldsymbol{\rho}}) \pm i\Lambda_{\mp}(\tilde{\boldsymbol{\rho}}, \zeta) \mathbf{d}_{\downarrow}(\tilde{\boldsymbol{\rho}}) \tag{2.5.8}$$

$$\Lambda_{\pm}(\tilde{\boldsymbol{\rho}}, \zeta) \equiv \frac{1}{\sqrt{2}} \sqrt{1 \pm \frac{B_1(\tilde{\boldsymbol{\rho}}, \zeta)}{\sqrt{B_1^2(\tilde{\boldsymbol{\rho}}, \zeta) + B_2^2(\tilde{\boldsymbol{\rho}}, \zeta)}}}, \tag{2.5.9}$$

which simplify to circular polarisations, $\mathbf{d}_{\pm}^{\text{circ}}$, along the axis $\tilde{\rho} = 0$, and to $\mathbf{d}_{\uparrow\downarrow}(\tilde{\boldsymbol{\rho}})$ defined by (2.3.25) in the absence of chirality, for which $B_2 = 0$. The associated eigenvalues are

$$A_{\pm} = B_0 \pm \sqrt{B_1^2 + B_2^2} \tag{2.5.10}$$

By defining 2×2 matrices

$$\mathcal{D}_{\pm} = \frac{1}{2} \left(\mathcal{I} \pm \frac{1}{\sqrt{B_1^2 + B_2^2}} \left\{ \frac{\tilde{\rho}}{\rho} B_1, B_2 \right\} \cdot \boldsymbol{\Sigma} \right), \tag{2.5.11}$$

which satisfy

$$\mathcal{D}_{\pm} \mathbf{d}_{\pm} = \mathbf{d}_{\pm}, \quad \mathcal{D}_{\pm} \mathbf{d}_{\mp} = 0, \tag{2.5.12}$$

we can write

$$e^{i\mathcal{F}_0} \mathbf{D} = (A_+ \mathcal{D}_+ + A_- \mathcal{D}_-) \cdot \mathbf{d}_0 \tag{2.5.13}$$

$$= A_+ (\mathbf{d}_+ \cdot \mathbf{d}_0) \mathbf{d}_+ + A_- (\mathbf{d}_- \cdot \mathbf{d}_0) \mathbf{d}_-. \tag{2.5.14}$$

This representation splits the propagator integral \mathbf{D} into two scalar waves A_{\pm} which are the eigenvalues of the diffracted field. For transparent crystals they are associated with orthogonal polarisations: the linear $\mathbf{d}_{\uparrow\downarrow}(\boldsymbol{\rho})$ states in a biaxial crystal, and the elliptical

$\mathbf{d}_\pm(\boldsymbol{\rho})$ states with chirality. Being orthogonal the two sets of waves $A_+\mathbf{d}_+$ and $A_-\mathbf{d}_-$ do not interfere, so the two diffraction integrals A_\pm give rise to independent phenomena.

In the absence of chirality $A_\pm = b_\pm$, that is, the simple integrals b_\pm are themselves the eigenwaves of the diffracted field. In the presence of chirality the eigenwaves A_\pm involve complicated square roots of integrals, but the simpler integrals b_\pm still represent waves in the different ‘ \pm ’ eigenpolarisations.

With absorption the eigenpolarisations are no longer orthogonal (and are generally elliptical). We shall see that the b_\pm states still represent a meaningful separation, serving as the natural continuation of the orthogonal states from a transparent crystal, and special phenomena arise from interference between b_+ and b_- .

For a gaussian incident beam, the diffraction integrals can be expressed as functions of a single variable. An obvious approach is to transform to variables in which the quadratic phase term $-\frac{1}{2}i\tilde{\zeta}\kappa^2$ has a gaussian form $-\frac{1}{2}s^2$ so the integral is fast converging, but a fatal side-effect is to make the oscillations of the integral faster and exponentially greater in magnitude, unsuitable for numerical methods. Instead we will use a form suitable for asymptotic analysis, obtained under the following scalings:

$$\begin{aligned}\boldsymbol{\sigma} &= \tilde{\kappa}\sqrt{\tilde{\zeta}}, & g &= \gamma\sqrt{\tilde{\zeta}} \\ \mathbf{r} &= \tilde{\boldsymbol{\rho}}/\sqrt{\tilde{\zeta}} & r_0 &= \rho_0/\sqrt{\tilde{\zeta}},\end{aligned}\tag{2.5.15}$$

yielding integral functions of a single variable defined by

$$C_m\left(\frac{\tilde{\boldsymbol{\rho}}}{\sqrt{\tilde{\zeta}}}\right) = \tilde{\zeta}B_m(\tilde{\boldsymbol{\rho}}, \tilde{\zeta}),\tag{2.5.16}$$

which obey the same differential relations as (2.5.6),

$$C_1(r) = \frac{1}{ig}C_2(r) = \frac{1}{r_0g}\frac{\partial^2}{\partial r\partial g}C_0(r).\tag{2.5.17}$$

An analogous scaling can be applied, of course, to A_\pm and b_\pm .

2.6 Asymptotics of the Geometrical Optics Limit . . .

We will show here how the optical path length enters into the propagator integral as a governing phase. We wish to consider the behaviour of the propagator integral in the asymptotic limit of large wavenumber k . This is the *geometrical optics* limit, where the

exact diffraction of waves can be approximated as the geometrical refraction of waves described by rays. Our approach will be the method of stationary phase, described in many texts (good accounts are in Heading (1962), Dingle (1973), Wong (1989), Fröman & Fröman (1965) with a more basic account in Born & Wolf (1959)). We will introduce the method here in a form physically entwined with the present problem.

Although the wavenumber has been scaled out in our analysis, recall that the optical path length $\Phi = -\mathbf{k} \cdot \mathbf{r}$ is proportional to k . The heart of the propagator integral is the wave derived in the previous section,

$$b_{\pm}(\tilde{\boldsymbol{\rho}}, \zeta) \equiv \frac{1}{2\pi} \int \int d\tilde{\boldsymbol{\kappa}} a(\tilde{\boldsymbol{\kappa}} + i\boldsymbol{\delta}) e^{-i\Phi_{\pm}(\tilde{\boldsymbol{\kappa}})}. \quad (2.6.1)$$

Assuming that the beam profile $a(\boldsymbol{\kappa})$ is not an exponentially fast varying function, we say it is slowly varying. In the geometrical optics limit the exponential dominates the behaviour of the integrand, which can therefore be characterised by the phase contours $\text{Re}\Phi = \text{constant}$, and amplitude contours $\text{Im}\Phi = \text{constant}$, of the exponential. We will generally consider either the cartesian double integral, say over $d\tilde{\boldsymbol{\kappa}} = d\tilde{\kappa}_x d\tilde{\kappa}_y$, or when the azimuthal integral can be done exactly we are left with a radial integral over $d\tilde{\kappa}$. We study the contours of Φ by continuing into the complex planes of $\tilde{\kappa}_x$ and $\tilde{\kappa}_y$, or $\tilde{\kappa}$.

It is best, both numerically and analytically, to integrate along lines of stationary phase so the integrand does not oscillate. This is the principle of *stationary phase*. Because Φ satisfies the Cauchy-Riemann equations, phase contours are also lines of steepest descent along which the integrand is decreasing fastest. Moreover this variation is exponential, so we can neglect the exponentially small contributions where an integration path tails off to infinity, approximating the integral only in the neighbourhood of: (i), *endpoints* – the finite endpoints of the integrand if they exist, which may not be small enough to ignore; and (ii), *saddlepoints* – where two phase contours cross so the integrand passes through either a maximum or a minimum.

Saddlepoints $\tilde{\boldsymbol{\kappa}}_n$ of the phase Φ satisfy

$$\nabla_{\tilde{\boldsymbol{\kappa}}}\Phi(\tilde{\boldsymbol{\kappa}}_n) = 0, \quad n = 1 \dots N, \quad (2.6.2)$$

where N is the order of the polynomial expression for $\tilde{\boldsymbol{\kappa}}$ obtained from $\nabla_{\tilde{\boldsymbol{\kappa}}}\Phi(\tilde{\boldsymbol{\kappa}})$. It is necessary to include up to second order terms in a Taylor expansion of the exponent, but for the slowly varying beam profile prefactor only the zeroth order term is needed, giving

a contribution near each saddlepoint of

$$b_n(\tilde{\rho}, \zeta) \equiv \frac{a(\tilde{\kappa}_n + i\delta) e^{-i\Phi(\tilde{\kappa}_n)}}{2\pi} \int \int d\tilde{\kappa} e^{-\frac{1}{2}i(\tilde{\kappa} - \tilde{\kappa}_n) \cdot ((\tilde{\kappa} - \tilde{\kappa}_n) \cdot \nabla_{\tilde{\kappa}}) \nabla_{\tilde{\kappa}} \Phi(\tilde{\kappa}_n)}. \quad (2.6.3)$$

There exists a unique *smooth deformation* of the real integration path, such that it lies *entirely along* phase contours and the integral converges; the integral is then given by summing over any saddlepoints traversed by this contour,

$$b(\tilde{\rho}, \zeta) \approx \sum_n b_n(\tilde{\rho}, \zeta). \quad (2.6.4)$$

The deceptively simple phrase ‘entirely along’ used here requires precise definition. *Smooth* means that no breaks are made in the path during deformation, requiring that it does not cross any poles (singularities) or branch points, and more importantly that its endpoints remain fixed. This means typically that the deformed path will have to lie along more than one phase contour, and the phrase *entirely along* implies that the connections between two contours (which do not lie along contours) can be neglected from the integration. Thus the connections must occur only where the function is infinitesimally small: where phase contours tail off to infinity in the direction of steepest descent. The phase contours of an analytic function are infinite lines, that is they do not terminate anywhere in the complex plane and do not form closed loops, so they always asymptote to infinity either in a direction of steepest ascent or descent. This applies also to functions which are analytic in any region not containing a pole or a branch point, so when chirality is included, deformation may take place across the two Riemann sheets introduced by a square root in Φ , so long as branch points are not crossed. After neglecting these connections we say the deformed path lies *entirely along* phase contours.

The procedure to identify this unique contour is to identify the N saddlepoints, to project paths from them along the directions of steepest descent, and to connect pairs of paths only where they approach asymptotically. The path which thus forms a smooth deformation of the original contour is unique and convergent, and any paths not forming a part of it are discarded from the integral.

The endpoint of the integral may present a maximum along the integration contour. We will encounter this in the propagator integral when evaluated in polar coordinates, at the endpoint $\tilde{\kappa} = 0$ of the radial integral. Labeling this point $n = 0$, its contribution to the integral is given by

$$b_0(\tilde{\rho}, \zeta) \equiv a(i\delta) e^{-i\Phi(0)} \int d\tilde{\kappa} e^{-i\tilde{\kappa}\Phi'(0)}, \quad (2.6.5)$$

that is, a wave scattered from the phase space direction $\tilde{\mathbf{k}} = 0$.

The integrals arising from endpoint and saddlepoint contributions are typically integrable analytically, and rather simple, but require careful considerations of phase which we will encounter in specific cases later. In particular there are three degeneracies that dominate the general behavior of the saddlepoints, and they are responsible for geometric interference and focusing. Let us now consider these.

If the second derivative of the phase vanishes then its expansion in (2.6.3) must be taken to third order, taking the generic form of an Airy integral. This condition can be expressed compactly by the vanishing of the Hessian determinant,

$$0 = \left| \frac{\partial^2 \Phi(\tilde{\mathbf{k}})}{\partial \tilde{\mathbf{k}}^2} \right| = \begin{vmatrix} \frac{\partial^2 \Phi(\tilde{\mathbf{k}})}{\partial \tilde{k}_x \partial \tilde{k}_x} & \frac{\partial^2 \Phi(\tilde{\mathbf{k}})}{\partial \tilde{k}_x \partial \tilde{k}_y} \\ \frac{\partial^2 \Phi(\tilde{\mathbf{k}})}{\partial \tilde{k}_y \partial \tilde{k}_x} & \frac{\partial^2 \Phi(\tilde{\mathbf{k}})}{\partial \tilde{k}_y \partial \tilde{k}_y} \end{vmatrix}. \quad (2.6.6)$$

These points are associated with the fold catastrophe (Poston & Stewart 1996), where two stationary points (saddlepoints) of the phase coalesce. In three dimensional position space these conditions define surfaces when Φ is real, called *caustics*, or lines when Φ is complex, called *complex whiskers* (Poston & Stewart 1976).

The set of saddlepoints included in the convergent integral depends on the parameters appearing in Φ . A saddlepoint may enter or leave the set when, as the parameters vary smoothly, two saddlepoints become connected by a phase contour. For two solutions $\tilde{\mathbf{k}}_i$ and $\tilde{\mathbf{k}}_j$ of (2.6.2), the loci of points satisfying that condition are lines in the complex space of each vector component of $\tilde{\mathbf{k}}$, given by

$$\text{Re} [\Phi(\tilde{\mathbf{k}}_i) - \Phi(\tilde{\mathbf{k}}_j)] = 0. \quad (2.6.7)$$

These are the *Stokes sets*, or *nonlocal bifurcation sets*, first identified in the asymptotics of the Airy function by Stokes (1847a, 1847b, 1864, 1902). In three dimensional position space they are surfaces. One saddlepoint, $\tilde{\mathbf{k}}_i$, is dominant over another, $\tilde{\mathbf{k}}_j$, if

$$\text{Im} \Phi(\tilde{\mathbf{k}}_i) > \text{Im} \Phi(\tilde{\mathbf{k}}_j), \quad (2.6.8)$$

and only the *subdominant* saddlepoint may ‘switch off’ at a Stokes set. The (exponentially larger) contribution of the dominant saddlepoint masks the disappearance of the subdominant saddlepoint, this dominance being maximal on a Stokes set, so that the discontinuous change generally causes no jump in the integral. In fact, it has been shown (Berry 1989) that even the disappearance of the saddlepoint is smooth, being described by the steep slope of an error function; for our purposes this smoothing will not be necessary.

The relative dominance of saddlepoints can exchange in pairs, across *anti-Stokes sets* given by

$$\text{Im} [\Phi(\tilde{\kappa}_i) - \Phi(\tilde{\kappa}_j)] = 0. \quad (2.6.9)$$

These also define lines in the complex $\tilde{\kappa}$ plane and surfaces in position space. In transparent media Φ will generally be real so anti-Stokes sets do not exist. In the presence of dichroism, however, the exchange of dominance occurs as an exponentially fast growth of the saddlepoint contributions. Because one contribution is increasing exponentially on either side of the anti-Stokes set, the set itself constitutes a locus of minimal amplitude, and is visible as an exponential decrease in the combined contribution to the integral. In the intensity plotted in position space, this therefore manifests as a dark surface.

2.7 . . . and Hamilton's Principle

Hamilton's equations for paraxial rays in a transparent medium take the form

$$\frac{\partial \boldsymbol{\rho}}{\partial \zeta} = \nabla_{\boldsymbol{\kappa}} H, \quad \frac{\partial \boldsymbol{\kappa}}{\partial \zeta} = -\nabla_{\boldsymbol{\rho}} H, \quad (2.7.1)$$

where the Hamiltonian H takes the eigenvalues of the Hamiltonian operator (2.3.12),

$$H(\boldsymbol{\kappa}) = \left\{ \begin{array}{ll} \frac{1}{2} n_2 \kappa^2, & \text{outside crystal} \\ \frac{1}{2} \kappa^2 \pm k w A \sqrt{(\boldsymbol{\kappa} - i\boldsymbol{\delta})^2 + \gamma^2}, & \text{inside crystal} \end{array} \right\}. \quad (2.7.2)$$

Let us see first how (2.3.19) would be derived geometrically. The optical path length Φ of plane waves $e^{-i\Phi}$ contains the transverse term $\boldsymbol{\kappa} \cdot \boldsymbol{\rho}$. Along the optic axis the path length is simply $k_z z \approx (k - \frac{1}{2} k_{\perp}^2 / k) z$ where $k = n k_0$, the refractive index being given by $n = 1$ outside the crystal and (2.2.5) inside the crystal. The optical path is measured from the source, which may be the focus for a beam and need not, as assumed by some authors, be placed at the entrance face of the crystal, because the optical path length from the source to the entrance face is cancelled by terms beyond the exit face. When we neglect a direction independent length $k_0(z - l + n_2 l)$ which will not contribute to the wave amplitude, we indeed obtain the optical path length found previously from the eigenvalues of the evolution operator \mathcal{F} ,

$$\Phi(\boldsymbol{\kappa}, \boldsymbol{\rho}, \zeta) = -\boldsymbol{\kappa} \cdot \boldsymbol{\rho} + \frac{1}{k w^2} \int_0^z dz H(\boldsymbol{\kappa}) \quad (2.7.3)$$

$$= -\boldsymbol{\kappa} \cdot \boldsymbol{\rho} + \frac{1}{2} \zeta \kappa^2 \pm V(\boldsymbol{\kappa} - i\boldsymbol{\delta}). \quad (2.7.4)$$

Applying Hamilton's first equation to (2.7.3) yields Hamilton's principle (Hamilton 1828), the statement that rays are extremal optical paths,

$$\nabla_{\boldsymbol{\kappa}} \Phi(\boldsymbol{\kappa}) = 0. \quad (2.7.5)$$

In the absence of dichroism (when $\tilde{\boldsymbol{\kappa}} = \boldsymbol{\kappa}$) therefore, Hamilton's rays correspond to the saddlepoint contributions (2.6.2) of the propagator integral. This correspondence is a consequence of both the integration contour and the wave surface being defined as lines of stationary phase; the stationary lines studied in the phase of the propagator integral are the extension into the complex plane of the wave surface. Hamilton's second equation states that the transverse wavevector is conserved along ray paths. In the simplest incarnation of geometrical optics envisaged by Hamilton, the condition for solutions to the ray equation (2.7.5) to contribute to the intensity is simply that they are real. However, complex solutions may represent valid wave effects, whose contribution can only be assessed by the consideration of Stokes surfaces.

The correspondence between rays and saddlepoints now allows us to make an intuitive extension of geometrical optics to absorbing media. Generally, when the Hamiltonian, optical path length, and wavevector are complex, the real rays derived as stationary points are an approximation to the saddlepoints of section 2.6. The real ray is the point on the real $\tilde{\boldsymbol{\kappa}}$ wavevector axis where a phase contour lies tangential to the axis. As illustrated in figure 2.4, this typically occurs close to a saddlepoint. In other words, the real ray corresponds to stationary phase *along* the axis of real $\tilde{\boldsymbol{\kappa}}$ values, close to but distinct from, the saddlepoint where $\tilde{\boldsymbol{\kappa}}$ is complex. Since the integration contour traverses a maximum of the integrand only by crossing a saddlepoint, a 'real ray' constitutes a much weaker approximation than the stationary phase method of section 2.6.

This distinction is not special to absorbing crystals. Berry (2004b) comments on the great improvement for a gaussian beam in a transparent crystal that occurs when the substitution (2.4.7) to a bundle of complex rays is made. This corresponds to shifting from the stationary phase point in the real wavevector to the saddlepoint with a complex wavevector – from the real ray to the exact ray in figure 2.4.

The saddlepoint contributions derived from the complexified Hamilton's principle (2.6.2) can be termed *complex rays*, generalizing Hamilton's principle (2.7.5) to absorbing media, for which no fixed paths exist in real space that conserve the wavevector. It is easy to show that the stationary phase method is equivalent to complexifying Hamilton's equa-

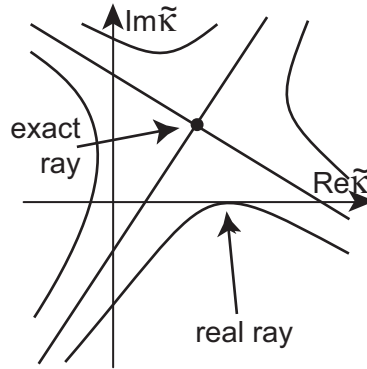


Figure 2.4: Real and complex rays in stationary phase analysis: phase contours of the diffraction integrand are illustrated in the complex plane of the wavevector $\tilde{\kappa}$. Complex rays correspond to saddlepoints of the integrand, and real rays, a weaker geometrical optics approximation, correspond to the point of stationary phase along the real axis.

tions, replacing the real wave and position vectors (and distance for a gaussian beam) with their complex counterparts, effectively reversing the derivation from (2.7.1) to (2.7.5) but in complex coordinates, with the result

$$\frac{\partial \tilde{\rho}}{\partial \zeta} = \nabla_{\tilde{\kappa}} H, \quad \frac{\partial \tilde{\kappa}}{\partial \zeta} = -\nabla_{\tilde{\rho}} H. \quad (2.7.6)$$

The geometric intensity is the sum of beam profiles $a(\tilde{\kappa}_n + i\delta)$ over the contributing rays, with a Jacobian multiplier giving the transformation into position space. Whether or not a solution to the complexified Hamilton's principle contributes as a physical ray must be determined by studying the Stokes and anti-Stokes surfaces. For complex rays there is also an exponential absorption prefactor, resulting in

$$I_{\text{geom}}(\tilde{\rho}, \zeta) = \frac{1}{2} \sum_n e^{\text{Im}(\Phi(\tilde{\kappa}_n) + \Phi_0)} \left| \frac{d\tilde{\rho}}{d\tilde{\kappa}_n} \right|^{-1} |a(\tilde{\kappa}_n)|^2. \quad (2.7.7)$$

The intensity of rays in transparent media is dominated by the sites of focusing, where rays crowd up forming an envelope of divergent geometrical intensity. For real rays in three dimensional position space this occurs along surfaces, for complex rays it is restricted to focal lines, and the general condition is the vanishing of the Hessian determinant

$$\left| \det \frac{d\tilde{\rho}(\tilde{\kappa})}{d\tilde{\kappa}} \right| = 0, \quad (2.7.8)$$

which is the same condition as (2.6.6). This crowding thus corresponds to the coalescence of saddlepoints in the propagator integral, occurring along caustic surfaces for real rays, or whiskers for complex rays.

Interestingly in absorbing media, focusing ceases to be the dominant feature in the intensity. As remarked by Berry & Howls (1990), this is because the divergence at a complex whisker can be swamped by an exponential gradient from the prefactor $e^{\text{Im}\Phi}$. Instead it is this gradient which dominates the intensity, characterised by anti-Stokes surfaces and attributable to *geometric interference*, that is, interference between complex rays. This is possible because complex rays contain phase information, and because, contrary to transparent media, the two interacting rays are generally nonorthogonally polarised. It is important to note that this geometric interference, attributed to the saddlepoints of the propagator integral, is distinct from wave interference attributable to the endpoints of the propagator integral, which is in no way a phenomenon of stationarity.

2.8 Inside the Crystal

The results throughout this thesis apply to the diffracted light field beyond the crystal's exit face, and by continuation to the virtual image field inside the crystal. This is the field that would be observed by focusing upon planes inside the crystal, using a lens for example, envisaged as the projection of virtual rays back into the crystal. To conclude this section I would like to remark on the *actual* geometric intensity of light propagating inside the crystal, which has been the starting point of most historical investigations.

It seems to have been Belskii & Khapalyuk (1978) who were the first to appreciate that, in an explicit expression for the observed intensity, the physical light field confined to the crystal would be irrelevant, drawing attention to the focal image plane $\zeta = 0$ and providing diffraction integrals for the image field. Nevertheless it is interesting, given the intricacy of the geometric patterns in the image field that we will discover later, to have some intuitive understanding of the pattern of rays which gives rise to them. We will restrict this consideration to transparent media and geometrical optics.

The actual ray propagation inside the crystal is obtained by integrating the optical path length (2.7.3) not to some $z > l$ beyond the exit face of the crystal, but to some $z < l$ inside the crystal. (The procedure is analogous for obtaining the actual wave field inside the crystal, but since this cannot be imaged we are not interested in interference

effects). It is the definition of the propagation distance ζ (2.3.15) that is key, and should perhaps be more appropriately termed *image distance*. It turns out that the result can be obtained by a simple transformation to conical coordinates associated with the conical propagation of rays constituting Hamilton's phenomenon. Taking the image field we first replace the propagation distance ζ by the (dimensionless) propagation distance from the source

$$\zeta \rightarrow \zeta' \equiv z/k_0 w^2. \quad (2.8.1)$$

We then replace the transverse position ρ by an angle of propagation θ_ρ from the optic axis,

$$\rho \rightarrow \theta_\rho \zeta', \quad (2.8.2)$$

replacing the radius ρ_0 of the conical refraction cone at the exit face by the scaled half-angle of the cone θ_0 ,

$$\rho_0 \rightarrow \theta_0 \zeta', \quad \theta_0 \equiv A n_2 k_0 w. \quad (2.8.3)$$

The two definitions of propagation distance necessarily agree at the exit face, where

$$\zeta = \zeta' = l/n_2 k_0 w^2 = \rho_0/\theta_0, \quad (2.8.4)$$

so that rays inside the crystal correctly refract at the exit face to form rays beyond the crystal.

Chapter 3

The Wave Surfaces

“a sound induction enabling us to predict, bearing not only stress, but torture: of theory actually remanding back experiment to read her lesson anew; informing her of facts so strange, as to appear to her impossible, and showing her all the singularities she would observe in critical cases she never dreamed of trying.”

Sir John Herschel on Hamilton’s discovery, 1841 (Graves 1882)

Fresnel’s ingenious theory of double refraction preceded Maxwell’s electrodynamic equations by almost 50 years, relying on geometrical arguments that extended the theories of Young and Huygens, making possible the discovery of conical refraction before Maxwell was even a year old. The wave surface, in both its standard interpretation and as a surface in the virtual field which I will present here, is invaluable to an intuitive understanding of double and conical refraction. We will derive Fresnel’s wave surface rigorously from Maxwell’s equations and discuss some of the interesting geometry associated with it, which is responsible for conical refraction and which led to its discovery, and then discuss the more useful virtual wave surface which is central to the phenomena expounded in this thesis.

3.1 Fresnel's Wave Surface and Hamilton's Cones

The wave surface is simply a phase contour. For a wave propagating in a medium with refractive index n , wavevector \mathbf{k} , and frequency σ , this is a level surface of the dispersion relation

$$\sigma(\mathbf{k}) = \frac{ck}{n(\mathbf{k})}. \quad (3.1.1)$$

Hamilton's equations state that a ray trajectory is given by the group velocity $\dot{\mathbf{r}} = \nabla_{\mathbf{k}}\sigma(\mathbf{k})$, and that the wavevector is conserved along a ray, $\dot{\mathbf{k}} = \nabla_{\mathbf{r}}\sigma(\mathbf{k}) = 0$. The former states that the rays are the normals to the wave surface, and therefore a small displacement $d\mathbf{k}$ with σ constant (anywhere in the wave surface) lies perpendicular to a ray, that is

$$\dot{\mathbf{r}} \cdot d\mathbf{k} = 0. \quad (3.1.2)$$

Energy flows along the Poynting vector

$$\mathbf{S} = \text{Re } \mathbf{E}^* \times \mathbf{H}, \quad (3.1.3)$$

which, from Maxwell's equations (2.1.11), satisfies

$$\mathbf{S} \cdot d\mathbf{k} = \frac{\sigma}{2} \text{Re} [\mathbf{E}^* \cdot d\mathbf{D} - \mathbf{D} \cdot d\mathbf{E}^* + \mathbf{H} \cdot d\mathbf{B}^* - \mathbf{B}^* \cdot d\mathbf{H}]. \quad (3.1.4)$$

For a transparent crystal the hermiticity of the constitutive relations (2.1.1) makes this vanish, $\mathbf{S} \cdot d\mathbf{k} = 0$, so the ray and Poynting vector directions coincide. Nonhermiticity in absorbing media means that $\mathbf{S} \cdot d\mathbf{k} \neq 0$, so the Poynting vector is not a wave surface normal, and therefore does not coincide with the (complex) ray direction.

To derive Fresnel's wave surface for a biaxial crystal we must write (2.1.12) in its dual form for \mathbf{E} instead of \mathbf{D} ,

$$\begin{aligned} \frac{1}{n^2} \mathcal{N}^{-1} \cdot \mathbf{E} &= -\hat{\mathbf{k}} \times \hat{\mathbf{k}} \times \mathbf{E} \\ &= \mathbf{E} - (\hat{\mathbf{k}} \cdot \mathbf{E}) \hat{\mathbf{k}}. \end{aligned} \quad (3.1.5)$$

\mathcal{N}^{-1} is just the diagonal matrix of squares of the principal refractive indices $\text{diag} [n_1^2, n_2^2, n_3^2]$, so we can rearrange this equation and write the j^{th} component as

$$\frac{E_j}{n^2} - \frac{\hat{\mathbf{k}} \cdot \mathbf{E}}{n^2 - n_j^2} \hat{k}_j = 0. \quad (3.1.6)$$

Multiplying this by \hat{k}_j , summing over j 's, then dividing by the first term $\hat{\mathbf{k}} \cdot \mathbf{E}/n^2$, gives upon some rearrangement the form of the wave surface originally stated by Fresnel,

$$\frac{\hat{k}_1^2}{\frac{1}{n^2} - \frac{1}{n_1^2}} + \frac{\hat{k}_2^2}{\frac{1}{n^2} - \frac{1}{n_2^2}} + \frac{\hat{k}_3^2}{\frac{1}{n^2} - \frac{1}{n_3^2}} = 0. \quad (3.1.7)$$

This equation, quadratic (as is clear from (3.1.6)) in the refractive index $n(\hat{\mathbf{k}})$, defines a two-fold surface generated by the wavevector $\mathbf{k} = k_0 n(\hat{\mathbf{k}}) \hat{\mathbf{k}}$, as the direction vector $\hat{\mathbf{k}}$ traces out all directions on the unit sphere. This is the wave surface depicted in figure 2.1 & 3.1(a). The optic axes, along which the two sheets of the wave surface intersect, were found in (2.1.20) from our own expression for the wave surface (2.1.17).

The wave surface is related to another surface that characterises \mathcal{N} called the index or tensor ellipsoid. It can be derived from the first constitutive relation in (2.1.1) by taking the dot product with \mathbf{D} , and noting that $\mathbf{E} \cdot \mathbf{D}$ is constant in the absence of dispersion (Landau et al. 1984), giving

$$\frac{D_1^2}{n_1^2} + \frac{D_2^2}{n_2^2} + \frac{D_3^2}{n_3^2} = \text{constant}. \quad (3.1.8)$$

In the direction space of \mathbf{D} this defines an ellipsoid with three unequal principal axes, which by a general property of ellipsoids possesses two circular cross sections, whose axes define the optic axes. This is shown in figure 3.1(b-c). When a wavevector is drawn from the centre of the ellipsoid the vibration directions, \mathbf{D} , lie in the transverse plane along

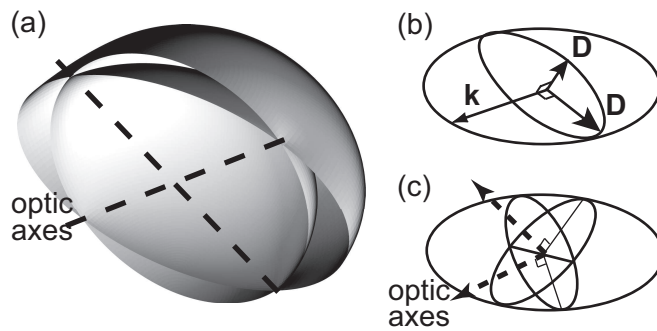


Figure 3.1: The optic axes: (a) cutaway of Fresnel's wave surface in direction space for a biaxial medium (3.1.7), showing the wave surface degeneracy along the optic axes; (b) the refractive index ellipsoid (3.1.8) showing a wavevector \mathbf{k} and corresponding directions of vibration \mathbf{D} ; c) the two circular sections of the ellipsoid and the optic axes normal to them.

the greatest and least radii of intersection with the ellipsoid (semimajor and semiminor axes of the elliptical section perpendicular to \mathbf{k}). If the wavevector points along the optic axis then all of these radii are equal (the section is circular), so the vibration direction is indeterminate. This is another, less geometrical, means of understanding the degeneracy responsible for conical refraction.

Let us now discuss conical refraction in the sense discovered by Hamilton. Let the wavevector \mathbf{k} lie along an optic axis, and let the vacuum constants $\mu_0 = \epsilon_0 = 1$. We can write the constitutive relation

$$\mathbf{E} = \bar{\mathcal{N}} \cdot \mathbf{D}, \quad (3.1.9)$$

where $\bar{\mathcal{N}}$ is the dielectric matrix, rotated from the $\{1, 2, 3\}$ principal axes to the $\{x, y, z\}$ frame, by rotation about the 2-axis so an optic axis lies along the z -direction. $\bar{\mathcal{N}}$ is determined by four conditions: elements involving the 2 (or y) rotation axis should remain fixed, the z -direction is degenerate so we must have $\bar{\mathcal{N}}_{xx} = \bar{\mathcal{N}}_{yy}$, and rotation does not change the trace and determinant. This uniquely sets

$$\bar{\mathcal{N}} = \frac{1}{n_2^2} \mathcal{I} + \begin{pmatrix} 0 & 0 & \sqrt{\alpha\beta} \\ 0 & 0 & 0 \\ \sqrt{\alpha\beta} & 0 & \alpha - \beta \end{pmatrix}, \quad (3.1.10)$$

(here \mathcal{I} is the 3×3 identity matrix) in terms of the biaxial anisotropy parameters defined in section 2.1. The matrix that generates the rotation $\hat{\mathcal{N}} = \mathcal{R} \bar{\mathcal{N}} \mathcal{R}^{-1}$ to the optic axis,

$$\mathcal{R} = \begin{pmatrix} \cos \theta_{\text{OA}} & 0 & -\sin \theta_{\text{OA}} \\ 0 & 1 & 0 \\ \sin \theta_{\text{OA}} & 0 & \cos \theta_{\text{OA}} \end{pmatrix}, \quad (3.1.11)$$

can then be used to imply the angle of the optic axis previously found in (2.1.20).

Let the electric displacement vector, which is transverse to the wavevector, have an angle χ to the x -axis,

$$\mathbf{D}^{\text{OA}} = D \begin{pmatrix} \cos \chi \\ \sin \chi \\ 0 \end{pmatrix}, \quad (3.1.12)$$

then the constitutive relation gives

$$\mathbf{E}^{\text{OA}} = \frac{D}{n_2^2} \begin{pmatrix} \cos \chi \\ \sin \chi \\ 2A \cos \chi \end{pmatrix}. \quad (3.1.13)$$

Thus the electric field vector traces out an ellipse as \mathbf{D} rotates, given by

$$\frac{1}{4} \left(E_x + \frac{E_z}{2A} \right)^2 + E_y^2 = \frac{D^2}{n_2^4}, \quad (3.1.14)$$

and the ray (Poynting vector), perpendicular to \mathbf{E} and \mathbf{H} , traces out a skewed cone

$$\mathbf{S} = \frac{D^2}{n_2^3} \begin{pmatrix} A(\cos 2\chi - 1) \\ A \sin 2\chi \\ 1 \end{pmatrix}. \quad (3.1.15)$$

As χ runs from 0 to π the Poynting vector completes a circuit of the optic axis, but the polarisation of the wave \mathbf{D} turns only half a circuit, a geometric phase effect characteristic of the conical point.

From (3.1.15) our definition of a *skewed cone* is clear: the axis of the cone is slanted such that the optic axis is itself a generator of the cone (lies in its surface and through its apex), while importantly the cross-section transverse to the optic axis remains circular. This is the source of the skew recognised in (2.3.1). The half-angle of this narrow cone is given exactly by

$$\tan 2\theta_{\text{cone}} = 2A, \quad (3.1.16)$$

and paraxially by

$$\theta_{\text{cone}} \approx A \quad (3.1.17)$$

$$\approx \frac{1}{n_2} \sqrt{(n_1 - n_2)(n_2 - n_3)}. \quad (3.1.18)$$

Equation (3.1.14) further shows that the wave surface near the optic axis direction has the shape of a pair of opposing cones, called a *conical* or *diabolical* point, with large half-angle $\pi/2 - \theta_{\text{cone}}$. A single ray incident upon the crystal thus degenerates into an infinite number of rays (\mathbf{S}), lying in the surface of a narrow cone, and this Hamilton termed *internal conical refraction*. At the exit face, the simple laws of refraction applying, each ray leaves the crystal with the direction it entered so the cone refracts into a cylinder.

The geometry of the wave surface is illustrated in figure 3.2(a), where the conical point is labelled A and the origin O, so the optic axis is OA. The wave surface possesses another degeneracy, a *tangent circle*, the locus of points where a single plane can contact the surface everywhere tangentially. The radial line perpendicular to this tangent plane is called the *binormal* OB. Such a circle encloses each optic axis, and from it springs a ring of parallel ray normals constituting an axial focal line. In the 1-3 (also x - z) plane

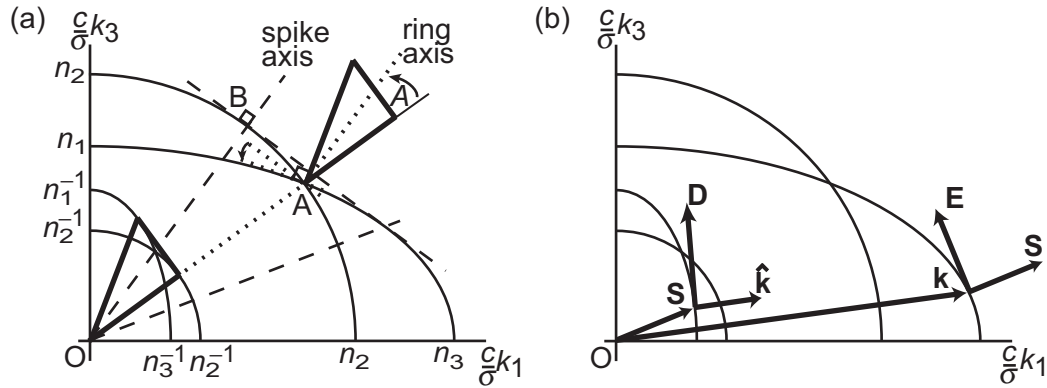


Figure 3.2: Duality of the wave and ray surfaces: (a) Geometry of the two surfaces, showing the optic axis OA , biradial OB , with the cones of internal (bold) and external (dashed) conical refraction, and the axes of the associated ring and axial focus. (b) The wave surface (outer) is generated by the wave vector \mathbf{k} , with the ray vector \mathbf{S} normal and the \mathbf{E} field tangential to it. Reciprocally, the ray vector \mathbf{S} generates the ray surface, with the ray vector \mathbf{S} normal and the \mathbf{D} field tangential to it.

illustrated, the direction of these normals is at an angle θ_{spike} to the vertical 3-axis, and from figure 3.2 and the equations (2.1.19) it is easy to find:

$$\sqrt{\frac{\alpha}{\beta}} = \tan \theta_{OA} = \frac{n_1}{n_3} \tan \theta_{OB} = \frac{n_3}{n_1} \tan \theta_{\text{spike}}. \quad (3.1.19)$$

Figure 3.2 also depicts the *ray surface*, dual to the wave surface in the sense indicated in part (b). The construction of this is due to Hamilton, though he attributes the theory of the existence of such duality to Cauchy (Hamilton 1837). Each wavevector \mathbf{k} generates a point on the wave surface at which the normal is a ray \mathbf{S} . Reciprocally, this ray vector generates a point on the ray surface at which the normal is the wavevector. The relative scale is fixed by the condition $\mathbf{k} \cdot \mathbf{S} = 1$. The electric \mathbf{E} and electric displacement \mathbf{D} vectors are everywhere tangential to the wave and ray surfaces respectively. As illustrated in figure 3.2(a) the degeneracy structure of the two surfaces must be connected thus: the conical point and tangent circle on the wave surface correspond respectively to a tangent circle and a conical point on the ray surface. Figure 3.3 illustrates this paraxially. The cone of internal conical refraction is exactly the cone of rays formed by joining the origin point O to the tangent circle T_A of the ray surface.

It was by this construction that Hamilton derived a second associated phenomenon,

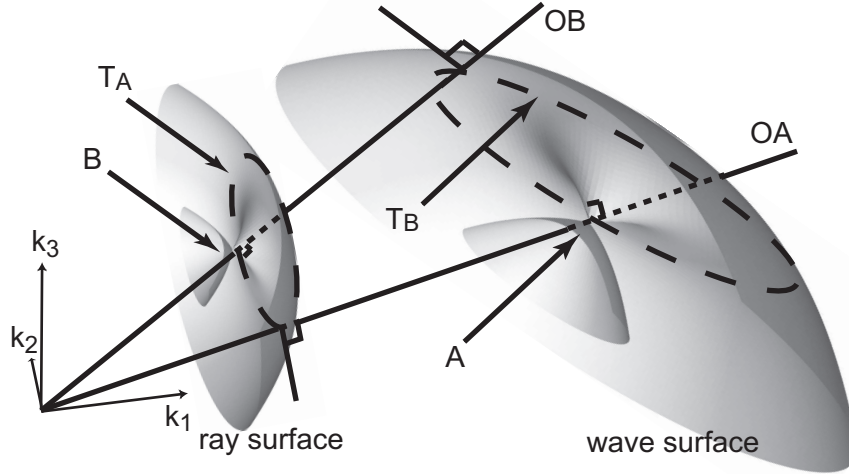


Figure 3.3: Geometry of internal and external conical refraction: a depiction of the wave and ray surfaces showing the correspondence between the optic axis OA , conical point A , and tangent circle T_A responsible for internal conical refraction, and between the binormal OB , conical point B , and tangent circle T_B responsible for external conical refraction. The paraxial regions are shown enlarged and angles are exaggerated for clarity.

external conical refraction, whereby a pencil of rays converging upon a crystal refracts into a single ray focused along its optic axis – note that this is just the focal line from the wave surface's tangent circle, a fact neglected ever since by all but Raman – which then refracts out of the crystal into another cone. The cone exiting the crystal is the cone of wavevectors formed by joining the origin O to the tangent circle T_B of the wave surface, and has half-angle B given by

$$\tan 2B = n_1 n_3 \sqrt{\alpha\beta}. \quad (3.1.20)$$

For beams of light containing a range of wave and ray directions, the phenomena of internal and external conical refraction transform into one another as a function of propagation distance. This can readily be seen from the wave surface construction by considering the different wave directions in a beam that contribute at different distances, and the form of the wave surface that scatters them, as was the approach taken by Raman et al. (1941). We shall study this in more detail in section 4.1.

Note that paraxially the angles A of internal, and B of external, conical refraction are equal,

$$A \approx B \approx \frac{1}{n_2} \sqrt{(n_1 - n_2)(n_2 - n_3)}, \quad (3.1.21)$$

and proportional to the index differences. The difference between them, with the anisotropy parameters regarded paraxially ($\alpha \approx 2(n_2 - n_1)/n_2^3$ and $\beta \approx 2(n_3 - n_2)/n_2^3$), is

$$A - B \approx \frac{n_2^4}{4} \sqrt{\alpha\beta} \left[\alpha - \beta + \frac{n_2^2}{8} \left(3(\alpha - \beta)^2 + 4\alpha\beta \right) \right], \quad (3.1.22)$$

which is proportional to the square of the two refractive index differences if they are distinct, or the cube if they are equal, and vanishes if $n_1^2 + n_3^2 = 2n_2^2$. For example, in aragonite paraxiality constitutes an 8.9% error, in the monoclinic double-tungstate KYb(WO₄)₂ it is 0.44%, and in naphthalene, which exhibits particularly strong conical refraction, with a large cone angle in which paraxiality might be assumed to be least applicable, this error is only 0.027%. The errors in the paraxial cone angle, A , compared to the exact cone angle, θ_{cone} , are 6.8%, 0.09%, and 0.33% for these three crystals respectively.

Voigt (1905*c*, 1905*b*) discussed the effect of chirality on Fresnel's wave surface. We will reserve this case for the following paraxial discussion of the virtual wave surface, which possesses exactly the same local geometry as Fresnel's wave surface, but rigorous analytic investigation is much simpler.

3.2 The Paraxial Phase Surfaces

In this thesis we are concerned with the image field. Rather than Fresnel's wave surface for the actual field, it is useful to define a wave surface associated with the image field. Outside the crystal these fields and surfaces are identical, but inside the crystal the image field is a *virtual field* (see section 2.8), and the wave surface associated with it will form a *virtual wave surface*.

Using the dimensionless variables defined in section 2.3 for plane waves and treating propagation distance as an evolutionary 'time', ray paths according to Hamilton's principle (2.7.5) satisfy

$$\boldsymbol{\rho}(\boldsymbol{\kappa}) = \nabla_{\boldsymbol{\kappa}} (\Phi(\boldsymbol{\kappa}) + \boldsymbol{\kappa} \cdot \boldsymbol{\rho}). \quad (3.2.1)$$

This defines rays $\boldsymbol{\rho}$ as normals to the surface $\Phi(\boldsymbol{\kappa}) + \boldsymbol{\kappa} \cdot \boldsymbol{\rho} = \frac{1}{2}\zeta\kappa^2 \pm V(\boldsymbol{\kappa})$ which, therefore, is the wave surface we seek. $V(\boldsymbol{\kappa})$ comprises the singularity structure of the wave surface

as a function of the transverse wavevector $\boldsymbol{\kappa}$. For a biaxial crystal we have $V(\boldsymbol{\kappa}) = \rho_0 \kappa$; the wave surface has a conical point along the optic axis

$$\kappa_{\text{OA}} = 0, \quad (3.2.2)$$

and a tangent circle of points

$$\kappa_{\text{ext}} = \rho_0 / \zeta \quad (3.2.3)$$

around which the normals are all parallel. This is shown in figure 3.4(a). With chirality we have $V(\boldsymbol{\kappa}) = \rho_0 \sqrt{\kappa^2 + \gamma^2}$, preserving the tangent circle now at

$$\kappa_{\text{ext}} = \gamma \sqrt{\zeta_{\text{cusp}}^2 / \zeta^2 - 1}, \quad (3.2.4)$$

but breaking the conical point degeneracy, leaving in its place a ring of inflection points

$$\kappa_{\text{c}} = \frac{\rho}{\zeta (1 - \zeta^2 / \zeta_{\text{cusp}}^2)} = \frac{\rho}{\zeta} \left(\frac{\rho_0}{\zeta \kappa_{\text{ext}}} \right)^2, \quad (3.2.5)$$

where

$$\zeta_{\text{cusp}} \equiv \frac{\rho_0}{\gamma}. \quad (3.2.6)$$

This is depicted in figure 3.4(b-c).

For completeness let us briefly discuss the dichroic wave surface obtained via (2.3.11). $\boldsymbol{\delta}$ is the smallest perturbation that breaks rotational symmetry about the conical point, splitting each optic axis into a pair of singular axes at $\boldsymbol{\kappa}_{\text{sing}} = \pm \mathbf{e}_3 \times \boldsymbol{\delta}$ at which the eigenpolarisations (2.3.30) are circular. This wave surface is shown in figure 3.4(d). More generally, including chirality, in the dichroism-dominated regime $\delta > \gamma$ the singular axes lie at

$$\boldsymbol{\kappa}_{\text{sing}} = \pm \mathbf{e}_3 \times \boldsymbol{\delta} \sqrt{\delta^2 - \gamma^2} / \delta, \quad (3.2.7)$$

approaching as chirality increases and annihilating when $\delta = \gamma$, shown in figure 3.4(e), leading to figure 3.4(f) where the degeneracy vanishes because chirality dominates, $\delta < \gamma$. As this happens the circular polarisation points remain fixed at $\pm \mathbf{e}_3 \times \boldsymbol{\delta}$, like ghosts of the departed nonchiral singular axes, called the *haunting theorem* by Berry & Dennis (2003). It was shown in (3.1.15) that a polarisation state rotates by π in a circuit of the conical point, called a $\frac{1}{2}$ -index polarisation singularity. The splitting of the optic axis into two singular axes means that each singular axis is a $\frac{1}{4}$ -index polarisation singularity, a polarisation state rotates by $\pi/2$ in a circuit of one singular axis, and by π in a circuit containing the pair.

The dichroic wave surface is complex and a branch cut connects the singular axes – branch points of the wave surface. The real part of the wave surface is the phase contour surface sought in the nonabsorbing case, while the newly introduced imaginary part is a contour of wave magnitude. Clearly such a thing does not exist in transparent media. (Circular dichroism, which can be introduced by making γ imaginary, for instance $\gamma \rightarrow i\delta$, spreads the singular axes into a ring of branch points $\kappa = \delta$ outside of which ($\kappa > \delta$) the wave surface is real, but inside of which it branches into Riemann surfaces.)

The complexity of the dichroic wave surface will not be of interest. For our purposes, as outlined in section 2.6, the wvector $\boldsymbol{\kappa}$ itself can take complex values, and it becomes perverse to plot the wave surfaces in real space. For this reason the dichroic wave surface does not yield geometrical insight akin to the transparent case. The singular axes, branch cut, and haunting theorem, therefore *do not* have obvious effects on the refracted light field, unlike the similar singularities of transparent media.

Returning to transparent crystals, the wave surface has a dual *ray surface* as in Hamilton's construction of Fresnel's surface. The normals to a ray surface $\Theta(\boldsymbol{\rho}) + \boldsymbol{\kappa} \cdot \boldsymbol{\rho}$ are the wavevectors, expressed as

$$\boldsymbol{\kappa}(\boldsymbol{\rho}) = \nabla_{\boldsymbol{\rho}}(\Theta(\boldsymbol{\rho}) + \boldsymbol{\kappa} \cdot \boldsymbol{\rho}) \quad (3.2.8)$$

$$= \left(\rho \mp \frac{\rho_0 \kappa}{\sqrt{\kappa^2 + \gamma^2}} \right) \frac{\boldsymbol{\rho}}{\rho \zeta}. \quad (3.2.9)$$

The duality between the surfaces can be expressed as a Legendre transformation,

$$\nabla_{\boldsymbol{\kappa}}(\Phi(\boldsymbol{\kappa}) + \boldsymbol{\kappa} \cdot \boldsymbol{\rho}) = [\nabla_{\boldsymbol{\rho}}(\Theta(\boldsymbol{\rho}) + \boldsymbol{\kappa} \cdot \boldsymbol{\rho})]^{-1}, \quad (3.2.10)$$

where ‘ -1 ’ denotes the inverse function. The ray and wave surfaces are simple for $\gamma = 0$, but with chirality the wave surface is of fourth order and the Legendre transformation produces an implicit function for the ray surface. The duality of degeneracies of the two surfaces is exactly analogous to that for Fresnel's surface depicted in figure 3.3.

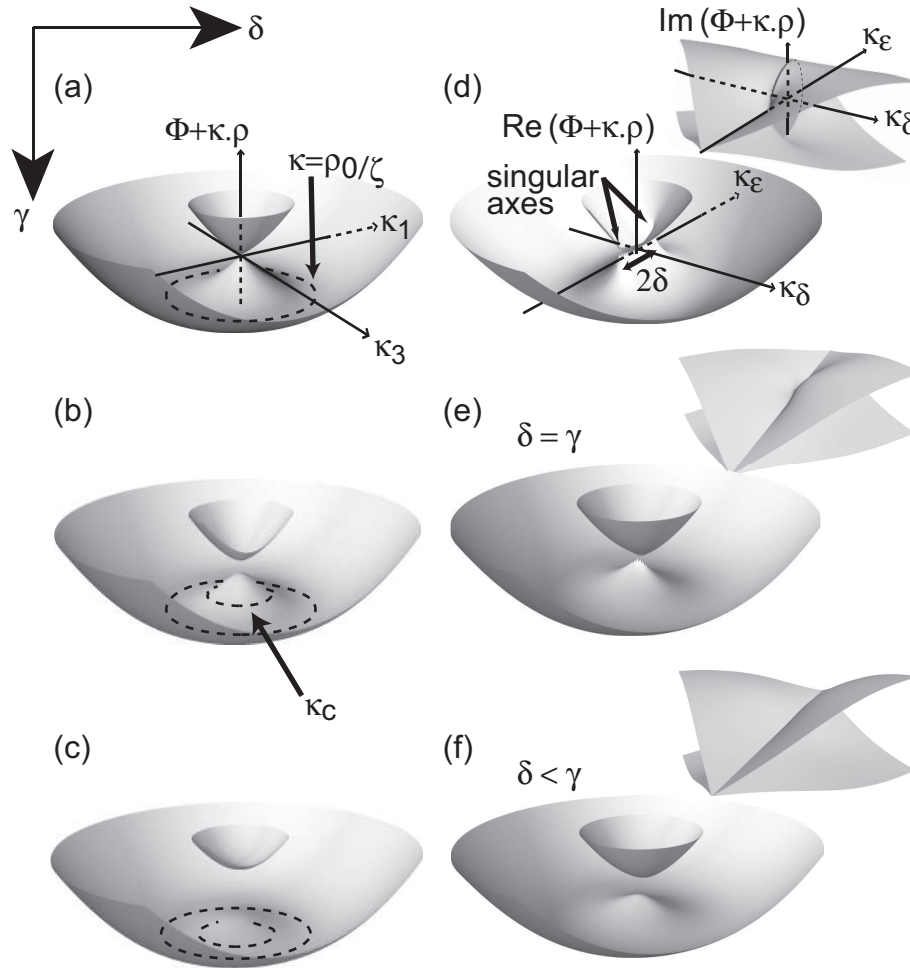


Figure 3.4: (a-c), The paraxial wave surfaces: (a) Hamilton's diabolical point: the paraxial wave surface for a biaxial medium ($\delta = \gamma = 0$), cutaway to show the diabolical point at $\kappa_{OA} = 0$ responsible for internal conical refraction, and the tangent circle at $\kappa_{\text{ext}} = \rho_0/\zeta$ responsible for external conical refraction; (b-c), The chiral wave surface: optical activity destroys the diabolical point, separating the sheets, but leaving a ring of inflection points (3.2.5), whose normals form a caustic "trumpet horn"; (d), The dichroic wave surface $\Phi_{\pm}(\kappa)$ is complex, and the conical point splits into a pair of singular axes at $\kappa_{\text{sing}} = \pm \mathbf{e}_3 \times \delta$ connected by a branch cut. The real part is the phase contour surface distorted by dichroism, and the imaginary part introduced by dichroism is a wave amplitude surface. (e-f), the singular axes approach as γ increases, annihilating at $\delta = \gamma$, but leaving behind the asymmetry of the imaginary wave surface.

Chapter 4

The Phenomena of “So-Called” Conical Diffraction

“in the teeth of all analogy”

from Dublin Uni. Mag. 1842 (Graves 1882)

Thus far we have laid out the mathematical framework underpinning conical diffraction, in crystals exhibiting the three fundamental optical degeneracies of birefringence, chirality, and dichroism. Here we study the phenomena that result from that theory.

Wherever possible we will follow an intuitive derivation based on simple geometric degeneracy assumptions that can be followed without the full rigour of the crystal theory in sections 2.1-2.3. This approach will be based on a monochromatic incident beam, represented as a superposition of paraxial plane waves with transverse wavevector profile $a(\boldsymbol{\kappa})$ and polarisation $\mathbf{d}_0 = \{d_{0x}, d_{0y}\}$. Position will be in dimensionless cylindrical coordinates comprised of the radius vector $\boldsymbol{\rho}$ and propagation distance ζ . A propagator integral then, (2.3.16), describes the diffracted beam,

$$\mathbf{D}(\boldsymbol{\rho}, \zeta) = \frac{1}{2\pi} \int \int d\boldsymbol{\kappa} e^{-i\mathcal{F}(\boldsymbol{\kappa}, \boldsymbol{\rho}, \zeta)} a(\boldsymbol{\kappa}) \mathbf{d}_0,$$

in terms of a 2×2 evolution matrix \mathcal{F} whose eigenvalues are optical path lengths Φ_{\pm} . Using the geometrical argument in the second paragraph of section 2.7 to find the optical path length, (2.3.19),

$$\Phi_{\pm}(\boldsymbol{\kappa}, \boldsymbol{\rho}, \zeta) = -\boldsymbol{\kappa} \cdot \boldsymbol{\rho} + \frac{1}{2}\zeta\kappa^2 \pm V(\boldsymbol{\kappa} - i\boldsymbol{\delta}),$$

we can directly infer \mathcal{F} in the form (2.3.14),

$$\mathcal{F}(\boldsymbol{\kappa}, \boldsymbol{\rho}, \zeta) = (-\boldsymbol{\kappa} \cdot \boldsymbol{\rho} + \frac{1}{2}\zeta\kappa^2) \mathcal{I} + \mathbf{V}(\boldsymbol{\kappa} - i\boldsymbol{\delta}) \cdot \boldsymbol{\Sigma}.$$

The traceless part of \mathcal{F} (that is $\mathbf{V} \cdot \boldsymbol{\Sigma}$) comprises some unknown crystal vector, $\mathbf{V}(\boldsymbol{\kappa})$, which we will show can be directly implied from consideration of the optical degeneracy. In dealing with complex quantities it will be important to define the square root as

$$\sqrt{x} \equiv |x|^{\frac{1}{2}} e^{\frac{1}{2}i\text{Arg}x}. \quad (4.0.1)$$

In section 4.1 we consider Hamilton’s original phenomenon in biaxial crystals, for which the diffraction theory was discovered by Belskii & Khapalyuk (1978), advanced by Berry (2004*b*) and reviewed by Berry & Jeffrey (2007), but is presented here in a different formulation with minor new results where noted. Section 4.6 details new experiments probing the emergence of the predicted asymptotic wave and ray phenomena of that theory, previously reported by Berry et al. (2006). The intervening sections consist of new theoretical predictions for the effect of chirality and dichroism on conical diffraction, and for the associated optical angular momentum. These results extend and elucidate several publications: section 4.2 extends Berry & Jeffrey (2006*a*) and Jeffrey (2006) to further discuss intensity in the focal image plane and inside the chiral crystal; sections 4.3 & 4.4 extend Berry & Jeffrey (2006*b*) and Jeffrey (2007) to general (nongaussian) beams, adding a note on circular dichroism in section 4.3.4; section 4.5 follows Berry et al. (2005).

Throughout, our interest will centre around the critical structure of the light field exiting the crystal rather than polarisation dependency. Therefore we will mainly present intensity images for an unpolarised incident beam, though analytic results will be entirely general.

4.1 Biaxial Crystals

A biaxial medium ($\delta = \gamma = 0$, \mathcal{N} real symmetric) propagates plane wave eigenstates $\mathbf{d}_{\uparrow\downarrow}(\boldsymbol{\kappa})$ defined by (2.3.25). They are the evolving eigenstates of a real symmetric matrix $\mathcal{F}(\boldsymbol{\kappa})$ which rotate half a turn in a circuit of the optic axis, which determines the traceless part of \mathcal{F} to be given by

$$\mathcal{F}^{\text{tr}} = \mathbf{V}(\boldsymbol{\kappa}) \cdot \boldsymbol{\Sigma} = \rho_0 \boldsymbol{\kappa} \cdot \{\sigma_3, \sigma_1\}, \quad (4.1.1)$$

yielding the propagator integral

$$\mathbf{D}(\boldsymbol{\rho}, \zeta) = \frac{1}{2\pi} \int \int d\boldsymbol{\kappa} e^{i(-\frac{1}{2}\zeta\kappa^2 + \boldsymbol{\kappa} \cdot \boldsymbol{\rho})} [\cos \rho_0 \kappa - i \hat{\boldsymbol{\kappa}} \cdot \boldsymbol{\Sigma} \sin \rho_0 \kappa] a(\boldsymbol{\kappa}) \mathbf{d}_0, \quad (4.1.2)$$

where $\hat{\boldsymbol{\kappa}} = \boldsymbol{\kappa}/\kappa$. Exploiting the circular symmetry of the integral with (2.5.2) and using the eigenwave representation of section 2.5, we can write simply

$$\mathbf{D} = b_+ \mathbf{d}_0 \cdot \mathbf{d}_{\uparrow} \mathbf{d}_{\uparrow} + b_- \mathbf{d}_0 \cdot \mathbf{d}_{\downarrow} \mathbf{d}_{\downarrow}, \quad (4.1.3)$$

where the eigenvalues are the diffraction integrals

$$\begin{aligned} b_{\pm}(\boldsymbol{\rho}, \zeta) &= B_0(\boldsymbol{\rho}, \zeta) \pm B_1(\boldsymbol{\rho}, \zeta) \\ &= \frac{1}{2\pi} \int \int d\boldsymbol{\kappa} a(\boldsymbol{\kappa}) e^{i(-\frac{1}{2}\zeta\kappa^2 + \boldsymbol{\kappa} \cdot \boldsymbol{\rho})} [\cos \rho_0 \kappa \mp i \hat{\boldsymbol{\kappa}} \cdot \hat{\boldsymbol{\rho}} \sin \rho_0 \kappa] \end{aligned} \quad (4.1.4)$$

$$= \int_0^{\infty} d\kappa \kappa a(\kappa) e^{-\frac{1}{2}i\zeta\kappa^2} [J_0(\rho\kappa) \cos \rho_0 \kappa \pm J_1(\rho\kappa) \sin \rho_0 \kappa], \quad (4.1.5)$$

and the eigenvectors are $\mathbf{d}_{\uparrow\downarrow}(\boldsymbol{\rho})$ as defined by (2.3.25). The second equality (4.1.5) assumes that the incident beam is circularly symmetric, $a(\boldsymbol{\kappa}) = a(\kappa)$. Otherwise this can be treated as an approximation for a slowly varying beam profile, placing the zeroth order approximation to $a(\boldsymbol{\kappa})$ outside the integral as part of a stationary phase analysis.

For an unpolarised or circularly polarised incident beam the intensity (2.3.22) is

$$I_{\text{unpol}} = \frac{|b_+|^2 + |b_-|^2}{2}. \quad (4.1.6)$$

For an incident beam linearly polarised at an angle χ to the horizontal axis (2.3.27), this is superposed with a simple pattern that rotates twice as fast as any rotation of the incident beam,

$$I_{\chi} = I_{\text{unpol}} + \frac{|b_+|^2 - |b_-|^2}{2} \cos(2\chi - \phi_{\boldsymbol{\rho}}), \quad (4.1.7)$$

where in polar coordinates $\boldsymbol{\rho} = \rho \{ \cos \phi_{\rho}, \sin \phi_{\rho} \}$.

The diffraction integrals (4.1.5) cannot be expressed in closed form but are suitable for numerical evaluation. Figures 4.2 and 4.1 show the diffracted light intensity for a gaussian incident beam, in planes transverse to the optic axis successively further from the focal image plane. In the focal image plane are a pair of concentric bright rings, encompassing a dark ring, and with a dark central disc. The bright focused rings spread, developing oscillations on the inner ring, fading away eventually to be dominated by a bright axial spike. Note that the location of the dark ring appears fixed. This behaviour is general to any incident beam, and further simulations (not shown) show that the precise profile differs significantly between beams only near the focal image plane.

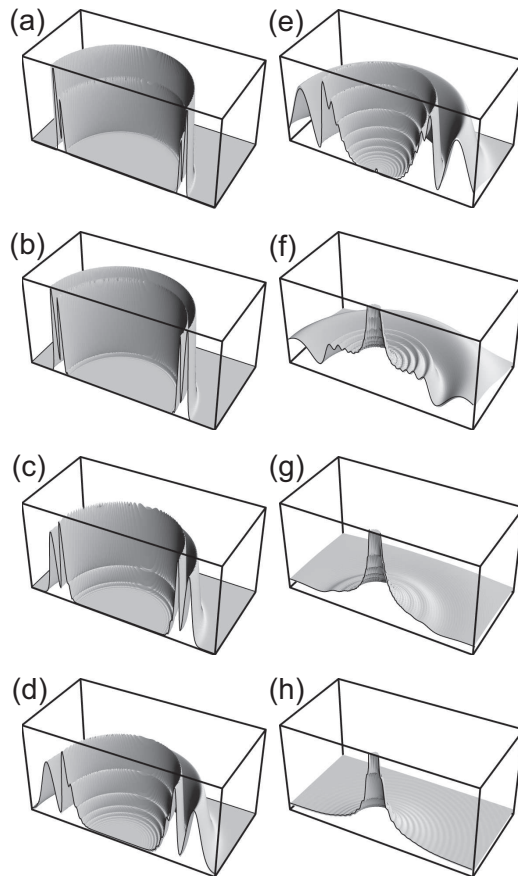


Figure 4.1: Evolution of the conical diffraction rings: theoretical 3D cutaway plots of conical diffraction intensities in figure 4.2

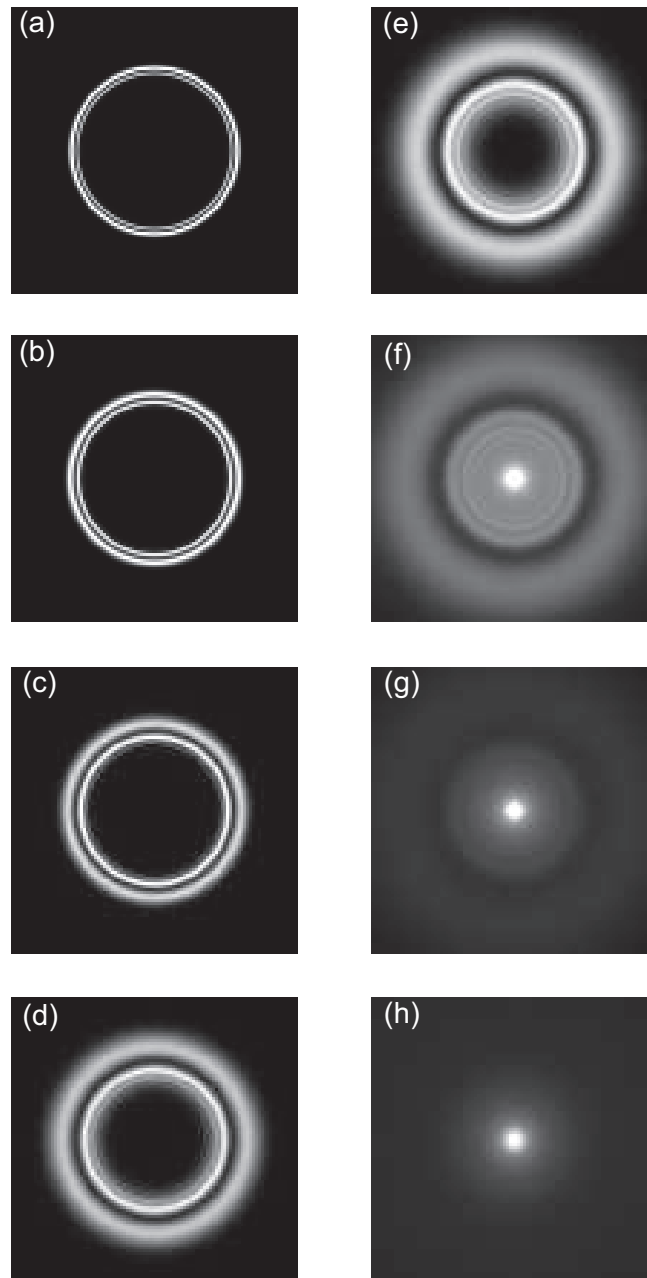


Figure 4.2: Simulation of the conical diffraction ring evolution: theoretical density plots of conical diffraction intensities (4.1.7) for $\rho_0 = 60$, at distances ζ equal to: (a) 1.8, (b) 3, (c) 6, (d) 12, (e) 18, (f) 30, (g) 42, (h) 98, from the focal image plane in units of the Rayleigh length for a gaussian incident beam.

4.1.1 So-called conical refraction

The eigenvalues of the evolution operator, \mathcal{F} , are the optical path lengths

$$\Phi_{\pm}(\boldsymbol{\kappa}) = -\boldsymbol{\kappa} \cdot \boldsymbol{\rho} + \frac{1}{2}\zeta\kappa^2 \pm \rho_0\kappa \quad (4.1.8)$$

of two refracted eigenrays. Hamilton’s principle (2.7.5) yields the ray equation

$$\boldsymbol{\rho} = (\zeta\kappa \pm \rho_0) \hat{\boldsymbol{\kappa}}, \quad (4.1.9)$$

describing rays emanating from a ring $\rho = \rho_0$, forming a diverging cylinder as distance ζ from the focal image plane increases. The wavevector solutions are

$$\boldsymbol{\kappa}_{\pm} = \frac{\rho \mp \rho_0}{\zeta} \hat{\boldsymbol{\rho}} : \left\{ \begin{array}{l} \nabla_{\boldsymbol{\kappa}} \Phi_{-}(\boldsymbol{\kappa}_{\pm}) = 0, \quad \rho < \rho_0 \\ \nabla_{\boldsymbol{\kappa}} \Phi_{\pm}(\boldsymbol{\kappa}_{\pm}) = 0, \quad \rho \geq \rho_0 \end{array} \right\}. \quad (4.1.10)$$

The geometric ray intensity (2.7.7) is given by summing over the two rays $\boldsymbol{\kappa}_{\pm}$,

$$I_{\text{geom}}(\rho, \zeta) = \frac{1}{2\rho\zeta^2} \sum_{\pm} |\rho \pm \rho_0| \left| a \left(\frac{\rho \pm \rho_0}{\zeta} \right) \right|^2. \quad (4.1.11)$$

Focusing occurs where the Hessian determinant

$$\left| \det \frac{d\boldsymbol{\rho}}{d\boldsymbol{\kappa}} \right| = \frac{\rho\zeta}{\kappa} \quad (4.1.12)$$

vanishes, that is in the focal plane $\zeta = 0$, and along an axial focal line $\rho = 0$. The quadratic divergence in the focal plane and linear divergence at the axial focus contrast with an anti-focus at $\rho = \rho_0$. This is a dark cylinder originating from $\kappa_{+} = (\rho - \rho_0)/\zeta = 0$, the conical point (3.2.2), near which the argument $\kappa_{-} = (\rho + \rho_0)/\zeta$ is typically beyond the observable range of the beam, so we can write

$$I_{\text{rings}}(\rho, \zeta) \approx \frac{|\rho - \rho_0|}{2\rho\zeta^2} \left| a \left(\frac{\rho - \rho_0}{\zeta} \right) \right|^2. \quad (4.1.13)$$

The intensity profiles of the two geometric cylinders (rings in ζ level-planes) are symmetric in intensity about the dark Hamilton cylinder $\rho = \rho_0$.

The origin of these cylinders as ray normals to the wave surface $\Phi_{\pm}(\boldsymbol{\kappa}) + \boldsymbol{\kappa} \cdot \boldsymbol{\rho}$ (figure 3.4(a)), are illustrated in figure 4.3. A beam illuminates directions over some neighbourhood of the conical point, producing ray normals as shown. Rays from the ‘+’ sheet of the wave surface give rise to the outer ring in figure 4.3(a), while those from the ‘-’ sheet are out of range of the beam, and the vanishing intensity of the single ray from the conical point produces Hamilton’s dark ring. The inner ring is produced by rays of the ‘+’

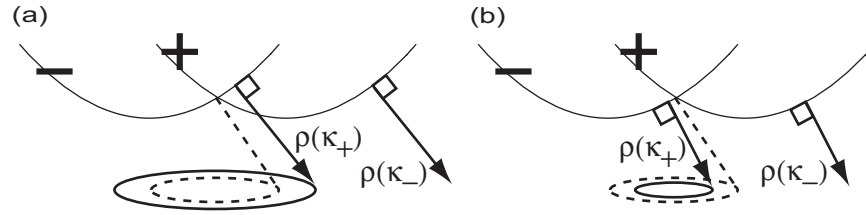


Figure 4.3: The rays of internal conical refraction: the dashed line is a mathematical abstraction, Hamilton's singular ray from the conical point, producing a dark ring at $\rho = \rho_0$. Around it: (a) $\rho > \rho_0$, outside the dark ring one ray (4.1.10) originates from each sheet of the wave surface; and (b) $\rho < \rho_0$, inside the dark ring both rays originate from the same sheet.

solution in (4.1.10), but in a direction where all rays originate from the '−' sheet of the wave surface, shown in figure 4.3(b).

This is the phenomenon of internal conical *diffraction*; already the spread of directions in the beam is necessary to describe the phenomenon beyond the abstraction described by Hamilton's conical *refraction*. Consider the fate of these rays as distance ζ from the focal image plane increases. Any beam will spread due to diffraction as it propagates, so that wave directions farther from the optic axis eventually contribute, accessing parts of the wave surface farther from the conical point. From the shape of the wave surface it is easy to see that the ray normals turn away from the cone direction as this happens, so the diffraction cone spreads, the inner cone becoming narrower and the outer cone becoming wider, accompanied by defocusing (increasing curvature of the wave surface) making the cones fainter. Near the tangent circle (3.2.3) of the wave surface at $\kappa_{\pm} = \rho_0/\zeta$, rays focus along the optic axis as illustrated in figure 4.4 – the region of external conical diffraction.

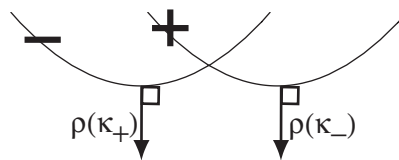


Figure 4.4: The rays of external conical refraction, scattered along the optic axis from the tangent circle at the turnover of the wave surface, produce a bright focal spike .

To describe this axial focal line we approximate (4.1.11) for small ρ ,

$$I_{\text{spike}}(\rho, \zeta) \approx \frac{\rho_0}{\rho \zeta^2} \left| a \left(\frac{\rho_0}{\zeta} \right) \right|^2, \quad (4.1.14)$$

which dominates over I_{ring} only far from the focal plane.

Note that in any direction in κ space the normals to the two sheets of the wave surface are rays associated with orthogonal polarisations. Also a π rotation about the optic axis rotates a polarisation to its orthogonal state. These facts combined mean that the ray pairs depicted in figures 4.3 & 4.4 are orthogonal.

For a gaussian beam we can soften the focal plane singularity in the geometric intensity by using the complex ray representation (2.4.7), replacing the distance ζ with $|\tilde{\zeta}| = \sqrt{1 + \zeta^2}$ and the beam profile with unity. This would predict the symmetric ring intensity profile I_{ring} to extend to the focal plane, where careful inspection of the exact wave intensity in figure 4.2(a) and 4.1(a) reveals the outer ring to be far brighter than the inner. Away from the focal plane the geometric approximation does capture the average intensity correctly, and the severe failure of the geometric approximation near the focal plane is indicative of the importance of wave effects: we will find that the dimming of the inner ring is an extreme effect of diffraction.

Using the transformation (2.8.2) we infer the ray trajectories of light inside the crystal that give rise to the above geometrical images,

$$\boldsymbol{\theta}_\rho = \boldsymbol{\kappa} \pm \theta_0 \hat{\boldsymbol{\kappa}}. \quad (4.1.15)$$

A ray incident along the optic axis, $\kappa = 0$, is refracted into Hamilton’s cone $\boldsymbol{\theta}_\rho = \theta_0$ inside the crystal. The intensity,

$$I_{\text{crystal}}(\theta_\rho, \zeta') = \frac{1}{2\theta_\rho \zeta'^2} \sum_{\pm} |\theta_\rho \pm \theta_0| |a(\theta_\rho \pm \theta_0)|^2, \quad (4.1.16)$$

reveals that, since the area of the wave surface scattering rays shrinks to zero at the conical point, Hamilton’s cone is in fact dark, and separates two concentric bright cones, which refract at the exit face into the bright cylinders (4.1.13). The origin of the axial focal line is evident at $\theta_\rho \approx 0$. We will present an image of this intensity when considering chiral crystals, in figures 4.13-4.15.

4.1.2 Diffraction in the rings

The bright rings (4.1.13) are only well developed for thick crystals, $\rho_0 \gg 1$, meaning that the geometric cone attains a radius sufficiently larger than the beam width to resolve the

bright cylinders. Away from the focal plane, $\zeta \gg 1$, we can use the asymptotic expansion of the Bessel function,

$$J_n(x) \approx \sqrt{\frac{2}{\pi x}} \cos\left(x - \frac{\pi(1+2n)}{4}\right), \quad (4.1.17)$$

to approximate the integrand of the diffraction integrals (4.1.5) for $\rho \approx \rho_0 \gg 1$, giving

$$J_0(\rho\kappa) \cos(\rho_0\kappa) \pm J_1(\rho\kappa) \sin(\rho_0\kappa) \approx \sqrt{\frac{2}{\pi\rho\kappa}} \cos\left((\rho \mp \rho_0)\kappa - \frac{\pi}{4}\right). \quad (4.1.18)$$

The resulting asymptotic ring formula is

$$b_{\pm}(\rho, \zeta) \approx \frac{1}{(i\zeta)^{3/4} \sqrt{\rho}} f(s_{\pm}, \zeta), \quad (4.1.19)$$

expressing the diffraction integrals (4.1.4) in terms of a function

$$f(s, \zeta) = \sqrt{\frac{2}{\pi}} \int_0^{\infty} d\tau \sqrt{\tau} e^{-\frac{1}{2}\tau^2} \cos\left(s\tau - \frac{\pi}{4}\right) a\left(\frac{\tau}{\sqrt{i\zeta}}\right), \quad (4.1.20)$$

which, were it not for the beam profile, would depend only on the saddlepoints of the integrand at

$$s_{\pm} = \kappa_{\pm} \sqrt{-i\zeta} = \frac{\rho \mp \rho_0}{\sqrt{i\zeta}}, \quad (4.1.21)$$

suggesting an asymptotic expansion (section 2.6).

Each of the b_{\pm} integrals contains a single saddlepoint s_{\pm} , reflecting their physical significance: the two integrals correspond distinctly to two orthogonal eigenwaves, originating from the two eigenpolarisations in the crystal, as a consequence of the eigenpolarisation decomposition (2.5.13), and the saddlepoints are just the geometric ray contributions (4.1.10). Careful consideration of phases shows that the b_+ integral also has a contribution from the endpoint $\kappa = 0$, a wave scattered from the conical point, with a unit-step determining that this exists only inside the Hamilton ring $\rho < \rho_0$ (the unit-step $T[.]$ was defined in (2.3.6)). To obtain correct phases it is best to transform to a new integration variable $t = \sqrt{\tau}$, and the asymptotic result, valid away from the focal plane and Hamilton's anti-focus $\rho_0 \gg |\rho - \rho_0| \gg \sqrt{\zeta} \gg 1$, is

$$f(s_+, \zeta) \approx a\left(\frac{s_+}{\sqrt{-i\zeta}}\right) e^{-\frac{1}{2}s_+^2} \sqrt{-s_+} (-1)^{\text{T}[-\text{Im}s_+]} - a(0) \frac{\text{T}[-\text{Res}_+]}{\sqrt{2}(-s_+)^{3/2}} \quad (4.1.22)$$

$$f(s_-, \zeta) \approx a\left(\frac{s_-}{\sqrt{-i\zeta}}\right) e^{-\frac{1}{2}s_-^2} \sqrt{-s_-}. \quad (4.1.23)$$

In the sense defined in (2.6.8), the endpoint term is dominant over the saddlepoint term in the asymptotic expansion, and yet the saddlepoint term is clearly the larger due to its

prefactor. This is an example of new mathematics discovered within conical diffraction (Berry 2004a), termed *asymptotic dominance by the subdominant exponential*. Interestingly, this supposed paradoxical phenomenon occurs throughout conical diffraction.

As in the geometric intensity (4.1.13), the argument involving s_- is typically out of the range of the beam profile ($a(\kappa_-)$ is small), with the result that only one of the diffraction integrals is significant,

$$|b_+| \gg |b_-|, \quad (4.1.24)$$

so we can write the propagator integral,

$$\mathbf{D}(\boldsymbol{\rho}, \zeta) \approx b_+(\boldsymbol{\rho}, \zeta) (\mathbf{d}_\uparrow \cdot \mathbf{d}_0) \mathbf{d}_\uparrow, \quad (4.1.25)$$

and the intensity,

$$I(\boldsymbol{\rho}, \zeta) \approx |b_+(\boldsymbol{\rho}, \zeta)|^2 |\mathbf{d}_\uparrow \cdot \mathbf{d}_0|^2. \quad (4.1.26)$$

We can separate terms from the geometric rays and endpoint wave corrections, into

$$|b_+(\boldsymbol{\rho}, \zeta)|^2 \approx \frac{1}{\rho\zeta} \beta_{\text{geom}} \left(\frac{\rho - \rho_0}{\zeta} \right) + \frac{\text{T} \left[\frac{\rho_0 - \rho}{\zeta} \right]}{\rho(\rho_0 - \rho)^3} \beta_{\text{end}} \left(\frac{\rho - \rho_0}{\zeta}, \frac{\rho - \rho_0}{\sqrt{i\zeta}} \right), \quad (4.1.27)$$

where

$$\beta_{\text{geom}}(\kappa_+) = |\kappa_+| |a(\kappa_+)|^2 \quad (4.1.28)$$

is just the geometric ray contribution appearing in (4.1.13), and

$$\beta_{\text{end}}(\kappa_+, s_+) = \frac{1}{2} |a(0)|^2 - \sqrt{2} a(0) a(\kappa_+) |s_+|^2 \cos \frac{1}{2} |s_+|^2 \quad (4.1.29)$$

introduces oscillations due to the endpoint of the diffraction integral $\kappa = 0$, that is, interference with a wave scattered from the conical point. Figure 4.5 shows the evolution of the bright rings exhibiting this asymptotic form.

From β_{geom} we can imply the location of the peaks of the two bright rings, at

$$\rho_{\text{ring}} = \rho_0 \pm \zeta/\sqrt{2}, \quad (4.1.30)$$

and from the cosine, which produces oscillations on the inner ring, we can imply the peak-to-peak width of the ring fringes

$$\Delta\rho_{\text{fringe}} = \frac{2\pi\zeta}{\rho_0 - \rho}. \quad (4.1.31)$$

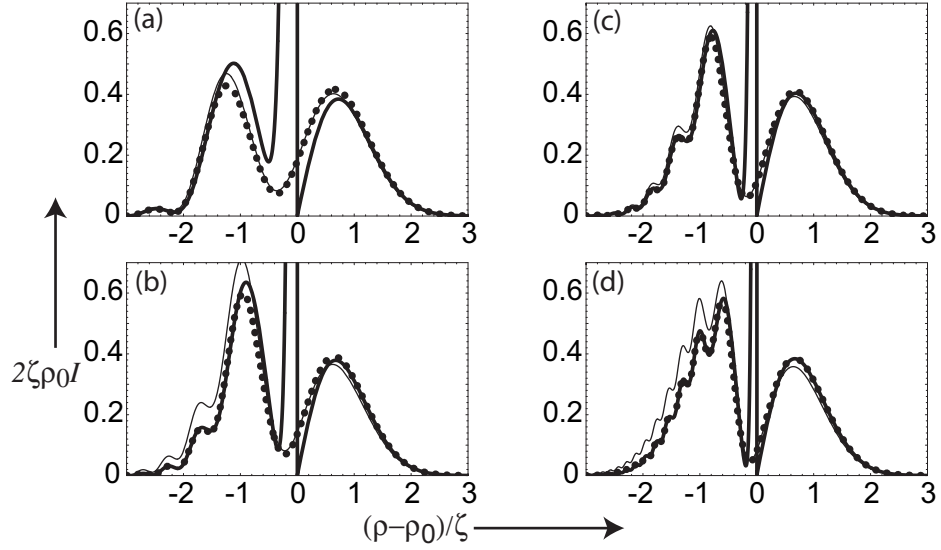


Figure 4.5: Asymptotic intensity of the secondary rings: exact (thin) from (4.1.4), asymptotic expansion (thick) from equation (4.1.27), and uniform approximation (dots) from equation (4.1.39), for: $\rho_0 = 20$ with (a) $\zeta = 3$, (b) $\zeta = 6$; and for $\rho_0 = 60$ with (c) $\zeta = 9$, (d) $\zeta = 18$.

The expansion (4.1.27) diverges near the dark ring due to a singular prefactor in the endpoint wave term, rendering it valid only for $\rho_0 - \rho > \sqrt{\zeta}$ and $\rho > \rho_0$, therefore correctly describing the smooth exponential decay outside the dark ring, and the fringes on the inner ring which get faster compared to the ring width as ζ increases. There are approximately $\zeta/2\pi$ of these fringes in the $1/e^2$ width $\zeta\sqrt{2}$ of the inner ring peak, eventually crowding toward the symmetric ring profile predicted geometrically. A subsequent approximation $1/\sqrt{\rho} \approx 1/\sqrt{\rho_0}$ in (4.1.19) made by Berry (2004b) inadequately describes the relative brightness of the rings, which requires the first correction

$$\frac{1}{\sqrt{\rho}} \approx \frac{1}{\sqrt{\rho_0}} \left(1 - \frac{\rho - \rho_0}{2\rho_0} \right). \quad (4.1.32)$$

The considerations above, compared to the geometric expressions (4.1.13) and (4.1.14), lead to the detailed schematic diagram in figure 4.6 which has not been shown explicitly before. For small ρ_0 and ζ (bottom picture) we identify regions where the inner ring separates from the axis leaving two well defined conical diffraction rings, setting the ‘thick crystal’ or ‘large ring-to-beam ratio’ condition more precisely at $\rho_0 \gg 1 + \zeta^2$ and showing just how clear the boundary is. For thick crystals (top picture) the regions where two geometric rings appear is clear, as is where they develop secondary oscillations, and the

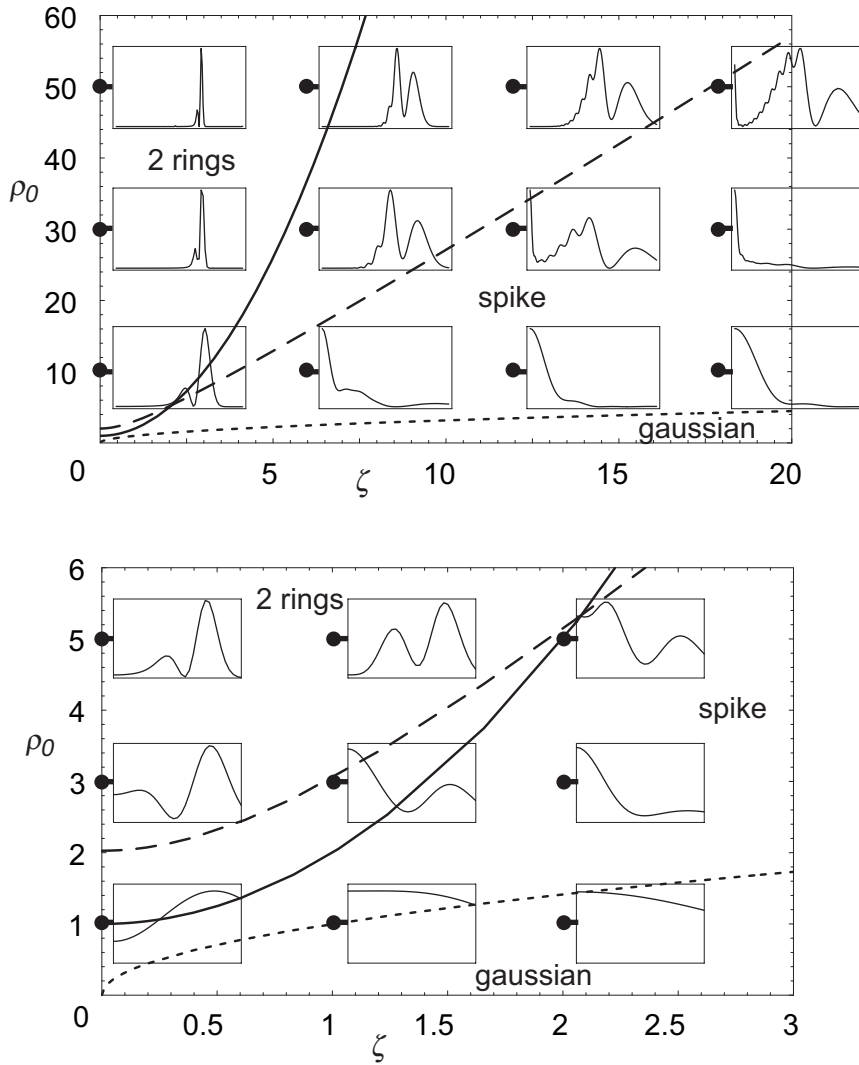


Figure 4.6: The regimes of conical diffraction: (top) the well developed rings and axial focal spike occur in well defined regions, showing also growth of oscillations with ρ_0 , and (bottom) at small ρ_0 the rings may not be resolved. The regions determined from the asymptotic formulae are: $\rho_0 \gg 1 + \zeta^2$ (full curve) is the thick crystal condition for the inner ring to be distinct from the axis, $\rho_0^3 \zeta^{-2} e^{-\rho_0^2/\zeta^2} \ll (2\pi^2 e)^{-1/2}$ (dashed curve) is the far field condition for dominance of the focal spike, and $\rho_0 \leq \zeta^{1/2}$ (dotted curve) is the very far field condition in which diffraction blurs out conical diffraction and the incident (gaussian in this case) beam profile returns.

transition to the axial focus. The experiments of Lloyd (1837) (see figure 1.1) inhabit the region $\rho_0 \approx 1$, showing why a thin crystal and wide beam allowed him to view only a poorly resolved outer ring, the dark ring having not fully formed.

The polarisation term in the intensity (4.1.26) is simple. If the incident beam is linearly polarised it is

$$\left| \mathbf{d}_\uparrow \cdot \mathbf{d}_\chi^{\text{lin}} \right|^2 = \cos^2 \left(\frac{1}{2} \phi_\rho - \chi \right), \quad (4.1.33)$$

for circular polarisation it is

$$\left| \mathbf{d}_\uparrow \cdot \mathbf{d}_\pm^{\text{circ}} \right|^2 = \frac{1}{2} \left| \cos \frac{1}{2} \phi_\rho \pm i \sin \frac{1}{2} \phi_\rho \right|^2 = \frac{1}{2}, \quad (4.1.34)$$

which is the same as for an unpolarised beam, found by averaging over any two orthogonal polarisations, for example

$$\left| \mathbf{d}_\uparrow \cdot \mathbf{d}_0^{\text{un}} \right|^2 = \frac{1}{2} \left(\left| \mathbf{d}_\uparrow \cdot \mathbf{d}_+ \right|^2 + \left| \mathbf{d}_\uparrow \cdot \mathbf{d}_- \right|^2 \right) = \frac{1}{2}. \quad (4.1.35)$$

The polarisation (2.3.26) in the rings, described by

$$\omega \approx e^{-i\phi_\rho}, \quad (4.1.36)$$

is independent of the incident polarisation, and linearly polarised with an orientation $\phi_\rho/2$ to the horizontal, shown in figure 1.3. Like the eigenstates in the crystal, this rotates only half a turn in a circuit of the optic axis, reflecting the presence of a $\frac{1}{2}$ -index polarisation singularity, a C (circular polarisation) point, in the dark center of the rings (and at exactly the centre for circular incident polarisation). The factor (4.1.33) reflects this structure: a linearly polarised incident beam will illuminate only part of the rings, one radius ($\phi_\rho = 2\chi + \pi$) being totally dark, and this dark brush rotates twice as fast as any rotation $\Delta\chi$ of the incident beam.

4.1.3 Uniformisation and rings in the focal image plane

The asymptotic expansion of (4.1.20) diverges near the Hamilton dark ring, and since this divergence comes from the endpoint term in (4.1.22) it exists only on the inner ring. The divergence can be smoothed out by a slightly more sophisticated approximation. By approximating the beam profile $a(\kappa)$ with its constant value $a(\kappa_+)$ at the saddlepoint of the integrand, the remaining integral can be evaluated in various forms involving standard

functions, three of which were presented by Belsky & Stepanov (1999) and Berry (2004b), and we give two alternative forms here:

$$\frac{f(s, \zeta)}{a\left(\frac{s}{\sqrt{-i\zeta}}\right)} \approx \sqrt{\frac{2}{\pi}} \int_0^{\infty} d\tau \sqrt{\tau} e^{-\frac{1}{2}\tau^2} \cos\left(s\tau - \frac{\pi}{4}\right) \quad (4.1.37)$$

$$= \frac{e^{-\frac{1}{2}s^2}}{2^{3/4}} \sqrt{\frac{2}{\pi}} \left[\left(\frac{3}{4}\right)! {}_1F_1\left[-\frac{1}{4}, \frac{1}{2}, \frac{1}{2}s^2\right] + s\sqrt{2} \left(\frac{5}{4}\right)! {}_1F_1\left[-\frac{1}{4}, \frac{3}{2}, \frac{1}{2}s^2\right] \right] \quad (4.1.38)$$

$$= \frac{e^{-\frac{1}{4}s^2} s^{3/2} \sqrt{\pi}}{4} \operatorname{sgn}[\operatorname{Re} s]^{3/2} \times \left[I_{-\frac{1}{4}}\left(\frac{1}{4}s^2\right) - I_{\frac{3}{4}}\left(\frac{1}{4}s^2\right) + \operatorname{sgn}[\operatorname{Re} s] \left(I_{-\frac{3}{4}}\left(\frac{1}{4}s^2\right) - I_{\frac{1}{4}}\left(\frac{1}{4}s^2\right) \right) \right], \quad (4.1.39)$$

in terms of confluent hypergeometric functions ${}_1F_1$ and modified Bessel functions of the first kind I_n (Abramowitz & Stegun 1972). Note that these are exact as stated, and that the function f/a is a function only of the variable s . Each of the b_+ and b_- polarisations can be written in terms of such functions $f(s_+, \zeta)$ and $f(s_-, \zeta)$ respectively, though for the well developed rings only the former is significant.

The saddlepoint expansion (4.1.27) suffers from the same focal image plane singularity as the geometrical intensity. This, as there, can be overcome for a gaussian incident beam by means of the complex ray representation but, as there, fails to correctly describe the inner ring, this time because the divergence of the endpoint term encroaches on the inner ring. Using the uniform approximation above, however, the divergence is removed completely. Furthermore, the gaussian complexification sets the beam profile to unity, so f itself becomes a function only of the saddlepoint variable s , valid for all $\zeta \ll \rho_0$, and (4.1.37) becomes exact.

The result is an extremely accurate expression for the well developed rings, compared to the exact in figure 4.5. In the focal image plane the profile is universal, shown in figure 4.7(a), scaling with the Hamilton radius ρ_0 and the distance $\rho - \rho_0$ from it. The dimming of the inner ring by diffraction is clear. The form (4.1.39) is suitable for asymptotic expansion and yields (4.1.22) subject to the gaussian complexification.

The uniform approximation above cannot be extended to the focal plane for a nongaussian incident beam, where further investigation requires considering special cases, only one other of which has been solved. Berry (2004b) derived the universal focal plane profile for a pinhole incident beam. This is achieved by using the fourier representation (2.3.8) for the beam, integrating first over the wavevector $\boldsymbol{\kappa}$, carrying out the azimuthal $\boldsymbol{\rho}$ integral

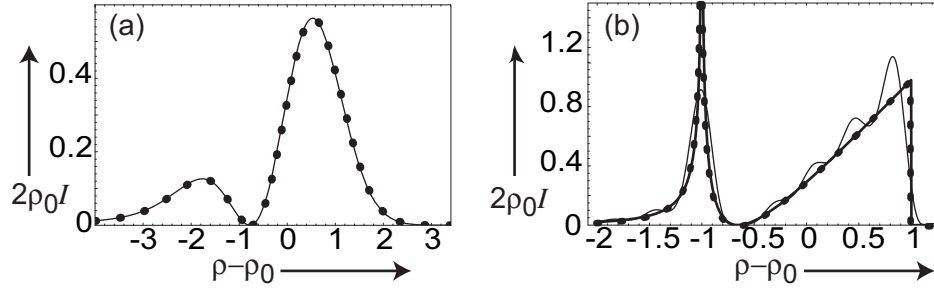


Figure 4.7: Rings in the focal image plane: the universal intensity profiles in the focal image plane for (a) a gaussian incident beam, exact (curve), and asymptotic approximation (dots) from equation (4.1.39); and, (b) a pinhole incident beam, exact (thick curve) and asymptotic (dots), and exact with aperture angle $16/k_0w$ (thin curve).

followed by a first order approximation in $|\rho - \rho_0| \ll \rho_0$, before finally simplifying the ρ integral. Noting that (4.1.24) holds, Berry obtains

$$b_+(\rho, 0) \approx \frac{2\sqrt{2}}{\pi\sqrt{\rho}} \left\{ \begin{array}{ll} 0, & \xi > 1 \\ \sqrt{2}E\left[\frac{1-\xi}{2}\right] - \frac{1}{\sqrt{2}}K\left[\frac{1-\xi}{2}\right], & |\xi| < 1 \\ \sqrt{1-\xi}E\left[\frac{2}{1-\xi}\right] + \frac{\xi}{\sqrt{1-\xi}}K\left[\frac{2}{1-\xi}\right], & \xi < -1 \end{array} \right\}_{\xi=\rho-\rho_0}, \quad (4.1.40)$$

in terms of the complete elliptic integrals E and K (for which we use the notation in MathematicaTM). Thus diffraction of the beam from a pinhole produces a brighter but narrower inner ring ($\xi < 0$), and a sharp outer ring ($\xi > 0$). Figure 4.7(b) shows that not only is this approximation indistinguishable from the exact wave integral, but the logarithmic singularity in the inner ring is indeed part of the exact wave theory.

Of course this singularity is unphysical, a matter that has not been discussed elsewhere. It originates in the slow convergence of the $\kappa \rightarrow \infty$ tail of the integral, and is physically smoothed by the presence of a finite aperture angle, either from the finite width of the crystal or some objective lens. This cuts the integral off at some finite κ_{aperture} , inducing oscillations in the universal profile, an example of which is overlaid in figure 4.7(b). The integral cannot then be solved analytically, but numerical integration yields the dependence of the profile on aperture angle $\kappa_{\text{aperture}}/k_0w$ shown in figure 4.8, approaching the universal form as the aperture grows toward infinite size.

In both the gaussian and pinhole incident beams, geometrical optics breaks down near the focal image plane due to focusing and diffraction is of prime importance. These cases

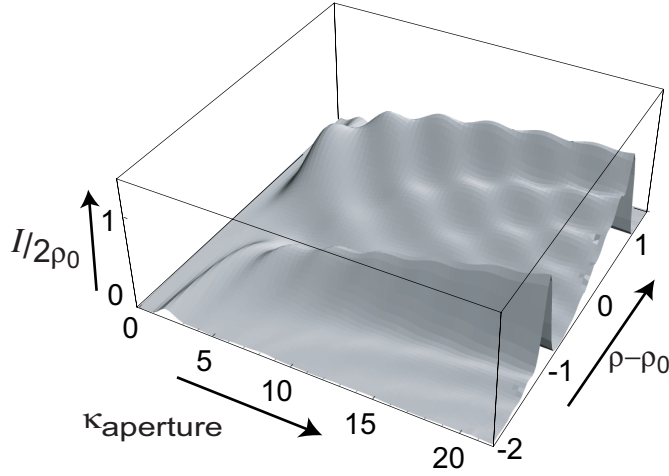


Figure 4.8: Aperture-induced oscillations in the focal plane: the intensity in the focal image plane for a pinhole incident beam depends strongly on the aperture angle κ_{aperture} , which determines the range of wave directions under observation. As the aperture angle increases the intensity evolves towards the universal profile in figure 4.7(b).

highlight different ways in which diffraction can play a role: for a gaussian beam the geometric intensity predicts symmetric rings, but diffraction dominates the inner ring, all but destroying it; for a pinhole beam poor collimation comes into play, and the observational aperture size produces interference which softens the logarithmic singularity from an infinite aperture.

4.1.4 The bright axial spike

The internal conical diffraction rings of the last two sections become fainter as distance ζ from the focal image plane increases, and the axial focus begins to dominate. In the axial region far from the focal plane $\rho \ll \rho_0 < \sqrt{\zeta}$, we can consider the Bessel functions and beam profile in the diffraction integrals (4.1.5) to be slowly varying. Evaluating them at the saddlepoints $\kappa_{\pm} \approx \rho_0/\zeta$ of the remaining integrals, we obtain

$$b_{\pm}(\rho, \zeta) \approx e^{i\frac{\rho_0^2}{2\zeta}} \frac{\rho_0}{\zeta} \sqrt{\frac{\pi}{2i\zeta}} a\left(\frac{\rho_0}{\zeta}\right) \left[J_0\left(\frac{\rho\rho_0}{\zeta}\right) \mp iJ_1\left(\frac{\rho\rho_0}{\zeta}\right) \right]. \quad (4.1.41)$$

This implies $|b_+|^2 = |b_-|^2$, so the intensity has no azimuthal dependence regardless of the incident beam's polarisation, and we can write

$$I(\rho, \zeta) \approx \frac{\pi \rho_0^2}{2\zeta^3} \left| a\left(\frac{\rho_0}{\zeta}\right) \right|^2 \left[\left| J_0\left(\frac{\rho_0 \rho}{\zeta}\right) \right|^2 + \left| J_1\left(\frac{\rho_0 \rho}{\zeta}\right) \right|^2 \right]. \quad (4.1.42)$$

This attains a maximum along the axis at $\zeta = \rho_0 \sqrt{2/3}$. The bright axial spike is surrounded by faint interference rings which spread outward as ζ increases. These ‘shoulders’ are the inflection points of the Bessel J_0 function (zeros of J_1) rather than maxima or minima, with a spacing of $\Delta\rho \approx \pi\zeta/\rho_0$, shown magnified in figure 4.9. A Taylor expansion of this result near the axis correctly yields the divergent geometric focus (4.1.14).

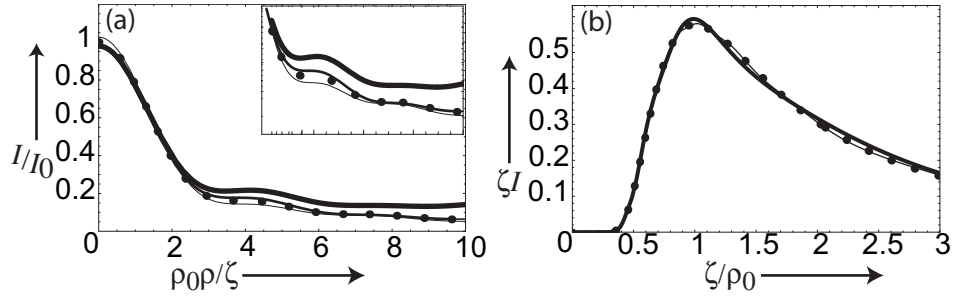


Figure 4.9: Intensity of the axial spike: (a) spike profile for $\rho_0 = 20$, approximation (4.1.42) scaled to unity on the axis (dotted curve), and exact intensity for $\zeta = 10$ (thick curve), $\zeta = 15$ (medium curve), $\zeta = 30$ (thin curve); (b) axial intensity ζI , approximation (4.1.47) (dots), and exact intensity for $\rho_0 = 20$ (thick) and $\rho_0 = 60$ (thin).

Along the axis itself, an asymptotic expansion of the diffraction integral contains a subdominant saddlepoint contribution, and a dominant endpoint contribution required for the correct limit at small ζ , giving

$$b_+(0, \zeta) = b_-(0, \zeta) \approx \sqrt{\frac{\pi}{2}} \frac{i\rho_0}{(i\zeta)^{3/2}} e^{i\frac{\rho_0^2}{2\zeta}} a\left(\frac{\rho_0}{\zeta}\right) - \frac{1}{\rho_0^2} a(0). \quad (4.1.43)$$

This again seemingly paradoxical result involves the subdominant exponential (first term) giving the greater contribution in the region of interest. For the intensity the subdominant saddlepoint term is sufficient, giving

$$I(0, \zeta) \approx \frac{\pi \rho_0^2}{2\zeta^3} \left| a\left(\frac{\rho_0}{\zeta}\right) \right|^2. \quad (4.1.44)$$

For a gaussian incident beam the integrals (4.1.5) can be evaluated exactly along the axis in terms of the error function. For this purpose the integrals defined in (2.5.5) or (2.5.16) are also suitable, satisfying

$$b_{\pm}(0, \tilde{\zeta}) = B_0(0, \tilde{\zeta}) = \frac{1}{\tilde{\zeta}} C_0 \left(\frac{\rho_0}{\sqrt{\tilde{\zeta}}} \right), \quad (4.1.45)$$

where

$$C_0(r_0) = 1 + r_0 \sqrt{\frac{i\pi}{2}} e^{\frac{1}{2}ir_0^2} \operatorname{erf} \left(\frac{r_0}{\sqrt{-2i}} \right). \quad (4.1.46)$$

An asymptotic expansion gives, in agreement with the general beam result above,

$$I(0, \zeta) \approx \frac{\pi \rho_0^2}{2\zeta^3} e^{-\frac{\rho_0^2}{\zeta^2}}. \quad (4.1.47)$$

The uniform scaling of this approximation is shown in figure 4.9(b).

4.2 Biaxial Crystals with Optical Activity

We define optical activity as the rotation of phase by a total amount $\rho_0\gamma$, of a circularly polarised plane wave propagating along the optic axis of a crystal, where γ specifies chirality and ρ_0 provides a convenient paraxial scaling. Written in terms of a hermitian antisymmetric matrix \mathcal{F}^{ch} , this is the eigenequation

$$\mathbf{D} = e^{-i\mathcal{F}^{\text{ch}}} \mathbf{d}_{\pm}^{\text{circ}} = e^{\mp i\rho_0\gamma} \mathbf{d}_{\pm}^{\text{circ}}, \quad (4.2.1)$$

uniquely determining \mathcal{F}^{ch} as

$$\mathcal{F}^{\text{ch}} = \rho_0\gamma\sigma_2. \quad (4.2.2)$$

Combined with biaxiality the paraxial effect of the crystal is therefore, up to a trace,

$$\mathcal{F}^{\text{tr}} = \mathbf{V}(\boldsymbol{\kappa}) \cdot \boldsymbol{\Sigma} = \rho_0 \{ \boldsymbol{\kappa}, \gamma \} \cdot \{ \sigma_3, \sigma_1, \sigma_2 \}. \quad (4.2.3)$$

The effect on a linearly polarised wave is to rotate the orientation,

$$\mathbf{D} = e^{-i\mathcal{F}^{\text{ch}}} \mathbf{d}_{\chi}^{\text{lin}} = \mathbf{d}_{\chi+\rho_0\gamma}^{\text{lin}}. \quad (4.2.4)$$

Exploiting circular symmetry of the propagator integral via (2.5.2) and using the eigenwave representation (2.5.5) to write $\mathbf{D} = [B_0\mathcal{I} + \{\hat{\boldsymbol{\rho}}B_1, B_2\} \cdot \boldsymbol{\Sigma}] \cdot \mathbf{d}_0$, we obtain $\mathbf{D}(\rho, \zeta)$ as defined by (2.5.5). Carrying out the azimuthal integration gives

$$\begin{Bmatrix} B_0(\rho, \zeta) \\ B_1(\rho, \zeta) \\ B_2(\rho, \zeta) \end{Bmatrix} = \int_0^{\infty} \mathbf{d}\kappa \kappa a(\kappa) e^{-\frac{1}{2}i\kappa^2\zeta} \begin{Bmatrix} J_0(\rho\kappa) \cos \rho_0 \sqrt{\kappa^2 + \gamma^2} \\ \frac{\kappa J_1(\rho\kappa)}{\sqrt{\kappa^2 + \gamma^2}} \sin \rho_0 \sqrt{\kappa^2 + \gamma^2} \\ \frac{\gamma J_0(\rho\kappa)}{i\sqrt{\kappa^2 + \gamma^2}} \sin \rho_0 \sqrt{\kappa^2 + \gamma^2} \end{Bmatrix}, \quad (4.2.5)$$

which was first written down as an extension to the Belskii-Khapalyuk theory by Belsky & Stepanov (2002).

The intensity for an unpolarised incident beam is simply the circularly symmetric sum of magnitudes

$$I_{\text{unpol}} = |B_0|^2 + |B_1|^2 + |B_2|^2. \quad (4.2.6)$$

Chirality distinguishes the handedness of circularly polarised incident beams with a circularly symmetric brightening or dimming,

$$I_{\pm} = I_{\text{unpol}} \mp 2\text{Re}[B_0^* B_2]. \quad (4.2.7)$$

Linear incident polarisation introduces azimuthal dependence, a swirl pattern whose orientation rotates twice as fast as that of the incident beam,

$$I_\chi = I_{\text{unpol}} + 2\text{Re} \left[e^{i(\phi\rho - 2\chi)} (\text{Re} [B_0 B_1^*] + \text{ilm} [B_1^* B_2]) \right]. \quad (4.2.8)$$

The chiral conical diffraction intensity for an unpolarised gaussian incident beam is shown in figures 4.10 and 4.11. In the focal image plane there is a set of bright concentric rings, whose brightness decreases with radius. As distance from the focal plane increases one outer ring dominates, eventually giving way to a bright axial spot surrounded by fainter rings. The range over which the bright outer ring shrinks to a spot depends on γ , as can be seen in figure 4.10, with the number and sharpness of interference fringes increasing with ρ_0 .

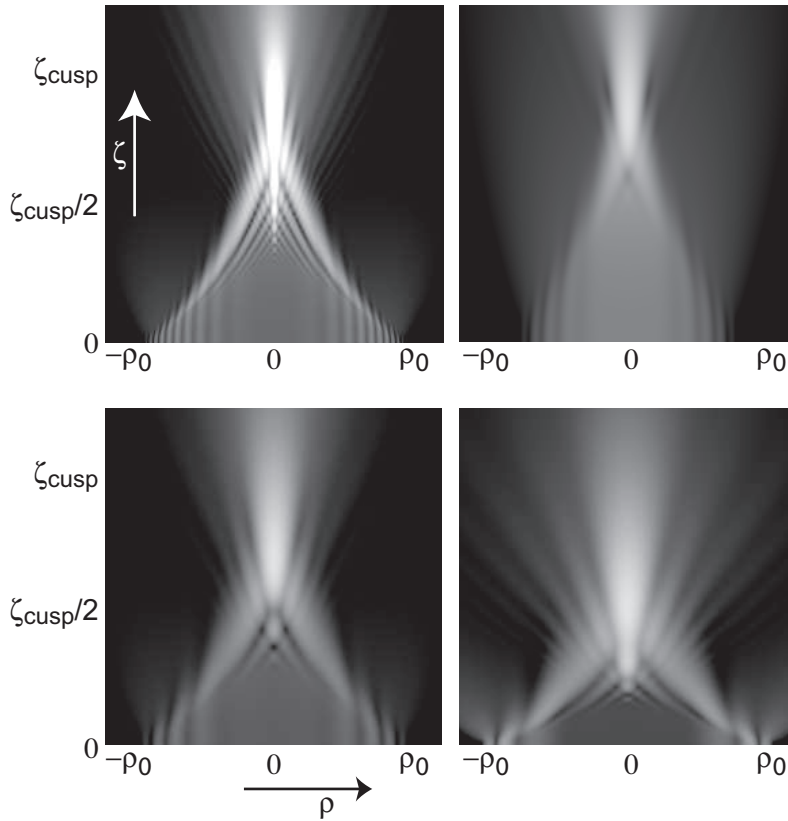


Figure 4.10: Intensity sections of the caustic horn for unpolarised incident beam, calculated using (4.2.5), for: (a) $\rho_0 = 50$, $\gamma = 1$, and $\rho_0 = 20$ with γ values: (b) 2, (c) 1, (d) 1/2.

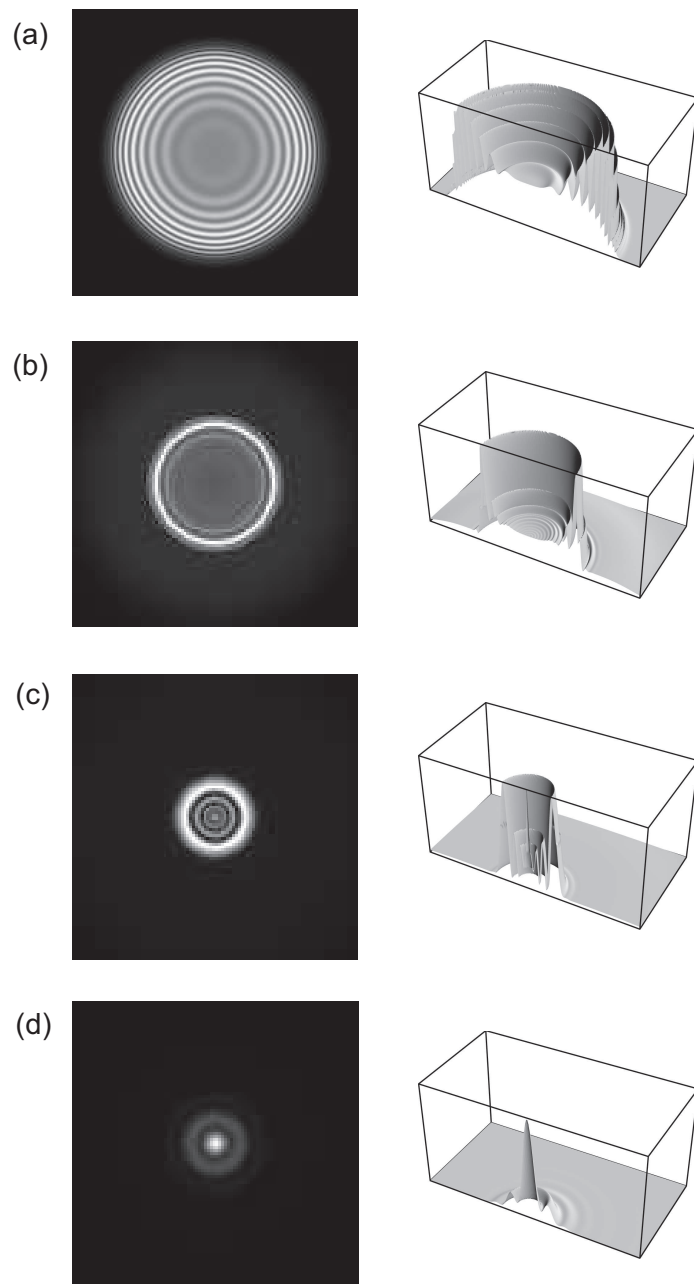


Figure 4.11: The rings of chiral conical diffraction: theoretical plots and 3D cutaways of intensities calculated using (4.2.5) for $\rho_0 = 50$, $\gamma = 1$, at distances ζ equal to : (a) $\zeta_{\text{cusp}}/50$, (b) $\zeta_{\text{cusp}}/5$, (c) $2\zeta_{\text{cusp}}/5$, (d) $7\zeta_{\text{cusp}}/5$.

4.2.1 The “trumpet horn” caustic of chiral conical refraction

Chirality breaks the conical point degeneracy of the optical path length,

$$\Phi_{\pm}(\boldsymbol{\kappa}, \boldsymbol{\rho}, \zeta) = -\boldsymbol{\kappa} \cdot \boldsymbol{\rho} + \frac{1}{2}\zeta\kappa^2 \pm \rho_0\sqrt{\kappa^2 + \gamma^2}. \quad (4.2.9)$$

Rays beyond the crystal are thus given by

$$\boldsymbol{\rho}_{\pm} = \left(\zeta \pm \frac{\rho_0}{\sqrt{\kappa^2 + \gamma^2}} \right) \boldsymbol{\kappa}, \quad (4.2.10)$$

which rearranges to a quartic ray equation

$$(\rho - \zeta\kappa)^2 (\kappa^2 + \gamma^2) - (\rho_0\kappa)^2 = 0 \quad (4.2.11)$$

with solutions

$$\boldsymbol{\kappa} = \kappa_n(\boldsymbol{\rho}, \zeta) \hat{\boldsymbol{\rho}}, \quad n = 1, 2, 3, 4, \quad (4.2.12)$$

given analytically in appendix A. The ray determinant, simplified using the ray equation to remove \pm signs, can be written

$$\left| \det \frac{d\boldsymbol{\rho}}{d\boldsymbol{\kappa}} \right| = \frac{\rho}{\kappa} \left(\zeta + \frac{(\rho/\kappa - \zeta)^3}{(\rho_0/\gamma)^2} \right). \quad (4.2.13)$$

The ζ dependent factor vanishes around a ring of inflection points (3.2.5) in the wave surface, which focuses rays around a rotationally symmetric caustic surface

$$\left(\frac{\rho_c}{\rho_0} \right)^{2/3} + \left(\frac{\zeta}{\zeta_{\text{cusp}}} \right)^{2/3} = 1, \quad (4.2.14)$$

whose apex is a spun cusp at $\zeta = \zeta_{\text{cusp}} = \rho_0/\gamma$. Despite the removal of the $\kappa = 0$ conical degeneracy, the wave surface still possesses the tangent circle (3.2.4), producing an axial focal line which threads the horn-shaped caustic.

The geometric intensity is summed over the real solutions to (4.2.11),

$$I(\boldsymbol{\rho}, \zeta) = \frac{1}{2\rho} \sum_n \left[\kappa \left(\zeta + \frac{(\rho/\kappa - \zeta)^3}{\zeta_{\text{cusp}}^2} \right)^{-1} |a(\kappa)|^2 \right]_{\boldsymbol{\kappa}=\boldsymbol{\kappa}_n(\boldsymbol{\rho}, \zeta)}. \quad (4.2.15)$$

Inside the caustic (where the left hand side of (4.2.14) is less than unity), there are four real rays. Two of these coincide on the caustic and vanish (become complex) outside it. The origin of these rays from the two sheets of the wave surface are illustrated in figure 4.12. In the absence of a conical point degeneracy, polarisation states rotate fully in a

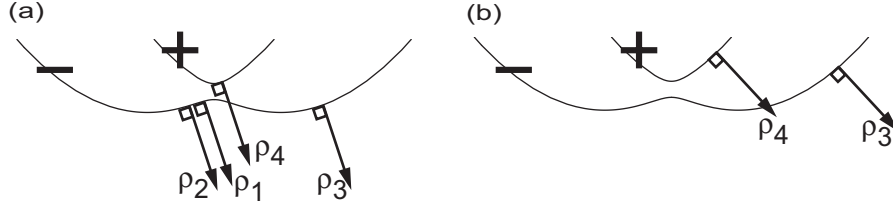


Figure 4.12: Rays of chiral conical refraction: (a) $\rho < \rho_c$, inside the caustic there are four real solutions of the ray equation (4.2.10), two of which coalesce on the inflection ring (see figure 3.4(b)); and (b) $\rho > \rho_c$, outside the caustic only two real solutions remain.

circuit of the optic axis, so two rays symmetric about the axis have the same polarisation but with a π phase difference. This means that the polarisations associated with the ‘-’ sheet rays are orthogonal to those of each ‘+’ sheet ray in figure 4.12.

The ray geometry suggests a natural scaling $\{u, v\} = \{\rho/\rho_0, \zeta/\zeta_{\text{cusp}}\}$, in terms of which the optical path length and intensity can be written in a universal form dependent only on u and v . Only with the introduction of phase information would we require γ , and only in considering the integrals $B_{1,2}$ would we require ρ_0 . This is a useful simplification but the scaling is singular for nonchiral crystals, so we do not use it here, but we do employ it in appendix A.

4.2.2 Voigt’s “Trompeten Trichters”: rays inside the chiral crystal

The optical path length of rays after refraction by the entrance face of the crystal is given, according to section 2.8, by

$$\Phi(\boldsymbol{\kappa}, \boldsymbol{\theta}_\rho, \zeta') = \zeta' \left(-\boldsymbol{\kappa} \cdot \boldsymbol{\theta}_\rho + \frac{1}{2}\kappa^2 \pm \theta_0 \sqrt{\kappa^2 + \gamma^2} \right), \quad (4.2.16)$$

giving rays with angular deflection

$$\boldsymbol{\theta}_{\rho\pm} = \left(1 \pm \frac{\theta_0}{\sqrt{\kappa^2 + \gamma^2}} \right) \boldsymbol{\kappa} \quad (4.2.17)$$

from the optic axis. The geometric intensity inside the crystal is given, returning to cartesian coordinates, by

$$I(\boldsymbol{\rho}, \zeta') = \frac{1}{2\rho\zeta'} \sum_n \left[\kappa \left(1 + \frac{(\rho/\zeta'\kappa - 1)^3}{(\zeta_{\text{cusp}}/\zeta_{\text{exit}})^2} \right)^{-1} |a(\boldsymbol{\kappa})|^2 \right]_{\boldsymbol{\kappa}=\boldsymbol{\kappa}_n(\boldsymbol{\rho}, \zeta')}, \quad (4.2.18)$$

where ζ_{exit} is the exit face of the crystal (2.8.4). As in the image field, the sum is over the real solutions $\kappa_n(\rho, \zeta')$ to the quartic ray equation obtained from (4.2.17).

The tangent circle of Fresnel’s wave surface for a chiral crystal focuses rays along the axis. The ring of inflection points produces a caustic ray cone inside the crystal given by

$$\left(\frac{\theta_{\rho+}}{\gamma}\right)^{2/3} + \left(\frac{\theta_0}{\gamma}\right)^{2/3} = 1. \quad (4.2.19)$$

This cone, and the envelope of normals producing it, was predicted by Voigt (1905*b*). Note that it is distinct from Hamilton’s nonchiral conical refraction cone which, with the conical point destroyed by chirality, leaves a faint conical remnant at an angle much larger than that of the caustic. Many twentieth century investigations mistakenly believed that this remnant would dominate the chiral phenomenon, prompting Voigt to dub it “sogenannte konische Refraktion”.

Clearly from (4.2.19) the caustic cone exists only when

$$\frac{\theta_0}{\gamma} = \frac{\zeta_{\text{cusp}}}{\zeta_{\text{exit}}} > 1, \quad (4.2.20)$$

that is, when the cusp in the image field lies outside the crystal. As γ increases Voigt’s cone emerges from the axial focal line and the cusp appears in the image field. The cone refracts out of the crystal to form the horn-shaped caustic of the image field, and at the exit face the two necessarily coincide over a ring with radius

$$\rho_{\text{exit}} = \rho_0 \left[1 - \left(\frac{\zeta_{\text{exit}}}{\zeta_{\text{cusp}}} \right)^{2/3} \right]^{3/2}. \quad (4.2.21)$$

Figures 4.13-4.15 illustrate this transition. Figure 4.13 shows the actual ray intensity, inside the crystal from (4.2.18) and beyond it from (4.2.15), in the nonchiral, chiral, and strongly chiral cases. The faint remnant of Hamilton’s cone can be seen at the same wide angle in the chiral images, along with the axial focal line. Voigt’s caustic cone and its refracted horn spring out of the axial focus as chirality increases, with the image cusp appearing from $\zeta \rightarrow \infty$ and eventually vanishing inside the crystal. Figure 4.14 shows the complete image field, with the cusp moving inside the crystal under strong chirality. The caustic cone reaches its maximum radius of $\rho = \rho_0$ in the focal image plane which is where, in the absence of chirality, the bright rings surrounding the dark anti-focus can be seen. Finally figure 4.15 illustrates the paths of rays refracted through the crystal, and in (a) it is seen that these project back onto two focal points (Hamilton’s dark ring) in the focal image plane.

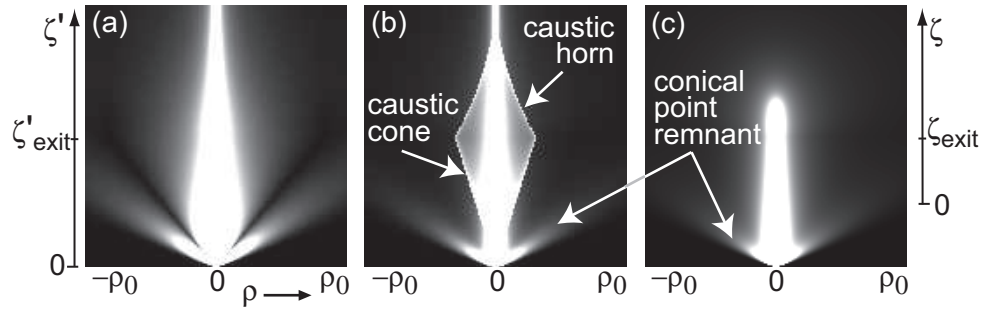


Figure 4.13: Ray intensity through the crystal, (entrance face $\zeta' = 0$ and exit faces $\zeta = \zeta' = \zeta_{\text{exit}}$), for $\zeta_{\text{cusp}}/\zeta_{\text{exit}}$ values: (a) 10^3 ; (b) 3; (c) $4/5$.

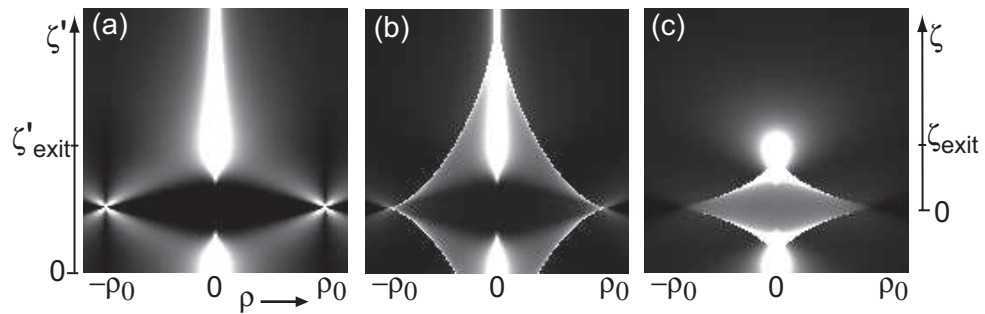


Figure 4.14: Projected ray intensity through the crystal, projected back within the crystal to the focal image plane $\zeta = 0$ and beyond, for the values in figure 4.13.

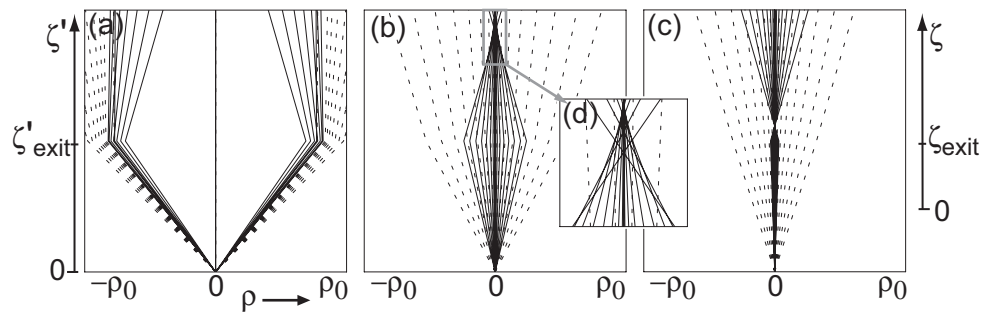


Figure 4.15: Ray trajectories through the crystal, for the values in figure 4.13, with (d), a magnification of the ray caustic. Rays from the ‘-’ sheet are full lines, rays from the ‘+’ sheet are dashed lines.

4.2.3 Diffraction and the caustic horn

For asymptotic analysis we choose the vector form of the chiral diffraction integrals (2.5.6). Using cartesian coordinates $\boldsymbol{\kappa} = \{\kappa_x, \kappa_y\}$ where κ_x lies along $\boldsymbol{\rho}$, the saddlepoints of the integrals satisfy the ray equations (4.2.10) and (4.2.11) with $\kappa_y = 0$.

Following section 2.6 we extract the ‘heart’ of the diffraction integrals, $b_{\pm}(\boldsymbol{\rho}, \zeta)$, whose phase can be expanded as

$$\Phi(\boldsymbol{\kappa}) = \Phi(\kappa_n) + \frac{(\kappa_x - \kappa_n)^2}{2} \frac{\partial^2}{\partial \kappa_x^2} \Phi(\kappa_n) + \frac{\kappa_y^2}{2} \frac{\partial^2}{\partial \kappa_y^2} \Phi(\kappa_n) + \dots \quad (4.2.22)$$

Note the vanishing of the first derivative at the saddlepoints $\boldsymbol{\kappa}_n$, the solutions to (4.2.12), each of which contributes

$$b_n(\boldsymbol{\rho}, \zeta) = \frac{a(\kappa_n)}{2\pi} e^{-i\Phi(\kappa_n)} \int_{-\infty}^{\infty} d\kappa_y e^{-i\frac{\rho}{\kappa_n} \kappa_y^2} \int_{-\infty}^{\infty} d\kappa_x e^{-i\frac{1}{2}(\kappa_x - \kappa_n)^2 \frac{\partial^2}{\partial \kappa_x^2} \Phi(\kappa_n)} \quad (4.2.23)$$

to the integral. As shown in figure 4.12, only one ray originates on the ‘+’ sheet of the wave surface $\Phi_+ + \boldsymbol{\kappa} \cdot \boldsymbol{\rho}$. This corresponds to one saddlepoint contribution which exists everywhere, a stability consistent with the fact that the Φ_+ part of the integral can be separated from the Φ_- part. The integral involving Φ_- then has three saddlepoints, which all lie on the real κ_x axis when $\{\boldsymbol{\rho}, \zeta\}$ is inside the caustic, and the stationary phase integration contour passes through all three as illustrated in figure 4.16. At the caustic (4.2.14) two saddlepoints coalesce, and outside the caustic they become complex

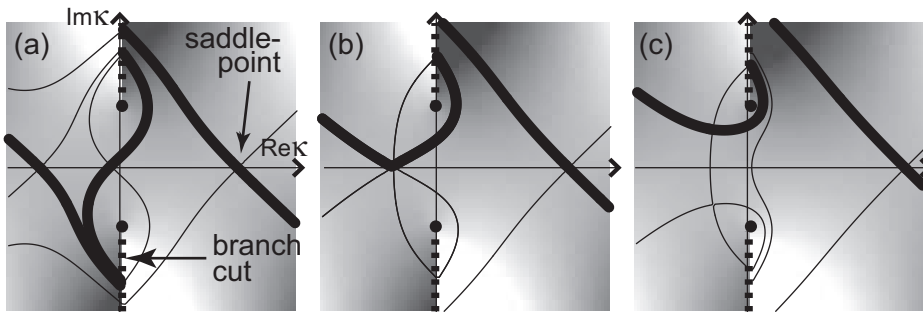


Figure 4.16: Saddlepoints of the wave function (4.2.23): the phase function Φ_- plotted (a) inside the caustic, (b) on the caustic, (c) outside the caustic; showing branch cuts (dashed), branch points (dots), phase contours (lines), integration contour (bold), integrand magnitude (shaded), and saddlepoints (crossings), plotted in the complex κ_x plane.

conjugates in the complex κ_x plane. The integration contour passes then through one saddlepoint that remains on the real axis and corresponds to a ray, but passes through only one of the two complex saddlepoints, which corresponds to an evanescent wave.

At the saddlepoints, using the ray equation (4.2.10), we can write the phase and its second derivative simply as

$$\Phi_{\pm}(\kappa_n) = \Psi_n \equiv -\kappa_n \rho + \frac{1}{2} \zeta \kappa_n^2 + \frac{\rho_0^2}{\rho/\kappa_n - \zeta} \quad (4.2.24)$$

$$\frac{\partial^2}{\partial \kappa_x^2} \Phi_{\pm}(\kappa_n) = \Psi_n'' \equiv \zeta + \frac{(\rho/\kappa_n - \zeta)^3}{\zeta_{\text{cusp}}^2}, \quad (4.2.25)$$

with the corresponding κ_y derivative vanishing trivially. The saddlepoint contributions integrate exactly to give

$$b_n(\rho, \zeta) = a(\kappa_n) \sqrt{\frac{\kappa_n}{-\rho \Psi_n''}} e^{-i\Psi_n}. \quad (4.2.26)$$

Then the first chiral diffraction integral is given by $B_0 \approx \frac{1}{2} \sum_n b_n$, and by differentiating (4.2.23) we obtain

$$B_m(\rho, \zeta) \approx \frac{1}{2} \sum_n c_m(\kappa_n) a(\kappa_n) \sqrt{\frac{\kappa_n}{-\rho \Psi_n''}} e^{-i\Psi_n}, \quad m = 0, 1, 2, \quad (4.2.27)$$

where

$$c_0(\kappa) = 1, \quad c_1(\kappa) = \frac{\kappa}{\rho_0} \left(\frac{\rho}{\kappa} - \zeta \right), \quad c_2(\kappa) = \frac{\gamma}{\rho_0} \left(\frac{\rho}{\kappa} - \zeta \right). \quad (4.2.28)$$

The intensity (4.2.6) under this approximation is then equivalent to the geometrical intensity (4.2.15), with the addition of: (i), a complex saddlepoint now included in the sum giving an evanescent wave outside the caustic, and (ii), a phase Ψ which provides the wave information associated with each ray, introducing interference between the three ‘—’ sheet rays. Figure 4.17 shows the resulting geometric intensity with wave interference, corresponding to the $\zeta > 0$ region of figure 4.14(b), decorated with interference and the evanescent wave which drops off exponentially outside the caustic.

The geometric approximation over complex rays and including phase contains all physical information about the diffracted light field from a biaxial chiral crystal. But it diverges along the caustic, along the focal line and, more severely, where the two intersect at the cusp. (Note that the geometrical intensity for chiral crystals does not diverge at $\zeta = 0$ except at $\rho = \rho_0$, implying that this is no longer strictly a focal plane). The divergence at the caustic can be removed for gaussian beams by use of the complex ray trick, the effect

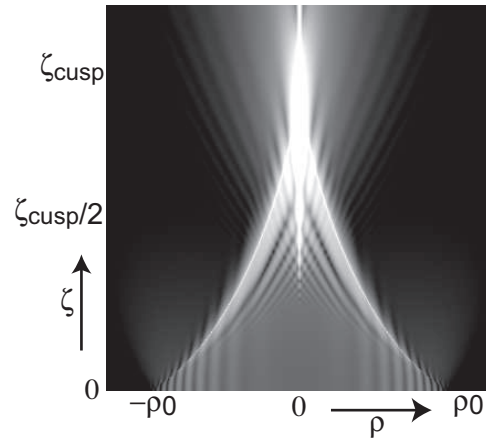


Figure 4.17: Geometrical optics with phase: density plot of intensity in the ρ - ζ plane for unpolarised incident beam, from stationary phase approximation (4.2.27), with $\rho_0 = 50$, $\gamma = 1$.

being to separate the caustic into Stokes and anti-Stokes sets, reducing the singularity to a small jump. In the next section we give a more powerful method for smoothing the caustic discontinuity for general beams, using the generic association of the caustic with the fold catastrophe and the Airy function.

4.2.4 Uniformisation over the caustic

To derive a uniform approximation (Chester et al. 1957) we map the divergent integrand onto a function with the same critical behaviour. To describe the caustic the function must have two stationary points which coalesce on a subset of the domain. The simplest such function is a cubic exponential. The cubic phase function is known as the *fold catastrophe* (Poston & Stewart 1996, Nye 1999), and the simplest integral obtained from it is the Airy function.

The chiral conical diffraction caustic concerns only two of the saddlepoint solutions (4.2.12). For convenience we will define these solutions as in appendix A, labeled so that their associated phases satisfy

$$\Phi(\kappa_4) > 0 > \text{Re}\Phi(\kappa_1) \geq \text{Re}\Phi(\kappa_2) > \Phi(\kappa_3), \quad (4.2.29)$$

in which case the caustic occurs when $\kappa_1 = \kappa_2$, the phases (and κ_n 's) are all real inside the caustic, and outside the caustic $\Phi(\kappa_1)$ and $\Phi(\kappa_2)$ are complex conjugates.

If we define

$$\alpha_{mn} = \frac{c_m(\kappa_n) a(\kappa_n)}{2} \sqrt{\frac{\kappa_n}{i\rho |\Psi_n''|}}, \quad (4.2.30)$$

we can write the stationary phase approximation (4.2.27) for the two caustic saddlepoint contributions as

$$B_m^{\text{SP}} = \alpha_{m1} e^{-i\Psi_1 + i\frac{\pi}{4}} + \alpha_{m2} e^{-i\Psi_2 - i\frac{\pi}{4}}. \quad (4.2.31)$$

The $\pm\pi/4$ phase comes from the sign of Ψ_n'' , consistent with κ_1 and κ_2 corresponding respectively to a maximum and minimum along the integration contour.

Uniformisation is achieved by mapping the phase $\Phi(\kappa)$ smoothly onto a cubic function

$$\Phi(\kappa) = \varphi(q) = \frac{1}{3}q^3 - sq + \lambda. \quad (4.2.32)$$

The κ_y part of the integral (4.2.23) can be carried out smoothly by stationary phase and does not concern us here. Applying this mapping to the κ_x part we have

$$\int_{-\infty}^{\infty} d\kappa_x c_m(\kappa_x) a(\kappa_x) \sqrt{\kappa_x} e^{-i\Phi(\kappa_x)} = \int_{-\infty}^{\infty} dq p(q) e^{-i\varphi(q)}. \quad (4.2.33)$$

The constants s and λ are found by considering the phase at the mutual saddlepoints $\kappa_{1,2} = q_{\pm} = \pm\sqrt{s}$, giving

$$\lambda = \frac{1}{2}(\Psi_1 + \Psi_2), \quad s = \left[\frac{3}{4}(\Psi_1 - \Psi_2)\right]^{2/3}. \quad (4.2.34)$$

It is necessary to expand the prefactor p in the mapped integrand to first order,

$$c_m(\kappa_x) a(\kappa_x) \sqrt{\kappa_x} = p(q) \approx p_0 + qp_1. \quad (4.2.35)$$

The constants p_j are found in terms of $d\kappa_x/d\rho$ at the stationary points of φ , by differentiating the mapping (4.2.32) twice with respect to q . The resulting mapped integrals consist of an Airy function (multiplying p_0) and its derivative (multiplying p_1), giving

$$B_m^{\text{uni}} = \sqrt{\pi} e^{-i\frac{1}{2}(\Psi_1 + \Psi_2)} \left[\frac{\alpha_{m1} + \alpha_{m2}}{s^{-1/4}} \text{Ai}(-s) + i \frac{\alpha_{m1} - \alpha_{m2}}{s^{1/4}} \text{Ai}'(-s) \right]. \quad (4.2.36)$$

This result is actually inevitable given the assumption that the uniform approximation takes the form

$$B^{\text{uni}} \sim e^{-i\lambda} [f_1 \text{Ai}(-s) + f_2 \text{Ai}'(-s)], \quad (4.2.37)$$

if s and λ are known to be given by (4.2.34); the unknowns $f_{1,2}$ are determined by the equality of the uniform and stationary phase approximations far from the caustic, where

$$\text{Ai}(-s) \approx \frac{1}{s^{1/4} \sqrt{\pi}} \sin\left(\frac{2}{3}s^{2/3} + \frac{\pi}{4}\right), \quad \text{Ai}'(-s) \approx \frac{s^{1/4}}{\sqrt{\pi}} \cos\left(\frac{2}{3}s^{2/3} + \frac{\pi}{4}\right). \quad (4.2.38)$$

The uniform intensity is almost indistinguishable from the exact in most regions; the comparison is shown in figure 4.18. The uniform approximation still diverges along the axis, though this only becomes significant at large ζ near the cusp, a higher order catastrophe, which we will consider in section 4.2.6.

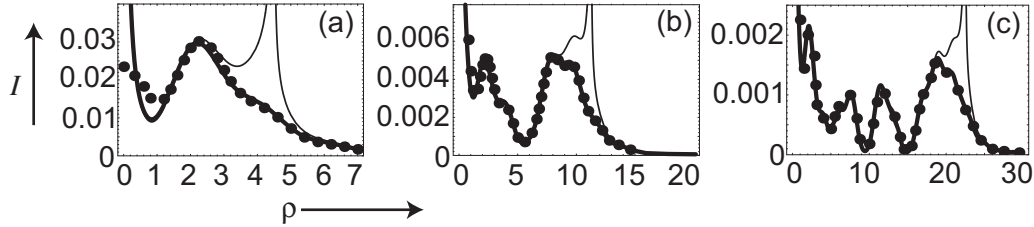


Figure 4.18: Asymptotics of the chiral Airy fringes: comparison of exact intensity from the integrals (4.2.5) (dots), stationary phase approximation from equation (4.2.27) (thin curves), and uniform asymptotic approximation using equation (4.2.36) (thick curves), where $\zeta = \zeta_{\text{cusp}}/2$, $\gamma = 1$, and ρ_0 equals: (a) 20, (b) 50, (a) 100.

4.2.5 The Stokes set

We have so far commented on the disappearance of ray solutions across the caustic and seen how this correctly reproduces the intensity, but there is also a Stokes surface. In the labelling convention (4.2.29) this encloses a region where the saddlepoint κ_3 ceases contributing to the integral by Stokes’ phenomenon illustrated in figure 4.19.

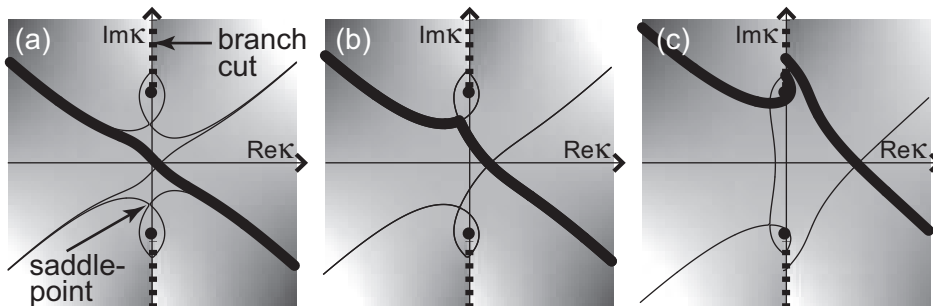


Figure 4.19: Stokes’ phenomenon: the phase function Φ_- plotted in the complex κ_x plane as a Stokes surface is crossed, showing the transition between (a) one saddlepoint, (b) phase contour degeneracy on the Stokes surface, (c) two saddlepoints. (cf figure 4.16).

In this instance the Stokes surface lies in the darkness far outside the caustic where $\text{Re}\Psi_1 = \text{Re}\Psi_2$, and is given by the Stokes conditions $\text{Re}\Psi_{1,2} = \text{Re}\Psi_3$, or

$$\Psi_3 = \frac{1}{2}(\Psi_1 + \Psi_2). \quad (4.2.39)$$

This surface has no analytic solution that we have found, but by writing the phase in the form

$$\zeta\Psi_n = \frac{1}{2}(\rho - \zeta\kappa_n)^2 + \frac{\rho\rho_0^2}{\rho - \zeta\kappa_n} - \frac{1}{2}\rho^2 - \rho_0^2, \quad (4.2.40)$$

the last two terms are irrelevant, and we can write the Stokes condition as

$$\frac{y_1}{y_3} = \frac{y_1^3 + 2\rho\rho_0}{y_3^3 + 2\rho\rho_0}, \quad y_n = \rho - \zeta\kappa_n, \quad (4.2.41)$$

where y_1 is interchangeable with y_2 .

Wright (1980) showed that near the cusp, the Stokes surface must have the form

$$\left(\frac{\rho}{\sqrt{5 + \sqrt{27}\rho_0}}\right)^3 + \left(\frac{\zeta}{3\zeta_{\text{cusp}}}\right)^2 \approx 1, \quad (4.2.42)$$

and far away (4.2.41) shows that it tends to the form $\rho/\rho_0 = \zeta/\zeta_{\text{cusp}}$. These conditions lead to an approximate expression for the Stokes surface:

$$\left(\frac{\zeta}{\zeta_{\text{cusp}}}\right)^2 - \frac{\epsilon\left(\frac{\rho}{\rho_0} - 1\right)^3}{1 + \epsilon\left(\frac{\rho}{\rho_0} - 1\right)} = 0, \quad \epsilon = \frac{2}{27}(5 + 3\sqrt{3}), \quad (4.2.43)$$

defining a horn-shaped surface, wider than the caustic, extending from the top of the cusp as shown in figure 4.20.

There is a further surface on which Ψ_4 satisfies the Stokes condition (4.2.39) in place of Ψ_3 , obtained from the Stokes surface by reflection in the cone $\rho/\rho_0 = \zeta/\zeta_{\text{cusp}}$. This is a false Stokes set, where the Stokes condition is satisfied but analysis of the stationary phase contours shows no corresponding degeneracy or change in topology. The reason is that the κ_4 solution is a saddlepoint of the separable Φ_+ part of the diffraction integral, or a ray normal of the '+' sheet of the wave surface, and cannot interact with the saddlepoints in the Φ_- part of the integral, since they are in the orthogonal polarisation.

which converges rapidly along the path $\arg t = -\pi/8$. Approximating the mapping by neglecting the quadratic term so $t\sqrt{2[t^2 + g\sqrt{2}]} \approx t\sqrt{2g\sqrt{2}}$, and defining

$$\xi_{\pm} \equiv \sqrt{2}(g \mp r_0), \quad \eta \equiv r\sqrt{2g\sqrt{2}}, \quad (4.2.47)$$

we differentiate to find the other integrals, giving the spun cusp form

$$\begin{aligned} C_0(r) &\approx 2 \left(\left(\frac{\eta}{2r} \right)^2 + i \frac{\partial}{\partial \xi} \right) \sum_{\pm} e^{\pm i r_0 g} J(\xi_{\pm}, \eta) \\ C_1(r) &\approx \frac{i\eta\sqrt{2}}{r} \frac{\partial}{\partial \eta} \sum_{\pm} \pm e^{\pm i r_0 g} J(\xi_{\pm}, \eta) \\ C_2(r) &\approx -\frac{\eta^2}{2r^2} \sum_{\pm} \pm e^{\pm i r_0 g} J(\xi_{\pm}, \eta). \end{aligned} \quad (4.2.48)$$

Figure 4.21 shows that this correctly describes the intensity near the cusp, but decorates the caustic

$$\frac{\rho}{\rho_0} \approx \sqrt{\frac{\zeta_{\text{cusp}}}{\zeta}} \left[\frac{2}{3} \left(1 - \frac{\zeta}{\zeta_{\text{cusp}}} \right) \right]^{\frac{3}{2}}, \quad (4.2.49)$$

which differs from the exact geometric caustic for small ζ (because of the approximated mapping), a region we have already dealt with in the previous section.

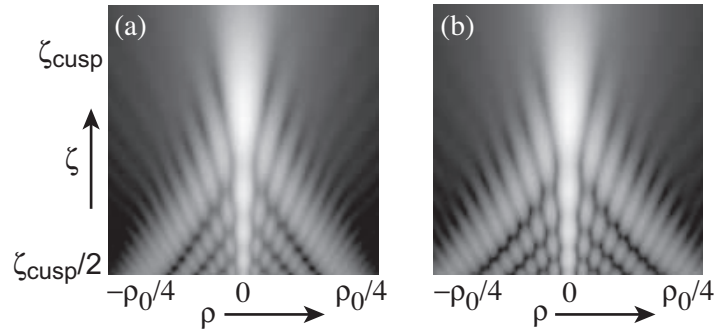


Figure 4.21: The spun cusp catastrophe: intensity near the cusp for $\rho_0 = 100$, $\gamma = 1$, (a) from the exact integrals (4.2.5), and (b) from the spun cusp approximation (4.2.48).

The diffraction integrals for a gaussian incident beam can be evaluated exactly on the $\rho = 0$ axis in terms of complementary error functions, extending the biaxial formula (4.1.46) to include chirality. From the gaussian beam integrals (2.5.16) we transform to a new integration variable

$$\sigma \rightarrow \sqrt{2t^2 - g^2}, \quad (4.2.50)$$

to obtain

$$\begin{aligned}
 C_0(0) &= \cos r_0 g + \frac{1}{2} r_0 e^{\frac{g^2 + ir_0^2}{2}} \sqrt{\frac{i\pi}{2}} \left[\operatorname{erfc} \left(\frac{g - r_0 \sqrt{i}}{\sqrt{2}} \right) - \operatorname{erfc} \left(\frac{g + r_0 \sqrt{i}}{\sqrt{2}} \right) \right] \\
 C_1(0) &= 0 \\
 C_2(0) &= -g e^{\frac{g^2 + ir_0^2}{2}} \sqrt{\frac{\pi}{2}} \left[\operatorname{erfc} \left(\frac{g - r_0 \sqrt{i}}{\sqrt{2}} \right) - \operatorname{erfc} \left(\frac{g + r_0 \sqrt{i}}{\sqrt{2}} \right) \right]. \quad (4.2.51)
 \end{aligned}$$

Figure 4.22 shows the axial intensity for thick crystals with different strengths of chirality. The scaling on the ζ axis makes it clear that the peak intensity does not always occur at the cusp, exhibiting a competition between the cusp of chirality and the axial focal line that survives from nonchiral biaxiality. This can also be seen in figure 4.10. For strong chirality $\gamma \gg 1$ in thick crystals $\rho_0 \gg 1$, the cusp manifests clearly as a maximum near $\zeta = \zeta_{\text{cusp}}$. As chirality decreases, focal line dominance brings the maximum to smaller ζ , towards $\zeta = \zeta_{\text{spike}} \equiv \rho_0 \sqrt{2/3}$ when $\gamma = 0$, that is when $\zeta/\zeta_{\text{cusp}} \sim \gamma \sqrt{2/3}$.

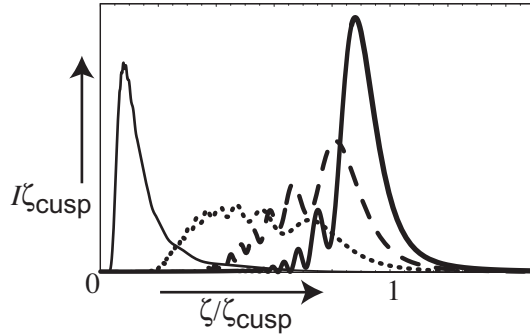


Figure 4.22: Cusp and spot competition: axial intensity from (4.2.51) for $\rho_0 = 100$, and γ equal to: 1/10 (thin), 1/2 (dotted), 1 (dashed), 2 (thick).

This behaviour can be understood in terms of the asymptotics of the error function. Labelling the arguments of the complementary error function in (4.2.51) as E^- and E^+ respectively, “ $\operatorname{erfc}(E^-) - \operatorname{erfc}(E^+)$ ” is an integral in the complex plane of the integrand e^{-t^2} from E^- to E^+ . For large ζ the endpoint E^+ is asymptotically close to the ‘wave line’ $\arg t = \pi/4$ and its contribution, decaying as $1/\zeta$, can be neglected. This endpoint contribution corresponds to the ray (κ_4 in section 4.2.3) originating on the ‘+’ sheet of the wave surface. For $0 \ll \zeta < \zeta_{\text{cusp}}$ the endpoint E^- is the dominant exponential in the asymptotic expansion of (4.2.51), (associated with the ray κ_1), but similarly to the non-chiral case (Berry 2004b) the axial intensity is dominated by the subdominant

exponential. The subdominant exponential comes from the integrand saddlepoint, where two rays (κ_2, κ_3) coalesce on the axial focus. This biaxial focal line with maximum at ζ_{spike} is the dominating axial feature for small γ . As ζ increases towards ζ_{cusp} the E^- endpoint contribution grows as $1/(\zeta_{\text{cusp}} - \zeta)$, then crosses a Stokes line which eliminates the saddlepoint contribution when $\zeta = \zeta_{\text{cusp}}$, and gives a $1/(\zeta - \zeta_{\text{cusp}})$ decay for $\zeta > \zeta_{\text{cusp}}$. If $\gamma > \sqrt{2/3}$, i.e. $\zeta_{\text{spike}} > \zeta_{\text{cusp}}$, the subdominant exponential never reaches its maximum, and the cusp becomes the dominating axial feature. These considerations are illustrated in figure 4.23, and embodied in the asymptotic expansion of the B_0 integral,

$$B_0(0, \zeta) \approx \frac{a_+}{\zeta} e^{-i\rho_0\gamma} + \frac{a_{\text{dom}}}{\zeta - \zeta_{\text{cusp}}} e^{i\rho_0\gamma} + \frac{a_{\text{sub}}}{\zeta^{3/2}} e^{j(\zeta)}, \quad \zeta \gg 1, \quad (4.2.52)$$

where

$$j(\zeta) = \frac{1}{2} \{ \gamma^2 z^{-1} (z - z^{-1}) + i(z + z^{-1}) \}, \quad z = \zeta/\zeta_{\text{cusp}} \quad (4.2.53)$$

To summarise more simply, the intensity at the cusp is of order $I(0, \zeta_{\text{cusp}}) \sim \frac{\pi\gamma^3}{4\rho_0}$, and the focal line maximum is of order $I(0, \zeta_{\text{spike}}) \sim \frac{\pi}{\rho_0} \left(\frac{3}{2}\right)^{3/4} e^{\frac{1}{2}\gamma^2 - \frac{3}{4}}$. The peak intensity from the focal line occurs at $\zeta \approx \sqrt{2/3}\rho_0$ and dominates over the cusp maximum for $\sqrt{2/3}\rho_0 < \rho_0/\gamma$, but for $\gamma > \sqrt{2/3}$ the spike never attains its maximum and the cusp dominates the axial intensity. Hence we can define a domain $\gamma > \sqrt{2/3}$, for which chirality dominates over biaxiality along the axis.

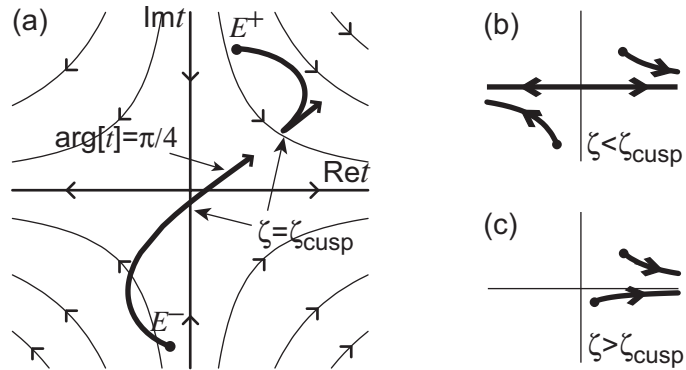


Figure 4.23: Stokes' phenomenon on the axis: loci of the endpoints E^\pm of the error function integral (4.2.51): (a), starting at $\zeta = 0$ and continuing to $\zeta = 10\zeta_{\text{cusp}}$, overlaying stationary phase contours of the integrand. Integration path includes: (b), 2 endpoints and a saddlepoint (responsible for axial focal line) when $\zeta < \zeta_{\text{cusp}}$, which vanishes in (c), as E^- crosses a Stokes line (imaginary t axis) when $\zeta > \zeta_{\text{cusp}}$.

4.2.7 Fringes near the focal plane

Historical interest in chiral conical diffraction has centred around the bright spiral of figure 1.4. This is observed at the exit face of the crystal, which is typically very close to the focal image plane, when the incident beam is linearly polarised. Figure 4.24 shows the evolution of the focal plane intensity profile with chirality for an unpolarised beam, from the two rings of Hamilton’s conical diffraction to the rings and central plateau of chiral conical diffraction. More intriguingly, figures 4.10 and 4.17 show that the interference fringes near the focal plane appear to be ζ independent, and for these a simpler analytic expression may be obtained that at last solves the problem of the historically irksome intensity spiral.

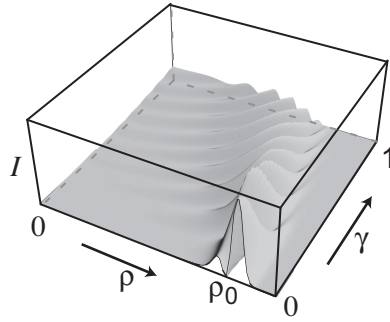


Figure 4.24: Focal image plane intensity profile varying with the optical activity γ

The geometric intensity obtained from (4.2.27), including wave effects, is valid down to the focal image plane and can be greatly simplified by approximating for small ζ . For this we consider strong chirality, $\gamma \gg 0$, away from the caustic, $\rho \ll \rho_0$, where the ray solutions are

$$\kappa_{1,3} \approx 0, \quad \kappa_{2,4} \approx \frac{\gamma\rho}{\sqrt{\rho_0^2 - \rho^2}}. \quad (4.2.54)$$

A set of spherical coordinates $\{\mathbf{u}, v\}$ will be useful, defined by

$$\mathbf{u} \equiv \frac{\boldsymbol{\rho}}{\rho_0}, \quad u^2 + v^2 = 1, \quad (4.2.55)$$

with which the geometrical approximation to leading order in ζ becomes

$$\begin{Bmatrix} B_0 \\ B_1 \\ B_2 \end{Bmatrix} \approx -\frac{\rho_0}{v^2 \zeta_{\text{cusp}}} e^{\frac{i\gamma^2 \zeta}{v^2}} a\left(\frac{\gamma u}{v}\right) \begin{Bmatrix} \sin(\rho_0 \gamma v) \\ u \sin(\rho_0 \gamma v) \\ -iv \cos(\rho_0 \gamma v) \end{Bmatrix}. \quad (4.2.56)$$

The propagation distance enters only as a phase, explaining the ζ independence of the intensity fringes. For an unpolarised incident beam the intensity of the rings is simply

$$I_{\text{unpol}}(u, 0) \approx \frac{1}{v^4 \zeta_{\text{cusp}}^2} \left| a \left(\frac{\gamma u}{v} \right) \right|^2 (1 - u^2 \cos 2\gamma \rho_0 v). \quad (4.2.57)$$

If we write a linear incident polarisation $\mathbf{d}_0 = \{d_{0x}, d_{0y}\}$ as a complex number $e^{i\chi} = d_{0x} + id_{0y}$, and use the representation (2.3.26), the near-focal plane polarisation is given by

$$\omega = \frac{e^{i(\chi - \frac{1}{2}\phi_{\boldsymbol{\rho}})} + e^{-i(\chi - \frac{1}{2}\phi_{\boldsymbol{\rho}})} (1 - iv \sin(\rho_0 \gamma v))}{e^{-i(\chi - \frac{1}{2}\phi_{\boldsymbol{\rho}})} + e^{i(\chi - \frac{1}{2}\phi_{\boldsymbol{\rho}})} (1 - iv \sin(\rho_0 \gamma v))} e^{i\phi_{\boldsymbol{\rho}}}. \quad (4.2.58)$$

For a linearly polarised incident beam, the swirl is given for $u \ll v \approx 1$ by

$$I_{\chi}(\mathbf{u}) \approx \frac{\left| a \left(\frac{\gamma u}{v} \right) \right|^2}{\zeta_{\text{cusp}}^2} \frac{1 - u^2 \cos 2\rho_0 \gamma v + 2u \sin \rho_0 \gamma v \sin(\rho_0 \gamma v - 2\chi + \phi_{\mathbf{u}})}{v^4}. \quad (4.2.59)$$

This is shown in figures 4.25(a)-(b), and compared to the exact intensity in figures 4.25(e)-(f). It also compares well to corresponding photographs taken by Schell & Bloembergen (1978*b*) and reproduced here in figure 1.4, which represents the only substantial experiment in chiral conical diffraction known to us. Taken from the exit face of an α -iodic acid crystal, their images are near-focal plane intensity patterns.

The spiral pattern is extracted from (4.2.59) by finding its radial maxima and minima. Considering only the trigonometric arguments to be fast varying, and neglecting the quadratic term for small u , the result is a pair of spirals,

$$\rho^2 = \rho_0^2 - \frac{1}{\gamma^2} \left(\frac{\pi n - \phi_{\boldsymbol{\rho}}}{2} + \chi \right)^2, \quad (4.2.60)$$

in terms of the azimuthal angle $\phi_{\boldsymbol{\rho}}$, with n odd and even giving respectively the bright (i.e. maximum) and dark (i.e. minimum) intensity spirals. These are shown overlaying the intensity in figures 4.25(c)-(d).

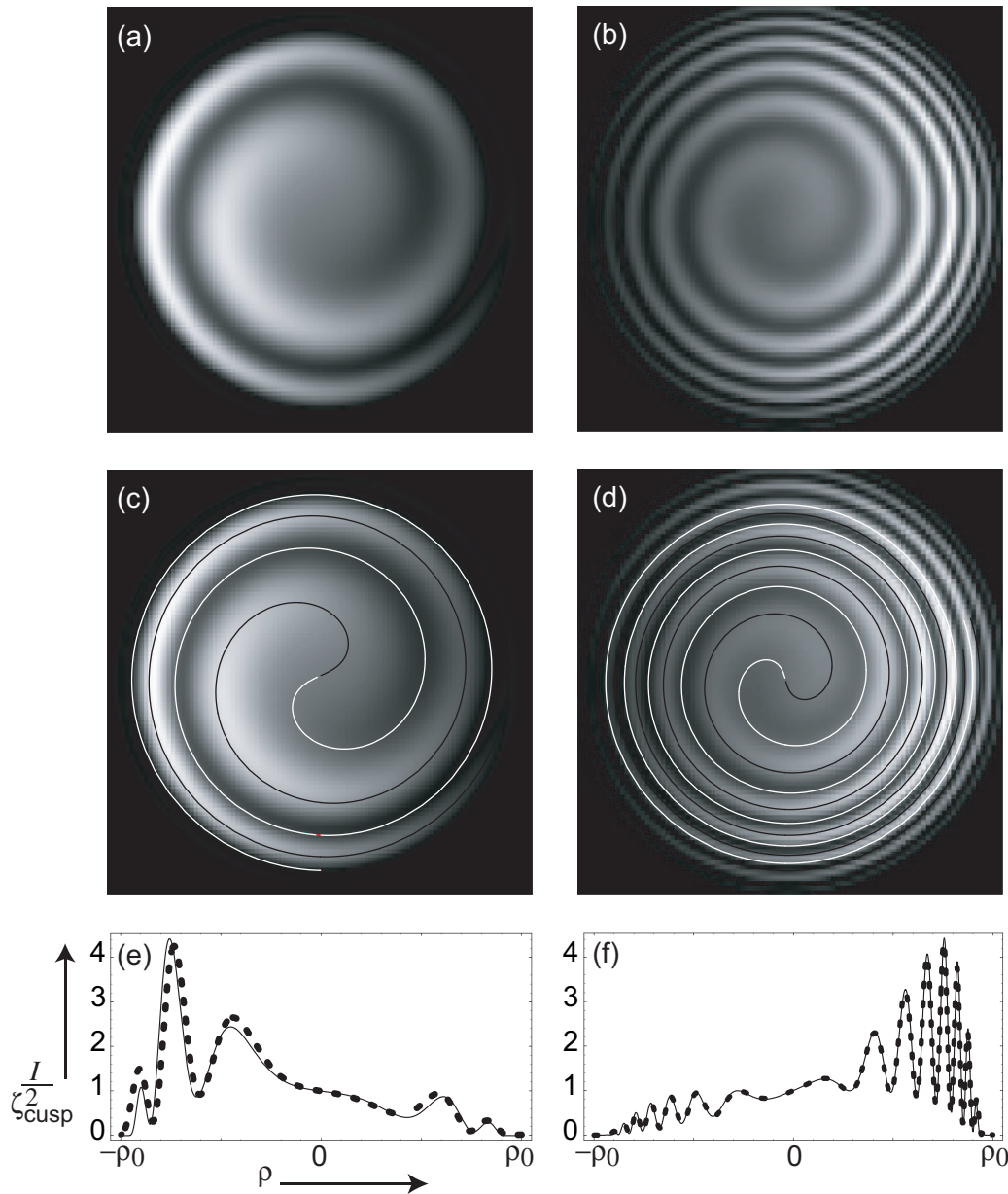


Figure 4.25: The chiral conical diffraction coffee swirl: theoretical focal image plane intensity corresponding to figure 1.4, for: (a) vertically polarised gaussian incident beam calculated from (4.2.57) with $\rho_0 = 10$ and $\gamma = 1$; and (b) horizontally polarised incident gaussian beam calculated from (4.2.59) with $\rho_0 = 30$ and $\gamma = 1.2$. These compare well to the experimental images. (c-d) correspond to (a-b) with bright maximum (black) and dark minimum (white) spirals (4.2.60) overlaid. (e-f) are horizontal axis profiles corresponding to (a-b), comparing the approximation (dots) to the exact calculated from the integrals (4.2.5).

4.3 Dichroic Biaxial Crystals

Let us now forget optical activity, setting $\gamma = 0$, and consider the effect of dichroism on conical diffraction.

Dichroism is the anisotropic absorption of light dependent upon polarisation. We will consider only linear dichroism, though the principles can be easily extended to include circular dichroism and we will make a few remarks on that case. We specify the maximal attenuation of a linearly polarised plane wave propagating along the optic axis by a parameter δ , along a preferential direction, constituting a vector $\boldsymbol{\delta}$.

We define a convenient scaling so that the maximal attenuation is $\rho_0\delta$, then by choosing coordinates in which $\boldsymbol{\delta} = \{\delta, 0\}$, the total effect of dichroism on a plane wave can be written in terms of a nonhermitian symmetric matrix \mathcal{F}^d as

$$\mathbf{D} = e^{-i\mathcal{F}^d} \mathbf{d}_0 = \begin{pmatrix} e^{-\rho_0\delta} & 0 \\ 0 & e^{\rho_0\delta} \end{pmatrix} \mathbf{d}_0, \quad (4.3.1)$$

uniquely determining \mathcal{F}^d up to a trace as

$$\mathcal{F}^d = -i\rho_0\delta\sigma_3 = -i\rho_0\boldsymbol{\delta} \cdot \{\sigma_3, \sigma_1\}, \quad (4.3.2)$$

where the second equality implies the extension to general coordinates.

This paraxial model assumes absorption in the crystal is only weakly anisotropic, which is reasonable for conical diffraction to be observable. It assumes also that the optic axes of biaxiality and dichroism, or the degeneracies of the real symmetric (2.1.2) and nonhermitian (2.1.9) parts of the dielectric tensor, are distinct. This is true in general. Coincidence of these directions would require the next order correction to the paraxial dichroism theory, constituting a complex cone radius ρ_0 . We will not consider this very special situation which does not fundamentally alter the resulting theory, but at the end of this section we will briefly consider the extreme case, in which dichroic anisotropy dominates over birefringent anisotropy and Hamilton's cone becomes imaginary.

Combined with biaxiality the paraxial effect of the crystal is therefore

$$\mathcal{F}^{\text{tr}}(\tilde{\boldsymbol{\kappa}}) = \rho_0\tilde{\boldsymbol{\kappa}} \cdot \{\sigma_3, \sigma_1\} = \mathbf{V}(\tilde{\boldsymbol{\kappa}}) \cdot \boldsymbol{\Sigma}, \quad (4.3.3)$$

in terms of the complex transverse wavevector $\tilde{\boldsymbol{\kappa}} = \boldsymbol{\kappa} - i\boldsymbol{\delta}$. Using the complexifying transformations (2.4.1) to (2.4.4), the propagator integral is obtained from the transparent

result (4.1.2) by the transformation $\mathbf{D}(\boldsymbol{\rho}, \zeta) \rightarrow e^{-i\mathcal{F}_0} \mathbf{D}(\tilde{\boldsymbol{\rho}}, \zeta)$, giving

$$\mathbf{D}(\tilde{\boldsymbol{\rho}}, \zeta) = e^{-i\mathcal{F}_0} [b_+(\tilde{\boldsymbol{\rho}}, \zeta) \mathcal{D}_+(\tilde{\boldsymbol{\rho}}, \zeta) + b_-(\tilde{\boldsymbol{\rho}}, \zeta) \mathcal{D}_-(\tilde{\boldsymbol{\rho}}, \zeta)] \mathbf{d}_0, \quad (4.3.4)$$

in terms of the diffraction integrals defined by (4.1.4). When discussing a gaussian incident beam we will instead use the complexifying transformations (2.4.1)-(2.4.2) and (2.4.7)-(2.4.10), and thus obtain the propagator integral from the transparent result by the transformation $\mathbf{D}(\boldsymbol{\rho}, \zeta) \rightarrow e^{-i\mathcal{F}_0} \mathbf{D}(\tilde{\boldsymbol{\rho}}, \tilde{\zeta})$, which gives

$$\mathbf{D}(\tilde{\boldsymbol{\rho}}, \tilde{\zeta}) = e^{-i\mathcal{F}_0} [b_+(\tilde{\boldsymbol{\rho}}, \tilde{\zeta}) \mathcal{D}_+(\tilde{\boldsymbol{\rho}}, \tilde{\zeta}) + b_-(\tilde{\boldsymbol{\rho}}, \tilde{\zeta}) \mathcal{D}_-(\tilde{\boldsymbol{\rho}}, \tilde{\zeta})] \mathbf{d}_0. \quad (4.3.5)$$

The breaking of circular symmetry by dichroism is an obstacle to numerical or analytic investigation of the diffraction integrals $b_{\pm}(\tilde{\boldsymbol{\rho}}, \zeta)$. Slow convergence of the two dimensional integrals (4.1.4) prevents any exact simulations for a pinhole beam being presented here, and our investigation will have to rely on asymptotic techniques. This will be remedied in section 4.3.3 for a gaussian beam, where the complex ray representation allows us to restate the integrals in the exact circularly symmetric form (4.1.5).

The eigenpolarisations in the emergent light field, $\mathbf{d}_{\uparrow\downarrow}(\tilde{\boldsymbol{\rho}})$ defined by (2.3.25), are in general elliptical, nonorthogonal, and are normalised only according to our definition (2.1.18) of the length of a complex vector.

The emergent light intensity is given by

$$I = e^{2\text{Im}\mathcal{F}_0} \left\{ \left(|b_+|^2 |\mathbf{d}_0 \cdot \mathbf{d}_+|^2 + |b_-|^2 |\mathbf{d}_0 \cdot \mathbf{d}_-|^2 \right) \left(|\cos \frac{1}{2} \phi_{\tilde{\boldsymbol{\rho}}}|^2 + |\sin \frac{1}{2} \phi_{\tilde{\boldsymbol{\rho}}}|^2 \right) + 2\text{Re} [b_+ b_-^* (\mathbf{d}_0 \cdot \mathbf{d}_+) (\mathbf{d}_0 \cdot \mathbf{d}_-)^* \mathbf{d}_+ \cdot \mathbf{d}_-^*] \right\}. \quad (4.3.6)$$

We will be concerned with an unpolarised incident beam, for which

$$I_{\text{unpol}} = e^{2\text{Im}\mathcal{F}_0} \left\{ \frac{|b_+|^2 + |b_-|^2}{2} \cosh^2 \text{Im}\Phi_{\tilde{\boldsymbol{\rho}}} - \text{Re} [b_+ b_-^*] \sinh^2 \text{Im}\Phi_{\tilde{\boldsymbol{\rho}}} \right\}. \quad (4.3.7)$$

For a circularly polarised incident beam this becomes

$$I_{\pm} = e^{\text{Im}[2\mathcal{F}_0 \mp \Phi_{\tilde{\boldsymbol{\rho}}}] \left\{ \frac{|b_+|^2 + |b_-|^2}{2} \cosh \text{Im}\Phi_{\tilde{\boldsymbol{\rho}}} \pm \text{Re} [b_+ b_-^*] \sinh \text{Im}\Phi_{\tilde{\boldsymbol{\rho}}} \right\}, \quad (4.3.8)$$

and for a linearly polarised incident beam with orientation angle χ ,

$$I_{\chi} = I_{\text{unpol}} + e^{2\text{Im}\mathcal{F}_0} \times \left\{ \frac{|b_+|^2 - |b_-|^2}{2} \text{Re} [\cos(2\chi - \phi_{\tilde{\boldsymbol{\rho}}})] - \text{Im} [b_+ b_-^*] \text{Im} [\cos(2\chi - \phi_{\tilde{\boldsymbol{\rho}}})] \right\}. \quad (4.3.9)$$

It is convenient to use coordinates in which the complexifying vector $\boldsymbol{\mu}$ ((2.4.3) or (2.4.8)) lies along the horizontal μ -axis, defining $\boldsymbol{\rho} = \{\rho_\mu, \rho_\nu\}$ such that

$$\tilde{\boldsymbol{\rho}} = \{\rho_\mu - i\mu, \rho_\nu\} = \sqrt{(\rho_\mu - i\mu)^2 + \rho_\nu^2} \{\cos \phi_{\tilde{\boldsymbol{\rho}}}, \sin \phi_{\tilde{\boldsymbol{\rho}}}\}, \quad (4.3.10)$$

which we will use for simulations. Note that the angle $\phi_{\tilde{\boldsymbol{\rho}}}$ is a complex number.

Note importantly that the diffractive effects of dichroism enter solely via the complexification $\boldsymbol{\rho} \rightarrow \boldsymbol{\rho} - i\zeta\boldsymbol{\delta}$, and therefore vanish in the focal image plane $\zeta = 0$.

4.3.1 Conical refraction complexified

The optical path length in a dichroic crystal is complex, with a $\tilde{\boldsymbol{\kappa}}$ dependent part

$$\Phi_\pm(\tilde{\boldsymbol{\kappa}}) = -\tilde{\boldsymbol{\kappa}} \cdot \tilde{\boldsymbol{\rho}} + \frac{1}{2}\zeta\tilde{\kappa}^2 \pm \rho_0\tilde{\kappa}, \quad (4.3.11)$$

and a constant Φ_0 given by (2.4.12). Hamilton's principle gives complex rays

$$\tilde{\boldsymbol{\kappa}}_\pm = \frac{\tilde{\boldsymbol{\rho}} \pm \rho_0}{\zeta\tilde{\rho}} \tilde{\boldsymbol{\rho}}. \quad (4.3.12)$$

Note that the complexified wave $\tilde{\boldsymbol{\kappa}}$ and position $\tilde{\boldsymbol{\rho}}$ vectors are parallel, but the original wave $\boldsymbol{\kappa}$ and position $\boldsymbol{\rho}$ vectors are not, being related by

$$\boldsymbol{\kappa}_\pm = \frac{\tilde{\boldsymbol{\rho}} \pm \rho_0}{\zeta\tilde{\rho}} \boldsymbol{\rho} - i\boldsymbol{\epsilon}, \quad (4.3.13)$$

where $\boldsymbol{\epsilon} = \pm \frac{\rho_0}{\tilde{\rho}}\boldsymbol{\delta}$ for a general beam, or for a gaussian beam misaligned from the optic axis, $\boldsymbol{\epsilon} = \boldsymbol{\kappa}_0 \pm \frac{\rho_0}{\tilde{\rho}}(\tilde{\zeta}\boldsymbol{\delta} + \boldsymbol{\kappa}_0)$. Also, this solution for $\boldsymbol{\kappa}$ is itself generally complex for real $\boldsymbol{\rho}$, so we must abandon the notion of real wavevectors in an absorbing medium.

The formulae derived for transparent crystals in section 4.1 now apply but with the complexified variables substituted in. Focusing occurs where the complexified determinant (4.1.12) vanishes, with two solutions: in the focal image plane $\zeta = 0$ we expect the focused image of the beam source, and axial focusing now occurs along the branch points of the complex transverse position vector, which we call the *branch axes*,

$$\tilde{\boldsymbol{\rho}} = 0 \quad \Rightarrow \quad \boldsymbol{\rho} = \boldsymbol{\rho}_b \equiv \pm \mathbf{e}_3 \times \boldsymbol{\mu}. \quad (4.3.14)$$

Thus the familiar bright axial spike is spread out along a branch cut of $\tilde{\boldsymbol{\rho}}$. Antifocusing will occur where $|\tilde{\rho} - \rho_0|$, or equivalently $\tilde{\kappa}$, vanishes. This is the direction in which Φ is degenerate, the singular axes (3.2.7), given in complex position space by $\tilde{\boldsymbol{\rho}} = \rho_0$. In a

transparent medium this corresponded to the conical point and Hamilton’s conical infinity of rays, but in the presence of dichroism it corresponds to only two real rays,

$$\tilde{\kappa} = 0 \quad \Rightarrow \quad \rho_s = \pm \mathbf{e}_3 \times \hat{\boldsymbol{\mu}} \sqrt{\rho_0^2 + \mu^2}, \quad (4.3.15)$$

scattered from the branch points of the complex wave surface, complexifying Hamilton’s dark anti-focal ring. This underlying geometry is illustrated in Figure 4.26.

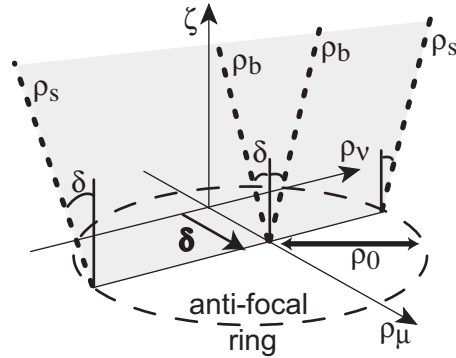


Figure 4.26: Loci of critical points of dichroic conical refraction in real space, showing: ρ_b , the branch axes where $\tilde{\rho} = 0$, and ρ_s , the rays scattered from the singular axes where $\tilde{\kappa} = 0$. For a gaussian incident beam Hamilton’s dark ring is shifted by the dichroism vector δ .

The geometric intensity is just the sum of magnitudes (4.1.11) in complexified variables modulated by an exponential absorption factor,

$$e^{-2\text{Im}\mathcal{F}_0} I = \frac{1}{2} \sum_{\pm} |b_{\pm}|^2 = \frac{e^{-\text{Im} \frac{\tilde{\rho}^2 + \rho_0^2}{\zeta}}}{2|\tilde{\rho}\zeta^2|} \sum_{\pm} e^{\pm 2\rho_0 \text{Im} \frac{\tilde{\rho}}{\zeta}} |\tilde{\rho} \pm \rho_0| \left| a \left(\frac{\tilde{\rho} \pm \rho_0}{\zeta} \right) \right|^2. \quad (4.3.16)$$

There are no Stokes sets (2.6.7), so the two ray solutions (4.3.12) exist everywhere. More important than focusing or antifocusing in an absorbing medium are the anti-Stokes sets (2.6.9), where the ‘ \pm ’ parts of (4.3.16) are equal, whose solution is simply

$$\text{Im} \tilde{\rho} = 0 \quad \Rightarrow \quad \boldsymbol{\rho} \cdot \boldsymbol{\mu} = 0 \text{ and } \rho > \mu. \quad (4.3.17)$$

This pair of half planes extend from the branch axes $\boldsymbol{\rho}_b$ outward in the ρ_v plane. They are the surfaces on which the two complex ray solutions have equal magnitude and exchange dominance. Since one ray contribution is exponentially increasing on either side of the set, the planes are exponentially darker than the surrounding regions and manifest as a

pair of dark brushes. Near the branch axes we can approximate the intensity for small $\tilde{\rho}$,

$$\frac{1}{2} \sum_{\pm} |b_{\pm}|^2 \approx \frac{\rho_0 e^{-\text{Im} \frac{\tilde{\rho}^2 + \rho_0^2}{\zeta}}}{|\tilde{\rho} \zeta^2|} \cosh \left(2\rho_0 \text{Im} \frac{\tilde{\rho}}{\zeta} \right) \left| a \left(\frac{\rho_0}{\zeta} \right) \right|^2, \quad (4.3.18)$$

from which it is clear that on the anti-Stokes surfaces the hyperbolic cosine is a minimum, yielding dark brushes.

Figure 4.27(a) shows the regions of dominance of the two ray contributions b_{\pm} , which swap across the anti-Stokes lines, visible along the ρ_{ν} axis as dark brushes separated by the bright branch cut. Figure 4.27(b) shows the corresponding regions special to a gaussian incident beam, which will be considered in section 4.3.3.

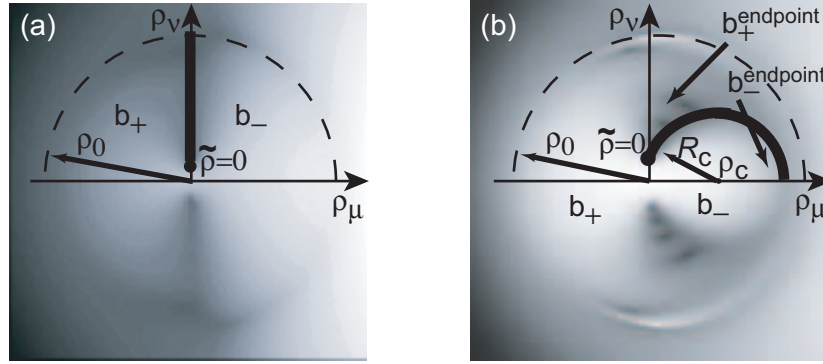


Figure 4.27: Dominant asymptotics of dichroic conical diffraction for (a) pinhole, and (b) gaussian, incident beam. Anti-Stokes lines (bold) – straight (4.3.17) in (a) and circular (4.3.28) in (b) – bound regions dominated by the two geometric rays b_{\pm} . The boundaries are completed by a branch cut connecting the branch axes $\tilde{\rho} = 0$. The dashed circle is Hamilton's ring. Regions where endpoint waves (sections 4.3.2 & 4.3.3) are significant are indicated. In the background is the corresponding logarithmic intensity, symmetric in ρ_{ν} , for $\rho_0 = 20$, $\mu = 5$.

4.3.2 Complex geometric interference

The diffraction integrals $b_{\pm}(\tilde{\rho}, \zeta)$ can be expressed in terms of the asymptotic ring function f defined by (4.1.19), which was derived by approximating the Bessel functions for large argument. Stationary phase analysis proceeds as in the transparent case, and the asymptotic expansion (4.1.22-4.1.23) applies directly.

Consider first only the saddlepoint terms, which endow the b_{\pm} geometric rays with phases. These phases cause geometric interference, which is greatest along the anti-Stokes

surfaces where $|b_+| = |b_-|$. Complete destructive interference requires also the equality of phases, $\arg b_+ = \arg b_-$, giving

$$e^{-2i\rho_0\tilde{\rho}/\zeta} = -i, \quad (4.3.19)$$

the solutions of which are a series of dark lines,

$$\operatorname{Re}\frac{\tilde{\rho}}{\zeta} = \frac{\pi}{\rho_0} \left(n + \frac{1}{4}\right), \quad n \in \mathbb{Z}^+, \quad (4.3.20)$$

lacing the dark brush anti-Stokes planes. The source of this interference must appear in the vector intensity (4.3.7). Far from the branch axes we have $\cosh^2 \operatorname{Im}\phi_{\tilde{\rho}} \approx 1$ and $\sinh^2 \operatorname{Im}\phi_{\tilde{\rho}} \approx 0$, so only the geometric sum of magnitudes (4.3.16) is significant. Near the branch axes however, both of these hyperbolic terms are large and we can approximate

$$\cosh^2 \operatorname{Im}\phi_{\tilde{\rho}} \approx \frac{1}{2} + \frac{\mu^2}{|\tilde{\rho}|^2}, \quad \sinh^2 \operatorname{Im}\phi_{\tilde{\rho}} \approx \frac{1}{2} - \frac{\mu^2}{|\tilde{\rho}|^2}, \quad |\tilde{\rho}| \ll 1. \quad (4.3.21)$$

The geometric interference term then becomes significant and for small $\tilde{\rho}$ is

$$\operatorname{Re}b_+b_-^* \approx \frac{\rho_0}{2|\tilde{\rho}\zeta^2|} \left| a \left(\frac{\rho_0}{\zeta} \right) \right|^2 e^{-\operatorname{Im}\frac{\tilde{\rho}^2 + \rho_0^2}{\zeta}} \sin \left(2\rho_0 \operatorname{Re}\frac{\tilde{\rho}}{\zeta} \right). \quad (4.3.22)$$

The dark interference spots are evident as maxima of the sine function, where the interference term gives the greatest drop in the intensity. The intensity approaches zero on the lines (4.3.17) and they manifest as C (circular polarisation) points.

Now consider the endpoint wave contribution to $b_+(\tilde{\rho}, \zeta)$, the last term in (4.1.22), which causes interference rings in transparent crystals. This is now a wave scattered from the singular axes $\tilde{\mathbf{k}} = 0$, diverging at the complexified Hamilton dark ring $\tilde{\rho} = \rho_0$ (the pair of wavevector branch points (4.3.15)). Figure 4.28 shows the intensity (4.3.7) for a

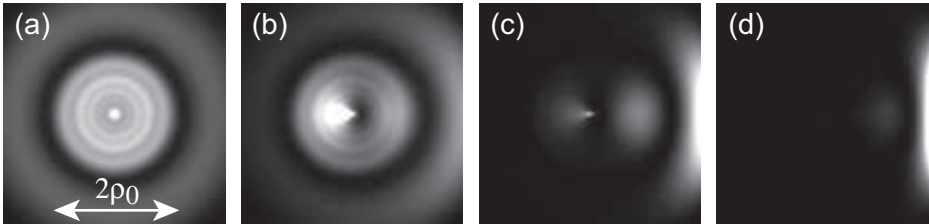


Figure 4.28: Transition from transparent to dichroic conical diffraction for a pinhole incident beam; intensity calculated using uniform approximation (4.1.38) for $\rho_0 = 20$, $\zeta = 6$, and dichroism δ directed to the right with $\mu = \delta\zeta$ equal to: (a) 0, (b) 1/2, (c) 1, (d) 2.

pinhole beam, in terms of the diffraction integrals given by (4.1.19), and we remove the above divergence by using the uniform saddlepoint approximation (4.1.38). We do not include the exponential ramp from \mathcal{F}_0 , whose effect would be an exponential horizontal modulation of the intensity; this simple effect was remarked on in section 2.4. Even without this exponential ramp the dichroic intensity is dominated by exponential gradients. In the absence of dichroism the geometric bright rings separated by the Hamilton dark ring can be clearly seen, with interference fringes on the inner ring from the endpoint of the diffraction integral. These features are quickly destroyed by dichroism, and leave in their place localised bright spots.

Figure 4.29 shows the rich structure revealed by a logarithmic intensity plot. Dichroism introduces the dark geometric brushes (4.3.17) visible along the vertical axis. Connecting them is the bright axial spot spreading between the branch axes (4.3.14). Eventually this brush dominates the intensity, overwhelming the dark antifocal ring. A magnification near a branch axis shows the dark spots (4.3.20) of complex geometric interference, and the divergence at the branch axes is visible only under much greater magnification.

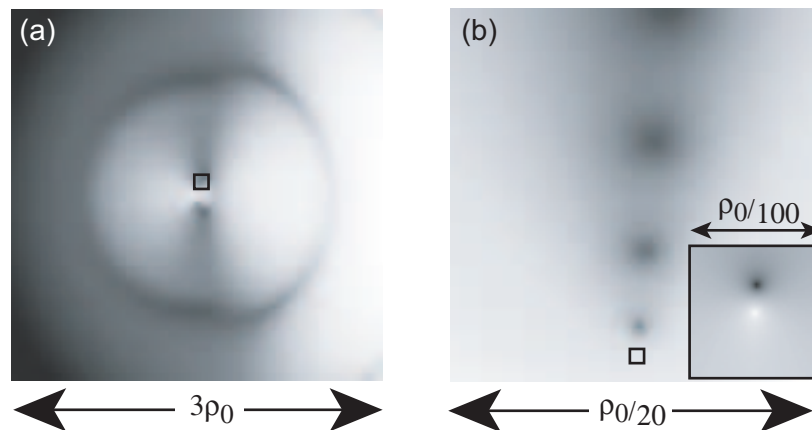


Figure 4.29: Complex ray interference for a pinhole incident beam: (a) is a logarithmic plot of intensity for $\rho_0 = 20$, $\zeta = 6$, and $\delta = 1$ showing the dark anti-Stokes brush (4.3.17), indicating a region near one branch axis, enlarged in (b), showing the dark spots (4.3.20) of interference between two complex rays, including a further enlargement around the branch axis which shows the highly localised divergence of this geometric approximation.

We can study the exponential intensity gradients in more detail along the ρ_μ axis, where they are most severe. From the asymptotics of the two different ray contributions, we have near the ρ_ν axis

$$e^{-\frac{\text{Re}(\tilde{\rho} \pm \rho_0)^2}{\zeta^2}} \approx e^{2\delta(\rho_\mu \mp \text{sgn}\rho_\mu)}, \quad \rho_\nu \approx 0, \quad (4.3.23)$$

showing a ramp $e^{2\delta\rho_\mu}$, greater than that of the $e^{-\delta\rho_\mu}$ prefactor from \mathcal{F}_0 . The ‘ \pm ’ condition reflects the swapping of b_+ and b_- across the branch cut between the branch axes. Further from the axis,

$$e^{-\frac{\text{Re}(\tilde{\rho} - \rho_0)^2}{\zeta^2}} \approx e^{\delta\left(2 - \left(\frac{\rho_\mu}{\delta\zeta}\right)^2\right)}, \quad \rho_\mu \ll \rho_\nu \ll \delta\zeta, \quad (4.3.24)$$

reflects the exponential gradient near the anti-Stokes surface.

In the region of the well developed rings $|\rho - \rho_0| \ll \sqrt{\zeta}$, the polarisation retains the same structure as transparent conical diffraction,

$$\frac{D_y}{D_x} \approx \tan \frac{1}{2}\phi_{\tilde{\rho}} \approx \tan \frac{1}{2}\phi_{\rho}, \quad \omega \approx e^{-i\phi_{\tilde{\rho}}} \approx e^{-i\phi_{\rho}}. \quad (4.3.25)$$

To this we can add a first correction from the asymptotic expansion of b_\pm , giving for $\rho \gg \mu$,

$$\frac{D_y}{D_x} \approx \left(1 - i\frac{\mu}{2\tilde{\rho}} \sec^2 \frac{1}{2}\phi_{\tilde{\rho}}\right) \tan \frac{1}{2}\phi_{\tilde{\rho}}. \quad (4.3.26)$$

The polarisation differs from the transparent pattern most greatly near the anti-Stokes surface (4.3.17), becoming quite intricate, and we will not study it further here.

4.3.3 Gaussian beams and the transition to double refraction

It was shown in section 2.4 that, for a gaussian beam, dichroism and beam misalignment are described by the single parameter μ defined by (2.4.8). Figure 4.30 shows the uniform saddlepoint approximation for the intensity with a gaussian incident beam, that is, the intensity (4.3.7) with the diffraction integrals given by (4.1.19) and (4.1.38), subject to the gaussian complexification (2.4.7). As μ increases it is seen that, under either dichroism or deflection from the optic axis, the diffracted beam undergoes transition from conical diffraction to double refraction.

For a gaussian incident beam the transformation to complex propagation distance $\tilde{\zeta}$ dramatically alters the form of the anti-Stokes surface. We cannot omit ζ from the condition (4.3.17) on the *cosh* argument, giving instead

$$\text{Im} \frac{\tilde{\rho}}{\tilde{\zeta}} = 0 \quad \Rightarrow \quad |\rho - \rho_c|^2 = R_c^2 \quad \text{and} \quad \mu\rho_\mu \geq 0, \quad (4.3.27)$$

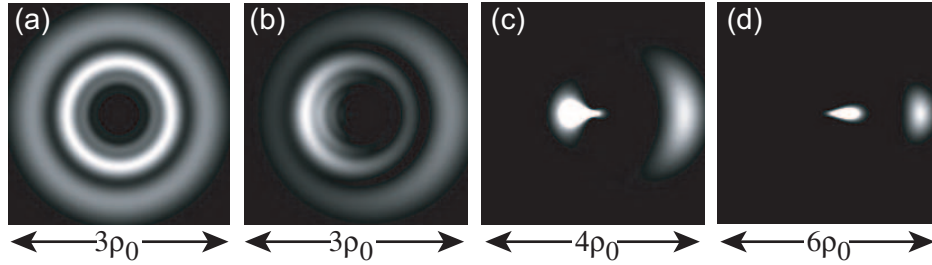


Figure 4.30: Transition from conical diffraction (a,e) to double refraction (d,h) for a gaussian incident beam: intensity calculated from approximation (4.1.38) for $\rho_0 = 20$, $\zeta = 6$, and nonhermiticity μ directed to the right with magnitude equal to: (a) 0, (b) 1/2, (c) 2, (d) 5.

a circular ring with centre ρ_c and radius R_c given by

$$\rho_c = \frac{1}{2\zeta} (\zeta^2 - 1) \mu, \quad R_c = \frac{\mu}{2\zeta} (\zeta^2 + 1), \quad (4.3.28)$$

with the arc joining the branch axes omitted. Expression (4.3.18) for the intensity near the branch axes has been written in a form that implies its extension to gaussian incident beams via $\zeta \rightarrow \tilde{\zeta}$. The anti-Stokes set corresponds to a minimum in the geometric intensity, a dark ring interrupted by the bright cut joining the branch axes. Near the focal plane the geometrical approximation, and this geometrical ring, diverge. For $\zeta \gg 1$ the ring grows linearly with ζ , sweeping out a funnel-like dark surface in the three dimensional intensity. The logarithmic intensity plot in figure 4.31(a) clearly shows this manifesting as a dark ring in a far field plane.

In the far field $\zeta \gg 1$ we have seen (section 4.1.4) that even for a gaussian beam we can treat the beam profile as slowly varying. The dark anti-Stokes ring (4.3.27) derived here for a gaussian beam, obtained by including the beam profile as a fast varying term in the phase, should be consistent at large ζ with the more general, but less accurate, result of dark anti-Stokes brushes (4.3.17). Indeed, as ζ becomes very large the radius of the dark ring (4.3.28) becomes large and most of the ring exists at radii far outside the region of interest, leaving only two arcs extending from the branch axes which tend asymptotically towards the planar form of the dark brushes.

Again the anti-Stokes surface is the site of maximal interference between the two sets of complex rays, and is laced by a set of dark lines given by replacing $\zeta \rightarrow \tilde{\zeta}$ in (4.3.20), originating in the maxima of the corresponding sine function in the complexified (4.3.22).

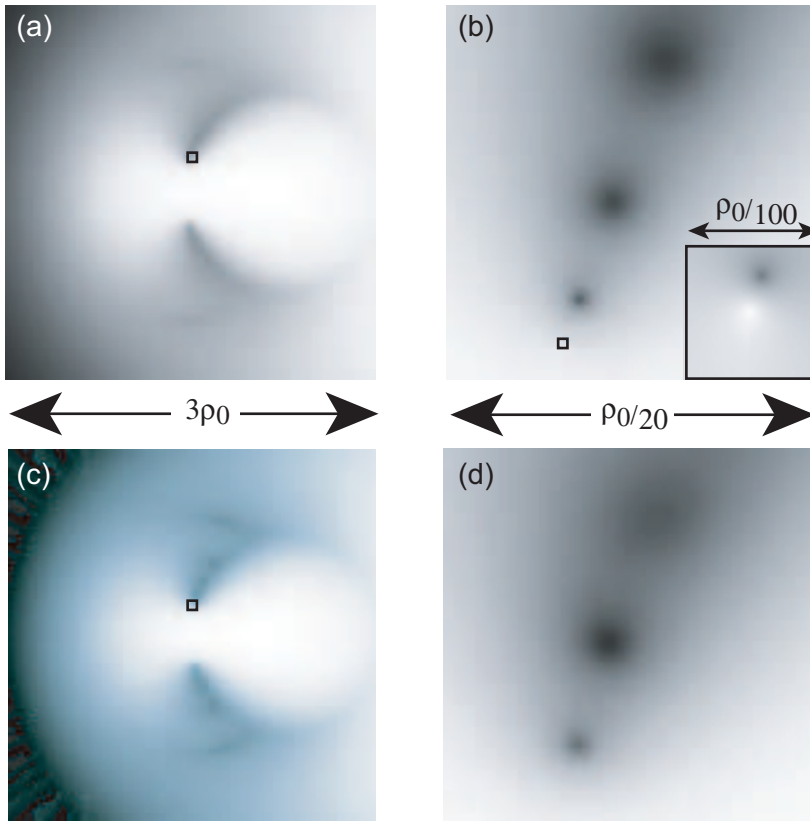


Figure 4.31: Complex ray interference for a gaussian incident beam: (a) is a logarithmic plot of Figure 4.30(d) revealing the dark adsorption ring (4.3.28), indicating a region near one $\tilde{\rho}$ branch axis, enlarged in (b), showing the dark spots (4.3.20) of interference between two complex rays, including a further enlargement of the branch axis which shows the highly localised divergence of this geometric approximation. (c-d) are the corresponding images calculated from the exact integrals, showing that the branch axis divergence is smoothed away by diffraction.

In a constant ζ plane, such as an image screen, these appear as darker spots decorating the already dark ring, shown in figure 4.31(b). The exact wave intensity from the diffraction integrals $b_{\pm}(\tilde{\rho}, \tilde{\zeta})$ defined by (4.1.5) is also shown in figure 4.31, agreeing very closely with the geometric images.

Figure 4.27(b) shows the exchange of regions of dominance across this anti-Stokes surface, which typically dominates the light intensity. This saddlepoint approximation, which in transparent crystals only describes the well developed rings and suffers linear

focal divergence near the axis, is very much more powerful in the presence of dichroism. The divergences still exist, but in the presence of exponential intensity gradients they become less significant, and in a logarithmic plot they appear highly localised. The effect is not only qualitative, indeed we have already seen in figure 4.31 in the axial region the geometric approximation correctly describes the ring and spots of interference, diverging only in a small neighborhood of the branch axes.

Somewhat surprisingly, this accuracy of the geometric approximation in the presence of dichroism allows it to describe the axial shoulders – faint interference rings decorating the axial spike – given in a transparent medium by (4.1.42), and here manifesting as the dark lines (4.3.20). Figure 4.32 shows the exact and geometric intensity profiles of the interference spots along the ρ_ν axis. Notice the extreme localisation of the geometric branch axis divergence at $\rho_\nu = 5$. The complexification of approximation (4.1.42) is also shown, and captures only the first few oscillations. As dichroism decreases, these well defined maxima and minima give way gradually to the flat shoulders characteristic of the transparent biaxial diffraction rings.

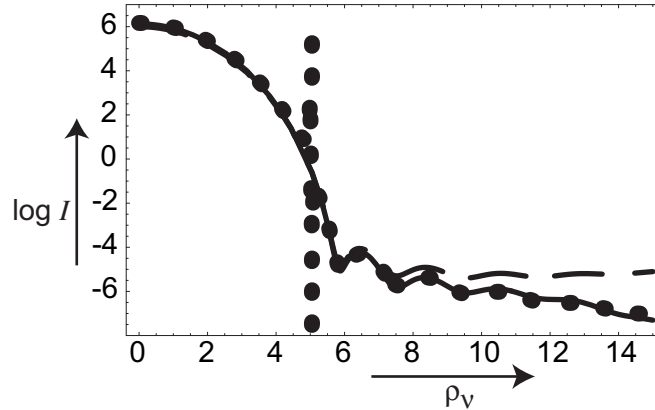


Figure 4.32: Dichroic spots and Bessel shoulders: intensity plotted along the ρ_ν axis with $\rho_0 = 20$, $\zeta = 16$, $\mu = 5$, dark spots of complex ray interference in the geometric intensity (dots) from (4.3.18) correspond to Bessel shoulders from the axial spike approximation (dashed) from (4.1.42); plotted against exact intensity (full curve).

Some discrepancy can be seen between exact and geometric intensities in figure 4.31(a)&(c) that is not attributable to singularities, and this is the effect of wave interference. Figure 4.33(d) shows this more clearly: the remnants of the secondary inner rings are visible out-

side the anti-Stokes ring. This occurs in the region of b_+ dominance and, as in transparent crystals, originates from the endpoint of the b_+ $(\tilde{\rho}, \tilde{\zeta})$ integral, the second term in the expansion of b_+ $(\tilde{\rho}, \tilde{\zeta})$ given by (4.1.22). Figure 4.33(a) shows that the inclusion of this term correctly captures the wave interference, at the expense of introducing divergence at the branch points of $\tilde{\kappa}$, at the intersection of the Hamilton dark ring and the ρ_ν axis.

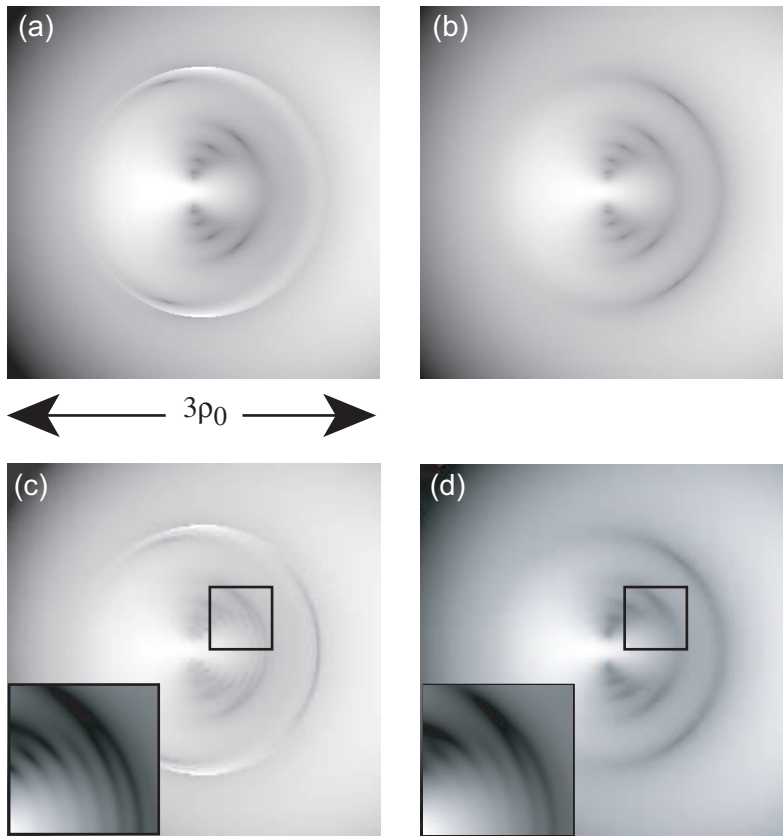


Figure 4.33: Endpoint interference for a gaussian beam: logarithmic plots corresponding to Figure 4.30(c) revealing the dark anti-Stokes ring (4.3.28) decorated by interference. (a), geometric intensity including the two rays and the endpoint from (4.1.22), showing the remnants of the transparent-crystal secondary diffraction rings; (b) uniform approximation (4.1.39) smoothing away the geometric focusing divergences at $\tilde{\rho} = 0$ and the complexified Poggendorff ring (4.3.15); (c) geometric intensity including also the higher order endpoint (4.3.30), giving new interference revealed in the enlargement; (d) exact intensity, showing the dark ring, secondary ring arcs, and higher order interference.

Closer inspection of 4.33(d) reveals very faint oscillations inside the anti-Stokes ring, shown magnified, whose location means they must originate in the b_- integral. In the asymptotic expansion (4.1.23) the leading order endpoint contribution of b_- vanishes. To find the first correction we must return to approximation (4.1.18) for the Bessel functions in the diffraction integrals, and include the next order term:

$$J_n(x) \approx \sqrt{\frac{2}{\pi x}} \left[\cos\left(x - \frac{\pi(1+2n)}{4}\right) - \frac{1+2n}{8x} \sin\left(x - \frac{\pi(1+2n)}{4}\right) \right]. \quad (4.3.29)$$

The result, like the endpoint of b_+ , depends on the quantity $s_+ = (\tilde{\rho} - \rho_0)/\tilde{\zeta}$ rather than $s_- = (\tilde{\rho} + \rho_0)/\tilde{\zeta}$, and gives

$$\sqrt{\tilde{\rho}} (i\tilde{\zeta})^{3/4} b_- (\tilde{\rho}, \tilde{\zeta}) \approx e^{-\frac{1}{2}s_-^2} \sqrt{s_-} - \frac{i\tilde{\zeta} T[-\text{Res}_+]}{2\tilde{\rho}\sqrt{-2s_+}}. \quad (4.3.30)$$

Figure 4.33(c) shows that this captures the higher order oscillations, and figure 4.34 shows how very accurately it does so.

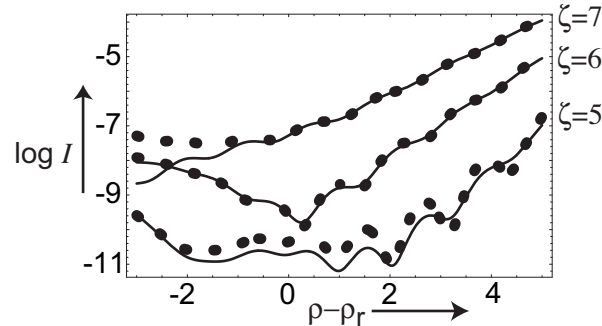


Figure 4.34: Higher order interference fringes: comparison of the approximation (4.3.30) (dots) to the exact intensity (full curve) for $\rho_0 = 20$ and $\mu = 2$, along the ρ_μ axis in the vicinity of the dark adsorption ring, where higher order endpoint interference is visible. The dark anti-Stokes ring crosses the ρ_μ axis at ρ_r .

The most severe divergence of the asymptotic expansion with endpoint contributions is on the complexified Hamilton dark ring (the lines (4.3.15)). This can be smoothed away by using the same uniform approximation (4.1.38) used for transparent crystals. Examples of the resulting transition are shown in figure 4.35 for later comparison to experiments. Near the focal plane the focused conical diffraction rings transform into tightly focused

double refraction spots, and in the farfield both the secondary inner rings and axial spot are visible during the transition. The sheets of the wave surface $\Phi_{\pm} + \boldsymbol{\kappa} \cdot \boldsymbol{\rho}$ from which the different structures originate are indicated, corresponding to regions dominated by each of the two wave eigenpolarisations.

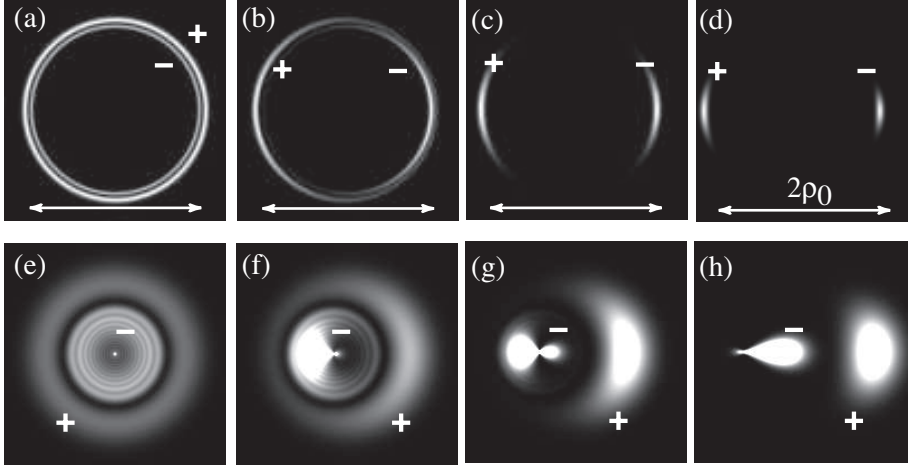


Figure 4.35: The transition from conical diffraction (a,e) to double refraction (d,h). Images simulated using approximation (4.1.38) in (4.3.5) for $\rho_0 = 60$; with $\zeta = 2$ and μ values: (a) 0, (b) 0.8, (c) 2.5, (d) 5; and with $\zeta = 25$ and μ values: (e) 0, (f) 0.4, (g) 0.9, (h) 3.5. The sheets of the wave surface from which the rings and spike originate, and the diameter $2\rho_0$ of Hamilton’s dark ring, are indicated.

This uniform approximation neglects higher order interference (4.3.30) from the first correction to the asymptotic expansion of the Bessel functions. This is easy to include in forms similar to (4.1.38), requiring a function

$$\frac{f^1(s, \zeta)}{a\left(\frac{s}{\sqrt{-i\zeta}}\right)} = \sqrt{\frac{2}{\pi}} \int_0^\infty \frac{dt}{\sqrt{t}} e^{-\frac{1}{2}t^2} \sin(st - \frac{\pi}{4}) \quad (4.3.31)$$

$$= \frac{e^{-\frac{1}{2}s^2}}{2^{5/4}} \sqrt{\frac{2}{\pi}} \left\{ -\left(\frac{1}{4}\right)! {}_1F_1\left[\frac{1}{4}, \frac{1}{2}, -\frac{1}{2}s^2\right] + s\sqrt{2} \left(\frac{3}{4}\right)! {}_1F_1\left[\frac{3}{4}, \frac{3}{2}, -\frac{1}{2}s^2\right] \right\} \quad (4.3.32)$$

$$= \frac{\sqrt{\pi} e^{-\frac{1}{4}s^2}}{2|s|^{1/2}} \left\{ s I_{\frac{1}{4}}\left[\frac{1}{4}s^2\right] - |s| I_{-\frac{1}{4}}\left[\frac{1}{4}s^2\right] \right\}, \quad (4.3.33)$$

and giving the correction

$$\sqrt{\tilde{\rho}} \left(i\tilde{\zeta}\right)^{3/4} b_{-}^{\text{endpoint}}(\tilde{\rho}, \tilde{\zeta}) = f(s_-) - \frac{i\tilde{\zeta} a(0) f^1(s_+)}{8\tilde{\rho}} \mathsf{T}[-\text{Res}_+]. \quad (4.3.34)$$

Finally, we note that the dichroic diffraction integrals can be evaluated exactly along the branch axes, yielding the optic axis formulae (4.1.45-4.1.46) with no complexification needed. So, interestingly, the intensity along the branch axes remains exactly equal to the intensity along the transparent optic axis when bifurcated by dichroism.

4.3.4 A note on circular dichroism

The theory above is easily extended to include circular dichroism – anisotropic absorption dependent on handedness of circular polarisation – by redefining the dichroism parameter δ as an imaginary part of the chirality parameter γ . The situation then bears more resemblance formally to a transparent crystal with optical activity, and the degeneracy structure is immediately obvious from examining the chiral formulae of section 4.2 with $\gamma \rightarrow i\delta$, whereby $\rho_0\delta$ is the maximal attenuation analogous to that for linear dichroism.

This corresponds to adding a real nonhermitian (antisymmetric) part to the dielectric tensor as discussed in section 2.1, and here no complex coordinates are required. The crystal vector $V(\kappa) = \sqrt{\kappa^2 - \delta^2}$ shows that circular dichroism splits the optic axis into a circular ring $\kappa = \gamma$ in position space, an L (linear polarisation) line (Nye 1999) separating regions of left and right handed circular polarisation. (Recall that linear dichroism split the optic axis into a pair of singular axes, C-points in position space). Outside the L-line the wave surface is real and scatters real rays similar to those of biaxial conical diffraction, so for $\delta \ll 1$ the beam that emerges is similar to that for a nonchiral transparent crystal. Inside the L-line the wave surface, and therefore rays, are complex (they have a complex wavevector), and exponential gradients dominate. In this instance there are no Stokes or anti-Stokes sets of interest, and the overriding gradient is an axial concentration of rays which swamps the conical diffraction rings. Figure 4.36 shows the intensity in the ρ - ζ plane as it is seen emerging from the crystal, for different values of δ , calculated from the chiral stationary phase approximation, (it has been verified that this is indistinguishable from the exact integrals).

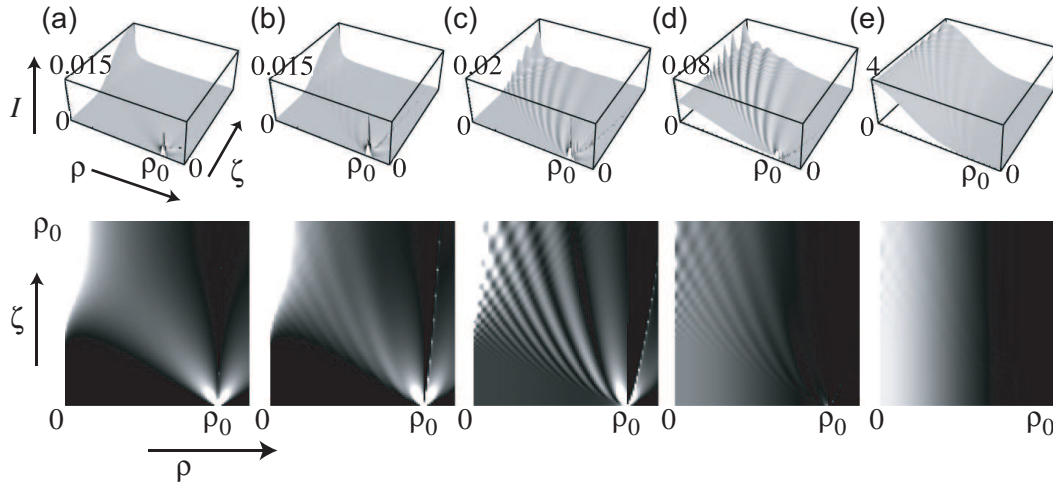


Figure 4.36: Circular dichroism in conical diffraction: geometrical intensity in the ρ - ζ plane calculated from (4.2.27) and (4.2.6) with $\gamma \rightarrow i\delta$, for $\rho_0 = 50$ with δ values: (a) 0.1, (b) 1, (c) 3, (d) 5, (e) 7. The familiar conical diffraction rings and axial focus can be seen for small δ , but circular dichroism swamps these with an exponential axial concentration of intensity.

4.3.5 Imaginary conical refraction

Let us consider briefly the opposite limit to elsewhere in section 4.3, so instead of treating absorption as a singular perturbation we let the crystal birefringence be isotropic, that is $\text{Re}\mathcal{N}_{\text{sym}} = \mathcal{I}/n_2^2$ in (2.1.2), and only the dichroic tensor (2.1.9) contains any anisotropy. The theory of this case is formally identical to the theory of conical refraction.

The nonhermitian part of the dichroic tensor determines a well-defined optic axis, corresponding to a conical point on a purely imaginary wave surface – the ‘wave magnitude’ surface discussed in section 3.2 – whose normals are rays with cone half-angle A . The anisotropy is then specified paraxially by the imaginary counterpart to Hamilton’s conical refraction ring radius, ρ_0 . The wave and geometric theories proceed as for the biaxial theory, with ρ_0 imaginary, so we define

$$\rho_0 = ip_0 \quad (4.3.35)$$

for real p_0 (note we are not redefining ρ which remains real). This dichroic parameter is larger than the perturbation μ , which we will set to zero, so the wave, ray, and position variables are all real, there are no complex rays to cause interference, and it is sufficient

to consider the geometric ray contributions

$$b_{\pm}^{\text{geom}} \approx -\frac{i}{\zeta} \sqrt{\frac{\rho \mp ip_0}{\rho}} e^{-\frac{(\rho \mp ip_0)^2}{2i\zeta}} a \left(\frac{\rho \mp ip_0}{\zeta} \right). \quad (4.3.36)$$

The intensity for an unpolarised beam thus contains no interference terms and is just the sum of magnitudes

$$\begin{aligned} I^{\text{unpol}} &= \frac{1}{2} |b_+(\rho, \zeta)|^2 + |b_-(\rho, \zeta)|^2 \\ &\approx \frac{\sqrt{\rho^2 + p_0^2}}{\rho \zeta^2} e^{-\frac{\rho^2 - p_0^2}{\zeta^2}} \left| a \left(\frac{\rho \mp ip_0}{\zeta} \right) \right|^2 \cosh \frac{2p_0\rho}{\zeta}. \end{aligned} \quad (4.3.37)$$

In contrast with the bright and dark cylinders that characterise transparent conical diffraction, this predicts one expanding bright cone of light beyond the crystal, due to a sort of anti-focusing of absorptive power. The profile across the cone surface is approximately gaussian regardless of the incident beam profile. Axial focusing is apparent in the formula above but proves to be visually insignificant against the exponentially bright cone. Computations from the exact wave integrals show it to be indistinguishable from the geometric approximation. Furthermore they confirm that, for large enough ζ , the axis does not even constitute a local intensity maximum; for a thick crystal, $p_0 \gg 1$, there is a maximum along the axis only for $\zeta < 1/\sqrt{3}$, and a minimum elsewhere.

Figure 4.37 shows the cone profile of imaginary conical refraction for a gaussian incident beam, with the intensity falling exponentially away from the focal plane, where the geometric intensity is singular.

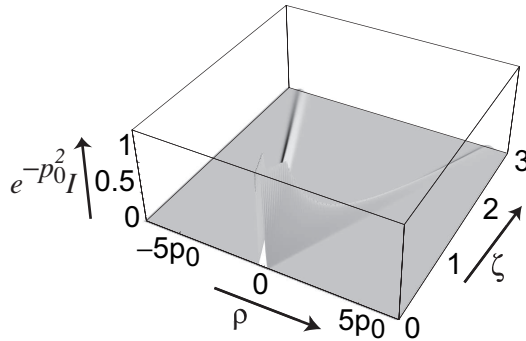


Figure 4.37: Imaginary conical refraction: intensity of rays refracted through a crystal with isotropic refractive index but anisotropic absorption $p_0 = 10$, producing a bright hollow cone, gaussian in the radial coordinate ρ , which decays exponentially with propagation distance ζ .

4.4 Dichroic Biaxial Crystals with Optical Activity

The most general case to be considered is that of diffraction along the optic axis of a crystal exhibiting biaxiality, chirality, and dichroism. The total anisotropic effect of such a crystal on a paraxial plane wave is specified by the traceless part of the evolution matrix

$$\mathcal{F}^{\text{tr}}(\tilde{\boldsymbol{\kappa}}) = \mathbf{V}(\tilde{\boldsymbol{\kappa}}) \cdot \boldsymbol{\Sigma} = \rho_0 \{\tilde{\boldsymbol{\kappa}}, \gamma\} \cdot \{\sigma_3, \sigma_1, \sigma_2\}. \quad (4.4.1)$$

The propagator integral is obtained from the transparent chiral integral in section 4.2 by the complexifying transformations (2.4.1) to (2.4.4), with the result $\mathbf{D}(\boldsymbol{\rho}, \zeta) \rightarrow e^{-i\mathcal{F}_0} \mathbf{D}(\tilde{\boldsymbol{\rho}}, \zeta)$, giving

$$\mathbf{D}(\tilde{\boldsymbol{\rho}}, \zeta) = e^{-i\mathcal{F}_0} \left[B_0(\tilde{\boldsymbol{\rho}}, \zeta) \mathcal{I} + \left\{ \frac{\tilde{\boldsymbol{\rho}}}{\tilde{\rho}} B_1(\tilde{\boldsymbol{\rho}}, \zeta), B_2(\tilde{\boldsymbol{\rho}}, \zeta) \right\} \cdot \boldsymbol{\Sigma} \right] \mathbf{d}_0, \quad (4.4.2)$$

in terms of the diffraction integrals $B_m(\tilde{\boldsymbol{\rho}}, \zeta)$ defined in (2.5.5), simplified in (4.2.5), and related to the eigenvalue diffraction integrals $A_{\pm}(\tilde{\boldsymbol{\rho}}, \zeta)$ by (2.5.11). The eigenvectors $\mathbf{d}_{\pm}(\tilde{\boldsymbol{\rho}})$ defined by (2.3.23) are generally nonorthogonal elliptical polarisations in the presence of absorption.

The most general expression for the exact wave intensity is then,

$$\begin{aligned} I &= \mathbf{D} \cdot \mathbf{D}^* \\ &= e^{2\text{Im}\mathcal{F}_0} \left(|A_+|^2 |\mathbf{d}_0 \cdot \mathbf{d}_+|^2 |\mathbf{d}_+|^2 + |A_-|^2 |\mathbf{d}_0 \cdot \mathbf{d}_-|^2 |\mathbf{d}_-|^2 \right. \\ &\quad \left. + 2\text{Re} [A_+ A_-^* (\mathbf{d}_0 \cdot \mathbf{d}_+) (\mathbf{d}_0 \cdot \mathbf{d}_-)^* \mathbf{d}_+ \cdot \mathbf{d}_-^*] \right) \quad (4.4.3) \\ &= e^{2\text{Im}\mathcal{F}_0} \left[|B_0|^2 + \frac{|\tilde{\rho}_x|^2 + |\tilde{\rho}_y|^2}{|\tilde{\rho}|^2} |B_1|^2 + |B_2|^2 \right. \\ &\quad + 2 \left(\text{Re} \left[B_0^* B_1 \frac{\tilde{\rho}_x}{\tilde{\rho}} \right] + \text{Im} \left[B_2^* B_1 \frac{\tilde{\rho}_y}{\tilde{\rho}} \right] \right) (|d_{0x}|^2 - |d_{0y}|^2) \\ &\quad + 4 \left(\text{Re} \left[B_0^* B_1 \frac{\tilde{\rho}_y}{\tilde{\rho}} \right] - \text{Im} \left[B_2^* B_1 \frac{\tilde{\rho}_x}{\tilde{\rho}} \right] \right) \text{Re} [d_{0x}^* d_{0y}] \\ &\quad \left. - 4 \left(\text{Re} [B_0^* B_2] + |B_1|^2 \frac{\text{Im} [\tilde{\rho}_x \tilde{\rho}_y^*]}{|\tilde{\rho}|^2} \right) \text{Im} [d_{0x}^* d_{0y}] \right]. \quad (4.4.4) \end{aligned}$$

The A_{\pm} diffraction integrals are most suited to the nonchiral case because of their correspondence directly to waves in the two polarisation eigenstates, when $A_{\pm} = b_{\pm}$. For the chiral case we may use the simpler b_{\pm} integrals, and have seen that b_+ corresponds to three interacting waves, but the B_m integrals, which are sums over the ‘ \pm ’ states, are most convenient because of their simple differential interrelations (2.5.6).

For an unpolarised incident beam the intensity simplifies to

$$I_{\text{unpol}} = e^{2\text{Im}\mathcal{F}_0} \left(|B_0|^2 + \frac{\tilde{\boldsymbol{\rho}} \cdot \tilde{\boldsymbol{\rho}}^*}{|\tilde{\rho}|^2} |B_1|^2 + |B_2|^2 \right). \quad (4.4.5)$$

A circularly polarised beam undergoes an added brightening or darkening dependent on the handedness,

$$I_{\pm} = I_{\text{unpol}} \mp 2e^{2\text{Im}\mathcal{F}_0} \left(\text{Re} [B_0^* B_2] + |B_1|^2 \text{Im} \left[\cos \phi_{\tilde{\rho}} \sin \phi_{\tilde{\rho}}^* \right] \right), \quad (4.4.6)$$

and a linearly polarised incident beam with orientation angle χ undergoes interference which rotates with 2χ ,

$$I_{\chi} = I_{\text{unpol}} + 2e^{2\text{Im}\mathcal{F}_0} \text{Re} \left[B_1 \left(B_0^* \cos [\phi_{\tilde{\rho}} - 2\chi] - iB_2^* \cos [\phi_{\tilde{\rho}} - 2\chi] \right) \right]. \quad (4.4.7)$$

As elsewhere, when considering gaussian beams we will make the simplifying transformation to a bundle of complex rays via the transformation (2.4.7). Figures 4.38 to 4.40 show the three dimensional structure of the logarithmic intensity field for an unpolarised gaussian incident beam. In figure 4.38 the bright Airy rings associated with the transparent caustic are clearly visible. As dichroism, or since this is a gaussian beam, misalignment with the optic axis, increases, a dark ring grows out from the axis, encircles a bright region, and is interrupted by bright focusing near the axis. This is reminiscent of the dark anti-Stokes ring (4.3.27) from the nonchiral case. As we shall see the connection is qualitatively true, though in this case the ring is not perfectly circular and a simple analytic expression is lacking.

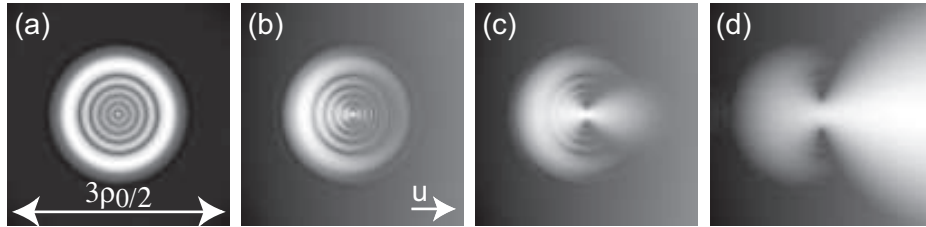


Figure 4.38: Chiral transition: logarithmic density plot of wave intensity in the $\zeta = \rho_0/3$ plane with $\rho_0 = 50$, $\gamma = 1$, and μ values: (a) 0, (b) 1, (c) 2, (d) 5. The direction of μ is indicated in (b).

The profiles in figure 4.39 show that the spun caustic surface is augmented by dichroism, most notably in the plane perpendicular to the dichroism vector μ . Figure 4.40 shows the striking three dimensional picture with circular symmetry broken by dichroism. We will see that these structures can be understood in terms of the same ray and wave techniques used in the previous sections.

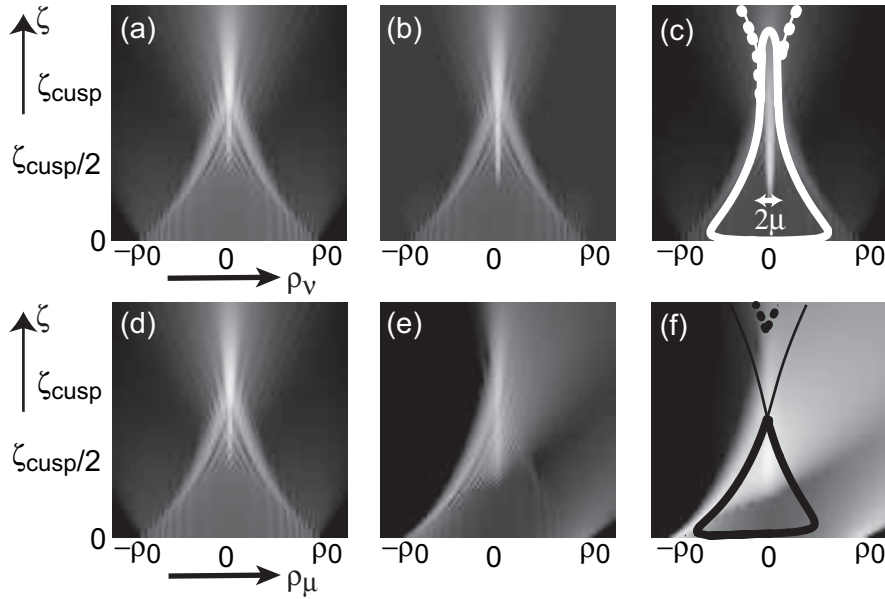


Figure 4.39: Dichroic chiral wave intensity profiles: logarithmic density plot of wave intensity for $\rho_0 = 50$, $\gamma = 1$. (a-c) show the $\rho_\mu = 0$ plane for μ values: (a) 0, (b) 1, (c) 2. (d-f) show the corresponding values in the $\rho_\nu = 0$ plane. (c) and (f) show the intersection of three distinct Stokes surfaces (thick, thin, and dotted curves) with these planes.

The key problems of interest are what happens to the caustic surface and the cusp under dichroism, features that must be understood in terms of Stokes sets. In particular the anti-Stokes sets have already been seen to dominate over focal features when absorption is present. The most striking feature of chiral conical diffraction, the spun cusp, which is unstable under nonhermitian perturbation, is the rotationally symmetric extension of Pearcey’s integral (Nye 1999), whose asymptotics for complex coordinates were studied by Paris (1991). We will see that the complexification of the spun cusp by a nonhermitian perturbation can be described simply and affects only one of its two variables.

4.4.1 Chiral conical refraction complexified

The geometric formulae (4.2.9) to (4.2.14) apply here, with the complexifying transformations $\rho \rightarrow \tilde{\rho}$ and $\kappa \rightarrow \tilde{\kappa}$ made everywhere. The solutions to the ray equation (4.2.10) are now generally four complex rays, and careful consideration of Stokes and anti-Stokes sets are required to determine where they exist physically.

The intensity is given by the complexification of the geometric intensity (4.1.11) mod-

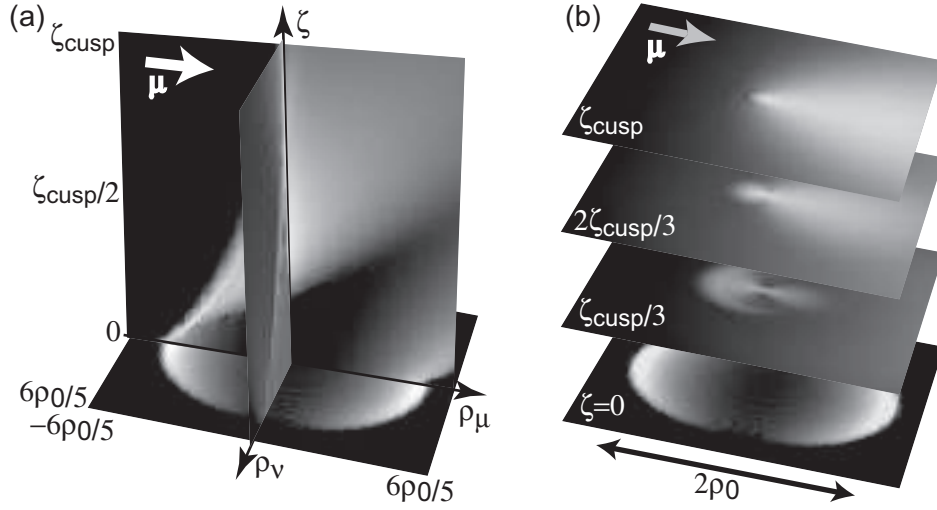


Figure 4.40: Dichroic intensity in 3d: logarithmic intensity sections in 3 dimensions for $\rho_0 = 50$, $\gamma = 1$, $\mu = 2$: (a) in the $\rho_\mu = 0$ plane, the $\rho_\nu = 0$ symmetry plane, and the $\zeta = 0$ focal image plane; and (b) in ζ level planes as shown. The direction of complexifying vector μ is shown.

ulated by an exponential absorption factor,

$$I(\tilde{\rho}, \zeta) = \frac{1}{2} \sum_n e^{\text{Im}[\Phi(\tilde{\kappa}_n) + \Phi_0]} \left| \frac{d\tilde{\rho}}{d\tilde{\kappa}_n} \right|^{-1} |a(\tilde{\kappa}_n + i\delta)|^2. \quad (4.4.8)$$

Many of the key features of the previous investigations will carry over to this case. That $\zeta = 0$ is not a focal plane in the presence of chirality applies also with dichroism. Since the complex transverse coordinate $\tilde{\rho}$ is independent of the chirality parameter γ , axial focusing along the branch axes (4.3.14) still occurs. This is visible at the center of figure 4.41, and in the exact intensity of figures 4.38, 4.39(a-c), and 4.40. In figure 4.39(a-c) the axial focus spreads out between the branch axes, which separate as dichroism increases, while along the μ direction in (d-f) the focus remains a thin focal spike.

The dominant feature in the intensity is a region where anti-Stokes sets have a high concentration, creating exponential darkening in figure 4.41 similar to the dark ring from figure 4.33, caused by exponentially fast pair-wise exchange of ray dominance involving all four of the complex rays. Outside of these regions the intensity is slow varying over large regions, and either exponentially large or exponentially small in a manner determined by the anti-Stokes sets. We can continue to identify the different ray solutions with the two eigenpolarisations in the crystal, or the two sheets of the complex wave surface as defined

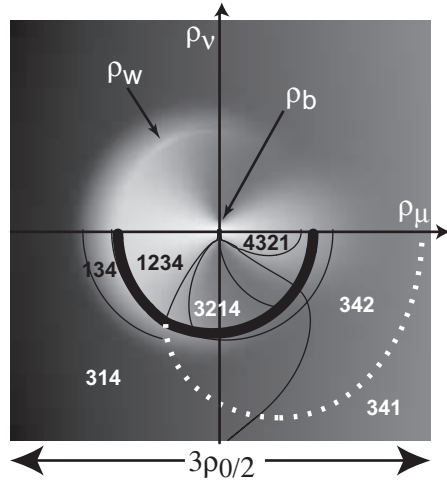


Figure 4.41: Ray intensity and Stokes lines: logarithmic density plot of ray intensity (4.4.8) for $\mu = 2$, $\rho_0 = 50$, $\gamma = 1$, $\zeta = 35$. The four rays are listed here in order of dominance in some key regions, with labels assigned in order of dominance in the brightest region. The dominance swaps in pairs across anti-Stokes lines (thin curves), one ray vanishes across the Stokes line (bold curve, also the bold curve in Figure 4.39), and the ray equation has a branch cut (dotted curve); these are shown only in the lower half, and are symmetric about the ρ_μ axis. The complex whisker ρ_w and branch axes ρ_b are shown.

by $\Phi_\pm(\tilde{\kappa})$ and (4.2.9). There are three rays obtained from Hamilton’s principle applied to Φ_- , labelled 1-3 in the figure, and only the ray labeled 4 originates from Φ_+ . Therefore the two dominant bright regions should exhibit the two distinct eigenpolarisations, nonorthogonality notwithstanding.

In the transparent chiral crystal the dominant focal feature is a horn-shaped caustic surface (4.2.14). This suffers the most drastic modification under dichroism, complexification reducing the dimensionality of the caustic surface to leave behind a focal line: the *complex whisker*.

4.4.2 The complex whisker

The Hessian determinant in (4.4.8) for $\tilde{\rho} \neq 0$ vanishes along the complexified caustic

$$\left(\frac{\tilde{\rho}}{\rho_0}\right)^{2/3} + \left(\frac{\tilde{\zeta}}{\zeta_{\text{cusp}}}\right)^{2/3} = 1, \tag{4.4.9}$$

defining a line of focusing between two sets of complex rays. As remarked in Berry & Howls (1990), such complex whiskers are generally subject to exponential damping from factors such as $e^{\text{Im}\Phi(\tilde{\mathbf{k}}_n)}$ in (4.4.8), reducing their significance as visible focusing. Although the whisker can be seen in figure 4.41, its lack of prominence is such that, when subject to weak diffractive smoothing, we can expect it to vanish from the visible intensity. Indeed, this is seen to be the case in the corresponding exact intensity in figure 4.38(c).

Nevertheless the caustic whisker is a significant locus of critical points in the geometric field. In figure 4.41 the complex whisker is seen to lie, consistent with its definition, at the intersection of Stokes and anti-Stokes sets. Dichroism effectively separates the two sets out of the caustic, leaving behind a caustic whisker at their intersection.

Using coordinates (4.3.10) in which the dichroism vector $\boldsymbol{\mu}$ lies along the horizontal ρ_μ axis, we consider first the geometric whisker that arises from a general incident beam, that is using real propagation distance ζ , in which case (4.4.9) simply defines a planar curve

$$\rho_\mu = 0, \quad \rho_\nu^2 = \mu^2 + \rho_0^2 \left[1 - \left(\frac{\zeta}{\zeta_{\text{cusp}}} \right)^{2/3} \right]^3. \quad (4.4.10)$$

Above $\zeta = \zeta_{\text{cusp}}$ this defines a hoop, whose vertical sides pass through $\zeta = \zeta_{\text{cusp}}$ on the branch axes, below which the two foci curve outward toward their maximal separation whereupon they terminate in the focal plane at $\rho_\nu = \sqrt{\rho_0^2 + \mu^2}$.

For a gaussian incident beam we can use the more accurate complex $\tilde{\zeta}$ representation, yielding the dramatically different result of a closed loop that curls out of the plane. At large ζ , as we expect, the whisker approximates the nongaussian planar whisker which is the projection of the gaussian whisker onto the $\rho_\mu = 0$ plane. However, at small ζ the gaussian whisker loops round smoothly, never meeting the focal plane and deviating far from $\rho_\mu = 0$. By expressing $\tilde{\zeta} = \zeta - i$ in complex polar form and approximating for a small argument that corresponds to $\zeta \gg 1$, the following very accurate approximation can be found:

$$\rho_\mu \approx \frac{\rho_0^2}{\mu \zeta_{\text{cusp}}} \left(\frac{\zeta_{\text{cusp}}}{\zeta} \right)^{1/3} \left[1 - \left(\frac{\zeta}{\zeta_{\text{cusp}}} \right)^{2/3} \right]^2 \quad (4.4.11)$$

$$\rho_\nu^2 \approx \mu^2 - \rho_\mu^2 - \zeta_{\text{cusp}} \left[1 - \left(\frac{\zeta}{\zeta_{\text{cusp}}} \right)^{2/3} \right] \left[\frac{4\rho_0^2}{3\zeta_{\text{cusp}}^3} - \rho_\mu \mu \left(\frac{\zeta}{\zeta_{\text{cusp}}} \right)^{1/3} \right]. \quad (4.4.12)$$

In the second line the $\rho_0^2/\zeta_{\text{cusp}}^3$ term is needed for the correct shape near $\zeta = \zeta_{\text{cusp}}$ but is small elsewhere, ρ_μ^2 is small near the highest arch section, while the ρ_μ term is small near the lowest arch section. These considerations yield the geometry detailed in figure 4.42.

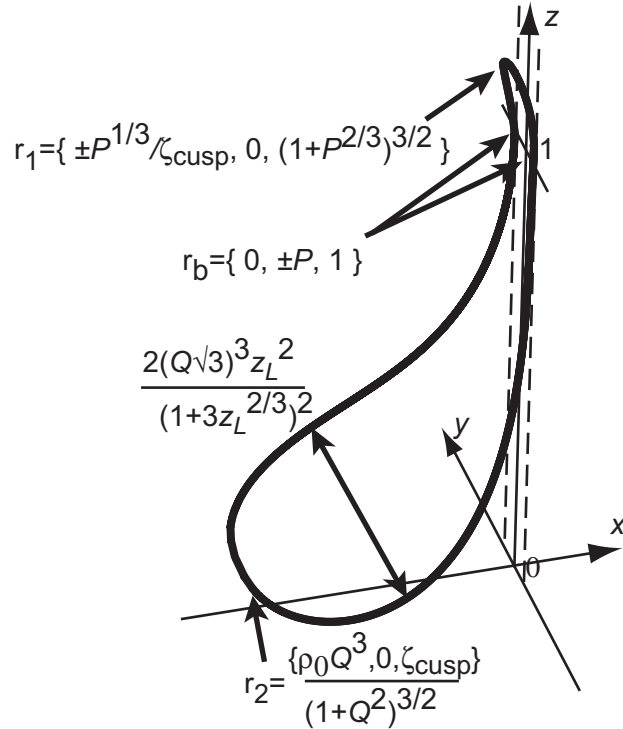


Figure 4.42: Geometry of the complex whisker, plotted from approximation (4.4.11,4.4.12) in scaled coordinates $\{x, y, z\} = \{\rho_\mu/\rho_0, \rho_\nu/\rho_0, \zeta/\zeta_{\text{cusp}}\}$, and the axial focal lines (dashed) where $\tilde{\rho} = 0$. The extreme coordinates of the whisker are shown, involving $P = \mu/\rho_0$, $Q = \mu/\gamma = P\zeta_{\text{cusp}}$ and $z_L = \left[\left(1 + \sqrt{4 + 3Q^2}\right) / (3 + 3Q^2) \right]^{3/2}$.

4.4.3 Diffraction

The effect of diffraction on the geometrical intensity is understood by studying the asymptotics of the diffraction integrals $B_m(\tilde{\rho}, \zeta)$, given by (4.2.27) with (4.2.24). The argument of the square root in (4.2.27) requires more careful consideration than in the transparent case.

The obstruction to an explicit expression of that argument valid for all $\{\rho, \zeta\}$ is the requirement that it vary smoothly throughout any given region, (not jumping at $\arg \Phi = \pi$ for example), except at a single branch cut where the unique subdominant and non-contributing complex rays swap, a possible choice of which is shown in figure 4.41. This can be quite easily solved for most regions once specified, and leads to the geometric intensity decorated by interference shown in figure 4.43.



Figure 4.43: Geometrical interference: logarithmic density plot of geometrical optics intensity (4.4.8) corresponding to Figures 4.41 and 4.38(c), endowing rays with phase.

Along the $\rho_\nu = 0$ axis, the geometric intensity is indistinguishable from the exact, and figure 4.44 shows how, at a typical value of ζ , the transparent features of the bright Airy rings associated with the caustic, and the axial focal spike, are swamped by exponential damping as dichroism increases.

Finally, figure 4.45 shows the geometric intensity near the complexified cusp.

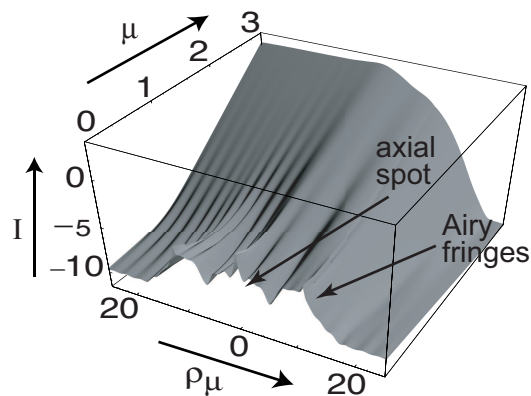


Figure 4.44: Exponential swamping of the chiral conical diffraction rings: logarithmic density plot of intensity on the $\rho_\nu = 0$ axis at $\zeta = 25$ for $\rho_0 = 50$, $\gamma = 1$. As μ increases from zero the symmetric Airy fringes associated with the caustic, and the bright axial spike, are overcome by an exponential gradient.

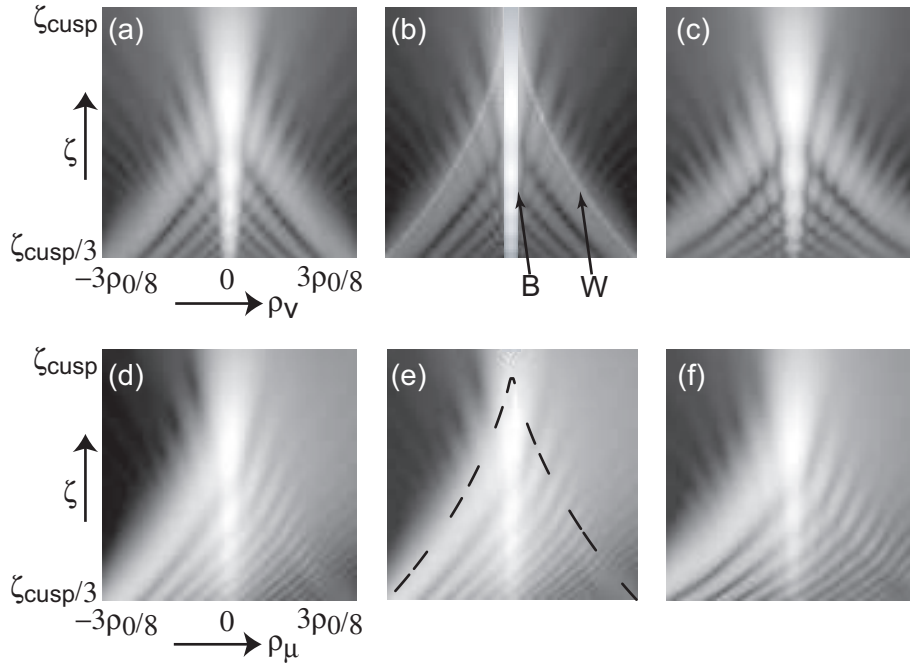


Figure 4.45: The complexified spun cusp: (a-c) Logarithmic density plot of intensity near the complexified spun cusp for $\rho_0 = 50$, $\gamma = 1$ and $\mu = 2$ in the $\rho_\mu = 0$ plane: (a) exact from (4.4.2); (b) geometrical optics (4.2.27) for $\zeta \gg 1$, which diverges along the complex whiskers W and $\tilde{\rho} = 0$ line B; (c) spun cusp approximation (4.2.48), smoothing the discontinuities but decorating the wrong caustic far from the cusp. (d-f) Intensity in the $\rho_\nu = 0$ plane corresponding to (a-c), with the Stokes line (dashed) shown in (b).

4.4.4 The complexified spun cusp

The cusp is identified physically by the intersection of two focal sets, and mathematically by the vanishing of the third derivative of $\Phi(\tilde{\mathbf{k}})$. This cannot be satisfied exactly for a gaussian beam because of the complex propagation distance $\tilde{\zeta}$, but the complex whisker (4.4.11) and branch axes (4.3.14) do approach with a distance $1/\zeta_{\text{cusp}} \ll 1$, at the two points z_b in figure 4.42. These are the points at which the more general whisker (4.4.10) and the branch axes intersect, with coordinates

$$\{0, \pm\mu, \zeta_{\text{cusp}}\}. \quad (4.4.13)$$

The gaussian diffraction integrals $C_m\left(\tilde{\rho}/\sqrt{\tilde{\zeta}}\right)$ have the same spun cusp approximation (4.2.48) as their transparent counterparts, subject to the relevant complexification

of coordinates. We have seen that this affects a dramatic breaking of circular symmetry. Considering the approximation $\tilde{\zeta} \approx \zeta$, that is, simplifying to real $\tilde{\zeta}$ for $\zeta \gg 1$ and including therefore general incident beams, the effect of dichroic complexification enters only into one of the two spun cusp control parameters, making η complex but leaving ξ_{\pm} real. The caustic of the spun cusp, given generally by $\eta^2 = (-\frac{2}{3}\xi_{+})^3$, becomes the complex whisker

$$\left(\frac{\tilde{\rho}}{\rho_0}\right)^2 = -\frac{\zeta_{\text{cusp}}}{\tilde{\zeta}} \left(\frac{2}{3} \cdot \frac{\tilde{\zeta} - \zeta_{\text{cusp}}}{\zeta_{\text{cusp}}}\right)^3. \quad (4.4.14)$$

Close to the complexified cusp (4.4.13) this is consistent with the previously derived whisker (4.4.10), where it can be written as

$$\rho_{\mu} \approx 0, \quad \rho_{\nu} \approx \pm\mu \mp \frac{\rho_0^2}{2\mu} \left(\frac{2}{3} \cdot \frac{\zeta - \zeta_{\text{cusp}}}{\zeta_{\text{cusp}}}\right)^3. \quad (4.4.15)$$

The intensity in terms of the complexified gaussian integrals is given by

$$I_{\text{unpol}} = \frac{\exp(2\text{Im}\mathcal{F}_0)}{1 + \zeta^2} \left(|C_0|^2 + \frac{\tilde{\rho}^* \cdot \tilde{\rho}}{|\tilde{\rho}|^2} |C_1|^2 + |C_2|^2 \right). \quad (4.4.16)$$

The complexified spun cusp approximation from (4.2.48), and the geometric approximation with $\tilde{\zeta} \rightarrow \zeta$, are compared to the exact wave integral intensity in figure 4.45. Both describe the diffraction decorating the cusp with great accuracy, including the spreading of the focal line between the branch axes in (a-c) and the overall horizontal exponential gradient in (d-f). The geometric intensity fails where it diverges at the branch axes and the complex whisker, but is correct across the Stokes line indicated, while the spun cusp approximation decorates the wrong caustic far from the cusp as in the transparent case.

Finally, we note that the dichroic diffraction integrals can be evaluated exactly along the branch axes, yielding the optic axis formulae (4.2.51) without any complexification. As in the nonchiral case, the axial intensity is preserved when the optic axis bifurcates into branch axes.

4.5 Angular Momentum in Conical Diffraction

4.5.1 Paraxial optical angular momentum

The striking phenomena of chiral and nonchiral conical diffraction are accompanied by similarly striking optical angular momentum effects. Orbital angular momentum of light is associated with the spatial distribution of the light field, and spin angular momentum is associated with the polarisation (Allen et al. 1992). Angular momentum effects are particularly significant in the presence of optical singularities, so interesting effects are to be anticipated with conical diffraction.

For a paraxial beam only the component of angular momentum along the optic axis will be significant. The orbital angular momentum is given by the local expectation value of the operator $\boldsymbol{\rho} \times (-i\hbar\nabla)$, integrated over the transverse electric field of the beam. The spin angular momentum is given by the integral of the local expectation value of the operator $\hbar\sigma_2$. Paraxially, as derived by Berry (1998), this can be expressed as

$$J_{\text{orb}} = \frac{\hbar l m \int \int d\boldsymbol{\rho} \mathbf{D}^* \cdot \partial_\phi \mathbf{D}}{\int \int d\boldsymbol{\rho} \mathbf{D}^* \cdot \mathbf{D}}, \quad J_{\text{sp}} = \frac{\hbar l m \int \int d\boldsymbol{\rho} \mathbf{e}_3 \cdot \mathbf{D}^* \times \mathbf{D}}{\int \int d\boldsymbol{\rho} \mathbf{D}^* \cdot \mathbf{D}}, \quad (4.5.1)$$

per photon, where ϕ is the azimuthal angle of $\boldsymbol{\rho}$. We will consider circularly symmetric incident beams, which have no orbital angular momentum, whose polarisation $\mathbf{d}_0 = \{d_{0x}, d_{0y}\}$ is associated with a spin angular momentum

$$J_{\text{inc},0} = 2\hbar l m d_{0x}^* d_{0y}. \quad (4.5.2)$$

This is zero for linear incident polarisation, and $\pm\hbar$ for circular.

The calculation of momenta for the diffracted beam emerging from the crystal based on the propagator integral (2.5.5) with (4.2.5) is lengthy, but simplifies greatly with the disappearance of odd terms when integrating over the angle ϕ , and subsequent use of Bessel transform identities. The result, independent of ζ and involving the momentum density of the incident beam

$$P \equiv \int_0^\infty d\kappa \kappa |a(\kappa)|^2, \quad (4.5.3)$$

is

$$J_{\text{orb}} = \frac{J_{\text{inc}}}{P} \int_0^{\infty} d\kappa \kappa |a(\kappa)|^2 \frac{\kappa^2 \sin^2(\rho_0 \sqrt{\kappa^2 + \gamma^2})}{\kappa^2 + \gamma^2} \quad (4.5.4)$$

$$J_{\text{sp}} = \frac{J_{\text{inc}}}{P} \int_0^{\infty} d\kappa \kappa |a(\kappa)|^2 \frac{\gamma^2 + \kappa^2 \cos(2\rho_0 \sqrt{\kappa^2 + \gamma^2})}{\kappa^2 + \gamma^2}, \quad (4.5.5)$$

with the total optical angular momentum given by

$$J = J_{\text{orb}} + J_{\text{sp}} = \frac{J_{\text{inc}}}{P} \int_0^{\infty} d\kappa \kappa |a(\kappa)|^2 \frac{\gamma^2 + \kappa^2 \cos^2(\rho_0 \sqrt{\kappa^2 + \gamma^2})}{\kappa^2 + \gamma^2}. \quad (4.5.6)$$

For the rest of this section we shall consider only a gaussian incident beam, for which $P = \frac{1}{2}$ and we can write

$$\begin{aligned} J_{\text{orb}} &= \frac{1}{2} J_{\text{inc}} \left(1 - e^{\gamma^2} [\gamma^2 E_1(\gamma^2) + F(\rho_0, \gamma)] \right) \\ J_{\text{sp}} &= J_{\text{inc}} e^{\gamma^2} [\gamma^2 E_1(\gamma^2) + F(\rho_0, \gamma)], \end{aligned} \quad (4.5.7)$$

in terms of the exponential integral

$$E_1(x) \equiv \int_x^{\infty} ds s^{-1} e^{-s}, \quad (4.5.8)$$

and an integral

$$F(\rho_0, \gamma) \equiv 2 \int_{\gamma}^{\infty} ds \left(s - \frac{\gamma^2}{s} \right) e^{-s^2} \cos 2\rho_0 s, \quad (4.5.9)$$

which can be expressed in terms of the error function, though we have not found that representation useful so we do not give it here. The variation of these momenta with biaxiality and chirality are shown in figure 4.46.

4.5.2 Nonchiral

For nonchiral crystals the exponential integral E_1 vanishes in (4.5.7), and the integral F simplifies leaving

$$J_{\text{orb}} = \frac{\sqrt{\pi}}{2} J_{\text{inc}} \rho_0 e^{-\rho_0^2} \text{erfi}(\rho_0) \quad (4.5.10)$$

$$J_{\text{sp}} = \sqrt{\pi} J_{\text{inc}} \left(1 - \rho_0 e^{-\rho_0^2} \right) \text{erfi}(\rho_0), \quad (4.5.11)$$

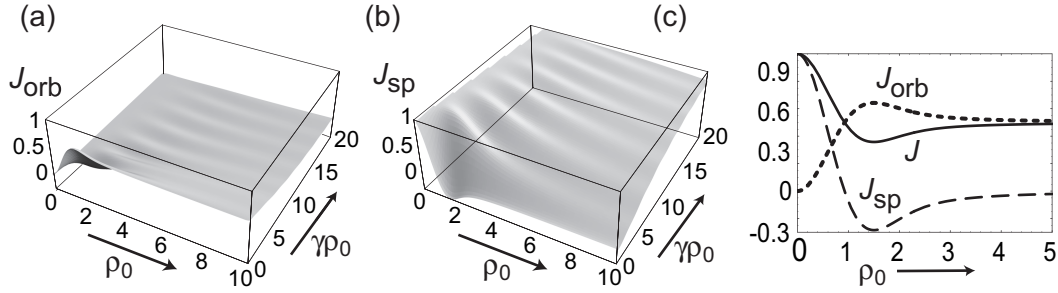


Figure 4.46: Angular momentum as a function of biaxiality ρ_0 and chirality γ showing: (a) J_{orb} , (b) J_{sp} , from (4.5.7), and (c) nonchiral momenta from (4.5.10).

in terms of the imaginary error function (or Dawson’s integral),

$$\text{erfi}(x) \equiv \frac{2}{\sqrt{\pi}} \int_0^x ds e^{s^2}. \quad (4.5.12)$$

The nonchiral angular momenta are shown in figure 4.46(c).

Well developed conical diffraction rings emerge for thick crystals, $\rho_0 \gg 1$, where the momenta simplify to

$$J \approx J_{\text{orb}} \approx \frac{1}{2} J_{\text{inc}}, \quad J_{\text{sp}} \approx 0. \quad (4.5.13)$$

This particularly striking result, that the incident angular momentum is halved and turned entirely from the spin to orbital variety, can be understood physically. The well developed rings are linearly polarised and hence carry no spin angular momentum, so, since the orbital angular momentum is generally a radially weighted average of the polarisation phase, J_{orb} will be proportional to the π geometric phase accumulated in a complete 2π circuit of the optic axis. This reflects the presence of the $\frac{1}{2}$ -index C point polarisation singularity existing somewhere in the dark region near the centre of the rings, (at the centre if the incident beam is circularly polarised), associated with a $\frac{1}{2}$ -integer orbital angular momentum.

4.5.3 Chirality dominated

In the chirality dominated regime of $\gamma \gg 1$ the angular momenta simplify to

$$J_{\text{orb}} \approx 0, \quad J \approx J_{\text{sp}} \approx J_{\text{inc}}. \quad (4.5.14)$$

A similarly striking result, this is obvious physically. Chirality changes only the phase of circular polarisation, having therefore no effect on orbital angular momentum. Chirality also uniformly rotates linear polarisation, not altering the total spin angular momentum.

4.5.4 Strongly biaxial or chiral crystals

For either strong biaxiality $\rho_0 \gg 1$ or strong chirality $\gamma \gg 1$ the oscillations in (4.5.7) and in figure 4.46(a-b) are small. They are contributed by the F integral in (4.5.7), with the exponential integral E_1 term and the constant giving the overall average momenta.

The weak oscillations come from the endpoint $s = \gamma$ of the F integral, physically constituting geometric interference between two rays, one from each sheet of the wave surface. The zeroth order term at the endpoint vanishes, but after integrating by parts twice, its asymptotic behaviour is given by

$$F(\rho_0, \gamma) \approx e^{-\gamma^2} \operatorname{Re} \frac{e^{-2i\gamma\rho_0}}{(\gamma + i\rho_0)^2}. \quad (4.5.15)$$

This approximation for F is shown in figure 4.47. From figure 4.46 it can be seen that the average angular momentum is of order unity over this range, and as ρ_0 increases the oscillations become vanishingly small.

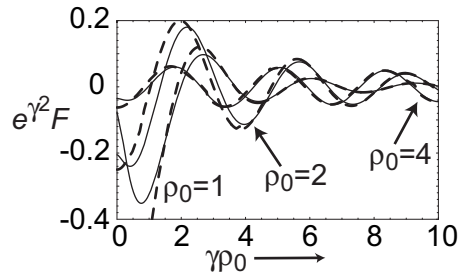


Figure 4.47: Asymptotic angular momentum oscillations: the oscillating function $e^{\gamma^2} F(\rho_0, \gamma)$ plotted against $\gamma\rho_0$, comparing the exact (4.5.9) (full curves) to the asymptotic approximation (4.5.15) (dashed curves), for the ρ_0 values indicated.

4.5.5 Torque on the crystal

The change in angular momentum associated with conical diffraction must be accompanied by a torque on the crystal that conserves momentum. This tends to rotate the crystal

about the optic axis with a magnitude $J_{\text{inc}} - J$ per photon in the incident beam. A further, much larger torque, arises from the skew of the geometric refraction cone relative to the optic axis. This torque is proportional to the rotation vector that rotates the cone axis to the optic axis, with a magnitude given by the rate of photon incidence multiplied by their angular momentum

$$J_{\text{ph}} = Al \times \text{photon momentum} = \frac{\hbar Al}{\lambda}, \quad (4.5.16)$$

where the photon wavelength is $\lambda = 2\pi/k$. The physical cone radius at the exit face, Al , is much larger than the wavelength of light in any typical situation being considered here, so $J_{\text{ph}} \gg \hbar$, whereas the torque associated with polarisation effects in the diffraction cone are of order \hbar or smaller.

4.6 Observations of Biaxial Conical Diffraction

In this section we aim to exploit our recent acquisition of a crystal of the monoclinic double-tungstate $\text{KGd}(\text{WO}_4)_2$, manufactured by the company Vision Crystal Technology AG (Goexe, Germany), to experimentally test the theory in section 4.1 and demonstrate the ease with which the asymptotic phenomena can be observed.

The crystal is of good optical quality, cut to a thickness of 25mm along its optic axis with a 3mm square transverse cross-section. The refractive indices of the crystal are not known to a higher accuracy than given in table 1.1. Since conical diffraction depends on the small differences (2.1.4) between the refractive indices, the uncertainty in these values constitutes a significant error on the half-angle of the conical refraction cone at approximately 1.0° . The cone attains a radius of 0.4mm at the exit face of the crystal.

The quality of the crystal is such that, with a $100\mu\text{m}$ diameter pinhole attached to one face, and viewed projecting sunlight from a window through the length of the crystal, two spots of double refraction are clearly visible, and can be easily made to spread into a fine gold ring. The optic axis direction is found by changing the orientation of the crystal in the plane coincident with the two spots (such that rotating the crystal does not change the direction connecting the spots), until they spread into lunes, then rings constituting the intersection of the unresolved conical diffraction cylinders with the eye, appearing in the focal image plane approximately halfway through the crystal. The phenomenon viewed in this manner must be reminiscent of that seen by Lloyd during his 1833 discovery with a somewhat poorer quality of crystal and pinhole, but a similar cone angle, and one feels compelled to express respect for the quality of his subsequent investigations.

In our investigations, light from a He-Ne laser (wavelength 632.8nm) was passed through a circular polariser, and focused by a 70mm lens onto the crystal along its optic axis. The precise location of the focus was not determined. The emerging light was magnified onto a screen 2 metres away using a 6.4mm focal length lens, producing image rings of diameter 265mm, which were photographed with a Fuji F610 digital camera. The experimental set up is shown in figure 4.48.

With the beam only approximately oriented two spots are imaged on the screen, exhibiting orthogonal linear polarisations consistent with double refraction. The optic axis direction is found by the procedure described above, and photographs of the resulting transition are shown in figure 4.49. This compares well to the theoretical transition in

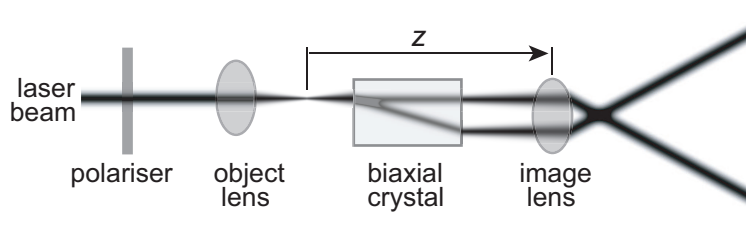


Figure 4.48: Observing conical diffraction: a collimated circularly polarised laser beam is focused through an object lens (focal length 70mm). The distance z is measured from the focus. A biaxial crystal of MDT (length 25mm), with faces cut perpendicular to its optic axis, refracts the beam, and the emerging cylinder (radius 0.4mm) is focussed by an image lens (focal length 6.4mm) onto a screen 2m away (image ring diameter 265mm).

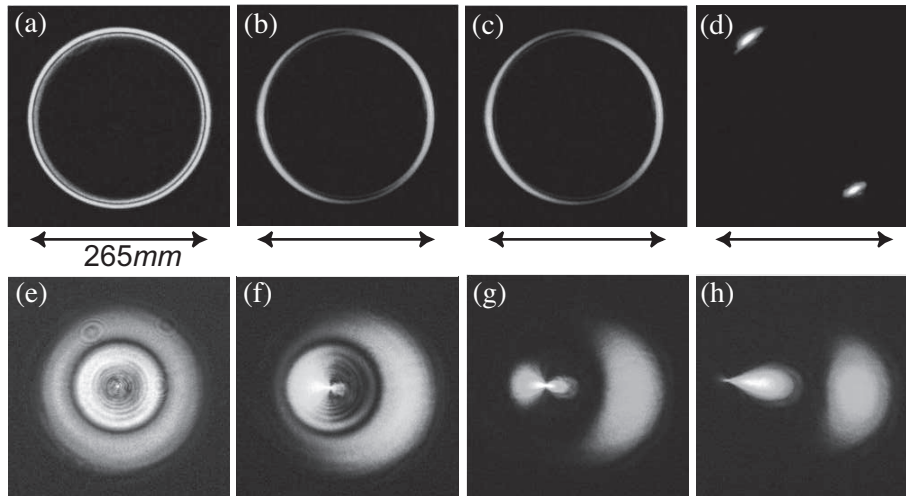


Figure 4.49: Photographs of the transition from (a,e) conical diffraction to (d,h) double refraction, as the incident beam is alligned away from the optic axis, in (a-d) the focal image plane and (e-h) the farfield, corresponding to the theoretical images in figure 4.35. The diameter of the rings, magnified onto a screen, is indicated.

figure 4.35. One spot spreads out to form the inner ring, one to form the outer ring, reflecting their separate origin from the two sheets of the wave surface. As the spots degenerate into conical diffraction rings their distinct orthogonal linear polarisations degenerate, remaining linear but ultimately exhibiting the same polarisation as each other, which rotates a half-turn in a circuit of the optic axis. This is observed by passing the exit

beam through a linear polariser, blocking out light totally along one radial direction and partially over the nearest $\pm 90^\circ$; this structure rotates with twice the angle of a rotation of the polariser. The transition has been explored in detail in Hamilton's initial predictions (Hamilton 1837), Lloyd's observational discovery (Lloyd 1837), and a numerical simulation of the light intensity (Dreger 1999).

Since the refractive indices are not known with sufficient certainty to usefully calculate the cone angle, the radius of Hamilton's ring at the exit face of the crystal was found by back calculating from its image on the observation screen when most focused, giving $0.44 \pm 0.01\text{mm}$. The waist width w was determined by projecting the laser beam through only the polariser and 70mm focusing lens, and measuring the $1/e$ width W of the laser spot on the screen at distance D . This was estimated by fitting a gaussian function to an intensity profile taken from a photograph of the spot, processed using MathematicaTM. The spreading of a gaussian beam is given by the formula

$$W = \sqrt{w^2 + (D/k_0w)^2} \approx D/k_0w, \quad (4.6.1)$$

from which we determined the waist width to be $w = 7.1 \pm 0.6\mu\text{m}$. The resulting biaxiality parameter,

$$\rho_0 = 60 \pm 10, \quad (4.6.2)$$

is large enough that the asymptotic phenomena of section 4.1 should present clearly.

Photographs of the light intensity observed on the screen are shown in figure 4.50, evolving from the rings of internal conical diffraction to the spot of external conical diffraction. Theoretical profiles from the exact diffraction integrals (4.1.4), and observed intensity profiles taken by averaging over azimuthal sectors of the photographs, are shown in figure 4.51. The theoretical ζ values in this and the corresponding figures 4.2 and 4.1 were calculated from the measured experimental distances z , except for the $z \sim 0$ image. Because the location of the focal image plane is difficult to find precisely, the focal plane image was matched by best fit, giving a ζ value of 1.8, and a corresponding z value of 0.9mm.

This uncertainty in ζ results from the tight focusing of the rings obtained with our large value of ρ_0 , which is accompanied by a sensitive dependence of the dimensionless propagation distance ζ on the physical distance z . From the definition of ζ (2.3.15) we have $\Delta\zeta = \Delta z/k_0w^2 \sim 1.998 \times \Delta z_{\text{mm}}$, so that near the focal plane where the intensity changes extremely fast with ζ due to severe diffraction effects, a physical adjustment on the order of a millimetre constitutes a sharp change in the intensity profile.

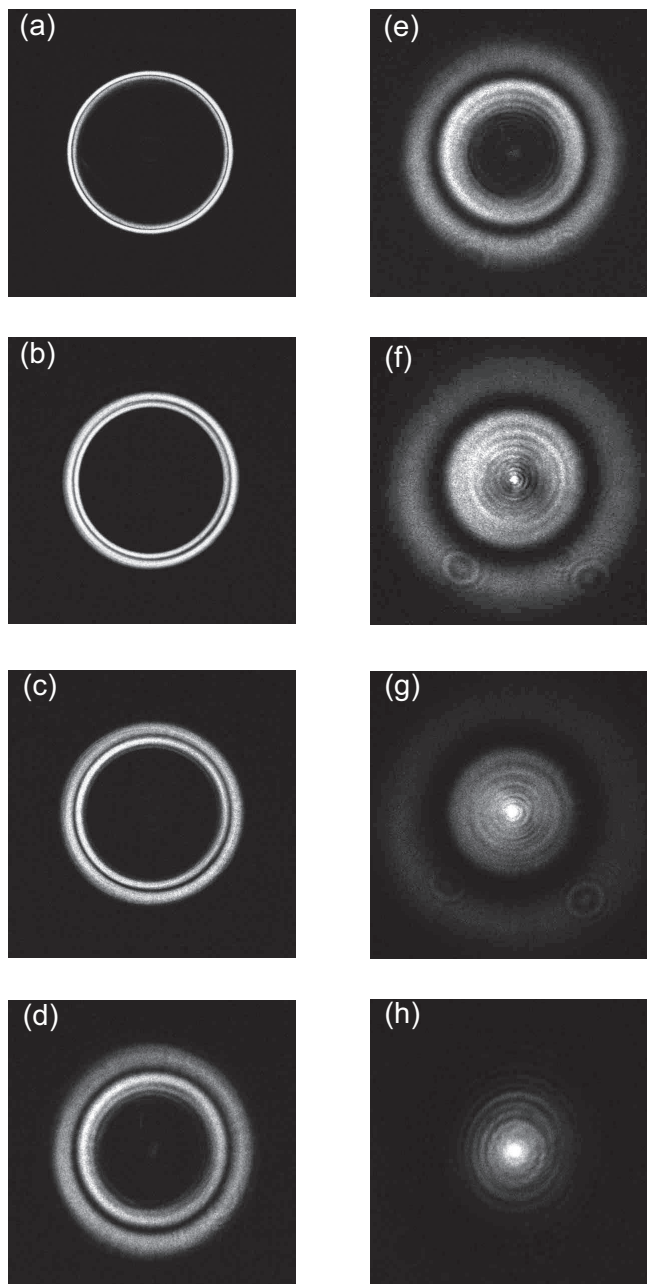


Figure 4.50: Photographs of the conical diffraction pattern from a 25mm slab of MDT, imaged at distances $\Delta z = \zeta k_0 w^2$ equal to: (a) ~ 0 , (b) 1.5, (c) 3.0, (d) 6.0, (e) 9.0, (f) 15.0, (g) 21.0, (h) 49.1, millimetres from the focal image plane. (The blemishes in the lower halves of (f) and (g) result from lens imperfections).

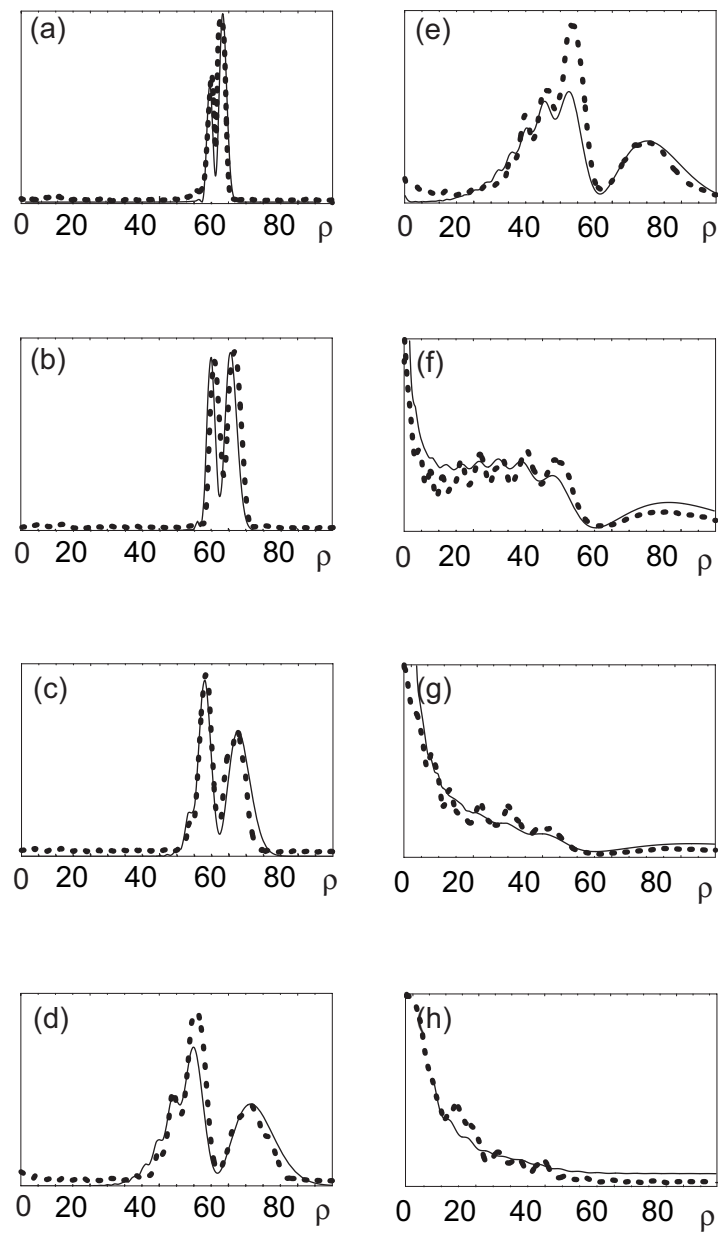


Figure 4.51: Conical diffraction profiles: graphs of radial intensity, comparing theoretical curves (full) from figure 4.2 to experimental intensity (dotted) from figure 4.50, obtained by averaging over a 10° annular sector of the digital photographs in MathematicaTM. Vertical scales are chosen for best fit.

The most distinct features of conical diffraction are the two bright rings, whose radii compare well to theoretical values in figure 4.52. For this purpose the theoretical values were taken from exact simulations rather than the asymptotic theory.

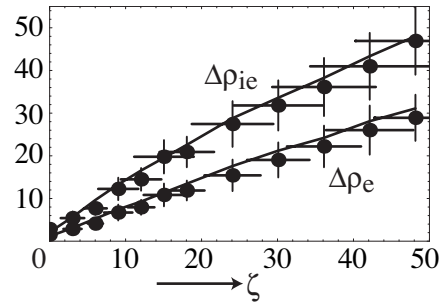


Figure 4.52: Ring dimensions; theoretical (curves) and observed (points) separations between the outer ring maximum and: for $\Delta\rho_{ie}$, the inner ring maximum, and for $\Delta\rho_e$, the dark ring. Errors in ρ arise from azimuthal averaging over the digital photographs, errors in ζ arise from the measurement error in w .

The observed and theoretical radii of the first two diffraction rings decorating the main inner ring are compared in figure 4.53, showing good agreement. The thickness of rings decreases with their radius, and their number increases with distance from the focal plane, in the manner predicted by the asymptotic theory.

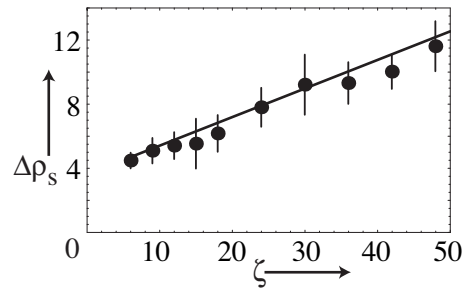


Figure 4.53: Theoretical (line) and observed (points) widths of the first secondary diffraction ring, $\Delta\rho_s$, measured between the two secondary ring maxima closest to the dark ring. Errors arise from azimuthal averaging over the digital photographs.

Discrepancies are visible in figure 4.51 in the far field $\zeta \gg 0$ images, where the rings surrounding the central spike appear to have prominent maxima and minima instead of the

shoulder-like inflections predicted by theory. It might be conjectured that a possible origin of such oscillations is the finite aperture size which gives oscillations in the focal plane for a pinhole beam, figure 4.7(b). This can be ruled out for two reasons: the finite aperture size effect arises from poor collimation which does not apply to the laser beam, and the oscillations seen here correspond in radius, if not in shape, to theory. This correspondence is evident in figure 4.54. As yet, therefore, we cannot explain the remaining discrepancy.

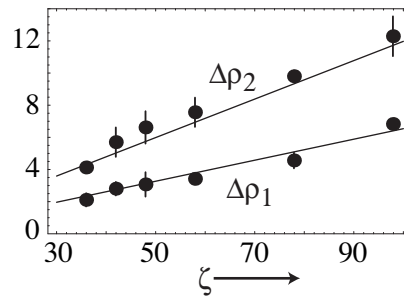


Figure 4.54: Theoretical (line) and observed (points) radii, $\Delta\rho_1$ and $\Delta\rho_2$, of the first two diffraction rings surrounding the axial spike. Theoretical radii are shoulders of the Bessel rings (equation (4.1.42)), experimental errors arise from azimuthal averaging over the digital photographs.

Chapter 5

Concluding Remarks

“I have been doing what I guess you won’t let me do when we are married, sitting up til 3 o’clock in the morning fighting against a hard mathematical difficulty.”

Sir George Gabriel Stokes, 1857, in a letter to his young lady (Stokes 1907)

The theory reported here describes the propagation of light along singular directions in anisotropic crystals. Of foremost importance are the simplifying principles of paraxiality, weak anisotropy, and geometrical optics. The first two of these allow the effect of a crystal on a beam of light to be specified by three optical parameters: the refraction cone size ρ_0 , transition parameter μ , and optical rotation γ . These encapsulate the leading order optical behaviour of a paraxial beam, including the eighteen components of the general complex dielectric tensor, the crystal length, the incident beam width and wavenumber, and a two-vector describing the beam alignment.

The ring-radius to beam-width ratio ρ_0 for a biaxial crystal determines the resolvability of the conical diffraction rings, well defined rings being obtained either with a narrow beam or a thick crystal. The outer ring is well described by geometrical optics, but diffraction of a wave scattered from the conical point dominates the profile of the inner ring. Near the focal plane this diffraction is most severe and makes the ring faint, the precise form depending on the incident beam profile. Two particular cases considered in section 4.1.3 highlight two very different ways in which diffraction can play a role: for a gaussian beam the geometric rings are symmetric about the anti-focal ring, however diffraction all but obliterates the inner ring; for a pinhole beam the exact wave theory demands poor

collimation of the beam be taken into account, introducing a finite aperture size which produces interference and softens the logarithmic singularity obtained otherwise.

Far from the focal plane any incident beam can be considered slowly varying and its profile becomes less important. Let us consider more rigorously the motivation behind the complex ray representation for a gaussian incident beam. The gaussian beam profile violates the assumption in section 2.6 that it is not an exponential function, and we must consider more carefully whether it is slowly varying. Recall that we obtain the diffracted field by superposing plane waves consisting of the beam profile, $e^{-\frac{1}{2}\kappa^2}$, and the phase term $e^{-i\Phi} = e^{i(\boldsymbol{\kappa}\cdot\boldsymbol{\rho} - \frac{1}{2}\zeta\kappa^2 \pm \rho_0\kappa)}$, and that the complexification of the gaussian beam involves the transformation $\zeta \rightarrow \tilde{\zeta} = \zeta - i$. Compare the coefficients of the quadratic beam exponent and the quadratic phase exponent, that is unity and $i\zeta$. When ζ is large the phase term will oscillate many times over the width of the gaussian beam, so the latter can be treated as slowly varying. When ζ is small the gaussian profile is relatively fast varying and its stationary approximation can be expected to fail. Fortunately, the complex source trick allows us to incorporate the beam profile into the phase term. Such tricks may be possible for other beams, but as can be readily seen the conditions are rather restrictive and none exists, for example, for the pinhole beam.

Complex rays enter into the geometric theory more crucially in the presence of the transition parameter μ . In any case, complex rays are paths through complex position space conserving the transverse part of the wavevector, and thereby satisfying Hamilton's dynamical equations (2.7.6). In an absorbing medium the instantaneous Poynting vector is time dependent (in section 3.1 we considered the time averaged Poynting vector) and not normal to any wave surface, though attempts have been made to define ray directions from it (Epstein 1929, Censor 1977, Echarri & Garea 1994). Interest remains in the interpretation of geometrical optics through complex rays (Bravo-Ortega & Glasser 1991). We have seen that the definition of complex rays as the saddlepoints of wave integrals provides a clear geometric insight through asymptotics. What we give up is the correspondence of a ray to any real path in space, but what we gain is a deep geometric understanding of refraction phenomena even in the presence of absorption. Combined with a knowledge of the corresponding rays in a transparent medium, the complex nature of these rays constitutes no intuitive obstacle to a detailed geometrical understanding.

It is important to note that the intuitive power of the ray concept does not rely on its representation of the path of some abstract object, and indeed the study of conical

refraction purely in terms of ray paths stood as an obstacle to its eventual solution for many years. The geometric constructions of rays as normals to wave surfaces are useful for building up a geometric insight in transparent crystals, but the central result of the ray method can be defined even in the abstract complex space of $\tilde{\rho}$ and $\tilde{\zeta}$. That central result is the intensity of ray crowding. From this geometric intensity we can directly infer the sites of geometric focusing which dominate diffraction in transparent crystals, and the sites of geometric interference along anti-Stokes sets which dominate in absorbing crystals, without any conceptual difficulties arising from dealing with complex spaces.

It is through the abstract transformation to complex coordinates that dichroism (non-hermiticity of the dielectric tensor) and misalignment of the incident beam (transition between double and conical refraction) are shown to give equivalent diffraction effects embodied in the parameter μ , and this is a genuinely surprising result. The unintuitive nature of this duality is reflected in its restriction to gaussian beams. This narrow applicability is not itself difficult to comprehend, the only requirement is that a misalignment of the incident beam modifies it by a direction dependent exponential, mimicking the exponential symmetry breaking of anisotropic absorption. Clearly this is satisfied by a gaussian beam, but a pinhole beam varies too slowly; other well collimated beams may satisfy this condition paraxially.

Although the notion of complex rays allows us to fully understand the geometrical optics of absorbing media as encountered here, one may still reserve some disappointment in the present lack of any association with visualisable paths in real space. Even for a gaussian beam in a transparent medium (or vacuum), for which both real rays (in a gaussian bundle) and complex rays (uniformly issuing from a point source) may be derived, the physical relation between them – the complexifying shift ‘ $-i$ ’ – lacks a clear geometrical interpretation.

The transition parameter $\mu = \zeta\delta + \kappa_0$ implies that dichroism δ causes no diffraction effects in the focal plane $\zeta = 0$, so the focal plane contains the bright focused double-ring image of biaxial conical diffraction. The entire image is modulated by an exponential ramp, which is an easily recognised unidirectional intensity slope unrelated to diffraction. It merely signifies the paraxial effect of direction dependent absorption. For a gaussian beam the shift to complex propagation distance also shifts the entire field a distance δ , given by (2.4.8) and depicted in figure 4.26.

Most important in the dichroic conical diffraction images are anti-Stokes surfaces,

which form dark brushes laced with darker interference lines, the latter identifiable approximately as loci of C points. For a gaussian beam the dark brushes loop round into a funnel with a perfectly circular cross-section, a beautiful geometry intimately linked to the complex $\tilde{\zeta}$ representation of a gaussian beam. Some remnant of these dark surfaces survives the addition of optical activity, becoming part of a very rich intensity structure that can be predicted accurately in terms of anti-Stokes sets. The effect of complexification on the spun cusp involves complexifying only the radial variable, causing a simple reduction of the rotationally symmetric caustic to a smoothly curved focal line.

The arguments employed to define the optical parameters $\{\rho_0, \delta, \gamma\}$ in sections 4.1-4.4 have the benefit of being easily extended to more general situations, as we have discussed for circular dichroism. Furthermore, they define the optical effects of biaxiality, optical activity, and dichroism, in terms of simple and measurable changes in the polarisation of plane waves. In this manner they are far more general than the rigorous derivation from Maxwell's equations in section 2.1. They avoid detailed questions as to the material causes of the effects. In particular, optical activity may depend on the wavelength of light used, it may manifest in the form of the Faraday effect, Raman optical activity, macroscopic chirality of the crystal lattice or microscopic chirality of the molecular constituents. Our motivation is not merely avoidance; the study of optically active crystals is ongoing, in particular how they rotate (Eimerl 1988) and refract (Silverman & Sohn 1986, Ghosh & Fischer 2006) light, and metamaterial technology, which is still in its adolescence, promises many new structures and mechanisms by which light may be manipulated. For example, Potts et al. (2004) have recently shown that wavelength-scale lattice structures in the form of swastika, triskella, or chiral fractals, can rotate the polarisation state of light. Also, conical refraction has already been studied in nonlinear (Shih & Bloembergen 1969, Bloembergen & Shih 1969) and inhomogeneous (Naida 1979) crystals and continues to generate interest. The three main effects considered here are the most fundamental means by which a medium might alter the state of light, and therefore represent the first approximation to a general theory of light propagating along axes of singularity.

The motivation for this general approach is also practical. The image size ρ_0 , rotation of polarisation γ , and the attenuation δ or alignment κ_0 , of a beam can be experimentally measured more easily than the eighteen coefficients of the dielectric tensor. In fact we have been unable to find any data recording the anisotropic absorption indices of crystals with which to compare the predictions of sections 4.3 and 4.4. We can estimate, however,

that the diffraction effects described therein are most prominent when the singular axes have an angular separation on the order of $2\delta/k_0w$, e.g. 1° for a He-Ne laser with $10\mu\text{m}$ waist. But the effects of dichroism as predicted here are likely to pose a great observational challenge and demand extremely sensitive measurements. The exponential ramp omitted from plots here will largely swamp anti-Stokes gradients, which themselves are revealed only in logarithmic plots.

The transition from conical diffraction to double refraction offers an easier means of studying the dichroic effects predicted here for gaussian beams, since the exponential absorption ramp is absent and, of course, there is no overall attenuation. Our own experimental images of transition in figure 4.49 do not contain sufficient dynamical range to be plotted logarithmically, though in their general appearance they do resemble the predicted intensity in figure 4.35.

Relevant to the growing technologies of novel materials, and the manipulation of individual atoms and molecules through the use of “optical tweezers” (Allen et al. 2003), are the changes in optical angular momentum which accompany conical diffraction, predicted in section 4.5. In principle the optical angular momentum formulae (4.5.1) can be extended to include dichroism, although we have not yet found any reasonable simplification of the resulting integrals. Nevertheless it would be interesting to further investigate the angular momentum change and torque associated with anisotropic absorption.

There are other interesting avenues to explore through conical diffraction, particularly involving the polarisation structure which we have barely touched upon. The theory given here is sufficient for direct calculation, exact or asymptotic, of the polarisation of the field. We have noted the geometric phase associated with the half rotation of polarisation around the bright biaxial conical diffraction rings, discovered by Hamilton and Lloyd, and hinted at its extension to absorbing crystals. We have also elucidated the intricate polarisation spiral of chiral conical diffraction. Consider for a moment a circularly polarised incident beam, \mathbf{d}_\pm , for which we can write the field conically diffracted through a biaxial chiral crystal as

$$\mathbf{D} = (B_0 \pm B_2) \mathbf{d}_\pm + B_1 \mathbf{d}_\mp. \quad (5.0.1)$$

This naturally splits the diffracted beam into the first term, called the *fundamental*, which retains the incident polarisation, and the second term which is a *vortex* beam, possessing an axial polarisation singularity due to the Bessel function J_1 in the B_1 integral, (therefore this splitting remains interesting in the absence of chirality when B_2 vanishes). The two

parts of the beam can thus be distinguished by the use of a circular polariser. Such intricate polarisation dependence is currently being developed by a company Crystalith (Jerusalem, Israel) for use in metrology, as a means of measuring distances far below the diffraction limit for use in the alignment of optical components. They view this as the first of many possible applications of conical diffraction technology.

Besides complex rays and paraxiality, the final simplifying principle in the theory of conical diffraction is the study of the image field. This avoids detailed and difficult study of the precise form of waves or rays inside the crystal, which cannot be directly imaged anyway. In particular this simplifies study of the angular momentum, which has been addressed elsewhere (Ciattoni et al. 2003) for paraxial beam propagation in uniaxial crystals. We have also shown how the formulae for the image field can be easily transformed to give the true field inside the crystal. Such a simple transformation is not possible in reverse because the image field contains more information.

To date, much of conical diffraction remains unexplored experimentally. Observations near the singular axes of a dichroic biaxial crystal (iolite) were made by Pancharatnam (1955*b*) but did not concern conical diffraction. Conical diffraction experiments have been performed on transparent crystals, most extensively the nonchiral case (Raman et al. 1941, Schell & Bloembergen 1978*b*), which is now well understood through our own investigations in section 4.6. The chiral case was studied by Schell & Bloembergen (1978*b*), although the caustic horn and ζ -dependent pattern predicted in section 4.2 remain to be investigated – these should be easy to observe.

Our own observations reported here for nonchiral transparent conical diffraction verify the emergence of the asymptotic phenomena predicted, including the widths, separations, and rate of growth of the geometric rings, axial focus, and interference rings. We have not been able to explain the observation of distinct maxima and minima surrounding the axial focus, instead of the faint shoulders predicted by theory. However our main aim is to demonstrate the ease with which observations can be made, and considerable improvement on the precision of these experiments is possible. A particularly interesting avenue for experimental study might be the connection between crystal dichroism and beam alignment for collimated beams.

We are currently aware of no published experimental observations capable of revealing the rich distance-dependent intensity structure beyond a biaxial crystal, either in the presence of optical activity and/or dichroism, or equivalently, of the transition from conical

diffraction to double refraction for transparent crystals with/without chirality.

The legacy of Hamilton's investigation into the diabolical point is tinged with contradiction. The phenomenon of conical *refraction* predicted by Hamilton is itself a curiosity, the abstraction of an idealised mathematical theory that occurs nowhere in nature. The physical phenomenon of conical *diffraction* can be understood geometrically, but only with the inclusion of wave effects from the outset in a geometric manner. The dominant and subdominant contributions to asymptotic expansions of the diffraction integrals swap prominence paradoxically as they thread the conical diffraction rings with a focal spike. The effect of optical activity is at once to smooth out the diabolical point, and to produce the more striking singularity of a caustic surface in the image field. The effects of anisotropic absorption are severe, washing out focusing with exponential gradients – the rich interference structures of complex rays uncovered under logarithmic enhancement.

Finally, with the geometry of a flat crystal slab and collimated beam, the theory retains some unnatural idealisation. In more general situations of arbitrary crystal geometry, or media which are not only anisotropic but inhomogeneous, refractive index degeneracies may be encountered locally by propagating waves. These situations are more similar to dynamical applications in quantum mechanics, chemistry, biochemistry and seismology. In understanding these far more complicated situations the idealised theory is an essential first step, and we offer some moves towards such generalisation in appendix B.

Appendix A

Solutions to the chiral quartic

The quartic ray equation (4.2.11) can be written conveniently as

$$(vq - u)^2 (q^2 + 1) - q^2 = 0, \quad (\text{A.0.1})$$

or

$$\left| \det \left((vq - u) \mathcal{I} + \frac{\mathbf{q} \cdot \boldsymbol{\Sigma}}{\sqrt{q^2 + 1}} \right) \right| = 0 \quad (\text{A.0.2})$$

in terms of scaled variables

$$\mathbf{u} \equiv \frac{\boldsymbol{\rho}}{\rho_0}, \quad v \equiv \frac{\zeta}{\zeta_{\text{cusp}}}, \quad \mathbf{q} = \frac{\boldsymbol{\kappa}}{\gamma}. \quad (\text{A.0.3})$$

Two of the four roots coalesce on the caustic

$$u^{2/3} + v^{2/3} = 1. \quad (\text{A.0.4})$$

The roots of the quartic equation can be expressed explicitly as

$$2vq_n \equiv (-1)^a u + M^{1/2} + (-1)^b \sqrt{2(u^2 - 3\Delta) - (M - u^2)} + (-1)^a 2u \frac{1 + v^2}{M^{1/2}}, \quad (\text{A.0.5})$$

in terms of the quantities

$$\Delta = \frac{1}{3}(u^2 + v^2 - 1) \quad \text{and} \quad M = u^2 + \left(\Omega^{1/3} - \Delta \Omega^{-1/3} \right)^2, \quad (\text{A.0.6})$$

where

$$\Omega = uv + \sqrt{u^2 v^2 + \Delta^3} \quad (\text{A.0.7})$$

is real outside the caustic and imaginary inside, for real u and v . The behaviour of these parameters is illustrated in figure A.1. The integers a and b may be either zero or unity and thus give rise to the four roots, for which a convenient choice of labels is

$$n = 2 - ab + (1 - a)(1 + b), \quad (\text{A.0.8})$$

so that

$$0 < q_4 < \text{Re}q_1 \leq \text{Re}q_2 < q_3. \quad (\text{A.0.9})$$

Equality is attained on and outside the caustic (where the left hand side of (A.0.4) is greater than or equal to unity), where the Re symbols are necessary since the roots $q_1 = q_2^*$ are complex. This convention is consistent with (4.2.29).

This is valid for positive u and v , and continued to negative values by $u \rightarrow |u|$ and $v \rightarrow |v|$. The continuation to complex coordinates in absorbing media is complicated by branch cuts, and the precise form of (A.0.5) must then be chosen to make the solutions continuous.

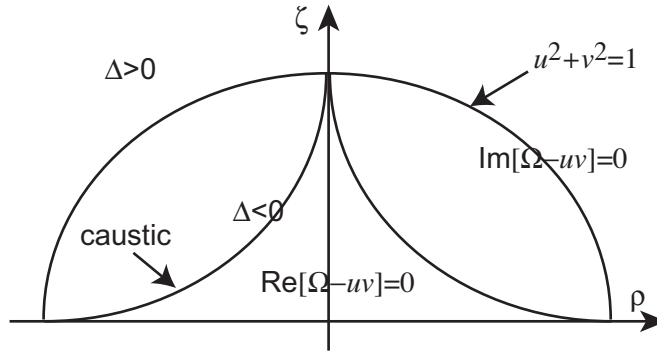


Figure A.1: Elements of the solutions to the quartic chiral ray equation: the quantity Δ is negative inside the circle $u^2 + v^2 = 1$ and positive outside, the quantity Ω is real outside the caustic and imaginary inside. The quartic equation for $u, v \in \mathbb{R}$ has 4 real roots outside the caustic and two inside.

In the absence of chirality, when $\gamma = 0$ and the scalings (A.0.3) are inappropriate, these four roots reduce to the two roots of the nonchiral ray equation. With the labeling convention above, the roots simplify as follows:

$$\gamma = 0 \quad \Rightarrow \quad \begin{aligned} \kappa_1 &= \frac{\rho_0 - \rho}{\zeta} \mathbb{T}[\rho_0 - \rho], & \kappa_2 &= 0, \\ \kappa_3 &= \frac{\rho + \rho_0}{\zeta}, & \kappa_4 &= \frac{\rho - \rho_0}{\zeta} \mathbb{T}[\rho - \rho_0]. \end{aligned} \quad (\text{A.0.10})$$

The general solution applies also to complex rays, where the variables u and v and the roots q are complex, for which a consistent labeling of solutions can only be made locally. In that case we require that the arguments of the four roots vary smoothly, except at a single branch cut surface in $\{\rho, \zeta\}$ space where two solutions switch discontinuously.

propagation distance ζ . Perhaps surprisingly, the formulations of the geometric and wave theories remain essentially the same as those for a crystal slab, with the new parameters inserted. Our results are consistent with the theory and experiment reported by Fève et al. (1994).

The beautiful geometry involved in spherical conical refraction is illustrated in figure B.1. Most important are the refracted cone angles, of which there are now two: the usual Hamilton cone of rays refracted into the crystal caused by the degeneracy of the optic axis, with cone half-angle A , and the cone into which this is refracted by the curvature of the exit face, with cone half-angle B . Snell's law at the exit face relates these paraxially by

$$\sin(4A + 2B) = n_2 \sin 2A. \quad (\text{B.0.1})$$

The refractive index along the optic axis of the crystal is the middle refractive index n_2 . Let the crystal be a sphere of radius r and diameter $l = 2r$ (it will be important to keep the two separate when considering the $r \rightarrow \infty$ flat slab limit). We are only interested in the change in optical path length of a paraxial ray due to the curvature of the crystal, which is proportional to a *refractive curvature*

$$c \equiv \frac{n_2 - 1}{r}. \quad (\text{B.0.2})$$

For a beam of width w and vacuum wavenumber k_0 , we work in terms of the familiar dimensionless variables, measuring transverse deviation ρ from the optic axis in units of the beam width, and propagation distance ζ along the optic axis in units of the diffraction length $k_0 w^2$. Let the dimensionless length of the crystal be $L = l/k_0 w^2$, and the dimensionless refractive curvature be $C = ck_0 w^2$.

A ray, striking the entrance face of the crystal at a distance ρ_1 from the optic axis, travels an optical path length $-\rho_1^2 C/2$ less than an axial ray; the quadratic power reflects the parabolic approximation of spherical curvature. If the ray subsequently traverses the crystal making an angle $\kappa/k_0 w$ with the optic axis, and strikes the exit face at a distance ρ_{exit} from the axis, its optical path length in the crystal includes the length $\kappa(\rho_{\text{exit}} - \rho_1)$, an isotropic shift $-\frac{1}{2}L\kappa^2/n_2$ due to birefringence, and Hamilton's conical shift $\pm\rho_0\kappa$ reflecting the conical point (we will neglect the skew of the cone here, which is easily incorporated by a coordinate transformation). The optical path length of a ray striking the exit face at the distance ρ_{exit} from the axis differs from an axial ray by $-\frac{1}{2}C\kappa^2$. After reaching a distance ρ from the optic axis having traveled a further distance D from the crystal, the

total optical path length of a ray is thus given by

$$\Phi(\kappa) = -\frac{C}{2}\rho_1^2 + \kappa(\rho_{\text{exit}} - \rho_1) - \frac{L}{2n_2}\kappa^2 \pm \rho_0\kappa - \frac{C}{2}\rho_{\text{exit}}^2 + \frac{1}{2D}(\rho - \rho_{\text{exit}})^2. \quad (\text{B.0.3})$$

We then apply Hamilton's principle. By minimising the optical path length with respect to ρ_{exit} we find

$$\frac{\partial\Phi}{\partial\rho_{\text{exit}}} = 0 \quad \Rightarrow \quad \rho_{\text{exit}} = \frac{\rho - \kappa D}{1 - CD}, \quad (\text{B.0.4})$$

and by minimising with respect to κ we find the ray solutions,

$$\begin{aligned} \frac{\partial\Phi}{\partial\kappa} = 0 \quad \Rightarrow \quad \kappa_{\pm} &= \frac{\rho + (\pm\rho_0 - \rho_1)(1 - CD)}{D + L(1 - CD)/n_2} \\ &\approx \frac{\rho \pm \rho_0(1 - CD)}{\frac{1}{n_2}(L + (n_2 - CL)D)}, \end{aligned} \quad (\text{B.0.5})$$

where $\rho_0 \gg \rho_1$ for well developed conical diffraction rings.

Note that when the refractive curvature vanishes we correctly obtain the optical path length for a flat slab,

$$\Phi^{C=0}(\kappa) = \kappa\rho \pm \rho_0\kappa - \frac{1}{2}\kappa^2 \left(\frac{L}{n_2} + D \right), \quad (\text{B.0.6})$$

in which the dimensionless propagation distance is

$$\zeta = \frac{L}{n_2} + D. \quad (\text{B.0.7})$$

Comparing (B.0.5) to the flat slab rays $\kappa_{\pm} = (\rho \pm \rho_0)/\zeta$, we can define parameters for the spherical crystal analogous to ρ_0 and ζ , given by

$$\rho_0 \rightarrow \rho_{\text{ball}} = \rho_0(1 - CD) \quad (\text{B.0.8})$$

$$\zeta \rightarrow \zeta_{\text{ball}} = \frac{L + (n_2 - CL)D}{n_2} = \zeta + \frac{CLd}{n_2}. \quad (\text{B.0.9})$$

The half-angle of the external cone obtained from this paraxial theory is $B \approx A(n - 2)$, consistent with Snell's Law (B.0.1).

The implication of these transformations is that all of the theory detailed in this thesis applies to spherical crystals, subject to this change of variables. The effect, as suggested by figure B.1, is to focus the refracted rays onto an axial point a distance $D = L/(n_2 - 2)$ from the exit face of the crystal, beyond which the image magnifies. Note that for $n_2 > 2$ the focal image plane $\zeta = 0$ is outside the crystal and the most focused rings can easily be imaged even without a lens, something impossible for flat slabs where the focus is inside the crystal.

Since ρ_{ball} is distance dependent it can be extremely large far from the crystal, satisfying the ‘thick crystal’ condition that we have relied on for slabs, but now regardless of the crystal’s size! At the opposite and less interesting extreme, in the plane $D = 1/C$ we have $\rho_{\text{ball}} = 0$. Recall that the asymptotic phenomena of well developed conical diffraction rings arise for $\rho_0 \gg 1$. For small ρ_0 the large width of the beam obscures the conical diffraction pattern which has not yet spread over a large enough conical section to be resolved. $\rho_0 \rightarrow \rho_{\text{ball}} = 0$ is the extreme situation in which the conical diffraction pattern is compressed into a single spot on the axis, reconstructing the incident beam as if the crystal were isotropic.

Furthermore, the evolution of the diffraction pattern, from focused rings, to secondary interference, to axial spot, depends on the dimensionless propagation distance ζ . We have already noted that the zero of this lies outside the crystal for $n_2 > 2$. But ζ_{ball} increases in proportion to $n_2 - CL = 2 - n_2$, so for a crystal whose refractive index is close to 2 (typical of the crystals in table 1.1) the diffraction pattern (and ζ) evolves very slowly, spreading the features that for a slab are typically contained within millimetres of the crystal, out over potentially huge distances, easily on the order of a metre or more.

This paraxial treatment allows us to extend the theory to arbitrary crystal geometries. Firstly the crystal need not be spherical. Let the exit face have a radius of curvature r as above, but let the entrance face have a radius of curvature r_1 for which we must define a new refractive curvature $C_1 = k_0 w^2 (n_2 - 1) / r_1$. It turns out that all of the C ’s above are unaffected, except for the first term in (B.0.3) where C is replaced by C_1 , whose only effect is a distance independent phase shift that has no effect on the intensity or ray geometry. The surfaces may then be arbitrarily curved, provided that the beam is well enough collimated that in the paraxial region the surfaces are approximately spherical with a large radius of curvature.

Finally we can consider the case in which the optic axis is not even perpendicular to the two (possibly curved) faces of the crystal. This introduces a direction dependency in the linear κ terms of the optical path length, which can be dealt with simply by a shift of origin of the transverse coordinate. The result is a simple skew of the diffraction pattern similar to the skew of Hamilton’s refraction cone, which can also be incorporated in the same manner. Thus in the transformed coordinates the theory will again be formally the same.

Appendix C

Glossary of key symbols

A few summary notes on notation: \mathcal{I} is the 2×2 identity matrix; operators (calligraphic font) are 2×2 matrices acting upon 2-vectors (bold face) transverse to the optic axis, with the exception of the crystal 3-vector \mathbf{V} and the Pauli 3-vector $\boldsymbol{\Sigma}$ throughout; in sections 2.1-2.2 and 3.1 only do we assume 3×3 matrices and 3-vectors. Following is a list of some key symbols used extensively throughout the thesis:

<i>Symbol</i>	<i>Definition</i>	<i>Description</i>
---------------	-------------------	--------------------

Variables concerning position space and the crystal:

$\boldsymbol{\Sigma}$	(2.1.15)	The 3-vector of Pauli matrices $\{\sigma_3, \sigma_1, \sigma_2\}$
A	(2.2.6)	Hamilton's conical refraction angle
$\boldsymbol{\rho}, \zeta$	(2.3.1), (2.3.15)	Dimensionless cylindrical position coordinates
$\tilde{\boldsymbol{\rho}}, \tilde{\zeta}$	section 2.4	Complexified position coordinates
$\mathbf{V}(\boldsymbol{\kappa})$	(2.3.10)	3-vector specifying the crystal
ρ_0	(2.3.9)	Biaxiality (ring resolution) parameter
γ	(2.3.9)	Chirality parameter
δ	(2.3.9)	Dichroism parameter
μ	(2.4.3)	Nonhermiticity parameter

Variables concerning plane waves:

$\boldsymbol{\kappa}$	(2.3.2)	Dimensionless transverse wavevector
$\tilde{\boldsymbol{\kappa}}$	section 2.4	Complexified transverse wavevector
$\mathcal{F}(\boldsymbol{\kappa}, \boldsymbol{\rho}, \zeta)$	(2.3.14)	2×2 evolution matrix, operator on plane waves
\mathcal{F}^{tr}	(2.3.14)	Traceless part of \mathcal{F} , $\mathcal{F}_{ij}^{\text{tr}} = \mathcal{F}_{ij} - \frac{1}{2}(\mathcal{F}_{11} + \mathcal{F}_{22})\mathcal{I}$
$\Phi(\boldsymbol{\kappa}, \boldsymbol{\rho}, \zeta)$	(2.7.4)	Optical path length of a refracted ray

Functions concerning the diffracted light beam:

		Complex electric displacement field 2-vector:
$\mathbf{D}(\boldsymbol{\rho}, \zeta)$	(2.5.5)	- of diffracted light beam
$\mathbf{D}_0(\boldsymbol{\rho}, \zeta)$	(2.3.3)	- of incident light beam
\mathbf{d}_0	(2.3.3)	Polarisation of incident light beam
$a(\boldsymbol{\kappa})$	(2.3.3)	Fourier profile of incident light beam
$I(\boldsymbol{\rho}, \zeta)$	(2.7.7)	Intensity of diffracted light beam
$b_{\pm}(\boldsymbol{\rho}, \zeta)$	(2.5.4)	Diffraction integral in eigenwave representation
$B_{m=0,1,2}$	(2.5.6)	Diffraction integral in differential representation
\mathbf{d}_{\pm}	(2.5.8)	Eigenpolarisations of the diffracted light field
$\mathbf{d}_{\chi}^{\text{lin}}$	(2.3.27)	Linear polarisation 2-vector
$\mathbf{d}_{\pm}^{\text{circ}}$	(2.3.28)	Circular polarisation 2-vector
ω	(2.3.26)	Complex polarisation variable

Quantities particular to gaussian beams:

$C_m(r)$	(2.5.17)	Single-variable diffraction integral
$\tilde{\zeta}$	(2.4.7)	Complex-source transformation of ζ
\mathbf{r}, r_0	(2.5.15)	Complex scaling of $\boldsymbol{\rho}$ and ρ_0
$\boldsymbol{\tau}, g$	(2.5.15)	Complex scaling of $\boldsymbol{\kappa}$ and γ
$\boldsymbol{\mu}$	(2.4.8)	Nonhermiticity / beam misalignment parameter

Bibliography

- Abramowitz M & Stegun I A 1972 *Handbook of mathematical functions* National Bureau of Standards Washington.
- Allen L, Barnett S M & Padgett M J 2003 *Optical Angular Momentum* IoP Bristol.
- Allen L, Beijersbergen M W, Spreeuw R J C & Woerdman J P 1992 Orbital angular momentum of light and the transformation of Laguerre-Gaussian laser modes *Phys Rev A* **45**, 8185–8189.
- Andruniow T, Ferre N & Olivucci M 2004 Structure, initial excited-state relaxation, and energy storage of rhodopsin resolved at the multiconfigurational perturbation theory level *PNAS* **101**(52), 17908 – 17913.
- Applegate B E, Barckholtz T A & Miller A M 2003 Explorations of conical intersections and their ramifications for chemistry through the Jahn-Teller effect *Chem Soc Rev* **32**, 38–49.
- Belafhal A 2000 Theoretical intensity distribution of internal conical refraction *Opt Commun* **178**, 257–268.
- Belskii A M & Khapalyuk A P 1978 Internal conical refraction of bounded light beams in biaxial crystals *Opt Spectrosc (USSR)* **44**, 436–439.
- Belsky A M & Stepanov M A 1999 Internal conical refraction of coherent light beams *Opt Commun* **167**, 1–5.
- Belsky A M & Stepanov M A 2002 Internal conical refraction of light beams in biaxial gyrotropic crystals *Opt Commun* **204**, 1–6.

- Berry M V 1989 Uniform asymptotic smoothing of Stokes' discontinuities *Proc R Soc Lond A* **422**, 7–21.
- Berry M V 1998 *in* M. S Soskin, ed., 'Singular optics' Vol. 3487 SPIE Frunzenskoe, Crimea pp. 6–13.
- Berry M V 2004a Asymptotic dominance by subdominant exponentials *Proc R Soc A* **460**, 2629–2636.
- Berry M V 2004b Conical diffraction asymptotics: fine structure of Poggendorff rings and axial spike *J Opt A* **6**, 289–300.
- Berry M V 2004c Physics of nonhermitian degeneracies *Czech J Phys* **54**, 1039–1047.
- Berry M V & Dennis M R 2003 The optical singularities of birefringent dichroic chiral crystals *Proc Roy Soc A* **459**, 1261–1292.
- Berry M V & Howls C J 1990 Stokes surfaces of diffraction catastrophes with codimension three *Nonlinearity* **3**, 281–291.
- Berry M V & Jeffrey M R 2006a Chiral conical diffraction *J Opt A* **8**, 363–72.
- Berry M V & Jeffrey M R 2006b Conical diffraction complexified: dichroism and the transition to double refraction *J Opt A* **8**, 1043–51.
- Berry M V & Jeffrey M R 2007 Conical diffraction: Hamilton's diabolical point at the heart of crystal optics *Prog Opt in press* .
- Berry M V, Jeffrey M R & Lunney J L 2006 Conical diffraction: observations and theory *Proc R Soc A* **462**, 1629–42.
- Berry M V, Jeffrey M R & Mansuripur M 2005 Orbital and spin angular momentum in conical diffraction *J Opt A* **7**, 685–690.
- Berry M V & Mount K E 1972 Semiclassical approximations in wave mechanics *Rep Prog Phys* **35**, 315–397.
- Bloembergen N & Shih H 1969 Conical refraction in nonlinear optics *Opt Comm* **1**(2), 70–72.
- Born M & Wolf E 1959 *Principles of Optics* Pergamon London.

- Bravo-Ortega A & Glasser A H 1991 Theory and application of complex geometric optics in inhomogeneous magnetized plasmas *Phys Fluids B* **3**(3), 529–536.
- Brodskii Y Y, Kondrat'ev I G & Miller M A 1969 Electromagnetic beams in anisotropic media i *Radiophys and Quantum Electron* **12**(9), 1047–1055.
- Brodskii Y Y, Kondrat'ev I G & Miller M A 1972 Electromagnetic beams in anisotropic media ii *Radiophys and Quantum Electron* **15**(4), 447–453.
- Censor D 1977 Fermat's principle and real space-time rays in absorbing media *J Phys A* **10**, 1781–1790.
- Chester C, Friedman B & Ursell F 1957 An extension of the method of steepest descents *Proc Camb Phil Soc* **53**, 599–611.
- Ciattoni A, Cincotti L & Palma C 2003 Angular momentum dynamics of a paraxial beam in a uniaxial crystal *Phys Rev E* **67**, 036618–1–10.
- Clary D C 2005 Geometric phase in chemical reactions *Science* **309**(5738), 1195–1196.
- De Smet D J 1993 4x4 matrix formalism applied to internal conical refraction *J Opt Soc Am A* **10**(1), 186–190.
- Deschamps G A 1971 Gaussian beam as a bundle of complex rays *Electronics Lett* **7**, 684–685.
- Dingle R B 1973 *Asymptotic Expansions: their derivation and interpretation* Academic Press London.
- Dreger M A 1999 Optical beam propagation in biaxial crystals *J Opt A* **1**, 601–616.
- Echarri R & Garea M T 1994 Behaviour of the Poynting vector in uniaxial absorbent media *Pure Appl Opt* **3**, 931–941.
- Eimerl D 1988 Quantum electrodynamics of optical activity in birefringent crystals *J Opt Soc Am B* **5**, 1453–1461.
- Epstein P S 1929 Geometrical optics in absorbing media *Proc Nat Acad Sci USA* **16**, 37–45.
- Fève J P, Boulanger B & Marnier G 1994 Experimental study of internal and external conical refraction in ktp *Opt Commun* **105**, 243–252.

- Fröman N & Fröman P O 1965 *JWKB Approximations* North-Holland Amsterdam.
- Ghosh A & Fischer P 2006 Chiral molecules split light: reflection and refraction in a chiral liquid *PRL* **97**, 173002–1–4.
- Graves R P 1882 *Life of Sir William Rowan Hamilton* Vol. 1 Hodges Figgis Dublin.
- Hahn S & Stock G 2001 Efficient calculation of femtosecond time-resolved photoelectron spectra *J Phys Chem B* **104**, 2331 – 2336.
- Haidinger W 1855 Die konische Refraction am Diopsid, nebst Bemerkungen ber einige Erscheinungen der konischen Refraction an Arragonit *Ann Phys Chem* **XCVI**, 469–487.
- Halász G J, Ágnes V, Baer R & Baer M 2007 Conical intersections induced by the Renner effect in polyatomic molecules *J Phys A* **40**, 267–272.
- Hamilton W R 1828 Theory of systems of rays *Trans Roy Irish Acad* **15**, 69–174.
- Hamilton W R 1837 Third supplement to an essay on the theory of systems of rays *Trans Roy Irish Acad presented to the Royal Irish Academy in 1832* **17**, 1–144.
- Heading J 1962 *An Introduction to Phase-Integral Methods* Methuen London.
- Herzberg G & Longuet-Higgins H C 1963 Intersection of potential energy surfaces in polyatomic molecules *Disc Faraday Soc* **35**, 77–82.
- Jeffrey M R 2006 *Conical diffraction in optically active crystals* IoP Online proceedings of Photon06: <http://photon06.org/Diffractive%20optics%20Thurs%2014%2015.pdf> (Jan 2007).
- Jeffrey M R 2007 The spun cusp complexified: complex ray focusing in chiral conical diffraction *J Opt A* **9**, 634–641.
- Juanes-Marcos J C, Althorpe S C & Wrede E 2005 Theoretical study of geometric phase effects in the hydrogen-exchange reaction *Science* **309**, 1227–1230.
- Kaye G W C & Laby T H 1973 *Tables of physical constants* Longman England.
- Keller J B 1961 Geometrical theory of diffraction *J Opt Soc Am* **52**(2), 116–130.

- Kirk N P, Connor J N L, Curtis P R & Hobbs C A 2000 Theory of axially symmetric cusped focusing: numerical evaluation of a Bessoid integral by an adaptive contour algorithm *J Phys A* **33**, 4797–4808.
- Kofler J & Arnold N 2006 Axially symmetric focusing as a cuspid diffraction catastrophe *Phys Rev B* **73**(235401), 1–15.
- Kravtsov Y A 1968 Two new asymptotic methods in the theory of wave propagation in inhomogeneous media *Sov Phys Acoust* **14**, 1–17.
- Kukura P & etc 2007 Structural observation of the primary isomerization in vision with femtosecond-stimulated Raman *Science* **310**, 1006–1009.
- Lalor E 1972 An analytical approach to the theory of internal conical refraction *J Math Phys* **13**, 449–454.
- Landau L D, Lifshitz E M & Pitaevskii L P 1984 *Electrodynamics of Continuous Media* 2 edn Pergamon Oxford.
- Lloyd H 1837 On the phenomena presented by light in its passage along the axes of biaxial crystals *Trans Roy Irish Acad* **17**, 145–158.
- McGloin D & Dholakia K 2005 Bessel beams: diffraction in a new light *Contemporary Physics* **46**(1), 15–28.
- McSkimin H J & Bond W L 1966 Conical refraction of transverse ultrasonic waves in quartz *J Acoust Soc Am* **39**, 499–505.
- Mead C A & Truhlar D G 1979 On the determination of Born-Oppenheimer nuclear motion wave functions including complications due to conical intersections and identical nuclei *J Chem Phys* **70**, 2284–2296. reprinted in pp 90-103 of Shapere and Wilczek 1989.
- Melmore S 1942 Conical refraction *Nature* **150**(3804), 382–3.
- Moskvin D N, Romanov V P & Val'kov A Y 1993 Green's functions of the electromagnetic field in biaxial media *Phys Rev E* **28**(2), 1436–1446.
- Naida O N 1979 Tangential conical refraction in a three-dimensional inhomogeneous weakly anisotropic medium *Sov Phys JETP* **50**, 239–245.

- Nye J F 1985 *Physical properties of crystals: their representation by tensors and matrices* Clarendon(Oxford).
- Nye J F 1999 *Natural focusing and fine structure of light: caustic and wave dislocations* IoP(Bristol).
- O'Hara J G 1982 The prediction and discovery of conical refraction by William Rowan Hamilton and Humphrey Lloyd (1832-1833) *Proc Roy Irish Acad* **82A**, 231–257.
- Pancharatnam S 1955*a* The propagation of light in absorbing biaxial crystals - i Theoretical *Proc Ind Acad Sci* **XLII**, 86–109.
- Pancharatnam S 1955*b* The propagation of light in absorbing biaxial crystals - ii Experimental *Proc Ind Acad Sci* **XLII**, 235–248.
- Paris R B 1991 The asymptotic behaviour of Pearcey's integral for complex variable *Proc R Soc A* **432**, 391–426.
- Perkal'skis B S & Mikhailichenko Y P 1979 Demonstration of conical refraction *Izv Vyss Uch Zav Fiz* **8**, 103–105.
- Poggendorff J C 1839 Ueber die konische Refraction *Pogg Ann* **48**, 461–462.
- Portigal D L & Burstein E 1969 Internal conical refraction *J Opt Soc Amer* **59**, 1567–1573.
- Portigal D L & Burstein E 1972 Effect of optical activity or Faraday rotation on internal conical refraction *J Opt Soc Amer* **62**, 859–864.
- Poston T & Stewart I N 1976 *Taylor expansions and catastrophes* Pitman(London).
- Poston T & Stewart I N 1996 *Catastrophe theory and its applications* Dover.
- Potter R 1841 An examination of the phaenomena of conical refraction in biaxial crystals *Phil Mag* **18**, 343–353.
- Potts A, Bagnall D M & Zheludev N I 2004 A new model of geometric chirality for two dimensional continuous media and planar meta-materials *J Opt A* **6**, 193–203.
- Raman C V 1921 Conical refraction in biaxial crystals *Nature* **107**(2702), 747.
- Raman C V 1942 The phenomena of conical refraction *Curr Science* **11**, 44–46.

- Raman C V, Rajagopalan V S & Nedungadi T M K 1941 Conical refraction in naphthalene crystals *Proc Ind Acad Sci* **A14**, 221–227.
- Rümpker G & Kendall J M 2002 A Maslov-propagator seismogram for weakly anisotropic media *Geophys J Int* **150**, 23–36.
- Rümpker G & Thompson C J 1994 Seismic waveform effects of conical points in gradually varying anisotropic media *Geophys J Int* **118**, 759–780.
- Schell A J & Bloembergen N 1978*a* Laser studies of internal conical diffraction i Quantitative comparison of experimental and theoretical conical intensity distribution in aragonite *J Opt Soc Amer* **68**, 1093–1098.
- Schell A J & Bloembergen N 1978*b* Laser studies of internal conical diffraction ii Intensity patterns in an optically active crystal, α -iodic acid *J Opt Soc Amer* **68**, 1098–1106.
- Schultz T 2004 A plant ABC transporter takes the lotus seat *Science* **306**(5696), 622 – 625.
- Shih H & Bloembergen N 1969 Conical refraction in second-harmonic generation *Phys Rev* **184**(3), 895–904.
- Silverman M P & Sohn R B 1986 Effects of circular birefringence on light propagation and reflection *Am J Phys* **54**, 69–76.
- Stepanov M A 2002 Transformation of Bessel beams under internal conical refraction *Opt Commun* **212**, 11–16.
- Stokes G G 1847*a* On the critical values of the sums of periodic series *Trans Camb Phil Soc* **8**, 533–610.
- Stokes G G 1847*b* On the numerical calculation of a class of definite integrals and infinite series *Trans Camb Phil Soc* **9**.
- Stokes G G 1863 Report on double refraction *Rept Brit Assoc Sci for 1862* pp. 253–283.
- Stokes G G 1864 On the discontinuity of arbitrary constants which appear in divergent developments *Trans Camb Phil Soc* **10**, 106–128.
- Stokes G G 1902 On the discontinuity of arbitrary constants that appear as multipliers of semi-convergent series *Acta Math* **26**, 393–397.

- Stokes G G 1907 *Sir George Gabriel Stokes, Memoirs and Scientific Correspondence* Vol. 1 Cambridge.
- Uhlmann A 1982 Light intensity distribution in conical refraction *Commns Pure App Math* **35**, 69–80.
- Voigt W 1902 On the behaviour of pleochroitic crystals along directions in the neighbourhood of an optic axis *Phil Mag* **4**, 90–97.
- Voigt W 1905a Bemerkung zur Theorie der konischen Refraktion *Phys Z* **6**, 672–673.
- Voigt W 1905b Theoretisches und Experimentelles zur Aufklaerung des optischen Verhaltens aktiver Kristalle *Ann Phys* **18**, 645–694.
- Voigt W 1905c Ueber die Wellen flaeche zweiachsiger aktiver Kristalle und ueber ihre konische Refraktion *Phys Z* **6**, 787–790.
- Voigt W 1906 Bemerkungen zur Theorie der konische Refraktion *Ann Phys* **19**, 14–21.
- Voigt W 1907 Ueber die sogenannte innere konische Refraktion bei pleocritischen Kristallen *Ann Phys* **20**, 108–126.
- Warnick K F & Arnold D V 1997 Secondary dark rings of internal conical refraction *Phys Rev E* **55**, 6092–6096.
- Watson G N 1944 *Bessel functions* Cambridge.
- Whittaker E 1951 *A history of theories of aether and electricity: the classical theories* Thomas Nelson and Sons Ltd.
- Wilkins D R 2005 *Perplexingly easy: selected correspondence between William Rowan Hamilton and Peter Guthrie Tait* Trinity College Dublin Press Dublin.
- Wong R 1989 *Asymptotic approximations to integrals* Academic Press New York and London.
- Wright F J 1980 The Stokes set of the cusp diffraction catastrophe *J Phys A* **13**, 2913–2928.